Linking Immature Auditory Processing with an Autism Phenotype in the *Bdnf*^{Pax2} KO Mouse Model

Dissertation

zur Erlangung des Grades eines
Doktors der Naturwissenschaften

der Mathematisch-Naturwissenschaftlichen Fakultät
und
der Medizinischen Fakultät
der Eberhard-Karls-Universität Tübingen

vorgelegt
von

Morgan Elizabeth Hess
aus Greenville, South Carolina, Vereinigte Staaten

2024

Tag der mündlichen Prüfung: 02.10.2024

Dekan der Math.-Nat. Fakultät:	Prof. Dr. Thilo Stehle
Dekan der Medizinischen Fakultät:	Prof. Dr. Bernd Pichler
1. Berichterstatter:	Prof. Dr. Marlies Knipper
2. Berichterstatter:	Prof. Dr. Steffen Hage
Prüfungskommission:	Prof. Dr. Marlies Knipper
	Prof. Dr. Steffen Hage
	Prof. Dr. Peter Ruth
	Jun.-Prof. Lena Veit

Erklärung / Declaration:

Ich erkläre, dass ich die zur Promotion eingereichte Arbeit mit dem Titel:

„Linking Immature Auditory Processing with an Autism Phenotype in the *Bdnf*^{Pax2} KO Mouse Model“

selbständig verfasst, nur die angegebenen Quellen und Hilfsmittel benutzt und wörtlich oder inhaltlich übernommene Stellen als solche gekennzeichnet habe. Ich versichere an Eides statt, dass diese Angaben wahr sind und dass ich nichts verschwiegen habe. Mir ist bekannt, dass die falsche Abgabe einer Versicherung an Eides statt mit Freiheitsstrafe bis zu drei Jahren oder mit Geldstrafe bestraft wird.

I hereby declare that I have produced the work entitled "Linking Immature Auditory Processing with an Autism Phenotype in the Bdnf^{Pax2} *KO Mouse Model", submitted for the award of a doctorate, on my own (without external help), have used only the sources and aids indicated and have marked passages included from other works, whether verbatim or in content, as such. I swear upon oath that these statements are true and that I have not concealed anything. I am aware that making a false declaration under oath is punishable by a term of imprisonment of up to three years or by a fine.*

Tübingen, den ....

Datum / Date Unterschrift /Signature

ABSTRACT

Hearing and cognition are tightly bound together in a link that enables complex processes such as language learning and communication. The establishment of this link critically depends on proper development of the ascending auditory pathway and its connections to higher order regions. Neural development occurs hierarchically in terms of complexity, meaning that mature sensory processing is a prerequisite for mature cognitive processing. Because sensory system development requires a series of maturational events occurring in sequence from the peripheral to the central nervous system, we hypothesized that a disruption in peripheral processes early in development can cascade along the ascending pathway and result in higher level cognitive deficits.

To examine the link between immature sensory processing and higher-level cognitive processes, we used a model in which brain-derived neurotrophic factor (*Bdnf*) was deleted from paired box gene 2 (*Pax2*)-expressing interneurons (INs) that migrate to lower brain regions, including the auditory brainstem, and the cochlea ("$Bdnf^{Pax2}$ KO"). As BDNF has been suggested to trigger neuronal maturation, this model is assumed to result in a specific subset of INs in the peripheral auditory system remaining in an immature state. This deletion affected not only the hearing of $Bdnf^{Pax2}$ KO mice but also higher-level cognitive processes, leading to social interaction deficits and stereotypic behavior—both core diagnostic criteria of autism spectrum disorder (ASD). We therefore here aimed to further characterize the phenotype of $Bdnf^{Pax2}$ KO mice on a functional, molecular, and structural level, and found that these mice exhibited neural response characteristics, excitatory and inhibitory molecular markers, and dendritic spine morphology consistent with other animal models of ASD.

Having validated a phenotype strongly consistent with ASD in this model, we then examined how the immature sensory processing of $Bdnf^{Pax2}$ KO mice led to this central phenotype. We discovered that a specific class of auditory nerve fibers remained under-responsive in these mice, which may reflect an immature state resulting from insufficient inhibitory shaping during development. We speculate that this persisting immaturity in the periphery interfered with the maturation of more complex, cognitive processes and resulted in an ASD phenotype.

The absence of a known disease mechanism causing ASD has hindered the search for effective treatment options. Thus, having identified a putative underlying neural mechanism in our model, we used two different treatment approaches tailored to nudge the phenotype of adult $Bdnf^{Pax2}$ KO mice back to a physiological state. First, a pharmaceutical approach was used to target the more central aspects of the phenotype, but it yielded no therapeutic benefit for $Bdnf^{Pax2}$ KO mice. We propose that this is because the central aspects of the phenotype are a secondary effect to the underlying peripheral deficit. Thus, the next treatment approach was a sensory-specific enrichment paradigm that targeted the more peripheral aspects of the phenotype. This treatment resulted in a reversal of the hearing phenotype of $Bdnf^{Pax2}$ KO mice but still did not recover cognitive aspects of the phenotype.

These findings indicate that, while more peripheral and comparatively simple sensory processing can be rescued during adulthood, more complex central processes cannot be. This would necessitate an early intervention strategy for developmental disorders such as ASD, using treatments that target the underlying peripheral, sensory deficits.

ZUSAMMENFASSUNG

Hören und Kognition sind eng miteinander verbunden und ermöglichen komplexe Prozesse wie das Erlernen von Sprache und Kommunikation. Die Entstehung dieser Verbindung hängt entscheidend von der richtigen Entwicklung der aufsteigenden Hörbahn und ihrer Verbindungen zu Regionen höherer Ordnung ab. Die neuronale Entwicklung erfolgt hierarchisch in Bezug auf die Komplexität, was bedeutet, dass eine ausgereifte sensorische Verarbeitung Voraussetzung für eine ausgereifte kognitive Verarbeitung ist. Da die Entwicklung des sensorischen Systems eine Reihe von Reifungsprozessen erfordert, die nacheinander vom peripheren zum zentralen Nervensystem ablaufen, stellten wir die Hypothese auf, dass eine Störung der peripheren Prozesse zu Beginn der Entwicklung kaskadenartig die aufsteigende Hörbahn durchlaufen und zu kognitiven Defiziten auf höherer Ebene führen kann.

Um den Zusammenhang zwischen unreifer sensorischer Verarbeitung und kognitiven Prozessen auf höherer Ebene zu untersuchen, haben wir ein Modell verwendet, bei dem der brain-derived neurotrophic factor (*Bdnf*) aus Interneuronen (INs) entfernt wurde, die das Paired-Box-Gen 2 (*Pax2*) exprimieren und in niedere Hirnregionen wie den auditorischen Hirnstamm und die Cochlea wandern („$Bdnf^{Pax2}$ KO“). Da vermutet wird, dass BDNF neuronale Reifung auslöst, wird angenommen, dass dieses Modell dazu führt, dass eine bestimmte Untergruppe von INs im peripheren auditorischen System in einem unreifen Zustand bleibt. Diese Deletion beeinträchtigt nicht nur das Hörvermögen von $Bdnf^{Pax2}$ KO-Mäusen, sondern auch kognitive Prozesse auf höherer Ebene, was zu Defiziten in der sozialen Interaktion und stereotypem Verhalten führt – beides zentrale diagnostische Kriterien für Autismus-Spektrum-Störungen (ASD). Wir haben daher versucht, den Phänotyp von $Bdnf^{Pax2}$ KO-Mäusen auf funktioneller, molekularer und struktureller Ebene weiter zu charakterisieren, und festgestellt, dass diese Mäuse neuronale Reaktionsmerkmale, exzitatorische und inhibitorische molekulare Marker und eine Dornenfortsatzmorphologie aufweisen, die mit anderen Tiermodellen von ASD übereinstimmen.

Nach der Validierung eines Phänotyps, der stark mit ASD in diesem Modell übereinstimmt, untersuchten wir, wie die unreife sensorische Verarbeitung von $Bdnf^{Pax2}$ KO-Mäusen zu diesem zentralen Phänotyp führte. Wir entdeckten, dass eine bestimmte Klasse von Hörnervenfasern bei diesen Mäusen unterempfindlich blieb, was auf einen unreifen Zustand infolge einer unzureichenden negativen Rückkopplung während der Entwicklung zurückzuführen sein könnte. Wir vermuten, dass diese fortbestehende Unreife in der Peripherie die Reifung komplexerer kognitiver Prozesse behindert und zu einem ASD-Phänotyp führt.

Das Fehlen eines bekannten Krankheitsmechanismus von ASD erschwert die Suche nach wirksamen Behandlungsmöglichkeiten. Nachdem wir in unserem Modell einen mutmaßlich zugrunde liegenden neuronalen Mechanismus identifiziert hatten, verwendeten wir zwei verschiedene Behandlungsansätze, um den Phänotyp erwachsener $Bdnf^{Pax2}$ KO-Mäuse wieder in einen physiologischen Zustand zu bringen. Zunächst wurde ein pharmazeutischer Ansatz verwendet, der auf die zentraleren Aspekte des Phänotyps abzielte, jedoch keinen therapeutischen Nutzen für $Bdnf^{Pax2}$ KO -Mäuse erbrachte. Wir vermuten, dass dies darauf zurückzuführen ist, dass die zentralen Aspekte des Phänotyps eine sekundäre Wirkung des zugrunde liegenden peripheren Defizits sind. Der nächste Behandlungsansatz war daher ein sensorisch-spezifisches Enrichmentparadigma, das auf die eher peripheren Aspekte des Phänotyps abzielte. Diese Behandlung führte zu einer Umkehrung des Hörphänotyps von $Bdnf^{Pax2}$ KO-Mäusen, konnte aber die kognitiven Aspekte des Phänotyps noch nicht wiederherstellen.

Diese Ergebnisse deuten darauf hin, dass zwar die eher peripheren und vergleichsweise einfachen sensorischen Verarbeitungsprozesse im Erwachsenenalter wiederhergestellt werden können, die komplexeren zentralen Prozesse jedoch nicht. Dies würde eine frühzeitige Interventionsstrategie für Entwicklungsstörungen wie ASD erforderlich machen, bei der Behandlungen eingesetzt werden, die auf die zugrunde liegenden peripheren sensorischen Defizite abzielen.

TABLE OF CONTENTS

1 INTRODUCTION

Hearing and cognition are two inextricably linked processes. Functional evidence for this link comes from reports showing that hearing loss is a major risk factor for the development of dementia (Livingston et al., 2017) and that this risk can be reduced by the early use of a hearing aid (Livingston et al., 2020). However, hearing ability and cognitive ability are not only linked in old age but also during development. Consideration of the interdependence of hearing and cognition in the developing brain is of critical importance for developmental disorders associated with auditory processing deficits, such as autism spectrum disorder (ASD).

In this work, we will see that ASD symptoms can arise from a mouse model in which no known ASD gene was directly deleted. We will then examine the basis of these ASD symptoms and see that they originate from the persistent immaturity of a critical structure in the peripheral auditory system, an effect that cascades along the ascending pathway and eventually affects higher-level cognitive processes. Next, we will attempt to recover this phenotype using two treatment approaches. The first will be an approach that targets the secondary central phenotype, and the second will be an approach that targets the primary peripheral phenotype. Finally, we will propose that our results necessitate an early therapeutic intervention targeting underlying sensory deficits in developmental disorders such as ASD.

To this end, in this first chapter, I will first explore the mature system of hearing and cognition to understand the functional dependence of these two processes in adults (see section 1.1). Then, I will present how the peripheral and central auditory system develop and explain how the development of higher-level processes is contingent upon lower-level processes having matured (see section 1.2). This foundation is crucial for understanding the basis of developmental disorders, such as ASD. Accordingly, I will then present ASD, going over the pathogenesis and associated models before proposing an underlying, unifying neural mechanism (see section 1.3). Finally, I will introduce the mouse model that we will use to examine this underlying neural mechanism (see section 1.4) before presenting the specific aims and objectives of this work, including two treatment approaches to attempt to recover the phenotype (see section 1.5).

1.1 HEARING AND COGNITION

The sense of hearing is crucial to be able to interact with the world. In animals, hearing is important for threat detection and interaction with conspecifics. However, for humans in particular, hearing is of special significance for us to be able to understand speech and communicate with one another. Speech is an incredibly complex stimulus with extremely fast and subtle variations in the waveform that are critical for understanding. To keep up with this, the auditory system is optimized to enable the speedy and faithful transmission of acoustic information.

1.1.1 The Ascending Auditory Pathway

Acoustic stimuli are created by vibrating air molecules that radiate in waves out from the source. Sound waves can be characterized by their waveform (shape as a function of time), phase (the fraction of a cycle completed since last passing through a reference point), amplitude (magnitude of displacement compared to a reference value), and frequency (number of repeating units per unit of time). However, most natural sounds, such as speech, tend to be complex waveforms that can be modeled as the sum of single sine waves (i.e., pure tones), which the auditory system then works to deconstruct into its single frequency components (Fettiplace, 2017; Gerhard, 2013). Sound-induced changes in air pressure are extremely small in magnitude, meaning that the auditory system must have several amplification mechanisms in place to ensure high sensitivity (Kandel, 2013).

The first amplification mechanism of the auditory system is in the outer ear, where the pinna and concha act as a funnel to capture sound waves and focus them into the ear canal towards the tympanic membrane, selectively amplifying frequencies around the range of human speech (**Figure 1.1A**, outer ear; Gerhard, 2013). The tympanic membrane forms the barrier between the external and middle ear, and upon its vibration, several mechanical forces in the middle ear function to further amplify the sound wave for optimal transmission into the fluid-filled environment of the inner ear (**Figure 1.1A**, middle ear; Fettiplace, 2017).

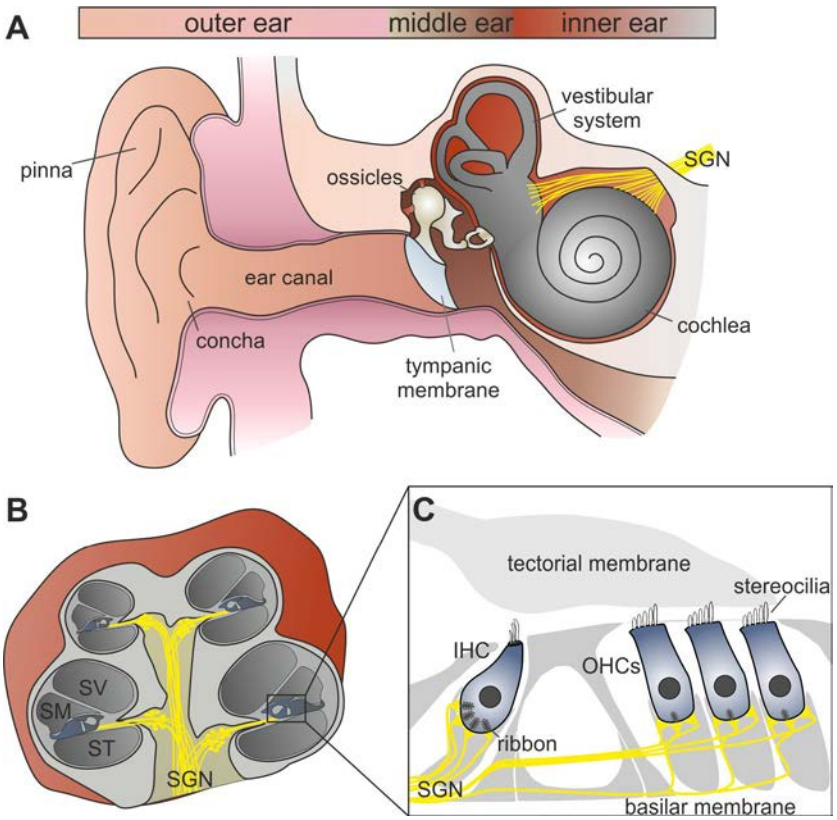

Figure 1.1. *The ear and cochlea. (**A**) Diagram of the outer, middle, and inner ear. (**B**) Cross-section of the cochlea. (**C**) Higher magnification of the organ of Corti. IHC, inner hair cell; OHC, outer hair cell; SGN, spiral ganglion neuron; SM, scala media; ST, scala tympani; SV, scala vestibuli.*

The first amplification mechanism is the transmission of the sound from the comparatively large area of the tympanic membrane to the much-smaller oval window, which forms the barrier to the inner ear. The second amplification function is accomplished by the lever motion of the ossicles, or middle ear bones called the malleus, incus, and stapes (**Figure 1.1A**, ossicles). The malleus is attached to the tympanic membrane and transmits its vibration to the stapes via the incus in a lever motion. The stapes is attached to the oval window and thus transmits the sound into the inner ear (Kandel, 2013). Together, these processes allow for a 100-fold amplification of the sound pressure from the outer ear to the inner ear.

The inner ear is composed of the vestibular system (i.e., the vestibule and the semicircular canals) and the cochlea, which is the structure responsible for the transduction of the mechanical sound stimulus into neural signals (**Figure 1.1A**, inner ear). “Cochlea” is the Latin word for “snail” because it is a small, coiled structure surrounded by bone that resembles a snail shell. Sound enters the cochlea by the vibration of the stapes on the oval window (Fettiplace, 2017).

Inside the cochlea are three fluid-filled chambers—the scala vestibuli, the scala tympani, and the scala media (**Figure 1.1B**, SV, ST, SM). Dividing the scala media and scala tympani is the basilar membrane, which vibrates in response to sound. The basilar membrane varies in stiffness and width, with its apical end being more flexible and wider than its base (Kandel, 2013). Acoustic stimuli displace the basilar membrane in a traveling wave that increases in amplitude and decreases in velocity until reaching a peak of maximum displacement (Gerhard, 2013). Due to the geometry of the basilar membrane, higher frequency tones peak near the base, while lower frequency tones peak near the apex (Von Békésy, 1960). Accordingly, the inner hair cells (IHCs) that are situated in the organ of Corti on the basilar membrane and are responsible for transducing acoustic stimuli into neural signals are also frequency-

tuned and respond according to the corresponding frequency of maximal displacement at that location (Kandel, 2013).

The traveling wave physically displaces the sensory hair cells that are situated upon the basilar membrane through a shearing motion that moves the endolymph between the basilar membrane and the tectorial membrane, which sits above the hair cells (**Figure 1.1C**; Fettiplace, 2017). The endolymph is able to move because of another membrane located at the basal end of the cochlea called the round window. The round window vibrates in opposite phase to the oval window, thus ensuring that the fluid is not compressed (Kandel, 2013; Zhang & Gan, 2013). The motion of the endolymph then bends the stereocilia, tiny hair-like structures protruding from hair cells, which physically pulls open ion channels and depolarizes the cell (Fettiplace, 2017). As the basilar membrane sits between the scala media, filled with positively charged endolymph, and the scala tympani, filled with negatively charged perilymph, ions flow along the electrical gradient towards the base of the cell (Gerhard, 2013).

Mammals have one row of IHCs and three rows of outer hair cells (OHCs; **Figure 1.1C**, IHC, OHCs). OHCs are electromotile, meaning that upon depolarization they physically expand and contract, pushing and pulling the tectorial membrane to which their stereocilia are attached, thereby increasing the fluid motion of the endolymph (Kandel, 2013). This process mechanically amplifies low-amplitude sounds entering the cochlea to optimize the system's sensitivity. This amplification distorts acoustic stimuli, which are then reflected out of the cochlea and can be measured by a sensitive microphone as the distortion product of otoacoustic emissions (DPOAE; Janssen et al., 2006). IHCs, on the other hand, are the sensory transducer cell. Upon displacement of their stereocilia, positively charged ions enter and depolarize the cell, triggering the release of neurotransmitters at the basal end (Gerhard, 2013). The neurotransmitter release of IHCs is incredibly rapid due to a specialized synaptic ribbon structure that docks vesicles close to the active zone to achieve high-frequency transmission (Glowatzki & Fuchs, 2002). Neurotransmitters then travel across the synaptic cleft and bind to glutamate receptors on afferent spiral ganglion neurons (SGNs).

SGNs can be divided into two subtypes. Type I SGNs account for 90–95% of all SGNs. They are large, myelinated fibers that innervate IHCs. Type II SGNs account for the remaining 5–10% of SGNs. They are small, unmyelinated fibers that innervate OHCs. While many type I SGNs can innervate a single IHC, many OHCs are innervated by a single type II SGN (Gerhard, 2013; Heil & Peterson, 2015; Kandel, 2013).

Type I SGNs are, as a population, optimized to have both an extremely wide dynamic range and to encode sensory stimuli with a high degree of temporal precision. This is accomplished by having fibers with a range of sensitivities and spontaneous rates (SRs). Low threshold, high-SR fibers are activated at the lowest sound pressure levels (SPLs), making them primarily responsible for setting the hearing threshold (Liberman, 1978). In addition, they provide the shortest latency response to a given stimulus, making them important for precise temporal sound coding (Bharadwaj et al., 2014). High threshold, low-SR fibers, on the other hand, are activated only at higher SPLs, but their activity is slower to saturate with increasing stimulus intensity. This makes them important for hearing in noisy environments (Heil & Peterson, 2015; Liberman, 1978). The functional contribution of these two fiber types can be predicted by measuring the peristimulus time response (PSTR) from electrodes placed near the round window.

The cochlea also receives efferent innervation from two classes of fibers that originate in the superior olivary complex in the brainstem (**Figure 1.2**, SOC). Medial olivocochlear (MOC) fibers are large, myelinated fibers that synapse directly onto the soma of OHCs to modulate their activity (Guinan, 2006). MOC activation rapidly (~100 ms) modulates OHC activity to dampen the cochlear response to sound, possibly to protect against noise damage (Kujawa & Liberman, 2001; Liberman et al., 1996). Additionally, constant activation of MOC efferents leads to a decrease in responses to continuous sounds such as background noise, thus aiding, for example, speech perception in noisy environments

(Guinan, 2006). Lateral olivocochlear (LOC) fibers, on the other hand, are small and unmyelinated. They synapse on dendrites of type I SGNs. Like MOC efferents, their activation also produces changes in cochlear responses, though on a much slower time scale (Guinan, 2006).

In the traditional presentation of the ascending auditory pathway, SGNs project to the cochlear nucleus, which is divided into dorsal and ventral nuclei (**Figure 1.2**, DCN, VCN). Neurons of the ventral cochlear nucleus project both to the dorsal cochlear nucleus and to the superior olivary complex, which then has projections to the inferior colliculus (IC; **Figure 1.2**, SOC, IC). The activity of the ascending auditory pathway can be measured as the auditory brainstem response (ABR) from subcutaneous electrodes placed near the ear. Each wave of the ABR correlates with the activity of a distinct structure along the ascending pathway, from wave I, which reflects the activity of the auditory nerve, to wave IV, which reflects the activity of the lateral lemniscus and IC (Burkard et al., 2007). The IC relays information to the thalamic medial geniculate body which then has projections to the primary auditory cortex (AC; **Figure 1.2**, MGB, AC). This is a very straightforward, bottom-up concept of sensory processing in which sensory information is analyzed in one direction (Kandel, 2013). In reality, of course, the system is much more interconnected, with top-down processes performing constant optimization and error correction (**Figure 1.2**, open arrows).

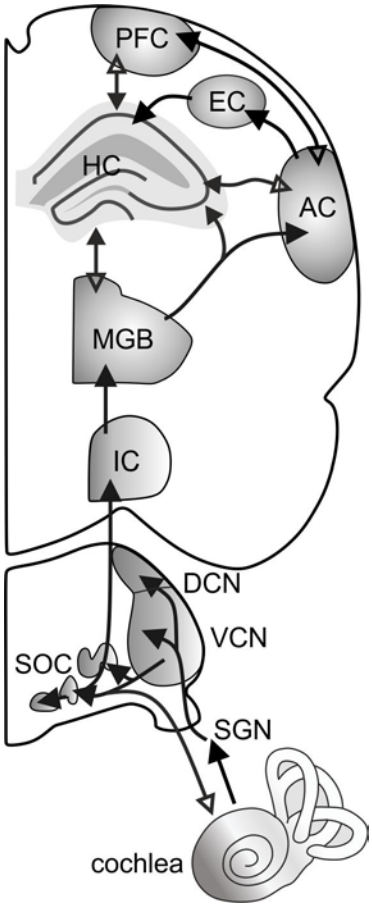

Figure 1.2. *The ascending auditory pathway. AC, auditory cortex; DCN, dorsal cochlear nucleus; EC, entorhinal cortex; HC, hippocampus; IC, inferior colliculus; MGB, medial geniculate body; PFC, prefrontal cortex; SGN, spiral ganglion neuron; SOC, superior olivary complex; VCN, ventral cochlear nucleus.*

1.1.2 The Hippocampus as Part of the Auditory System

Traditionally, the conversation about the auditory pathway stops when the primary AC projects to the secondary AC and association areas (**Figure 1.2**, AC). However, in order to interact effectively with the world, sensory information must be constantly updated and integrated with information processed elsewhere in the brain, such as motor activity, emotion, or memory.

The hippocampus, sometimes called the "memory center" of the brain, is a structure that has a well-established role in episodic memory and spatial navigation (O'Keefe & Dostrovsky, 1971; Scoville & Milner, 1957; Zola-Morgan et al., 1991). It is composed of two major parts: the dentate gyrus and the cornu Ammonis (CA), which is subdivided into CA1, CA2, and CA3 in rodents. The major input source of the hippocampus is a projection from the entorhinal cortex, which is highly connected and receives input from many subcortical and cortical structures, including the AC (**Figure 1.2**, EC, AC). The major output of the hippocampus comes from the CA1 region, which receives information through a characteristic trisynaptic circuit.

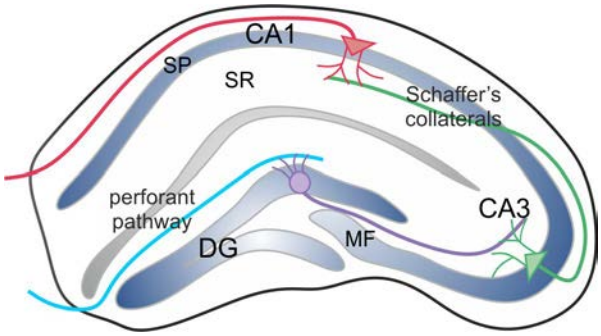

Figure 1.3. *Trisynaptic circuit of the hippocampus. Blue, perforant pathway. Purple, mossy fibers (MF). Green, Schaffer's collaterals. Red, CA1 pyramidal neurons. DG, dentate gyrus; SP, stratum pyramidale; SR, stratum radiatum.*

In the first synapse of the trisynaptic circuit, the entorhinal cortex projects to the granule cells of the dentate gyrus via the perforant pathway (**Figure 1.3**, blue). In the second synapse, the granule cells of the dentate gyrus project to the pyramidal neurons of the CA3 region via mossy

fibers (**Figure 1.3**, purple). In the third synapse, CA3 pyramidal neurons project to the CA1 region via Schaffer's collaterals (**Figure 1.3**, green). Axons from CA1 then project out from the hippocampus to the entorhinal cortex and other cortical and subcortical regions, including the AC (**Figure 1.3**, red; **Figure 1.2**, HC, PFC, AC; Fröhlich, 2016). The functionality of this circuit can be measured through stimulating the Schaffer's collaterals with a high-frequency stimulation and measuring the long-lasting activity increase in the dendrites of CA1 pyramidal neurons, termed long-term potentiation (LTP; Nicoll, 2017).

The hippocampus also has a much less understood role in hearing and sound perception. It has been known for nearly 30 years that the hippocampus responds to sound (Bickford & Wear, 1995; Manohar et al., 2022; Moita et al., 2003; Moxon et al., 1999) and other sensory stimuli (Cooper et al., 1998; Gener et al., 2013; Levy et al., 2004; Manohar et al., 2022; Martin et al., 2007; Tamura et al., 1992). In fact, some researchers propose that the role of the hippocampus is integral for the auditory percept, suggesting that it integrates sensory information into a perceptual whole, among other things (Billig et al., 2022).

The deep role of the hippocampus in auditory processing is reflected by the wide variety of responses it has to acoustic stimuli. The hippocampus responds to sound in passive and active listening, its activity can be entrained by sound, it links acoustic stimuli with other sensory stimuli to form episodic memories, it aids in the processing of complex stimuli like music, speech, or emotional sound, and its activity and structure can be shaped by auditory experience or lack thereof (for a review, see Billig et al., 2022). It is by appreciating these functions that the hippocampus has been referred to as part of a "non-canonic" auditory system.

With this in mind, it becomes obvious that when auditory input to the hippocampus is lost (e.g., because of noise-induced hearing loss or age-related hearing loss), hippocampal function would decline. Indeed, functional evidence for this comes from the report that hearing loss is the largest modifiable risk factor for dementia (Livingston et al., 2017). Remarkably, this risk can be mitigated upon the use of hearing aids (Livingston et al., 2020).

As the hippocampus is critical for integrating sensory information into a perceptual whole that we can then use to navigate and interact with the world, and its activity is shaped by experience, then this process would critically depend on the proper development of precise bottom-up sensory encoding.

1.2 Development of the Auditory System

1.2.1 Development of the Inner Ear

The vertebrate inner ear is derived from the embryonic ectoderm. At the edges of the neural plate, the otic placode can be recognized as early as embryonic day (E) 3–6 in mice. From there, the otic placode folds in on itself and forms the otic cup. At E9.5, the otic cup forms the otic vesicle. Cells then delaminate from the otic vesicle and form the cochleovestibular ganglion, which later splits into the separate cochlear and vestibular ganglia. Meanwhile, the otic vesicle undergoes a period of strong proliferative growth before specialized cell types begin differentiating (Torres & Giraldez, 1998). IHCs can be identified as early as E14.5, and, likely after a short delay, OHCs follow (Bulankina & Moser, 2012).

Afferent and efferent fibers can be observed in the mouse oocyst as early as E11.5 and E12, respectively, but their innervation pattern is branched and tangled. SGNs undergo a pruning process and by E15.5 they appear as single unbranched fibers. At E16.5, the first SGN innervation of OHCs can be observed, and by E18.5, both afferent and efferent fibers extend through all three rows of OHCs (Bulankina & Moser, 2012).

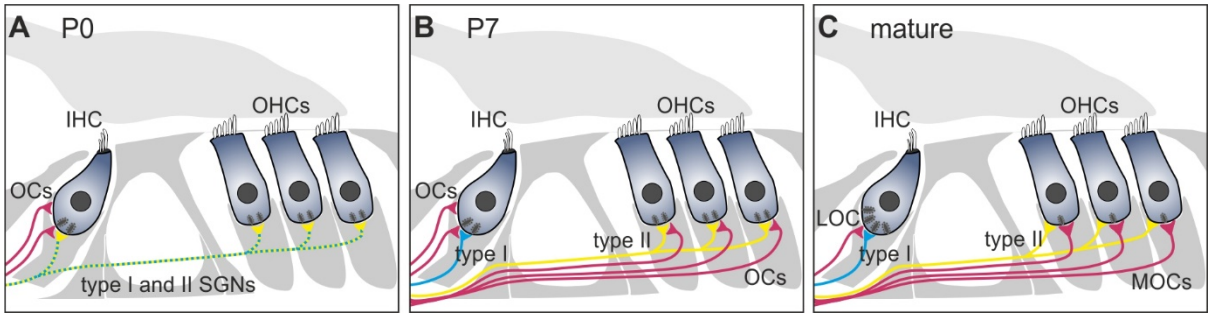

Figure 1.4. *Maturation of afferent and efferent innervation of the cochlea. (**A**) Innervation pattern at P0 depicting the type I and II afferent SGNs (yellow and blue) and the olivocochlear efferents (OC, magenta). (**B**) Innervation pattern at P7 depicting the newly differentiated type I (blue) and type II (yellow) SGNs innervating IHCs and OHCs, respectively, and the OC efferents. (**C**) Innervation pattern at P12 and onward, reflecting the mature configuration of afferents and efferents. Adapted from Bulankina & Moser, 2012.*

At birth, murine IHCs have three types of synapses: (1) immature synapses from afferents to the IHC soma, (2) transient synapses from MOC efferents to the IHC soma, and (3) synapses from LOC efferents onto the dendrites of afferents. OHCs, on the other hand, only have afferent fiber innervation (**Figure 1.4A**; Bulankina & Moser, 2012). By postnatal day (P) seven, type I SGNs innervating IHCs and type II SGNs innervating OHCs can be distinguished, but IHCs still exhibit the transient MOC innervation. Additionally at P7, efferents can be found in close proximity to OHCs for the first time (**Figure 1.4B**; Bulankina & Moser, 2012). By hearing onset at P12, the configuration of afferents and efferents has reached its mature state, with the transient axo-somatic innervation of IHCs by MOC efferents having disappeared in favor of axo-dendritic innervation of type I SGNs by LOC efferents and MOC innervation of OHCs (**Figure 1.4C**; Bulankina & Moser, 2012).

After the basic circuitry is in place, the type I SGNs further specify into different subclasses, distinguished by their SR and response thresholds, as previously described (see section 1.1.1). However, the mechanism leading to the differentiation of these fiber types is still under debate. Shrestha et al. (2018) showed that, prior to hearing onset, genetic markers of low- and high-SR fibers are already present in mice at E18.5; however, their expression at that point is still broad and overlapping. By P3, the expression of the markers starts becoming more restricted. This process continues over the first three weeks of postnatal development until the expression resembles the mature state by P26. Critically, the genetic differentiation of low-SR fibers from high-SR fibers is dependent upon spontaneous activity of the IHC prior to hearing onset (Shrestha et al., 2018).

This discovery may at first seem contradictory to an earlier study published by Grant et al. (2010), which studied the emergence of the functional characteristics of low- and high-SR fibers. At P11 in mice, they measured only relatively small EPSCs in SGNs, driven by the release of single vesicles. Only after hearing onset (P19–21) were they able to record much larger signals that were driven by the release of seven to nine vesicles (Grant et al., 2010). The recorded activity from prior to hearing onset was speculated to be driven by activation of low-SR fibers that were already functioning at their mature level, while the later activity was driven by a functional emergence of high-SR fibers, whose maturation was dependent upon sensory experience. Thus, the differentiation of high-SR fibers and the emergence of their mature response characteristics depends on activity both before and after hearing onset.

As high-SR fibers enable the shortest latency response to a given stimulus (Heil et al., 2008; Knipper et al., 2021; Meddis, 2006), they are critical for fast auditory processing, and their immaturity or dysfunction has been suggested to play a role in central auditory processing disorders, such as those present in ASD and schizophrenia (Knipper et al., 2021).

1.2.2 Development of the Cortex

Neural development has been suggested to operate in a series of “checkpoints” that occur in sequence and must be achieved before proceeding to the next stage (Ben-Ari & Spitzer, 2010). If a neuron or set

of neurons fail to reach a certain developmental checkpoint, the developmental process is halted and they continue to function at that immature state (Ben-Ari & Spitzer, 2010). This process is integral for achieving the complexity seen in the adult nervous system that can rapidly process and respond to complex sensory stimuli.

Centrally, the development of fine-grained processing of stimuli in all sensory systems occurs in response to microcircuit formation between inhibitory interneurons (INs) and excitatory pyramidal neurons—a process dependent upon sensory experience (for a review, see Ferrer & De Marco Garcia, 2022).

Neuronal Migration. In general, all sensory cortices undergo similar and parallel developmental trajectories. First, the circuitry of excitatory neurons is established early in embryonic development by radial migration from the ventricular zone to the cortical plate, guided by radial glia (Meyerink et al., 2020). Then thalamocortical axons begin invading the developing cortex, waiting in the subplate for layer IV neurons to reach their destination before contacting them (Sur & Rubenstein, 2005).

INs, on the other hand, must migrate much further than their pyramidal neuron counterparts and thus reach their final destination later. INs migrating to higher brain regions (i.e., the telencephalon) and lower brain regions (i.e., the midbrain, hindbrain, and spinal cord) originate from different brain regions, express different molecular markers, and follow different developmental trajectories.

INs migrating to higher brain regions mainly originate in the medial ganglionic eminence, anterior entopeduncular area, and, to a lesser extent, the lateral ganglionic eminence. They migrate through several streams in three broad and partially overlapping phases (Marin & Rubenstein, 2001). In early stages (E11.5 in mice), the cells migrate from the medial ganglionic eminence and anterior entopeduncular area to the striatum, cortical marginal zone, and subplate. In mid-stages (E12.5–14.5), the cells migrate from the medial ganglionic eminence to the striatum, sub-ventricular zone/lower intermediate zone, and the subplate. In late stages (E14.5–16.5), the cells migrate from the lateral ganglionic eminence and medial ganglionic eminence to the cortex (Marin & Rubenstein, 2001). This process is controlled by a number of different transcription factors, including *Pax6*, *Nkx2.1*, and *Gsh2* (Marin & Rubenstein, 2001). Additionally, activation of the brain-derived neurotrophic factor (BDNF) receptor TrkB is required to trigger the migratory behavior (Behar et al., 1997; Marin & Rubenstein, 2001).

However, there is another, lesser-known pool of INs that migrate to lower brain regions whose differentiation depends on the expression of paired box gene 2 (*Pax2*). *Pax2* is a transcription factor that is expressed in the developing eye, optic nerve, inner ear, midbrain, hindbrain, spinal cord, and kidney (Dressler et al., 1990; Nornes et al., 1990). Early in development (E7.5), *Pax2*-expressing INs are found in the ventricular zone and later migrate to lower brain regions, including the cerebellum, hindbrain, spinal cord, and a few thalamic regions (Fotaki et al., 2008; Larsson, 2017; Maricich & Herrup, 1999; Nornes et al., 1990; Rowitch et al., 1999).

At birth, both excitatory pyramidal neurons and inhibitory INs have reached their final destinations, though the circuitry is still not yet in a mature state. INs are initially produced in excess, with approximately 30–40% of them eventually being eliminated (Denaxa et al., 2018; Wong et al., 2018). This process is mediated by intrinsically generated neural activity during the first postnatal weeks that leads to a desynchronization of cortical activity, thereby enabling the encoding of sensory input later in development (Golshani et al., 2009; Luhmann & Khazipov, 2018).

Additionally, at birth the actions of γ-Aminobutyric acid (GABA; the main inhibitory neurotransmitter in the adult brain) are excitatory rather than inhibitory. In a concurrent process, the excitatory-to-inhibitory switch of GABA initiates an extensive maturation and rearrangement of neurons during the first two postnatal weeks, putting in place mature signaling characteristics in preparation for critical period plasticity that is brought on by sensory experience.

Excitatory-to-Inhibitory Switch. The binding of GABA to its receptor opens a Cl^- channel, so the intracellular Cl^- concentration determines whether GABA binding leads to an efflux (depolarization) or influx (hyperpolarization) of Cl^-, and, by extension, also whether GABA acts as an excitatory or inhibitory neurotransmitter. Throughout development, Cl^- homeostasis is maintained by a balance of the Na-K-2Cl co-transporter (NKCC1) and the K-Cl co-transporter (KCC2) which increase and decrease intracellular Cl^- levels, respectively. Early in postnatal development, NKCC1 is highly expressed, leading to GABA triggering a Cl^- efflux and thus depolarization (**Figure 1.5A**). At this point during development, neural activity in the AC is dominated by spontaneous, synchronous activity that originates from the cochlea (Tritsch & Bergles, 2010) and follows the same pattern as the later tonotopic organization (Babola et al., 2018; Ferrer & De Marco Garcia, 2022).

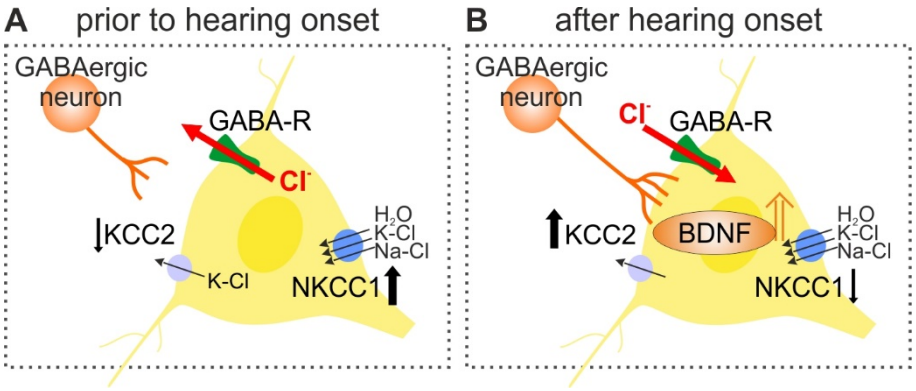

Figure 1.5. *Excitatory-to-inhibitory switch of GABA. **(A)** Prior to hearing onset, NKCC1 is densely expressed, while KCC2 is not. GABA thus triggers a depolarization in immature neurons. **(B)** After hearing onset, the expression of KCC2 increases while the expression of NKCC1 decreases. This shift in expression enables the hyperpolarizing actions of GABA. Adapted from Knipper et al., 2021.*

The excitatory-to-inhibitory switch of GABA has been observed as early as P5–6 (Lohrke et al., 2005). This switch occurs due to an upregulation of KCC2, at which point the Cl^- gradient reverses and GABA triggers a Cl^- influx and thus hyperpolarization (**Figure 1.5B**). In the ascending auditory pathway, this excitatory-to-inhibitory shift occurs in a region-specific manner from the first postnatal week onwards (Lohrke et al., 2005).

BDNF has been suggested to modulate the excitatory-to-inhibitory switch of GABA by increasing the expression of KCC2 (**Figure 1.5B**, Knipper et al., 2021; Wardle & Poo, 2003). As BDNF is activity-driven and upregulated in the cochlea as early as P4 then along ascending circuits shortly after (Singer et al., 2014), it is possible that BDNF is activated in a bottom-up manner by the spontaneous glutamate release of IHCs, driving the excitatory-to-inhibitory switch in an ascending fashion.

This process would prime auditory circuits for the subsequent period of strong experience-driven plasticity brought about by hearing onset.

Critical Periods. Once the cortical connectivity is in place and the signaling circuitry is matured, the system is then heavily sculpted by experience in distinct time windows known as critical periods (Katz & Shatz, 1996). These, like the excitatory-to-inhibitory shift, occur hierarchically in a region-specific manner (LeBlanc & Fagiolini, 2011).

While critical periods are of utmost importance for proper maturation of sensory processing, they are also extremely vulnerable to damage. First, the presence, absence, and quality of sensory stimulation at this stage in development can heavily influence the mature neural response to stimuli, so it is essential that peripheral processes develop properly for cortical processes to mature (LeBlanc & Fagiolini, 2011). Second, critical periods are tightly regulated by a precise balance of excitatory and inhibitory transmission (Fagiolini et al., 2004; Iwai et al., 2003; LeBlanc & Fagiolini, 2011), so if the excitation-inhibition (E/I) balance is off during development, this could have devastating consequences throughout

life. This is of particular concern for developmental disorders such as ASD, which has been linked both to altered sensory processing (Ocak et al., 2018) and to an E/I imbalance (Contractor et al., 2021; Hussman, 2001; Marin, 2012).

1.3 AUTISM SPECTRUM DISORDER

ASD is a pervasive developmental disorder with an incidence of approximately 1%. The Diagnostic and Statistical Manual of Mental Disorders, 5th Edition, lays out the following diagnostic criteria for ASD:

- *"Persistent deficits in social communication and social interaction across multiple contexts, as manifested by the following,*
  - *Deficits in social-emotional reciprocity*
  - *Deficits in nonverbal communicative behaviors used for social interaction*
  - *Deficits in developing, maintaining, and understanding relationships*
- *Restricted, repetitive patterns of behavior, interests, or activities, as manifested by at least two of the following,*
  - *Stereotyped or repetitive motor movements, use of objects, or speech*
  - *Insistence on sameness, inflexible adherence to routines, or ritualized patterns of verbal or nonverbal behavior*
  - *Highly restricted, fixated interests that are abnormal in intensity or focus*
  - *Hyper- or hyporeactivity to sensory input or unusual interest in sensory aspects of the environment.*" (*Diagnostic and statistical manual of mental disorders (5th ed.)*, 2013)

The DSM-V also describes associated features that are common in individuals with ASD but are not diagnostic criteria per se. These include intellectual impairment, language impairment, motor deficits, self-injury, anxiety, depression, seizures, and catatonic activity (*Diagnostic and statistical manual of mental disorders (5th ed.)*, 2013).

Symptoms of ASD are generally recognized in early childhood, with delayed language acquisition being the first sign (*Diagnostic and statistical manual of mental disorders (5th ed.)*, 2013). ASD is diagnosed four times more often in males than females (*Diagnostic and statistical manual of mental disorders (5th ed.)*, 2013), though some of this disparity has been attributed to social and cultural factors that lead to an underdiagnosis of ASD in women (Ochoa-Lubinoff et al., 2023).

What is important to note is that ASD is an incredibly heterogeneous disorder in terms of its severity, with some individuals displaying unparalleled talents, able to live and function independently, and others experiencing devastating symptoms and requiring lifelong care. One of the most well-established predictive factors for individual outcome is the presence and severity of intellectual disability and language impairment (*Diagnostic and statistical manual of mental disorders (5th ed.)*, 2013).

1.3.1 Pathogenesis and Models

Despite its prevalence, the pathogenesis of ASD is still not fully understood. It is diagnosed solely on the basis of behavioral traits, meaning that there is not yet a common diagnostic marker. ASD can be caused by certain genetic conditions, epigenetic changes, or environmental effects, yet the majority of cases remain idiopathic, without any identifiable cause.

Pathogenesis. Genetic causes of ASD can range from single gene mutations to copy-number variations to a polygenic accumulation of common mutations (Ergaz et al., 2016; Varghese et al., 2017). Single gene mutations often lead to ASD with other accompanying symptoms, sometimes termed "syndromic ASD," the most common of which being mutations in *FMR1*, leading to Fragile X syndrome (Ergaz et al., 2016). Additionally, several epigenetic changes have been implicated in ASD, including immune dysregulation, microglial activation, oxidative stress, mitochondrial dysfunction, and many others

(Ergaz et al., 2016). Finally, several environmental factors have been linked to the development of ASD. These include prenatal exposure to certain chemicals, such as valproic acid. Further, maternal infection and inflammation during pregnancy has also been considered a risk factor (Ergaz et al., 2016).

Despite this, the majority of ASD cases do not have any identifiable cause. Syndromes with a known genetic or environmental basis have been contrastingly viewed by researchers as either under the umbrella of a wider ASD diagnosis or as clinically distinct entities that simply have an overlapping behavioral presentation with idiopathic ASD. For the purpose of this work, we will ascribe to the first view, as we will later discuss and propose a unifying mechanism that could underlie genetic, environmental, and idiopathic ASD.

Rodent Models. Rodent models of ASD are similarly heterogenous. They can generally be separated into three categories that resemble the three causal factors in humans (Ergaz et al., 2016; Varghese et al., 2017). The first are genetically modified animal models, in which a genetic modification or deletion is made based on a known genetic cause of the disease. More than 200 genetic rodent models of ASD have been generated (*SFARI Gene*, 2024). The most commonly used model is likely the *Fmr1* KO, a model of Fragile X syndrome, as it is the most common genetic cause of ASD. There also exist environmentally induced models of ASD, which mimic the environmental causes of ASD in humans. This is generally accomplished by exposing pregnant animals to chemicals or infection, or by provoking inflammation. Finally, there are also spontaneous models of ASD, in which no genetic modification was made, yet they present with an ASD phenotype. This is observed in some inbred mouse strains (Varghese et al., 2017).

With all animal models, but particularly for a disease as distinctly human as ASD, the question of transferability arises: is research done on animal models representative enough to transfer across species to humans?

Rodent models can indeed be extremely useful for diseases with distinct diagnostic markers that are replicable in animals, such as are available for cancer or diabetes. However, as previously mentioned, there is not yet a common diagnostic marker for ASD. It can also be convincingly argued that ASD is a uniquely human disease that is diagnosed based on behavioral symptoms, and since rodents do not behave like humans, ASD cannot be recapitulated in a rodent model.

One approach to solve this species gap would be to use genetic or environmental rodent models, in which a genetic or environmental modification known to cause ASD in humans is applied to rodents. Then the fact that these mouse models exhibit a behavioral phenotype similar to humans when measured with a specifically developed battery of tests would point to their validity in spite of the obvious limitations arising from the simple fact that rodents are not humans. However, this approach is also limited for ASD because the majority of cases are idiopathic.

Another approach, then, would be to search for a common neural mechanism that may underlie all forms of ASD—genetic, environmental, and idiopathic—and study animal models without that neural mechanism. Indeed, the fact that individuals with ASD exhibit similarities in their symptoms despite a wide variety of causes points to a common pathogenic mechanism (Contractor et al., 2021).

1.3.2 An Underlying Neural Mechanism

It has been proposed that, in spite of the wide variety of causal factors, individuals with ASD have a core underlying difference in their neural circuitry (Contractor et al., 2021). This is suggested by the fact that so many of the symptoms and atypical behaviors are shared in this patient population, despite the heterogeneity in severity.

Interneuron Dysfunction. One of the earliest unifying theories of ASD was an E/I imbalance resulting from a global decrease in GABAergic inhibition (Hussman, 2001). This hypothesis had the advantage of being able to explain the co-occurrence of seizures in some ASD cases, but it has more recently

proven too broad and inflexible to account for the diversity of neural activity changes observed in all ASD patients (O'Donnell et al., 2017).

This view has therefore been updated to a more nuanced view of E/I changes that acknowledges the variety of GABAergic IN subclasses, their different roles based on brain state, and the specificity of their actions (Contractor et al., 2021). In this updated model of IN dysfunction, particular focus has been placed on parvalbumin-expressing (PV) INs, a specific class of fast-spiking GABAergic INs. Evidence for the theory of PV-IN dysfunction comes from the following observations that have been replicated in ASD patients and across several animal models.

The first piece of evidence is a reduced density or expression of PV. This was first suggested in postmortem studies of human brains that reported changes in GABAergic INs in the cerebellum and hippocampus of ASD patients (Lawrence et al., 2010; Palmen et al., 2004). Another study later specified this, reporting fewer PV-INs in the prefrontal cortex of ASD patients (Hashemi et al., 2017), a finding which has been replicated in both genetically (Chen et al., 2017; Filice et al., 2016; Godavarthi et al., 2014; Selby et al., 2007; Wen et al., 2018) and environmentally induced animal models of ASD (Canetta et al., 2016; Gogolla et al., 2009).

The second piece of evidence is a hypofunction of PV-INs. This is closely tied to the first observation, as the development of intracortical networks is a dynamic, experience-driven process (see section 1.2.2). Thus, PV-IN hypofunction could impact the survival of PV-INs, leading to their reduced density. PV-IN hypofunction was replicated using a variety of techniques across different cortical regions in both genetically (Antoine et al., 2019; Banerjee et al., 2016; Berryer et al., 2016; Berzhanskaya et al., 2016; Chen et al., 2020; Goel et al., 2018; Krishnan et al., 2015; Lazaro et al., 2019; Mao et al., 2015; Michaelson et al., 2018; Rotaru et al., 2018; Selimbeyoglu et al., 2017; Wallace et al., 2012) and environmentally induced animal models of ASD (Canetta et al., 2016).

A final piece of evidence supporting the theory of PV-IN dysfunction in ASD comes from electroencephalography (EEG) data. EEG enables the recording of electrical activity in the brain via electrodes placed either on the scalp or directly in or on the brain. By doing so, one can measure the rhythmic oscillatory neural activity, which is responsible for many processes, including sensory integration and cognitive functions (Buzsaki & Wang, 2012). Of particular importance for ASD is gamma band activity, as it is associated with network activity and cognition, and PV-INs play a critical role in its generation (Cardin et al., 2009; Sohal et al., 2009). An increased resting-state gamma band oscillatory activity was first observed in animal models and has since been replicated in humans with Fragile X syndrome (Ethridge et al., 2017) and in both genetically (Kissinger et al., 2020; Lovelace et al., 2018; Pirbhoy et al., 2020; Radwan et al., 2016; Talbot et al., 2018) and environmentally induced animal models of ASD (Canetta et al., 2016; Cheaha & Kumarnsit, 2015; Tyzio et al., 2014).

As inhibitory IN circuitry is already laid out by birth and then undergoes pruning and rapid maturation by sensory onset (P12 in the mouse auditory system), a PV-IN dysfunction early on in development would be devastating for all subsequent developmental steps, including critical period plasticity. This is supported by findings of several studies that observed abnormal critical period plasticity in the visual system of ASD models (Dolen et al., 2007; Sato & Stryker, 2010; Tropea et al., 2009; Yashiro et al., 2009).

While the sheer volume of research supporting this model of PV-IN dysfunction makes it incredibly convincing, there are still some outstanding questions that continue to cast doubt as to whether PV-IN dysfunction is the root cause or simply another secondary consequence of some other dysfunction. Most notably, when in development do these changes occur and how?

It is currently unclear whether the deficits in PV-INs begin already in the embryonic stages of neurogenesis and migration or only later in the activity-dependent pruning stage. The pruning stage occurs in the first postnatal weeks in rodents and is activity-dependent, as detailed in section 1.2.2.

When considering that at this developmental stage, activity in the AC originates from spontaneous activity in the cochlea (Tritsch & Bergles, 2010), it becomes reasonable to consider that the PV-IN deficit may instead have an earlier, peripheral origin.

Sensory Development Dysfunction. As beautifully suggested by LeBlanc and Fagiolini (2011), *"It is interesting to consider a model in which defects in the development of primary sensory abilities are the original problem, which then results in a cascading effect on higher integrative areas of the brain."*

Indeed, an extremely well-documented and overarching commonality in ASD patients with otherwise normal hearing are auditory processing disorders (e.g., Brandwein et al., 2015; Edgar et al., 2015; Foss-Feig et al., 2017; Kwakye et al., 2011; Roberts et al., 2010; Stroganova et al., 2020). This is so prevalent and pervasive that some researchers even consider it a key feature of ASD (Bellis, 2011; Irwin et al., 2017; Stevenson et al., 2018; Stewart et al., 2018).

With this in mind, we revisit the idea of a model of ASD caused by an underlying sensory system immaturity.

This becomes compelling when we consider the developmental requirements for fine-grained processing of stimuli. In short, to acquire precise stimulus encoding, the responses of the auditory system are tuned and shaped by sensory experience during a critical period after sensory onset (see section 1.2.1). The initiation of critical periods throughout the nervous system occurs hierarchically in a region-specific manner, with basic sensory processing maturing before complex cognitive processing. It is reliant upon basic neural circuitry being in place by the time of sensory onset; thus, inhibitory INs must have formed synapses with excitatory pyramidal neurons, which is dependent upon intrinsically generated activity in sensory cortices (see section 1.2.2). In the AC, this early spontaneous activity is generated in the cochlea (Tritsch & Bergles, 2010). Thus, if a structure that will later become critical for precise encoding of stimuli (e.g., high-SR fibers) fails to reach a particular developmental "checkpoint," its maturation could halt, and the effects of this could cascade along the ascending pathway and result in dysfunctional higher-level integrative and cognitive processes.

1.4 *BDNF*^{PAX2} KO MOUSE MODEL

To examine the hypothesis that immature peripheral sensory processing can contribute to an ASD phenotype through a cascading mechanism that eventually affects central, cognitive processes, we use the *Bdnf*^{Pax2} KO mouse model. This is not an established model for ASD, and, in fact, no known gene related to ASD is deleted in the *Bdnf*^{Pax2} KO model. Instead, in this model, *Bdnf* is deleted in *Pax2*-expressing INs. Recall that *Pax2*-expressing INs migrate from ventricular regions to lower brain regions, including the cochlea and auditory brainstem (see section 1.2.2, neuronal migration). BDNF, on the other hand, is responsible for the upregulation of KCC2 that reverses the intracellular Cl^- gradient and thus changes the actions of GABA from excitatory to inhibitory (see section 1.2.2, excitatory-to-inhibitory switch). Consequently, in *Bdnf*^{Pax2} KO mice, a select group of inhibitory INs in the peripheral auditory system are assumed to remain in an immature state.

Bdnf^{Pax2} KO mice were originally generated to study the auditory system, so their hearing phenotype has been extensively described. At the level of the cochlea, *Bdnf*^{Pax2} KO mice had normal hearing sensitivity (i.e., thresholds) but fewer IHC ribbon synapses and less exocytosis at the IHC synapse in the midbasal cochlear turn, which encodes higher-frequency stimuli (Chumak et al., 2016; Zuccotti et al., 2012). In addition, ABR wave I, reflecting the response of the auditory nerve, was found to have a lower amplitude in *Bdnf*^{Pax2} KO mice (Chumak et al., 2016; Eckert et al., 2021; Zuccotti et al., 2012).

At the brainstem level, *Bdnf*^{Pax2} KO mice exhibited reduced inhibitory strength and higher SRs in the dorsal cochlear nucleus, leading to coarser tuning curves and a less-precise encoding of stimuli (Eckert et al., 2021). Additionally, ABR wave IV, reflecting the response of the IC and lateral lemniscus, was found to have both a lower amplitude and a delay in *Bdnf*^{Pax2} KO mice (Chumak et al., 2016; Eckert et

al., 2021; Zuccotti et al., 2012). Further, the high-frequency inhibitory strength in IC neurons was lower in *Bdnf*^{Pax2} KO mice, again leading to coarser tuning curves and a less-precise encoding of stimuli (Chumak et al., 2016).

Temporal sound coding, as measured through the auditory steady state response (ASSR) in response to amplitude-modulated stimuli, was impaired in *Bdnf*^{Pax2} KO mice (Eckert et al., 2021), similar to the auditory processing disorders that have been widely reported in ASD patients and associated animal models (Ocak et al., 2018; Wilde et al., 2022).

Aside from the hearing phenotype, it was also recently observed that *Bdnf*^{Pax2} KO mice have a behavioral phenotype that is reminiscent of ASD, exhibiting deficits in social interaction, stereotypic behaviors, higher anxiety, and impaired memory function (Eckert et al., 2021). Interestingly, *Bdnf*^{Pax2} KO mice also had fewer PV-IN synapses and more expression of activity-regulated cytoskeleton-associated protein (expressed in excitatory neurons; Vazdarjanova et al., 2006) in the AC and hippocampus but not in the somatosensory cortex and cerebellum (Eckert et al., 2021), consistent with the local circuit E/I imbalance that has been extensively reported in ASD models (see section 1.3.2).

As ASD is an extremely heterogeneous disorder without a common biological marker, it may shed light on a common neural mechanism to examine a model in which no known ASD genes are directly deleted that nevertheless displays an ASD phenotype.

1.5 AIMS & OBJECTIVES

1.5.1 Replicate ASD Phenotype on a Central Level

For the *Bdnf*^{Pax2} KO mouse model to be considered useful in studying an underlying pathogenesis of ASD, several aspects of an ASD phenotype still need to be replicated in this model. These include functional evidence of a cortical E/I imbalance, structural evidence of a learning deficit, and altered neural response characteristics.

As previous results suggest that *Bdnf*^{Pax2} KO exhibit a circuit-specific E/I imbalance on a molecular level (Eckert et al., 2021), we will further characterize this by examining molecular markers for excitatory and inhibitory synapses in the hippocampus (see section 2.10.2). Then we will perform EEG and measure the spontaneous activity to determine if an E/I imbalance is reflected on a functional level in the AC (see section 2.7.1). We will particularly focus on the gamma oscillations which are generated by PV-INs and heavily implicated in models of ASD.

Next, as ASD is often associated with intellectual disability, we will examine the microstructure of the hippocampus to validate the previously observed learning deficits (Eckert et al., 2021) on a structural level. This will be done by examining the dendritic spines in CA1 pyramidal neurons (see section 2.11). Spines are specialized, dynamic structures that change their size and shape in response to neuronal activity and are thus critical for learning and memory (Nimchinsky et al., 2002).

Finally, we will examine the neural response characteristics of *Bdnf*^{Pax2} KO mice. In all structures of the auditory system measured to date, *Bdnf*^{Pax2} KO mice have displayed weaker and coarser responses, indicating a deficit in sensory processing. By performing EEG in the AC and measuring the local field potentials (LFPs) in response to acoustic stimuli, we can confirm this auditory processing deficit in a higher-level structure (see section 2.7.2). In addition, this technique allows us to distinguish activity related to bottom-up sensory processing (evoked activity) from activity related to sensory integration (induced activity) to potentially reveal a more pervasive effect of the deletion.

1.5.2 Determine Origin of ASD Phenotype

If *Bdnf*^{Pax2} KO mice can indeed recapitulate a wide range of ASD characteristics, we then aim to determine the origin of the phenotype. As the genetic modification of this model primarily affects the peripheral auditory system, this will be accomplished by measuring the activity of specific structures early in the auditory system.

First, to examine the auditory nerve activity, the compound action potential (CAP) will be measured (see section 2.8.1). As the auditory nerve is made up of fibers with a range of different SRs and response thresholds that have different functional roles, PSTRs will then be measured to parse out the contribution of different auditory nerve fiber types (see section 2.8.2). Finally, to examine the activity of the MOC efferents, which not only modulate OHC activity in adulthood but also shape IHC development through transient synapses prior to hearing onset, the MOC DPOAE will be measured (see section 2.4.3).

When the origin of the phenotype is determined, it should then be theoretically possible to target this underlying pathogenic neural mechanism with treatments that nudge it towards the healthy physiological state. Thus, two treatment approaches will be considered, which are detailed in the upcoming sections 1.5.3 and 1.5.4.

1.5.3 Recover the Phenotype with a Cognitive Stimulator

The first treatment approach will be a pharmaceutical intervention that targets the more cognitive aspects of the phenotype of *Bdnf*^{Pax2} KO mice. Namely, a phosphodiesterase (PDE) 9A inhibitor (i) will be used. This drug inhibits a PDE9A isoform that degrades cyclic guanosine monophosphate (cGMP)—a second messenger implicated in a variety of biological functions, including smooth muscle relaxation, vasodilation, metabolic supply, and many others (Kleppisch & Feil, 2009; Potter, 2011). PDE9A is the most widely expressed PDE in the brain (Andreeva et al., 2001; Van Staveren et al., 2003) and is also expressed in the cochlea (Marchetta, Mohrle, et al., 2020).

PDE9 inhibitors have previously been used in the context of neurodegenerative diseases and schizophrenia, having been shown to improve memory function (Hutson et al., 2011; Kroker et al., 2014; Rosenbrock et al., 2019; van der Staay et al., 2008). In addition, a recent study from our lab found that a PDE9i can protect against stress-induced hearing loss (Savitska et al., 2022). Further, a PDE9i improved social interaction deficits in a rodent model of maternal immune activation, associated with ASD (Scarborough et al., 2021).

The fact that a PDE9i has been used in other models to improve all aspects that are affected in the phenotype of *Bdnf*^{Pax2} KO mice, including hearing, memory, and social behavior, makes it a suitable treatment option for this mouse model. Thus, to determine the effect of a PDE9i on *Bdnf*^{Pax2} KO mice, the hearing function will be measured prior to treatment, then *Bdnf*^{Pax2} KO mice will be injected with either a PDE9i or a vehicle for ten days, after which the hearing function will be measured again (see section 2.5.2). Finally, the memory function will be assessed through *ex vivo* electrophysiology measurements of LTP (see section 2.14).

1.5.4 Recover the Phenotype with Sound Enrichment

To complement this more central, pharmaceutical approach, a second treatment approach will be used that targets the more peripheral aspects of the phenotype of *Bdnf*^{Pax2} KO mice. Namely, exposure to an enriching acoustic stimulus, 10 kHz, 80 dB SPL, for 40 minutes, henceforth called simply "80 dB," will be used.

This particular form of enrichment is especially appealing for this model because it specifically targets the auditory system, which may experience selective effects of the deletion. Further, it has previously been shown that a one-time exposure to 80 dB increases ABR wave amplitudes, and that the increased

activity in the auditory system propagates to the hippocampus and improves memory function even two weeks later (Matt et al., 2018).

Thus, to assess the effect of 80 dB on *Bdnf*^{Pax2} KO mice, their hearing function will be measured prior to exposure, then *Bdnf*^{Pax2} KO mice will be exposed to either 80 dB or sham; 14 days later, their hearing function will be measured again (see section 2.5.1). Finally, mice will either undergo a series of behavioral tests assessing memory (see section 2.9.1) and social behavior (see section 2.9.2), or memory function will be assessed through *ex vivo* measurements of LTP (see section 2.14).

2 METHODS

2.1 ANIMALS & CARE

The care and use of mice and the experimental protocols were reviewed and approved by the University of Tübingen, Veterinary Care Unit and by the Animal Care and Ethics Committee of the Regional Board of the Federal State Government of Baden-Württemberg, Germany, and followed the guidelines of the European Union Directive 2010/63/EU for animal experiments.

Bdnf^{Pax2} KO mice were obtained by crossing one mouse line in which Cre expression is controlled by a *Pax2* promoter (Ohyama & Groves, 2004) and another mouse line in which the protein coding exon IX of *Bdnf* is flanked by *loxP* sites (Rios et al., 2001), both obtained from the Mutant Mouse Regional Research Center (The Jackson Laboratory, Bar Harbor, ME, USA). Littermates that were homozygous *Bdnf* floxed but Cre negative were used as controls.

Table 2.1. *Primers for genotyping. Bdnf, brain-derived neurotrophic factor; Pax2, paired box gene 2.*

Gene of Interest	Sequence	bps
Pax2 Cre	for: 5'-acgaccaagtgacagcaatg-3' rev: 5'-ccatgcctcgaccagtttag-3'	350 bp
Bdnf flox	for: 5'-tgtgattgtgtttctggtgac-3' rev: 5'-gccttcatgcaaccgaagtatg-3'	437 bp wt 487 bp flox

For genotyping, tissue samples from individual ear marking of the mice were used. The tissue was stored at -20ºC until use. For DNA isolation, 20 µl lysis buffer (NucleoType Mouse PCR, Macherey-Nagel, Düren, Germany) was mixed with 0.5 µl proteinase K (Macherey-Nagel, Düren, Germany), then added to each tissue sample. The mixture was shaken for two minutes at room temperature, then for two to three minutes at 98ºC to inactivate the proteinase K. For the polymerase chain reaction (PCR), a master mix was prepared that contained 12.5 µl HS Taq Master Mix (Biozym Scientific GmbH, Hessisch Oldendorf, Germany), 1.5 µl of the primer (**Table 2.1**) and 8 µl of double-distilled H_2O per sample. 22 µl of the master mix was mixed with 3 µl of the previously isolated DNA.

The PCR program consisted of an initial activation at 94ºC for four minutes, followed by five cycles of a 30-second denaturing step at 94ºC, a 30-second annealing and extension step at 65ºC, and 30 seconds at 72ºC. This was followed by 30 cycles of another 30-second denaturing step at 94ºC, a 30-second annealing and extension step at 55ºC, and 30 seconds at 72ºC, ending with 5 minutes at 72ºC.

The PCR product was kept at 4ºC until the gels were run. 1.5% agarose gel was prepared by mixing 1.5 g agarose in 100 ml 1x Tris-acetate-ethylenediaminetetraacetic acid buffer. Directly before samples were loaded into the gel, DNA-dye (AppliChem GmbH, Darmstadt, Germany) was added to each sample and briefly vortexed. 5 µl of DNA ladder (Life Technologies GmbH, Darmstadt, Germany) diluted 1:1 in the DNA-dye was loaded into the first well, then 10 µl of the samples were loaded to the subsequent wells. The electrophoresis chamber was set at 120 V, 400 mA for approximately 90 minutes. Gels were then imaged under ultraviolet light and the genotype determined by visual identification of the PCR bands.

For all experiments, both male and female mice were used. Animals were aged between 1.8 and 8.2 months at the beginning of the experiments.

2.2 EXPERIMENTAL DESIGNS

2.2.1 Experiments with Untreated Mice

All mice underwent an initial hearing measurement to ensure normal hearing thresholds (see section 2.4). One group of mice, consisting of eight control mice and nine *Bdnf*^{Pax2} KO mice, was used for EEG recordings (see section 2.7). Another group of mice, consisting of 11 control mice and 12 *Bdnf*^{Pax2} KO mice, was used for electrocochleography recordings (see section 2.8). After the completion of the measurements, mice were immediately sacrificed, and the brain and cochleae were collected. The brains of mice used for EEG recordings were used for Golgi staining to analyze dendritic spine morphology (see section 2.11) or for toluidine blue staining to confirm electrode positions (see section 2.13). The brains of mice used for electrocochleography recordings were used for histology by immunohistochemistry (see section 2.10.2).

2.2.2 Experiments with 80 dB Exposure and Phosphodiesterase 9A Inhibitor Treatment

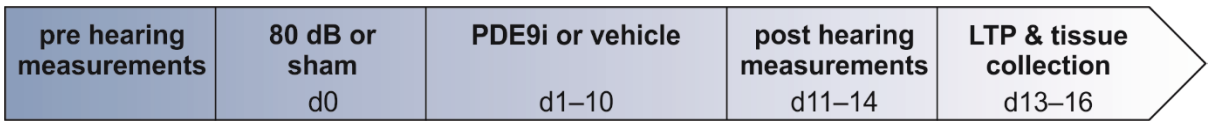

Figure 2.1. *Timeline for experiments with 80 dB SPL exposure ± PDE9i treatment. LTP, long-term potentiation; PDE9i, phosphodiesterase 9A inhibitor.*

Before treatment, all mice underwent an initial hearing measurement to assess baseline hearing function (see section 2.4; **Figure 2.1**). At the beginning of the first measurement, blood was taken from the tail vein of each anesthetized mouse to later assess the baseline corticosterone levels (see section 2.6). Within one and a half weeks of the first hearing measurement, mice underwent either 80 dB SPL sound exposure or a sham exposure (see section 2.5.1). For the following ten days, mice were injected intraperitoneally with either the PDE9i or a vehicle (see section 2.5.2). One to four days after the completion of the pharmaceutical treatment, a second hearing measurement was performed (see section 2.4). Two days later, mice were sacrificed, and the brains and cochleae were collected. Brains were split into the two hemispheres, one of which was used for field excitatory postsynaptic potential (fEPSP) recording (see section 2.14).

The project therefore consisted of the following eight experimental conditions, comprised of eight mice per condition:

1. Control, sham exposure + vehicle injection
2. *Bdnf*^{Pax2} KO, sham exposure + vehicle injection
3. Control, 80 dB SPL sound exposure + vehicle injection
4. *Bdnf*^{Pax2} KO, 80 dB SPL sound exposure + vehicle injection
5. Control, sham exposure + PDE9i injection
6. *Bdnf*^{Pax2} KO, sham exposure + PDE9i injection
7. Control, 80 dB SPL sound exposure + PDE9i injection
8. *Bdnf*^{Pax2} KO, 80 dB SPL sound exposure + PDE9i injection

However, only experimental conditions 1, 2, 5, and 6 will be discussed in the present work.

2.2.3 Experiments with 80 dB Exposure

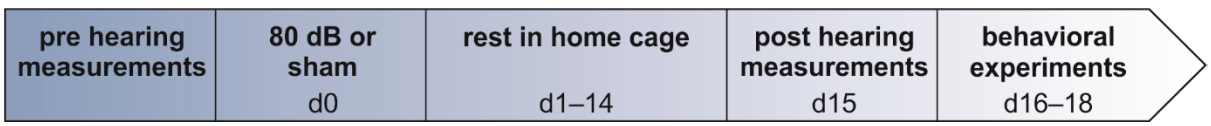

Figure 2.2. *Timeline for experiments with 80 dB SPL exposure treatment.*

All mice underwent an initial hearing measurement to assess baseline hearing function (see section 2.4; **Figure 2.2**). Within one week of the first hearing measurement, mice underwent either 80 dB SPL sound exposure or a sham exposure (see section 2.5.1). 14 days later, a second hearing measurement was performed (see section 2.4). Behavioral experiments were performed in the following three days (see section 2.9), after which, mice were sacrificed, and the brains and cochleae were collected for immunohistochemistry (see section 2.10).

The project therefore consisted of the following four experimental conditions:

1. Control, sham (14 mice)
2. *Bdnf*^{Pax2} KO, sham (15 mice)
3. Control, 80 dB SPL sound exposure (15 mice)
4. *Bdnf*^{Pax2} KO, 80 dB SPL sound exposure (16 mice)

2.3 ANESTHESIA

For hearing measurements (see section 2.4), 80 dB SPL sound exposure or sham (see section 2.5.1), EEG recordings (see section 2.7), and electrocochleography recordings (see section 2.8), mice were anesthetized using a four-component drug, here referred to as "FDDA". This consisted of fentanyl (0.05 mg/kg bodyweight, Fentanyl-hameln®, Hameln Pharma plus GmbH, Hameln, Germany) as a narcotic and analgesic, midazolam (2.5 mg/kg bodyweight, Midazolam-hameln®, Hameln Pharma plus GmbH) as a relaxation agent, medetomidine (0.5 mg/kg bodyweight, Sedator®, Albrecht GmbH, Aulendorf, Germany) as a sedative, and atropine sulfate (0.2 mg/kg bodyweight, B. Braun, Melsungen, Germany) to prevent bradycardia. This mixture was diluted with sterile water to an injection volume of 10 ml/kg and injected intraperitoneally. If necessary, anesthesia could be re-injected subcutaneously after one hour with one third of the initial dosage.

At the conclusion of the non-terminal measurements, mice were injected with a three-component antidote consisting of naloxone (1.2 mg/kg bodyweight; Naloxon-hameln®; Hameln Pharma plus GmbH, Hameln, Germany) to antagonize the fentanyl, flumazenil (0.55 mg/kg bodyweight; Flumazenil®; Fresenius Kabi, Bad Homurg, Germany) to antagonize the midazolam, and atipamezole (2.5 mg/kg bodyweight; Antisedan®; VETOQUINOL GmbH, Ravensburg, Germany) to antagonize the medetomidine. The antidote was diluted with sterile water to an injection volume of 10 ml/kg and injected subcutaneously.

2.4 HEARING MEASUREMENTS

Hearing function was assessed before and after treatment (see section 2.5) by measuring the ABR and ASSR. For all hearing measurements, animals were anesthetized by an intraperitoneal injection of FDDA (see section 2.3). To ensure proper depth of anesthesia, the hindlimb was briefly pinched with forceps. When the mouse no longer had a toe withdrawal reflex, it was placed in a soundproof chamber (IAC 400-A, Industrial Acoustics Company GmbH, Niederkrüchten, Germany) on a pre-warmed heating pad. Eye protecting gel was applied to prevent eyes from drying (Vidisic®, Dr. Mann Pharma, Bausch + Lomb GmbH, Germany).

For ABR and ASSR recordings, three silver wire electrodes were inserted subdermally at the back (ground electrode), the vertex (reference electrode), and below the ear (active electrode). A microphone Bruel & Kjaer 4939, Naerum, Denmark) was used to calibrate and record the acoustic stimuli.

A subset of mice underwent DPOAE recordings, during which an acoustic coupler connected to two loudspeakers (Beyerdynamic DT-911, Heilbronn, Germany) was placed in the ear canal, after ensuring that the ears were free and clear of earwax.

2.4.1 Auditory Brainstem Response

The ABR was used to determine the animal's hearing threshold, i.e., the lowest possible SPL evoking a response signal distinguishable from the baseline noise. The summed neuronal activity of specific structures along the ascending auditory pathway was also determined from the suprathreshold ABR waveforms. These waves are correlated with the activity of distinct anatomical structures in the ascending auditory pathway, with wave I reflecting the activity of the auditory nerve, wave II reflecting the activity of the cochlear nucleus, wave III reflecting the activity of the superior olivary complex, and wave IV reflecting activity of the IC and lateral lemniscus (Melcher & Kiang, 1996).

ABRs were evoked using click (100 µs) and noise-burst (1 ms) stimuli presented at attenuation levels of 105 to 5 dB, increasing in 5 dB steps. On the ear with better hearing thresholds, frequency-specific thresholds were determined by presenting pure-tone stimuli (3 ms, including 1 ms $\cos^2$ rise and fall envelope) of 2, 2.83, 4, 5.66, 8, 11.31, 16, 22.63, 32, and 45.2 kHz at SPLs from 10 to 100 dB, increasing in 5 dB steps.

Stimuli were generated with an input/output card (PCIe-6259, National Instruments, Austin, TX, USA) in an IBM compatible computer. The SPL of the stimuli was modulated by custom-made amplifier and attenuator systems (Wulf Elektronik, Frankfurt, Germany). The measured signals were bandpass filtered from 200 Hz to 5 kHz (F1, 6-pole Butterworth hardware filter, Wulf Elektronik) and amplified by 100,000. The analog/digital rate was 20 kHz. Each stimulus had a recording interval of 16 ms and was directly repeated and averaged up to 512 times (click and noise-burst stimuli) or 256 times (pure-tone stimuli).

ABR thresholds for click, noise-burst, and pure-tone stimuli were manually determined during the measurement by identifying the lowest stimulus level at which the ABR signal could be distinguished from the baseline noise level.

Thresholds from all ears were averaged and are displayed as mean ± SEM. Normal distribution was assessed using the Shapiro-Wilk normality test ($\alpha = 0.05$). For click and noise-burst stimuli, differences between the means were compared using the two-tailed Student's t-test (parametric) / Mann-Whitney test (non-parametric) or using a paired two-tailed t-test (parametric). For pure-tone stimuli, differences between the means were compared using a 2-way ANOVA. Statistical calculations and visualizations were performed using GraphPad Prism (version 10.2.0, GraphPad Software, Boston, MA, USA).

For the fine structure analysis of ABR waves, a customized program (PEAK, programmed by Lukas Rüttiger, University of Tübingen ENT clinic) was used to assign positive and negative peaks to the ABR. The extracted peaks were then manually assigned a wave label (I through IV) based on the relative time of the peak, then growth functions for each ear relative to the hearing threshold were constructed for the amplitude of wave I and IV.

Growth functions from all ears were averaged and are displayed as mean ± SEM. Normal distribution was assumed. Differences between the means were compared using a 2-way ANOVA with Bonferroni's multiple comparison test. Statistical calculations and visualizations were performed using GraphPad Prism.

In experiments with the PDE9i and/or 80 dB exposure, which consisted of pre- and post-measurements, the difference in the ABR wave growth functions between these two measurements (delta) was calculated in order to compare the treatment effect between different experimental conditions. For each ear, the pre-treatment growth function was subtracted from the post-treatment growth function to allow for visualization of amplitude gain (positive values) or loss (negative values) as a result of treatment.

Deltas from all ears were averaged and are displayed as mean ± SEM. Normal distribution was assumed. Differences between the means were compared using a 2-way ANOVA with Sidak's multiple comparisons test. Statistical calculations and visualizations were performed using GraphPad Prism.

2.4.2 Auditory Steady State Response

Amplitude-modulated stimuli were presented to evoke ASSRs, which can be used to assess the integrity of temporal sound coding in higher-level structures in the auditory system. The stimulus consisted of a sinusoidal carrier temporally modulated by a lower frequency. The contribution of the neurons that can fire fast enough to phase-lock to the modulation frequency was measured as the spectral power (fast Fourier transform) at the first harmonic.

ASSRs were evoked from the ear with the lower hearing threshold using a carrier frequency of 11.31 kHz and a modulation frequency of 512 Hz. For the amplitude growth function, the amplitude-modulated stimuli were presented at a modulation depth of 100% at stimulus levels between -10 and 60 dB relative to threshold in 5 dB steps. For the modulation depth function, the carrier was presented at 40 dB relative to threshold and modulated in depths of 100%, 71%, 50%, 35%, 25%, 18%, 12%, 8.8%, 6.2%, 4.4%, 3.1%, 2.2%, 1.6%, 1.1%, and 0% (unmodulated). ASSR responses to amplitude-modulated tones were recorded in epochs of 1,114 ms, filtered (50–2,000 Hz 6th order bandpass Butterworth), amplified (80 or 100 dB), and sampled at 50 kHz by 16-bit analog/digital conversion of a 5 or 10 V input range by the input/output card (PCIe-6259, National Instruments, Austin, TX, USA). Stimuli were directly repeated and averaged 32 times.

Using a customized program (CAP, programmed by Lukas Rüttiger, University of Tübingen ENT clinic), the spectral power of each stimulus was determined by fast Fourier transform. From the fast Fourier transform, the spectral amplitude at the modulation frequency (first harmonic) and the spectral amplitude of the noise level from neighboring frequency (± 8 Hz) were extracted. From these, the signal-to-noise ratio (SNR; dB) was calculated.

Growth and depth functions from all mice were averaged and are displayed as mean ± SEM. Normal distribution was assumed. Differences between the means were compared using a 2-way ANOVA with Bonferroni's multiple comparison test. Statistical calculations and visualizations were performed using GraphPad Prism.

In experiments with 80 dB exposure, which consisted of pre- and post-measurements, the deltas of the ASSR growth and depth functions were calculated in order to compare the treatment effect between different experimental conditions. For each mouse, the pre-treatment growth or depth function was subtracted from the post-treatment growth or depth function to allow for a visualization of SNR increase (positive values) or SNR decrease (negative values).

Deltas from all ears were averaged and are displayed as mean ± SEM. Normal distribution was assumed. Differences between the means were compared using a 2-way ANOVA with Sidak's multiple comparisons test. Statistical calculations and visualizations were performed using GraphPad Prism.

2.4.3 Distortion Product of Otoacoustic Emissions & Medial Olivocochlear Adaptation

The DPOAE were used to assess OHC function (Janssen et al., 2006). OHCs are electromotile and undergo a conformational change in response to acoustic stimuli; this process forms the basis for cochlear amplification. The active length changes of OHCs distorts the acoustic stimulus, which is reflected out of the cochlea along the ossicles back through the ear canal, allowing it to be recorded with a sensitive microphone. As this process depends on the OHCs alone, it gives a much more accurate representation of OHC function as compared to ABR thresholds, which additionally determined by a neuronal contribution (Ruttiger et al., 2017).

The cubic 2*f1−f2 DPOAE was measured for f2 = 1.24*f1 and L1=L2+10 dB. Stimuli were presented at f1 varying from 1.59 to 25.8 kHz and f2 varying from 1.96 to 31.99 kHz, with L1 at 50 dB SPL. For the growth function, seven frequency pairs were presented, with f2 varying from 4 to 32 kHz in half octave steps. Each frequency pair was presented with L1 and L2 constantly increasing in 5 dB steps starting at -5 dB SPL and finishing at 65 dB SPL. A microphone (MK231, Microtech Gefell, Germany;

Preamplifier Brüel & Kjaer 2670, Naerum, Denmark) connected to the coupler was used to measure the emissions.

The maximum amplitude from the fast Fourier transform was analyzed using Microsoft Excel, which computed the 2*f1−f2 response of each frequency at L1 = 50 dB SPL. The threshold was manually defined as the lowest SPL response that met three or more of the following criteria:(1) the signal is at least 5 dB above the average noise, (2) the signal is above the local noise, (3) the signal is part of a rising growth function, (4) the subsequent point does not drop below the average noise, and (5) the subsequent point does not drop below the local noise. Data is displayed as mean ± SEM. Normal distribution was assumed. Differences between the means were compared using either a two-tailed Student's t-test or a 2-way ANOVA with Bonferroni's multiple comparisons test. Statistical calculations and visualizations were performed using GraphPad Prism.

We measured the rapid modulation (~100 ms) of OHC electromotility by MOC efferents, which suppress OHC motility (Kujawa & Liberman, 2001; Liberman et al., 1996), as previously described (Wolter et al., 2018). The MOC response was evoked by synchronously presenting two primaries with frequencies f2 = 11.3 kHz and f1 = 9.11 kHz (100 ms, including 2 ms $\cos^2$ rise and fall envelope). Each stimulus had a recording interval of 500 ms and was directly repeated 128 times. In order to cancel the primary components, the phases of the stimuli were rotated by 90º (f1) and 180º (f2) for each subsequent presentation (Dalhoff et al., 2015).

Measured signals were bandpass filtered (1/8 octave) around the DPOAE frequency, amplified by 40 dB, then averaged and Hilbert-transformed to extract the envelope of 2*f1–f2 DPOAE response in the time domain using a customized program (ShowSingleSweeps, programmed by Lukas Rüttiger, University of Tübingen ENT clinic). For each measured ear, the DPOAE amplitude was normalized to the response peak (10 ms window after stimulus onset). The MOC efferent-mediated adaptation was defined as the difference between the response peak and the plateau (the last 10 ms before stimulus offset).

Data from all measured ears were averaged and are displayed as mean ± SEM. Normal distribution was assumed. Differences between the means were compared using a two-tailed Student's t-test. Statistical calculations and visualizations were performed using GraphPad Prism.

2.5 TREATMENT APPROACHES

2.5.1 80 dB Exposure

For sound exposure, animals were anesthetized by an intraperitoneal injection of FDDA (see section 2.3) and placed on a turntable facing forward in a pre-warmed reverberating chamber with tilted, non-parallel walls (50 × 50 × 50 cm). After 20 minutes, mice were turned so they were facing backwards on the turntable for the second half of the exposure. In total, sound exposure lasted 40 minutes. A calibrated loudspeaker in the ceiling (DR45N, Visaton, Haan, Germany) and six loudspeakers in the walls (Soundcraft piezo, Conrad Electronic, Hirschau, Germany) were used to deliver the sound and achieve a mostly homogenous exposure. A 10 kHz tone at 80 dB SPL was generated by a signal generator (Wulf Elektronik, Frankfurt, Germany). Click and noise-burst thresholds were measured directly after noise exposure. Animals undergoing sham exposure were treated under identical conditions, but the speakers remained switched off.

2.5.2 Phosphodiesterase 9A Inhibitor

3 mg of PDE9i (BAY 73-6691, Bayer Vital GmbH, Leverkusen, Germany) were dissolved in 500 µl EtOH and diluted with 9.5 ml of 10% Solutol (BASF, Mannheim, Germany). The vehicle solution contained the same dilution medium without the PDE9i.

Both the PDE9i and vehicle were administered by intraperitoneal injections for ten consecutive days at approximately the same time each day (± 1.5 hr).

2.6 CORTICOSTERONE ANALYSIS

At the beginning of the first and last hearing measurement, 50 µl of blood was collected from the tail vein within ten minutes of the initial anesthesia injection. Blood was centrifuged (ThermoFisher Scientific, MA, USA) for five minutes at 2.8 × g to separate the serum. The serum was then stored at -80ºC until use.

The concentration of corticosterone was assessed with a corticosterone ELISA kit (Enzo Life Sciences, Farmingdale, NY, United States). All solutions came to room temperature before use. For the assay buffer solution, 5 ml of the provided Assay Buffer 15 Concentrate was diluted with 45 ml double-distilled H_2O. For the standards, 100 µl of the provided Corticosterone Standard (200,000 pg/ml corticosterone) was diluted with 900 µl of the assay buffer solution. The standards were serially diluted such that the final concentrations of corticosterone were 20,000, 4,000, 800, 160, and 32 pg/ml. For the wash buffer, 5 ml of the provided Wash Buffer Concentrate was diluted with 95 ml of double-distilled H_2O. For the samples, 5.5 µl of each plasma sample was diluted (in duplicate) with 5.5 µl of the provided steroid displacement reagent and briefly vortexed. After five minutes, 209 µl of the provided assay buffer was added and vortexed, making the final dilution 1:40.

For the assay, the provided 96-well plate was used (donkey anti-sheep IgG microtiter plate). First, 100 µl of the assay buffer were pipetted into the nonspecific binding well and the positive control well. Then, 100 µl of the standards were pipetted into the appropriate wells. Next, 100 µl of the samples were pipetted into the appropriate wells. After, 50 µl of assay buffer was pipetted into the non-specific binding well, then 50 µl of the provided ELISA conjugate was pipetted into all wells except the total activity and blank wells. Finally, 50 µl of the provided ELISA antibody was pipetted into all wells except the blank, total activity, and non-specific binding wells. The plate was then covered and incubated at room temperature for two hours, shaken at ~500 rpm.

After incubation, the contents of the plate were emptied and 400 µl of wash solution were added to every well. After three washes, 5 µl of the provided ELISA conjugate was added to the total activity wells and 200 µl of the provided p-Npp substrate (p-nitrophenyl phosphate in buffer) was added to every well. The plate was incubated for one hour, after which 50 µl of stop solution was added to every well.

The plate was read immediately at 405 nm with a FLUOstar OPTIMA plate reader (BMG LABTECH GmbH, Offenburg, Germany). The net optical density bound for each standard and sample was calculated by subtracting the average non-specific binding optic density from the average optic density bound. To calculate the binding of each pair of standard wells as a percentage, the previously calculated net optical density was divided by the net optic density of the positive control wells, then multiplied by 100. Finally, the percent bound was plotted against the concentration of corticosterone for the standards.

The corticosterone level for each experimental condition was averaged and is displayed as mean ± 95% confidence interval. Differences between the means were compared using a two-tailed Student's t-test. Statistical calculations and visualizations were performed using GraphPad Prism.

2.7 ELECTROENCEPHALOGRAPHY RECORDINGS

For EEG measurements, mice were anesthetized by an intraperitoneal injection of FDDA (see section 2.3). Mice were then placed on a heating pad pre-warmed to 37ºC and their head was secured in a stereotactic setup. Throughout the surgery and subsequent measurements, breathing was monitored, and oxygen was supplied. For local anesthesia, 20–40 µl of 2% xylocaine (AstraZeneca, Wedel, Germany)

was injected subcutaneously at the incision sites. For the surgery, the scalp was cut with a scalpel and the connective surface was removed from the skull using 2% H_2O_2.

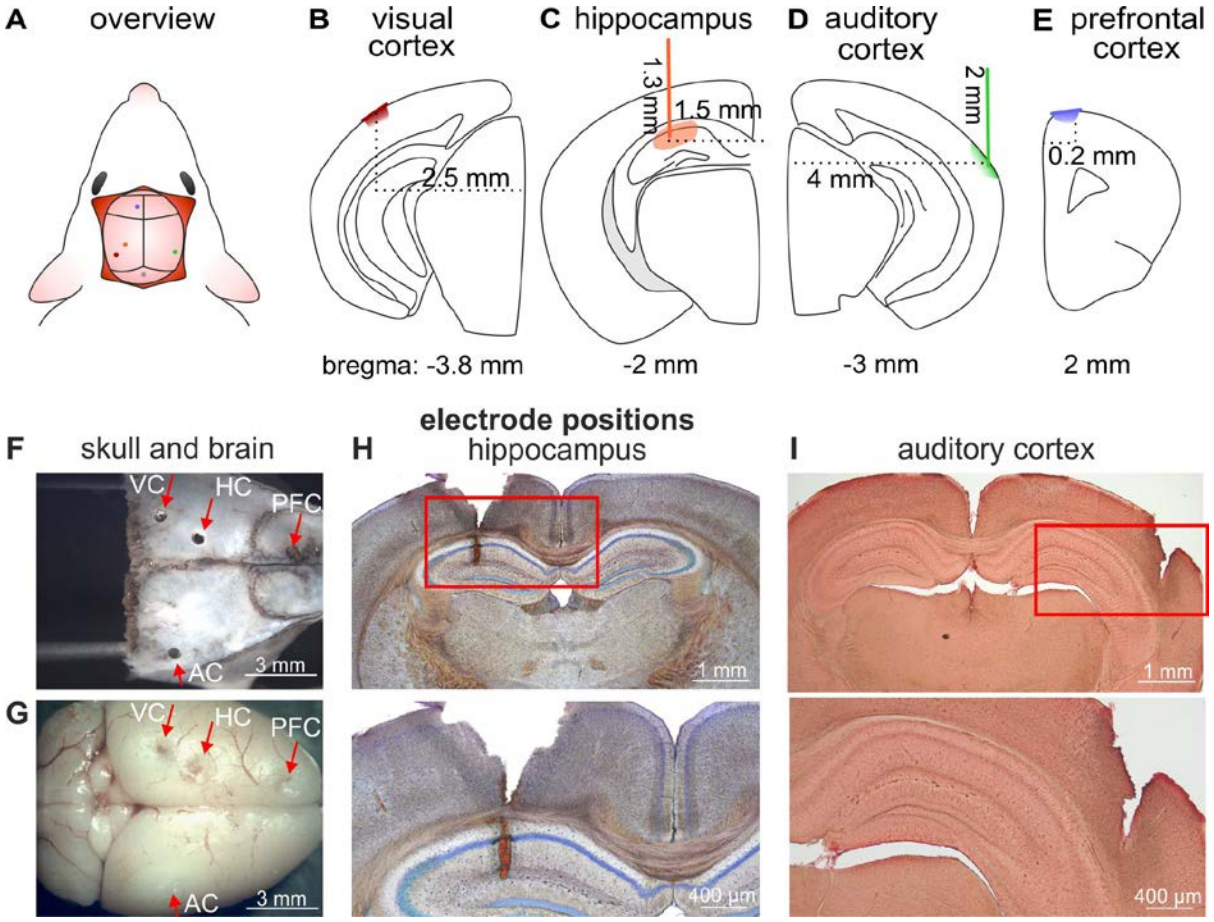

Figure 2.3. *Electrode placement for EEG recordings. (**A**) Overview of craniotomy indicating electrode positions of (B–E) and the position of the reference electrode on the cerebellum (gray; 1 mm ventral from lambda). (**B**) Position of the electrode placed on the surface of the visual cortex (coordinates: 2.5 mm lateral and 3.8 mm posterior to bregma). (**C**) Position of the electrode inserted into the hippocampus (coordinates: 1.5 mm lateral and 2 mm posterior to bregma, 1.3 mm ventral to skull). (**D**) Position of the electrode inserted into the AC (coordinates: 4 mm lateral and 3 mm posterior to bregma, 2 mm ventral to skull). (**E**) Position of the electrode placed on the surface of the prefrontal cortex (coordinates: 0.2 mm lateral and 2 mm anterior to bregma). (**F**) Representative photo of a skull indicating holes drilled for electrode placement (red arrows). (**G**) Representative photo of a brain indicating placement of surface and insertion electrodes (red arrows). (**H**) Representative photo of brain stained with toluidine blue indicating the position of the hippocampus electrode at approximately bregma -2 mm at a lower magnification (2x, top) and higher magnification (4x, bottom). (**I**) Representative photo of brain stained with toluidine blue indicating the position of the auditory cortex electrode at approximately bregma -3 mm at a lower magnification (2x, top) and higher magnification (4x, bottom). Red frames in the top panels (**H**) and (**I**) indicate the area of the higher magnification photos in the bottom panels. AC, auditory cortex; HC, hippocampus; PFC, prefrontal cortex; VC, visual cortex.*

First, the position of bregma and lambda were identified, and all coordinates were calculated and marked onto the skull using a permanent marker (**Figure 2.3A, F, G**). Then, 1 mm holes were drilled (NSK Ultimate XL-D, NSK Europe GmbH, Eschborn, Germany) into the skull at each coordinate. For the reference electrode, a hole was drilled 1–2 mm posterior to the lambda. For the recording electrodes, holes were drilled above the left visual cortex (**Figure 2.3B**, VC; 2.5 mm lateral and 2 mm posterior to bregma), left hippocampus (**Figure 2.3C**, HC; 1.5 mm lateral and 2 mm posterior to bregma), right AC (**Figure 2.3D**; 4 mm lateral and 3 mm posterior to bregma), and right prefrontal cortex (**Figure 2.3E**, PFC; 0.2 mm lateral and 2 mm anterior to bregma). A custom silver wire electrode (0.125 mm) insulated by varnish and silicone ending in a small silver bead was placed inside the holes for the reference, prefrontal cortex, and visual cortex on the surface of the brain; they were glued in place using Histoacryl® (B. Braun, Melsungen, Germany). For the AC and hippocampus, the electrodes were glued into 27G cannulas which were inserted into the brain (hippocampus: 1.3 mm ventral from skull, **Figure**

2.3H; AC: 2 mm ventral from skull, **Figure 2.3I**) and glued in place using Histoacryl®. Electrode placement was verified afterwards ex vivo in brain slices using toluidine blue staining (see section 2.13). The results obtained from the AC will be discussed in the present work.

After all electrodes were placed, the mouse was carefully moved to a soundproof chamber and placed on a heating pad pre-warmed to 37ºC. Electrodes were connected to an active head stage (LabRat AC16LR, Tucker Davis Technologies, Alachua, FL, USA). The signal was transferred to a programmable gain amplifier (PGA16 Rev.B, Multichannel Systems MCS, Reutlingen, Germany). The PGA allowed recording of signals between 5 Hz and 5 kHz at an amplification of 5000. The output of the PGA was connected to a multi-input/output measurement card (PCIe-6259, National Instruments, Austin, TX, USA) housed in a personal computer.

2.7.1 Resting State Activity

The resting state activity was recorded from 1000 epochs of 1 s duration each in which no acoustic stimulus was presented. Epochs were Fourier transformed using the FFT function in Matlab (version R2021b) and averaged over all animals in each experimental condition.

2.7.2 Local Field Potential Recording

LFPs in response to acoustic stimuli were obtained by presenting pure-tone stimuli (100 ms) at low (4.66, 5.66, 6.66 kHz), mid- (10.3, 11.3, 12.3 kHz), and high frequencies (21.7, 22.7, 23.7 kHz). Each stimulus was repeated 2000 times with a recording interval of 507 ms.

Responses were resampled using the eeglab anti-aliasing filter cutoff function in Matlab (rate 3000 Hz, cutoff 0.8, bandwidth 0.2; Delorme & Makeig, 2004). Artifacts were detected and rejected by a variance-amplitude criterion that rejects the 5% of trials with the highest variance. Then the first 100 ms of the recording were segmented and transformed by fast Fourier transform (rectangular window). Evoked and induced responses were separated by phase-coherent and phase-incoherent averaging, respectively. Evoked responses were computed by simple time domain averaging, peak-to-peak (min/max within predefined time interval) analysis of voltage values. Induced responses were computed by computation of peak-to-peak (min/max within predefined time interval). Oscillatory frequency bands were defined as follows: alpha (8–15 Hz), beta (15–25 Hz), low gamma (25–35 Hz), mid-gamma (35–65 Hz), and high gamma (65–125 Hz).

The LFP amplitude for each genotype was averaged and is displayed as the mean ± SEM. Results were statistically evaluated by permutation analysis and non-parametric signed-rank testing across genotypes for individual oscillatory frequency bands and stimulus conditions. The nine stimulus frequencies were grouped into the low, mid-, and high frequencies for statistical analysis.

2.7.3 Auditory Steady State Responses of Electroencephalography

ASSRs were evoked by presentation of an 11.31 kHz carrier frequency. For the growth function, the carrier frequency was amplitude-modulated by frequencies of either 10, 40, or 128 Hz at 100% modulation depth; the stimulus was presented from 10 to 90 dB SPL in 10 dB steps. For the transfer function, the stimulus was presented at 90 dB SPL at 100% modulation depth, while the carrier was amplitude-modulated by frequencies of 5, 10, 16, 20, 32, 40, 64, 80, 128, 160, 256, 320, 512, 640, 1024, 1280, 2048 Hz. Stimulus duration was 1000 ms with a recording interval of 1207 ms. Stimuli were repeated 64 times and averaged.

Like the LFPs, ASSRs were resampled using the eeglab anti-aliasing filter cutoff function (rate 3000 Hz, cutoff 0.8, bandwidth 0.2). Artifacts were detected and rejected by a variance-amplitude criterion that rejects the 5% of trials with the highest variance. Then the first 100 ms of the recording were segmented and transformed by fast Fourier transform (rectangular window). Evoked and induced responses were separated by phase-coherent and phase-incoherent averaging, respectively. Evoked responses were computed by simple time domain averaging, peak-to-peak (min/max within predefined

time interval) analysis of voltage values. Induced responses were computed by computation of peak-to-peak (min/max within predefined time interval). Oscillatory frequency bands were defined as follows: alpha (8–15 Hz), beta (15–25 Hz), low gamma (25–35 Hz), mid gamma (35–65 Hz), and high gamma (65–125 Hz).

The ASSR amplitude for each genotype was averaged and is displayed as mean ± SEM. Results were statistically evaluated by permutation analysis and non-parametric signed-rank testing across genotypes for individual oscillatory frequency bands and stimulus conditions.

2.8 ELECTROCOCHLEOGRAPHY RECORDINGS

For electrocochleography recordings, mice were anesthetized by an intraperitoneal injection of FDDA (see section 2.3). The fur behind the ear was removed and the skin was disinfected with Octenisept® (Schülke & Mayr GmbH, Norderstedt, Germany). Mice were then placed on a heating pad pre-warmed to 37ºC and 20–40 µl of 2% xylocaine (AstraZeneca, Wedel, Germany) was injected subcutaneously at the incision sites.

For the surgery, the skin behind the ear was cut to expose the bony bulla that surrounds the cochlea. Muscles, nerves, and connective tissue were moved aside allowing a small hole (0.6 mm diameter) to be drilled (NSK Ultimate XL-D, NSK Europe GmbH, Eschborn, Germany) into the bulla. The hole allowed access to the round window of the cochlea, near which was placed a custom silver wire electrode (0.125 mm) insulated by varnish and silicone ending in a small silver bead. This was fixed in place using Histoacryl® (B. Braun, Melsungen, Germany). Then, the skin above the ear was closed and the mouse was placed in a soundproof chamber (IAC 400-A, Industrial Acoustics Company GmbH, Niederkrüchten, Germany) on a pre-warmed heating pad.

2.8.1 Compound Action Potential

CAP responses from the auditory nerve were evoked by presenting click stimuli (100 µs) at SPLs from 0 to 100 dB, increasing in 5 dB steps, and by presenting pure-tone stimuli (3 ms, including 1 ms $\cos^2$ rise and fall envelope) between 2 and 32 kHz at SPLs from 0 to 100 dB, increasing in 5 dB steps. The measured signals were amplified and filtered (DC, 50 kHz lowpass). The analog/digital rate was 100 kHz. Stimuli were repeated in recording intervals of 50 ms and responses were averaged for 60 repetitions.

Thresholds were manually determined during the measurement by identifying the lowest stimulus level at which the CAP signal could be distinguished from the baseline noise level. Thresholds from all ears were averaged and are displayed as mean ± SEM. Normal distribution was assessed using the Shapiro-Wilk normality test ($\alpha = 0.05$). For click stimuli, differences between the means were compared using the two-tailed Student's t-test. For pure-tone stimuli, differences between the means were compared using a 2-way ANOVA with Bonferroni's multiple comparisons test. Statistical calculations and visualizations were performed using GraphPad Prism.

2.8.2 Peristimulus Time Response

PSTRs were evoked by presenting a pseudo-randomized noise-burst auditory stimulus of 200 ms length with a 2.5 ms onset and offset ramp ($\cos^2$-shaped) with alternating polarity. The noise had a center frequency of 5.6, 8, 11.3, 16, or 22.6 kHz, bandwidth of 1/3 octave, and was presented at SPLs from 10 to 80 dB, increasing in 10 dB steps. The measured signals were bandpass filtered from 1 to 30 kHz and amplified by ×5000. Each 200 ms stimulus had a recording window of 410 ms, an interstimulus interval of 420 ms, and was repeated 100 times.

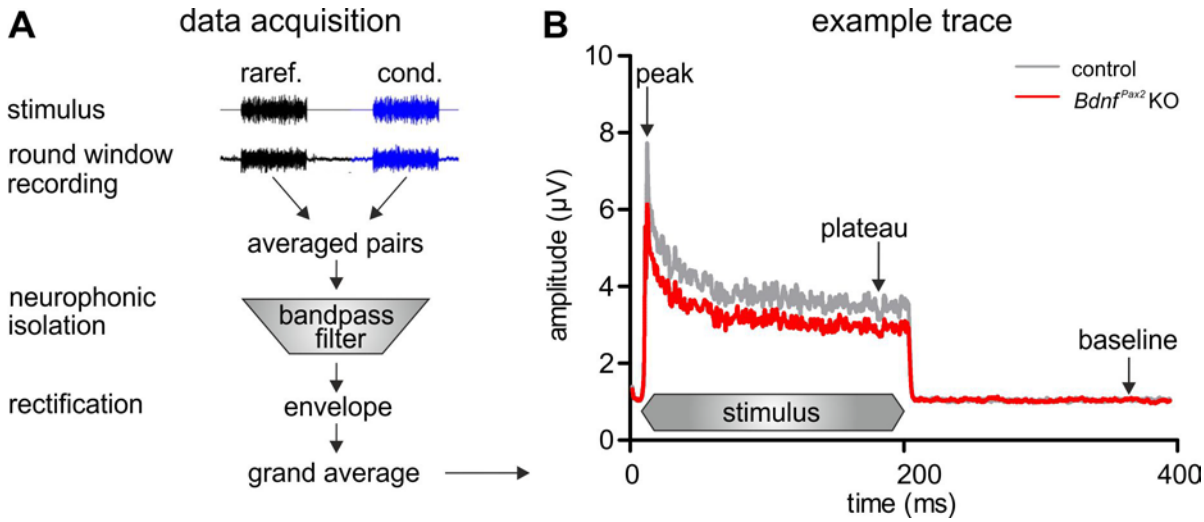

Figure 2.4. *PSTR recording and analysis. (**A**) Data acquisition process. Two consecutive noise-band stimuli of alternating rarefaction and condensation polarities are presented, and the responses to the stimulus pairs from the electrode at the round window are recorded. The response pairs are subsequently averaged and bandpass-filtered to isolate the neurophonic response. The function is then rectified by taking the envelope and then averaged across all repetitions. (**B**) The resulting signal consists of an initial onset peak, followed by a rapid adaptation, plateauing to a steady-state response until the stimulus ends. Representative traces of control (gray) and Bdnf^{Pax2} KO mice (red) are displayed.*

For analysis, the two consecutive signals of opposite polarities were averaged in order to isolate the neurophonic signal (**Figure 2.4A**). The signal was bandpass filtered by software from 300 to 1200 Hz, rectified, and smoothed (1 ms window; **Figure 2.4A**). The maximum amplitude in the first 30 ms after the stimulus onset was defined as the peak, and the average amplitude in the last 30 ms before stimulus offset was defined as the plateau (**Figure 2.4B**). From these, the peak/plateau ratio was calculated and averaged for all animals of the same experimental condition and are displayed as mean ± SEM. Normal distribution was assumed. Differences between the means were compared using a 2-way ANOVA with Bonferroni's multiple comparisons test. Statistical calculations and visualizations were performed using GraphPad Prism.

2.9 Behavioral Experiments

Behavioral experiments were conducted between 9am and 5pm. After each trial, the chambers were cleaned with 70% EtOH to remove odors of the previous mouse in the experiment. Behavior was recorded with a GoPro Hero7 Black camera (GoPro GmbH, Munich, Germany) and subsequently analyzed offline.

2.9.1 Novel Object Recognition Test

The novel object recognition test (Lueptow, 2017) was conducted in a chamber made from polyvinyl chloride (38 × 45 cm). The experiment consisted of two phases conducted on two consecutive days. In the first learning phase, mice were placed in the middle of the chamber that contained two identical objects in opposite corners. The mouse was allowed to explore the chamber for ten minutes and was then removed. In the second test phase, one of the objects was replaced with a novel object. The mouse was again placed in the chamber for ten minutes and allowed to explore. The location of the novel object was alternated for each cohort.

Recorded videos of the experiment were manually analyzed for the length in seconds that the mouse spent directly sniffing each of the objects. Excluded from the definition of "direct sniffing" were instances when the mouse did not intentionally approach the object, was on top of the object, or was engaged in repetitive behavior near the object (e.g., grooming).

A discrimination index was calculated using the following formula:

$$discrimination\ index = \frac{sniffing\ novel\ object\ (sec) - sniffing\ familiar\ object(sec)}{sniffing\ novel\ object\ (sec) + sniffing\ familiar\ object(sec)} \times 100$$

The direct sniffing and discrimination indices were averaged for animals of each experimental condition and are displayed as mean (normally distributed) or median (non-normally distributed). Normal distribution was assessed using the Shapiro-Wilk normality test (α = 0.05). Differences between the means were compared using a two-tailed Student's t-test (direct sniffing) or the Kruskal-Wallis test with Dunn's multiple comparisons test (discrimination index). Statistical calculations and visualizations were performed using GraphPad Prism.

2.9.2 Social Interaction Test

Crawley's sociability test (Silverman et al., 2010) was conducted in a rectangular three-chamber box made from polyvinyl chloride (19 × 45 cm per chamber). The chambers were separated by walls with removable doors. A wire cup was placed in the two outer chambers; one cup was empty and the other contained a "stranger" mouse (an age- and sex-matched mouse of the same line, but without prior contact to the experimental mouse). The experimental mouse was placed in the center chamber for five minutes to allow it to adapt to the environment; during this time, access to the outer chambers was blocked by the doors. After the adaptation, the doors were opened and the mouse was allowed to explore for ten minutes. The wire cup containing the stranger mouse was alternated for each cohort.

Recorded videos of the experiment were manually analyzed for the length in seconds that the mouse spent directly sniffing each of the wire cups. Excluded from the definition of "direct sniffing" were instances when the mouse did not intentionally approach the cup, was climbing on the cup, or was engaged in repetitive behavior near the cup. Additionally, the latency of the first entrance to each chamber, the number of entrances to each chamber, and the time spent in each chamber were calculated. An "entrance" was defined as all four paws passing through the door.

During the social interaction test, the repetitive and anxious behavior of the mice were also measured. As a metric for repetitive behaviors, the time mice spent grooming was measured. As a metric for anxiety, the time mice spent freezing was measured.

Data are displayed as mean (normally distributed) or median (non-normally distributed). Normal distribution was assessed using the Shapiro-Wilk normality test (α = 0.05). Differences between the means were compared using a two-tailed Student's t-test, one-way ANOVA (parametric) / Kruskal-Wallis test (non-parametric) with Sidak's (parametric) or Dunn's (non-parametric) multiple comparisons test. Statistical calculations and visualizations were performed using GraphPad Prism.

2.10 IMMUNOHISTOCHEMISTRY

Table 2.2. *Primary and secondary antibodies used. CtBP2, C-terminal binding protein 2; PV, parvalbumin; vGlut1, vesicular glutamate transporter 1.*

Primary Antibodies	Species	Dilution	Company	Catalog Number
Anti-CtBP2	rabbit (polyclonal)	1:750	American Research Products Inc™	10-P1554
Anti-PV	rabbit (polyclonal)	1:2000	Abcam	AB11427
Anti-vGlut1	guinea pig (polyclonal)	1:1000	Synaptic Systems	135 304
Secondary Antibodies	**Species**	**Dilution**	**Company**	**Catalog Number**
Cy3	goat (anti-rabbit)	1:1500	Jackson ImmunoResearch Laboratories	111-166-003
Alexa 488	goat (anti-guinea pig)	1:500	Molecular Probes	A11073

2.10.1 Cochleae

Cochleae were isolated from the bulla and immersed in 2% paraformaldehyde for 2 h. They were transferred to 0.4% paraformaldehyde and stored at 4ºC until sectioning. Before sectioning, cochleae were decalcified for 45 min in RDO Rapid Decalcifier (Apex Engineering Products Corporation, Aurora, IL, USA) and stored overnight in 25% sucrose Hanks buffered saline. Cochleae were then embedded in Tissue-Tek® O.C.T. Compound (Miles Laboratories, Elkhart, IN, USA), sectioned in 10 µm slices using a cryostat (Leitz 1720 Digital Cryostat, Leica Biosystems, Wetzlar, Germany), and mounted on SuperFrost*/plus microscope slides at -20ºC.

For immunohistochemical staining, sections were thawed and the tissue was permeated for 10 min using 0.1% Triton X-100 (Sigma-Aldrich, Munich, Germany), rinsed with 100 mM PBS, then blocked with 4% normal goat serum for 30 min at room temperature. After incubation, the blocking solution was discarded and slices were incubated with the primary antibodies (**Table 2.2**), which had been diluted in PBS-containing 0.5% bovine serum albumin, overnight at 4ºC. The primary antibodies were incubated for 1 h with appropriate secondary antibodies (**Table 2.2**) diluted in PBS-containing 0.5% bovine serum albumin. Sections were rinsed three times in 1x PBS for ten minutes per rinse. Finally, sections were mounted with Vectashield mounting medium containing DAPI (Vector Laboratories, Newark, CA, USA) to visualize cell nuclei.

Stained samples were viewed using an upgraded Olympus BX63 microscope (EVIDENT Europe GmbH, Hamburg, Germany). Images were acquired using a Hamamatsu ORCA-Flash4.0 LT PLUS monochrome camera (Hamamatsu Photonics K.K., Herrsching, Germany) and analyzed with CellSens Dimension software (OSIS GmbH, Münster, Germany). Slices were imaged over ~15 µm in an image stack along the z-axis. Images were then three-dimensionally deconvoluted using CellSens Dimension's built-in algorithm. Typically, an image stack consisted of 30 images with 0.28 µm between images.

Counting of immunopositive dots was performed manually at the time of imaging. For each mouse, between two and four cochlear sections were individually stained and analyzed, the average of which was used for further statistical analyses. Data are displayed as mean. Normal distribution was assessed using the Shapiro-Wilk normality test ($\alpha = 0.05$). Differences between the means were compared using a one-way ANOVA with Sidak's multiple comparisons test. Statistical calculations and visualizations were performed using GraphPad Prism.

2.10.2 Brains

Brains were dissected and fixed in 2% paraformaldehyde for 48 h before being transferred to 1% paraformaldehyde and stored at 4ºC until sectioning. Brains were sectioned in 60 µm coronal slices using a vibratome (Leica VT1000S Vibrating Blade Microtome, Leica Biosystems, Wetzlar, Germany). Slices were stored in cryoprotectant (150 g of sucrose in 200 ml 1x PBS and 150 ml ethylene glycol, volume adjusted to 500 ml with 1x PBS) at -20ºC until use.

For immunohistochemical staining, slices were first rinsed two times in 1x PBS for 15 min per wash, then were permeated and blocked for 30 min with 3% bovine serum albumin containing 0.2% Triton X-100 (Sigma-Aldrich, Munich, Germany). After incubation, the solution was discarded and slices were incubated with the primary antibodies (**Table 2.2**), which had been diluted in 1.5% bovine serum albumin containing 0.1% Triton-X 100 (Sigma-Aldrich, Munich, Germany), overnight at 4ºC in a humidified chamber. After incubation, the primary antibody solution was removed and slices were washed three times in 1x PBS for 15 min per wash. The primary antibodies were detected by incubation for 1 h at room temperature with appropriate secondary antibodies (**Table 2.2**), which had been diluted in 1.5% bovine serum albumin containing 0.1% Triton-X 100 (Sigma-Aldrich, Munich, Germany). After incubation, slices were washed three times in 1x PBS for 15 min per wash. Finally, the slices were mounted with Vectashield mounting medium with DAPI (Vector Laboratories, Newark, CA, USA).

Stained samples were viewed using the upgraded Olympus BX63 microscope (EVIDENT Europe GmbH, Hamburg, Germany). Images were acquired using a Hamamatsu ORCA-Flash4.0 LT PLUS monochrome camera (Hamamatsu Photonics K.K., Herrsching, Germany) and analyzed with CellSens Dimension software (OSIS GmbH, Münster, Germany). Slices were imaged over ~15 µm in an image stack along the z-axis. Typically, the image stacks consisted of 30 images with 0.28 µm between images. Images were then three-dimensionally deconvoluted using CellSens Dimension's built-in algorithm.

Image stacks were analyzed using the free software ImageJ (NIH, Bethesda, MD, USA). For each stack, the three channels were split and analyzed separately as a maximum intensity projection over the z-axis. A binary mask was created using the default parameters. A region of interest (270 × 270 pixels for 1024 × 1024 images and 540 × 540 pixels for 2048 × 2048 images) was placed on the dendrites of the pyramidal neurons in each single-channel picture. Afterward, the average fluorescence intensity within the region of interest was calculated. For analysis, the data were normalized between groups in order to account for variability in staining. For each animal, one slice was processed and three to five images per animal were averaged and used for further statistical analyses.

Data are displayed as mean ± SEM. Normal distribution was assessed using the Shapiro-Wilk normality test ($\alpha = 0.05$). Differences between the means were compared using a two-tailed Student's t-test. Statistical calculations and visualizations were performed using GraphPad Prism.

2.11 GOLGI-COX STAINING

Golgi-Cox staining was performed using the FD Rapid GolgiStain™ Kit (FD NeuroTechnologies, Columbia, MD, USA). Brains were dissected and immersed in the A:B impregnation solution (prepared 1–2 days before dissection). After one day, the impregnation solution was replaced and the brains were then stored in the dark for nine additional days at room temperature; twice a week during this period, the tissue container was gently swirled. After the impregnation period, brains were transferred to solution C. After one day, the solution C was replaced and brains for stored in the dark for two additional days at room temperature. Afterwards, the brains were cut in 150 µm coronal sections using a vibratome (Leica VT1000S Vibrating Blade Microtome, Leica Biosystems, Wetzlar, Germany) and mounted on gelatin-coated slides (FD NeuroTechnologies, Columbia, MD, USA).

The slides dried overnight in the dark at room temperature. For staining, slides were rinsed two times for four minutes each in double-distilled H_2O before being placed in the staining solution D:E for ten minutes. Slides were then rinsed two more times for four minutes each in double-distilled H_2O then dehydrated in sequential four-minute rinses of 50%, 75%, and 95% EtOH. After, slides were dehydrated in 100% EtOH three times for four minutes each and cleared in xylene three times for four minutes each. Slides were covered using Eukitt® Quick-hardening mounting medium (Sigma-Aldrich, Darmstadt, Germany).

Stained samples were viewed using the upgraded Olympus BX63 microscope (EVIDENT Europe GmbH, Hamburg, Germany). Images were acquired using a DP28 color camera (EVIDENT Europe GmbH, Hamburg, Germany) at 60x magnification. The first dendritic branch extending from the main apical shaft of pyramidal neurons in the hippocampal CA1 region were selected for analysis. Excluded from further analyses were instances where (i) neurons were not completely impregnated, (ii) dendritic branches were damaged, (iii) dendritic branches were interrupted by other dendrites, and (iv) dendritic branches were shorter than 20 µm. For each animal, four to eight dendrites were imaged and processed.

Spine analysis and classification was performed using the Reconstruct software (Fiala, 2005). For each dendrite, segments of at least 30 µm were analyzed. All protrusions directly contacting the dendritic segment were labelled as spines. The spine density was calculated as the number of protrusions per µm. The length and width of each spine was also measured and transferred to a data spreadsheet where the

spines were classified hierarchically according to the following definitions in that order (Risher et al., 2014):

1. Branched: manually entered
2. Filopodia: length > 2 µm
3. Mushroom: width > 0.6 µm
4. Long thin: length > 1 µm
5. Thin: length-to-width ratio > 1
6. Stubby: length-to-width ratio ≤ 1

Data are displayed as mean ± SEM. Normal distribution was assessed using the Shapiro-Wilk normality test ($\alpha = 0.05$). Differences between the means were compared using a two-tailed Student's t-test. Statistical calculations and visualizations were performed using GraphPad Prism.

2.12 In-Situ Hybridization

Table 2.3. *Primer for riboprobe. NO-GC, nitric oxide–sensitive guanylyl cyclase.*

Gene of Interest	Accession Number	Sequence	bps
NO-GC β1	AF297083.1	for: 5'-atcctcttcagcggcattgtg-3' rev: 5'-tgcattggttccttcttgccc-3'	536 bp

Brains were dissected and fixed in 2% paraformaldehyde for 48 h before being transferred to 1% paraformaldehyde and stored at 4ºC until sectioning. Brains were sectioned in 60 µm coronal slices using a vibratome (Leica VT1000S Vibrating Blade Microtome, Leica Biosystems, Wetzlar, Germany). Sections were stored in cryoprotectant (150 g of sucrose in 200 ml 1x PBS and 150 ml ethylene glycol, volume adjusted to 500 ml with 1x PBS) at 20ºC until use.

First, slices were washed two times for five minutes each with 1x PBS. Positive charges were then blocked by a five-minute incubation in 0.25% acetic anhydrate. Slices were once again washed two times for five minutes each with 1x PBS. The tissue was then dehydrated in sequential one-minute rinses of 70%, 95%, and twice in 100% EtOH. Slices were then incubated in chloroform for five minutes to remove lipophilic substances before being rehydrated in sequential one-minute rinses of 100% (twice), 95%, and 70% EtOH. Slices were then washed for five minutes with 2x saline-sodium citrate (0.3 M NaCl, 0.03 M sodium citrate, pH 7.0) and incubated for one hour at 37º in the prehybridization buffer (Sigma, Munich, Germany). Custom-designed riboprobes (**Table 2.3**) were diluted in the Microarray Hybridization Buffer (GE Healthcare, Freiburg, Germany) and incubated for 10 min at 65ºC, then put on ice until use. Slices were incubated with the riboprobes in a moist formamide chamber at 58ºC overnight. Afterwards, slices were washed for 20 min in 2x saline-sodium citrate, 20 min in 1x saline-sodium citrate, and 20 min in 0.5x saline-sodium citrate at hybridization temperature. They were then washed for five minutes in Tris-HCl with 0.05% Tween 20 (Applichem, Darmstadt, Germany) and incubated for 30 min in blocking reagent (Roche, Mannheim, Germany). The anti- digoxigenin antibody (Roche, Mannheim, Germany) was then applied and slices were incubated for 30 min at 37ºC, after which they were washed two times for 15 min each in Tris-HCl (Applichem, Darmstadt, Germany). Slices were then rinsed in alkaline phosphatase buffer (100 mM Tris, 100 mM NaCl, pH 9.5) and incubated with 500 µl of substrate (50 mg/ml 5-bromo-4-cloro-3-indolyl phosphate, p-toluidine salt (Sigma-Aldrich, Munich, Germany) in 100% *N,N*-dimethylformamide, 50 mg/ml Nitro Blue Tetrazolium (Biomol, Hamburg, Germany) in 70% *N,N*-dimethylformamide, 10 ml alkaline phosphatase buffer) until the sense probe gave a signal, upon which the reaction was stopped by applying double-distilled H_2O. Slices were rinsed twice more for 15 min each in double-distilled H_2O and the staining was fixed using 95% EtOH for 15 min then washed two times for ten minutes each with double-distilled H_2O. Finally, slices were mounted using Kaisers Gelatin (Merck, Darmstadt, Germany).

Stained samples were viewed using an upgraded Olympus BX63 microscope (EVIDENT Europe GmbH, Hamburg, Germany). Images were acquired using a DP28 color camera (EVIDENT Europe GmbH, Hamburg, Germany).

Images were analyzed using the free software ImageJ (NIH, Bethesda, MD, USA). For the color of the staining, obtained from drawing a region of interest over a representatively stained area, the average pixel intensity across the image was measured and subsequently subtracted from 255. For each animal, duplicate stainings were performed, and four to six images were taken per staining in each region analyzed. The resulting eight to 12 images were then averaged and used for further statistical analyses. Data are displayed as mean with individual data points. Normal distribution was assessed using the Shapiro-Wilk normality test ($\alpha = 0.05$). Differences between the means were compared using a two-tailed Student's t-test. Statistical calculations and visualizations were performed using GraphPad Prism.

2.13 Toluidine Blue Staining

Brains were dissected and fixed in 2% paraformaldehyde for 48 h before being transferred to 1% paraformaldehyde and stored at 4ºC until sectioning. Brains were sectioned in 60 µm coronal slices using a vibratome (Leica VT1000S Vibrating Blade Microtome, Leica Biosystems, Wetzlar, Germany). For confirmation of electrode positions of the EEG measurements, slices were washed for five minutes in 1x PBS then submerged for 30 seconds in 1% toluidine blue in acetate buffer (pH 3.9). Slices were washed twice with double-distilled H_2O and mounted on slides and covered with Mowiol® 4-88 Mounting Medium (Merck Millipore, Darmstadt, Germany).

Stained samples were viewed using an upgraded Olympus BX63 microscope (EVIDENT Europe GmbH, Hamburg, Germany). Images were acquired using a DP28 color camera (EVIDENT Europe GmbH, Hamburg, Germany). Electrode position was confirmed by referencing the mouse brain atlas (Franklin & Paxinos, 2008).

2.14 Field Excitatory Postsynaptic Potential Recordings in Hippocampal Slices

Mice were deeply anesthetized with CO_2 then sacrificed by decapitation. Brains were immediately dissected and submerged in oxygenated ice-cold dissection buffer (127 mM NaCl, 1.9 mM KCl, 1.2 mM KH2PO4, 26 mM NaHCO3, 10 mM D-glucose, 2 mM MgSO4, and 1.1 mM CaCl2). They were immediately sectioned in 400 µm coronal slices using a vibratome Leica VT1000S Vibrating Blade Microtome, Leica Biosystems, Wetzlar, Germany), still immersed in the ice-cold dissection buffer saturated with 5% CO_2 and 95% O_2. Slices were then incubated in artificial cerebrospinal fluid (127 mM NaCl, 1.9 mM KCl, 1.2 mM KH2PO4, 26 mM NaHCO3, 10 mM D-glucose, 1 mM MgSO4, 2.2 mM CaCl2; pH 7.4) for 1 h at 30ºC, after which they were stored at room temperature.

Recordings were performed in a submerged-type recording chamber (Warner Instruments, Holliston, MA, United States). A stimulation electrode (TM53CCINS, WPI, Sarasota, FL, United States) and a recording electrode (artificial cerebrospinal fluid–filled glass pipette, 2–3 MΩ) were positioned in the stratum radiatum region of the hippocampus to record Schaffer collateral fEPSPs. Signals were amplified with an Axopatch 200B (Molecular Devices, San Jose, CA, United States), digitized at 5 kHz with an ITC-16 (HEKA, Reutlingen, Germany) and recorded using WinWCP from the Strathclyde Electrophysiology Suite (University of Strathclyde, Glasgow, UK).

Stimuli (100 µs) were delivered through a stimulus isolator (World Precision Instruments, Friedberg, Germany). For an individual slice, the strength of the stimulation that evoked 40–60% of the maximal fEPSP slope was chosen for further recordings. First, paired-pulse facilitation was measured by presenting two stimuli with varying interstimulus intervals (10, 20, 50, 100, 200, and 500 ms). Then, the baseline fEPSP was measured for 15–20 min (0.067 Hz), a high-frequency stimulation was applied

(1 s, 100 Hz), and the fEPSP was measured for 1 h to analyze LTP (0.067 Hz). The same stimulus intensity was used for all recordings in each slice.

For analyses, four traces were averaged for each single data point in all measurements. Slices were excluded from analysis if they did not show a stable fEPSP baseline (SD > 12%). The fEPSP baseline was determined by averaging the fEPSP slopes from the 15–20 min period before high-frequency stimulation. The percentage of LTP was calculated by averaging the fEPSP slopes from the 50–60 min period after high-frequency stimulation and dividing that by the average baseline fEPSP slope. Data is presented as mean ± SEM. Normal distribution was assessed using the Shapiro-Wilk normality test ($\alpha = 0.05$). Differences between the means were compared using a two-tailed Student's t-test. Statistical calculations and visualizations were performed using GraphPad Prism.

For paired-pulse facilitation, the slope and amplitude ratios were respectively calculated by dividing the second fEPSP slope and amplitude by the first fEPSP slope and amplitude at each interstimulus interval. This was then averaged across all slices for each experimental condition. Data is presented as mean ± SEM. Normal distribution was assessed using the Shapiro-Wilk normality test ($\alpha = 0.05$). Differences between the means were compared using a 2-way ANOVA with Sidak's multiple comparisons test. Statistical calculations and visualizations were performed using GraphPad Prism.

3 RESULTS

Bdnf^{Pax2} KO mice were previously described to have normal hearing sensitivity (i.e., thresholds), but significantly impaired activity of every structure of the auditory system measured to date, spanning from the exocytosis at the inner hair cell synapse to the auditory responses of the midbrain and auditory thalamus (Chumak et al., 2016; Eckert et al., 2021; Zuccotti et al., 2012). *Bdnf*^{Pax2} KO mice have additionally been shown to have compromised temporal sound coding, reflected by slower responses to acoustic stimuli and poorer responses to more complex, amplitude-modulated stimuli (Eckert et al., 2021). This phenotype is strikingly reminiscent of patients with ASD, who generally exhibit lower-amplitude ABRs and disrupted temporal sound coding (Wilde et al., 2022). Therefore, to validate the previously described hearing phenotype of *Bdnf*^{Pax2} KO mice with particular focus to the aspects that may suggest an ASD phenotype, the hearing function was tested at various levels of the ascending auditory pathway.

To first ensure that mice did not exhibit hearing loss, hearing thresholds were measured by placing a subcutaneous electrode at the back as the ground (**Figure 3.1A**, gray), at the vertex as the reference (**Figure 3.1A**, blue), and below the ear to record (**Figure 3.1A**, red). Click, noise-burst, and pure-tone stimuli were presented at increasing intensities and the threshold was defined as the lowest stimulus level in which the ABR signal could be distinguished from the baseline noise (**Figure 3.1A**, lower panel, red line).

As expected based on previous observations (Chumak et al., 2016; Eckert et al., 2021; Zuccotti et al., 2012), the present cohort of *Bdnf*^{Pax2} KO mice did not differ from controls in their click, noise-burst, or pure-tone thresholds (**Figure 3.1B,C**, click: Mann-Whitney U test, $U = 1098$, $p = 0.18$, control: $n = 50/25$, *Bdnf*^{Pax2} KO: $n = 52/26$ ears/mice; noise-burst: Mann-Whitney U test, $U = 1131$, $p = 0.26$, control: $n = 50/25$, *Bdnf*^{Pax2} KO: $n = 52/26$ ears/mice; pure-tone: 2-way ANOVA, $F(1, 573) = 0.43$, $p = 0.51$, control: $n = 31/25$, *Bdnf*^{Pax2} KO: $n = 31/26$ ears/mice).

The ABR can not only be used to determine the animal's hearing threshold, but it is also a powerful measurement that can reveal the summed neuronal activity of specific structures along the ascending auditory pathway (**Figure 3.1D**; Burkard et al., 2007). In the present work, wave I and wave IV will be examined to gain insight into more peripheral (wave I, auditory nerve) and more central responses (wave IV, IC and lateral lemniscus; **Figure 3.1D**).

To examine the functionality of the auditory nerve of *Bdnf*^{Pax2} KO mice, the fine structure of supra-threshold ABR wave I was analyzed. Consistent with previous observations (Chumak et al., 2016; Eckert et al., 2021; Zuccotti et al., 2012), *Bdnf*^{Pax2} KO mice exhibited significantly lower ABR wave I amplitude in comparison to littermate controls (**Figure 3.1E**, 2-way ANOVA, $F(1, 1746) = 138.3$, $p < 0.0001$, Bonferroni's multiple comparisons test, control: $n = 57/29$, *Bdnf*^{Pax2} KO: $n = 62/31$ ears/mice).

Impaired activity in the auditory nerve can either be propagated to later structures in the auditory pathway or can be compensated for by an increased activity of later structures (Marchetta, Savitska, et al., 2020; Mohrle et al., 2016; Savitska et al., 2022); thus, the fine structure of supra-threshold ABR wave IV was analyzed, representing activity of the IC and the lateral lemniscus. Confirming previous observations (Chumak et al., 2016; Eckert et al., 2021; Zuccotti et al., 2012), *Bdnf*^{Pax2} KO mice were not able to compensate for the reduced auditory input, exhibiting a lower ABR wave IV amplitude in comparison to littermate controls (**Figure 3.1F**, 2-way ANOVA, $F(1, 1724) = 106.7$, $p < 0.0001$, Bonferroni's multiple comparisons test, control: $n = 56/29$, *Bdnf*^{Pax2} KO: $n = 62/31$ ears/mice).

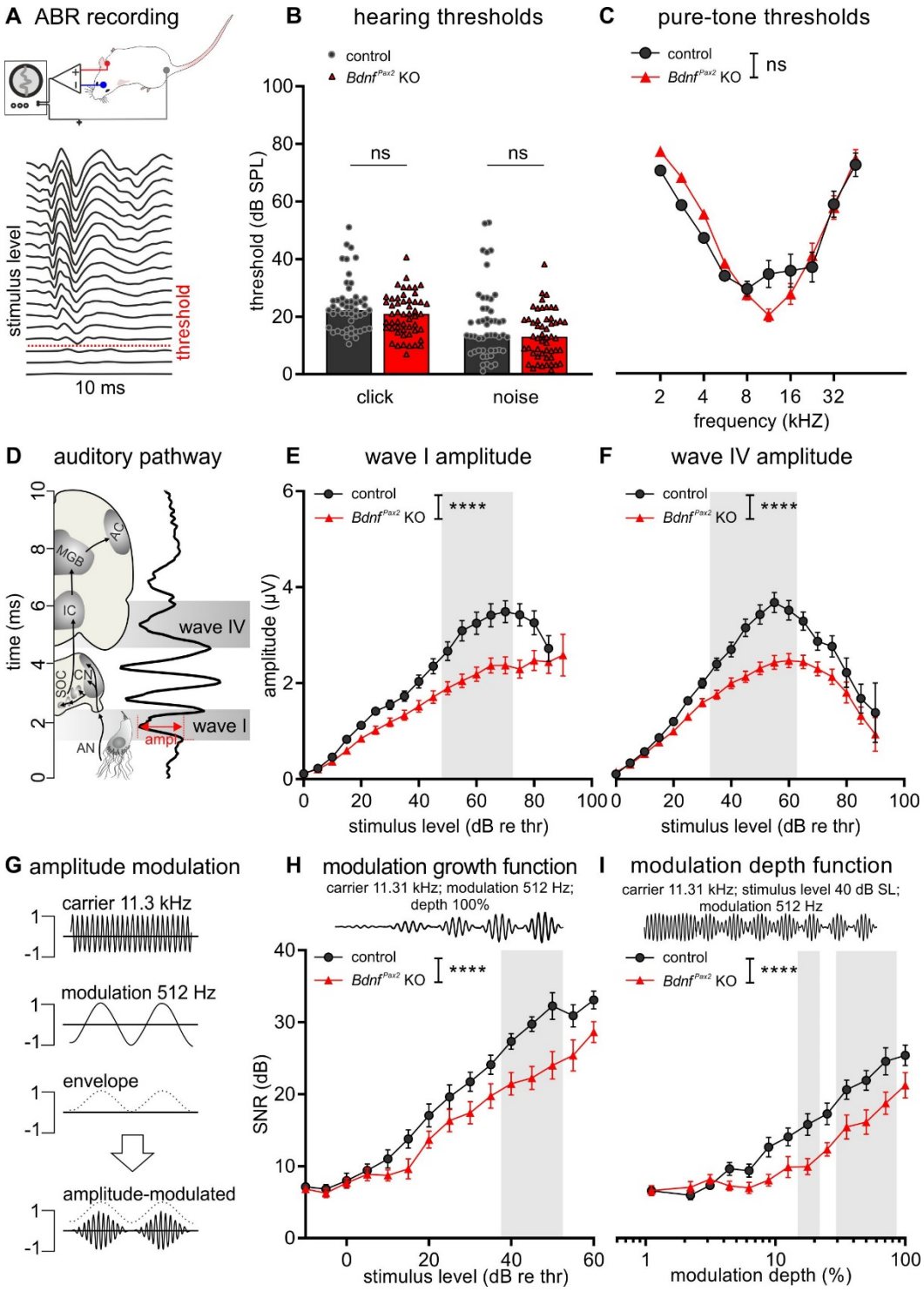

Figure 3.1. *Hearing phenotype of Bdnf^{Pax2} KO mice. (**A**) Schematic of electrode placement for ABR recording and threshold determination, with the dotted red line depicting the hearing threshold. (**B**) Hearing thresholds of control (black circles) and Bdnf^{Pax2} KO mice (red triangles) in response to click and noise-burst stimuli. Symbols, ears; bar, median. (**C**) Hearing thresholds of control and Bdnf^{Pax2} KO mice in response to pure-tone stimuli. (**D**) Schematic of the auditory pathway and the ABR waves that are correlated with the neural activity of specific structure(s), with gray highlights indicating ABR wave I—correlated with the activity of the auditory nerve—and ABR wave IV—correlated with the activity of the IC and lateral lemniscus. AC, auditory cortex; AN, auditory nerve; CN, cochlear nucleus; MGB, medial geniculate body; SOC, superior olivary complex. (**E,F**) ABR wave I (**E**) and IV (**F**) amplitude of control and Bdnf^{Pax2} KO mice, with the gray area indicating stimulus levels for which the post hoc test was significant. (**G**) Schematic of the amplitude-modulated stimulus used to evoke ASSRs, depicting the 11 kHz carrier frequency, 512 Hz modulation frequency, and envelope, resulting in the amplitude-modulated stimulus used in the measurements. (**H,I**) Modulation growth function (**H**) and modulation depth function (**I**) SNR of control and Bdnf^{Pax2} KO mice, with the gray area indicating stimulus levels for which the post hoc test was significant. Mean ± SEM. **** = $p < 0.0001$, ns = not significant.*

To determine if the auditory system of *Bdnf*^{Pax2} KO mice could follow more complex, amplitude-modulated acoustic stimuli, ASSRs in response to amplitude-modulated tones were measured. An 11 kHz carrier frequency was amplitude-modulated with a frequency of 512 Hz (**Figure 3.1G**); the discharge of neurons phase-locks to the modulation frequency (Lin et al., 2009) and this phase-locking is measured as the ASSR. Confirming previous observations (Eckert et al., 2021), *Bdnf*^{Pax2} KO mice exhibited a lower signal-to-noise ratio (SNR) compared to littermate controls in response to stimuli of increasing loudness and modulation depths (**Figure 3.1H,I**, modulation growth: 2-way ANOVA, $F(1, 566) = 56.12$, $p < 0.0001$, Bonferroni's multiple comparisons test, control: $n = 19$, *Bdnf*^{Pax2} KO: $n = 21$ mice; modulation depth: 2-way ANOVA, $F(1, 468) = 48.36$, $p < 0.0001$, Bonferroni's multiple comparisons test, control: $n = 19$, *Bdnf*^{Pax2} KO: $n = 19$ mice). This indicates that *Bdnf*^{Pax2} KO mice have an impairment in phase-locking that impacts their ability to process complex auditory stimuli.

Taken together, this suggests that *Bdnf*^{Pax2} KO mice have normal basic hearing function (i.e., thresholds) but impaired sound processing already at the level of the auditory nerve and along the ascending auditory pathway and difficulties following more complex, amplitude-modulated acoustic stimuli. Not only does this confirm previous results, but importantly, this hearing phenotype mimics that reported in ASD patients, which trend towards lower ABR wave amplitudes and slower responses (Wilde et al., 2022).

3.1 CHARACTERIZING THE CENTRAL PHENOTYPE OF *BDNF*^{PAX2} KO MICE

3.1.1 Excitation-Inhibition Imbalance in *Bdnf*^{Pax2} KO Mice

Bdnf^{Pax2} KO mice have previously been reported to have a behavioral phenotype reminiscent of ASD, exhibiting repetitive behavior, less sociability, higher stress levels, and impaired memory function (Eckert et al., 2021); however, it is not yet known whether *Bdnf*^{Pax2} KO mice also exhibit neural response characteristics in line with these. Notably, an imbalance between excitatory and inhibitory activity is considered a key feature in ASD patients (for a review, see Marin, 2012) which has also been observed in mouse models (for a review, see Gogolla et al., 2009).

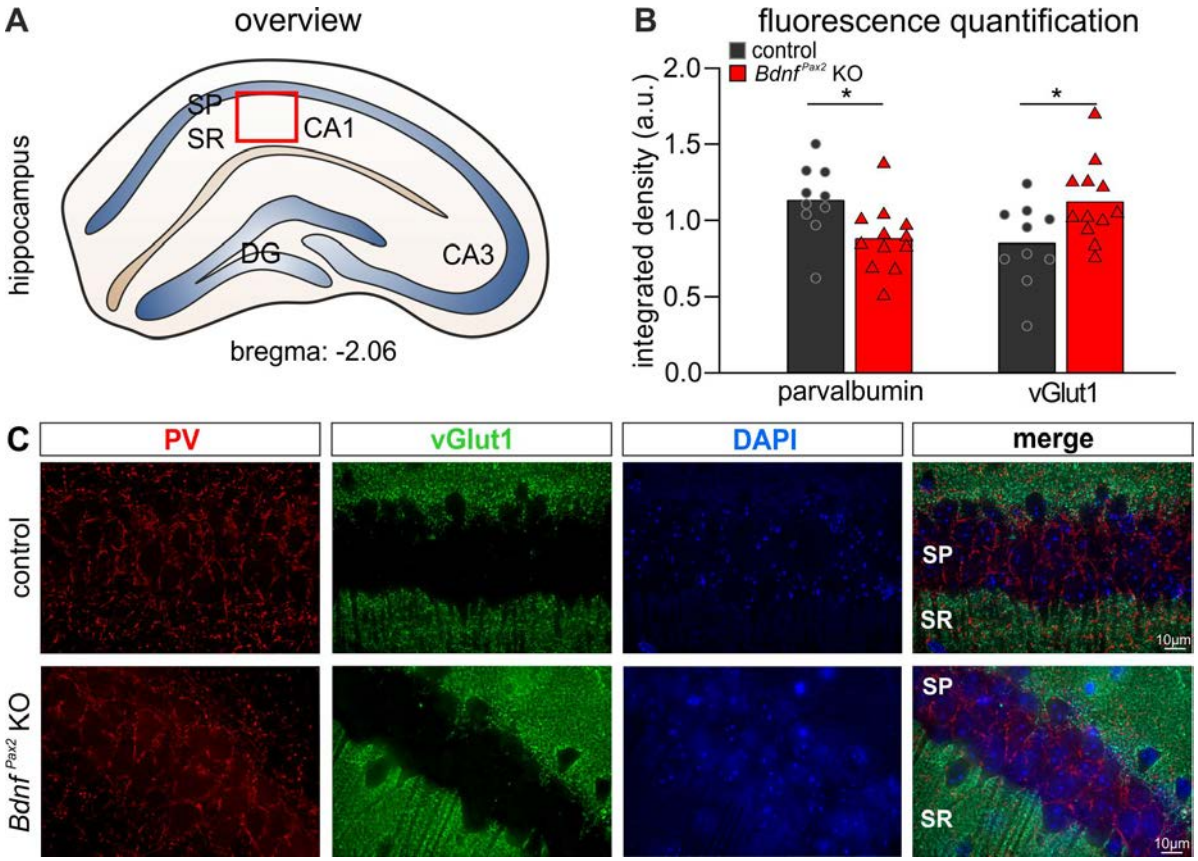

Figure 3.2. *Excitatory and inhibitory molecular markers. (**A**) Schematic of the hippocampus showing the region in which images were taken (red box). DG, dentate gyrus; SP, stratum pyramidale; SR, stratum radiatum. (**B**) Integrated density of the fluorescence intensity in control (black circles) Bdnf*^{Pax2} *KO mice (red triangles) for PV (left) and vGlut1 (right). Symbols, animals; bars, mean. (**C**) Exemplary photos from control (top) and Bdnf*^{Pax2} *KO mice (bottom) of PV (1*st *panel), vGlut1 (2*nd *panel), DAPI (3*rd *panel), and merged (4*th *panel). * = $p < 0.05$.*

To determine whether *Bdnf*^{Pax2} KO mice exhibit this E/I imbalance, immunohistochemistry was performed and the protein expression of PV and vesicular glutamate transporter 1 (vGlut1) was measured as markers of inhibitory and excitatory synapses, respectively. The expression of the aforementioned proteins was measured from images taken of the stratum radiatum (**Figure 3.2A**, SR), a hippocampal region where the Schaffer's collaterals contact the dendrites of CA1 pyramidal neurons. In this region, *Bdnf*^{Pax2} KO mice exhibited significantly lower PV fluorescence levels and significantly higher vGlut1 fluorescence levels in comparison to littermate controls, indicating that *Bdnf*^{Pax2} KO mice have a higher baseline excitation level (**Figure 3.2B,C**, PV: unpaired two-tailed Student's t-test, $t(20) = 2.586$, $p = 0.018$, control: $n = 10$, *Bdnf*^{Pax2} KO: $n = 12$ mice; vGlut1: unpaired two-tailed Student's t-test, $t(20) = 2.40$, $p = 0.026$, control: $n = 10$, *Bdnf*^{Pax2} KO: $n = 12$ mice).

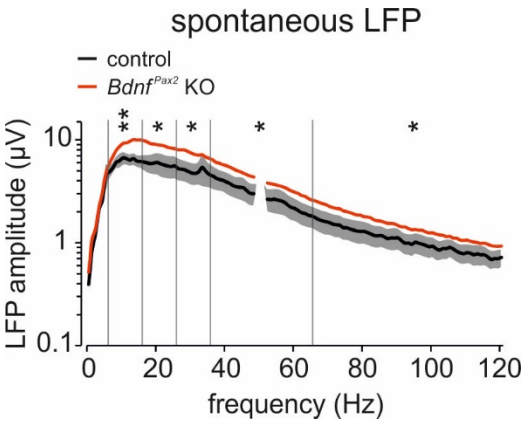

Figure 3.3. *Spontaneous LFP in AC. Spontaneous LFP amplitude of control (black, mean ± 95% confidence interval) and Bdnf^{Pax2} KO mice (red, mean). Vertical lines indicate the alpha (5–15 Hz), beta (15–25 Hz), low-gamma (25–35 Hz), mid-gamma (35–65 Hz), and high-gamma (65–125 Hz) oscillatory frequency bands. * = $p < 0.05$, ** = $p < 0.01$.*

In order to functionally confirm the molecular indications of a hyperexcitable neural state in cortical regions, spontaneous LFPs (i.e., without any acoustic stimulus) were measured from an electrode inserted into the AC. *Bdnf*^{Pax2} KO mice indeed had significantly higher spectral power across the alpha (5–15 Hz), beta (15–25 Hz), low gamma (25–35 Hz), mid-gamma (35–65 Hz), and high gamma (65–125 Hz) oscillatory frequency bands (**Figure 3.3**, alpha: permutation analysis, $Z = 2.13$, $p = 0.008$, control: $n = 8$, *Bdnf*^{Pax2} KO: $n = 9$ mice; beta: permutation analysis, $Z = 2.08$, $p = 0.014$, control: $n = 8$, *Bdnf*^{Pax2} KO: $n = 9$ mice; low gamma: permutation analysis, $Z = 2.07$, $p = 0.011$, control: $n = 8$, *Bdnf*^{Pax2} KO: $n = 9$ mice; mid-gamma: permutation analysis, $Z = 1.09$, $p = 0.020$, control: $n = 8$, *Bdnf*^{Pax2} KO: $n = 9$ mice; high gamma: permutation analysis, $Z = 1.88$, $p = 0.020$, control: $n = 8$, *Bdnf*^{Pax2} KO: $n = 9$ mice).

The oscillatory frequency bands differ in their function due to biophysical constraints, with high frequency oscillations (e.g., beta, gamma) being associated with local processing and low frequency oscillations (e.g., alpha) being associated with long-range interactions (Uhlhaas & Singer, 2013). Thus, a disruption in the baseline activity of both low and high frequency oscillations, as observed here in *Bdnf*^{Pax2} KO mice, suggests an inability to maintain appropriate baseline oscillatory power, thus possibly impacting the perceptual integration of stimuli.

3.1.2 Neural Response Patterns in *Bdnf*^{Pax2} KO Mice

The baseline (i.e., spontaneous) neural synchronization can impact the subsequent processing and perception of sensory inputs (Jansen & Brandt, 1991; Makeig et al., 2002; Simon & Wallace, 2016). Therefore, we measured the LFPs in response to pure-tone stimuli of increasing frequencies. In control mice, a strong event-related potential (ERP) in response to 11 and 22 kHz tones was observed, which was much weaker in *Bdnf*^{Pax2} KO mice (**Figure 3.4A**, gray arrows). To quantify this, the peak-to-peak amplitude of the first 50 ms of single ERPs (i.e., the LFP) in response to pure-tone stimuli was calculated. *Bdnf*^{Pax2} KO mice were found to exhibit significantly lower LFP amplitudes in comparison to controls in the best hearing frequency range and in the high frequency range (**Figure 3.4B**, 10–12 kHz: permutation analysis, $Z = 2.06$, $p = 0.016$, control: $n = 8$, *Bdnf*^{Pax2} KO: $n = 9$ mice; 21–23 kHz: permutation analysis, $Z = 2.05$, $p = 0.016$, control: $n = 8$, *Bdnf*^{Pax2} KO: $n = 9$ mice).

Sensory input generates two different kinds of activity: evoked and induced. Evoked activity is phase-locked to the stimulus onset and is generally considered to reflect the bottom-up processing of sensory information, while induced activity is not phase-locked and reflects the integration of sensory input with ongoing activity, thus representing top-down influences (Yusuf et al., 2017).

We therefore analyzed the evoked and induced LFP in response to pure-tone stimuli, breaking down the responses into the different frequency bands based on their spectral content. *Bdnf*^{Pax2} KO mice exhibited significantly lower evoked LFP amplitudes in the alpha, beta, low gamma, and mid-gamma bands across all stimulus frequencies in comparison to controls (**Figure 3.5A**, alpha: Mann-Whitney U test, $U = 9$, $p < 0.01$, control: $n = 8$, *Bdnf*^{Pax2} KO: $n = 9$ mice; beta: Mann-Whitney U test, $U = 0$, $p < 0.01$, control: $n = 8$, *Bdnf*^{Pax2} KO: $n = 9$ mice; low gamma: Mann-Whitney U test, $U = 6$, $p < 0.01$, control: $n = 8$, *Bdnf*^{Pax2} KO: $n = 9$ mice; mid-gamma: Mann-Whitney U test, $U = 14$, $p < 0.05$, control: $n = 8$, *Bdnf*^{Pax2} KO: $n = 9$ mice).

When further analyzing the band-specific differences by triads of stimulus frequencies, *Bdnf*^{Pax2} KO mice had significantly lower LFP amplitudes in the alpha band in response to tones in the best hearing frequency range (10–12 kHz) and the high frequency range (21–23 kHz) in comparison to controls (**Figure 3.5A**, 10–12 kHz: Mann-Whitney U test, $U = 16$, $p < 0.05$, control: $n = 8$, *Bdnf*^{Pax2} KO: $n = 9$ mice; 21–23 kHz: Mann-Whitney U test, $U = 9$, $p < 0.01$, control: $n = 8$, *Bdnf*^{Pax2} KO: $n = 9$ mice). In the beta and low gamma bands, *Bdnf*^{Pax2} KO mice had significantly lower LFP amplitudes in response to low frequency (4–6 kHz), best frequency, and high frequency tones in comparison to controls (**Figure 3.5A**, 4–6 kHz beta: Mann-Whitney U test, $U = 6$, $p < 0.01$, control: $n = 8$, *Bdnf*^{Pax2} KO: $n = 9$ mice; 4–6 kHz low-gamma: Mann-Whitney U test, $U = 10$, $p < 0.01$, control: $n = 8$, *Bdnf*^{Pax2} KO: $n = 9$ mice; 10–12 kHz beta: Mann-Whitney U test, $U = 0$, $p < 0.01$, control: $n = 8$, *Bdnf*^{Pax2} KO: $n = 9$ mice; 10–12 kHz low-gamma: Mann-Whitney U test, $U = 9$, $p < 0.01$, control: $n = 8$, *Bdnf*^{Pax2} KO: $n = 9$ mice; 21–23 kHz beta: Mann-Whitney U test, $U = 4$, $p < 0.01$, control: $n = 8$, *Bdnf*^{Pax2} KO: $n = 9$ mice; 21–23 kHz low-gamma: Mann-Whitney U test, $U = 9$, $p < 0.01$, control: $n = 8$, *Bdnf*^{Pax2} KO: $n = 9$ mice). In the mid-gamma band, *Bdnf*^{Pax2} KO mice had significantly lower LFP amplitudes in response to low frequency and best frequency tones in comparison to controls (**Figure 3.5A**, 4–6 kHz: Mann-Whitney U test, $U = 14$, $p < 0.05$, control: $n = 8$, *Bdnf*^{Pax2} KO: $n = 9$ mice; 10–12 kHz: Mann-Whitney U test, $U = 17$, $p < 0.05$, control: $n = 8$, *Bdnf*^{Pax2} KO: $n = 9$ mice).

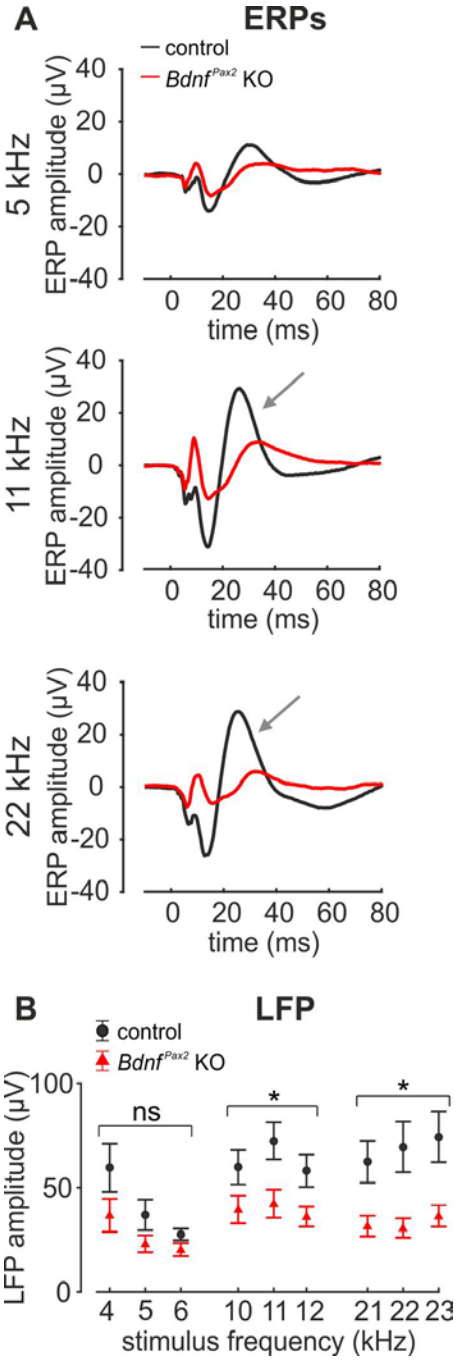

Figure 3.4. *Auditory-evoked potentials. (**A**) Average traces of ERPs of control (black) and Bdnf*^{Pax2} *KO mice (red) in response to pure-tone stimuli of 5 kHz (top), 11 kHz (middle), and 22 kHz (bottom). Gray arrows indicate LFP. (**B**) Peak-to-peak amplitude of the first 50 ms after stimulus onset of single ERPs averaged for control (black circles) and Bdnf*^{Pax2} *KO mice (red triangles). Mean ± SEM. * = p < 0.05, ns = not significant.*

When analyzing the induced activity across all stimulus frequencies, *Bdnf*^{Pax2} KO mice had significantly higher LFP amplitudes in the beta band (**Figure 3.5B**, Mann-Whitney U test, $U = 18$, $p < 0.05$, control: $n = 8$, *Bdnf*^{Pax2} KO: $n = 9$ mice). When further analyzing this by triads of stimulus frequencies in the beta band, *Bdnf*^{Pax2} KO mice had significantly higher LFP amplitudes in response to stimuli in the best hearing frequency range (**Figure 3.5B**, Mann-Whitney U test, $U = 17$, $p < 0.05$, control: $n = 8$, *Bdnf*^{Pax2} KO: $n = 9$ mice).

Taken together, the overall decreased evoked activity partially accompanied by an increased induced activity in response to acoustic stimulation in *Bdnf*^{Pax2} KO mice replicates some observations in ASD patients and mouse models (Holley et al., 2022; Wilde et al., 2022).

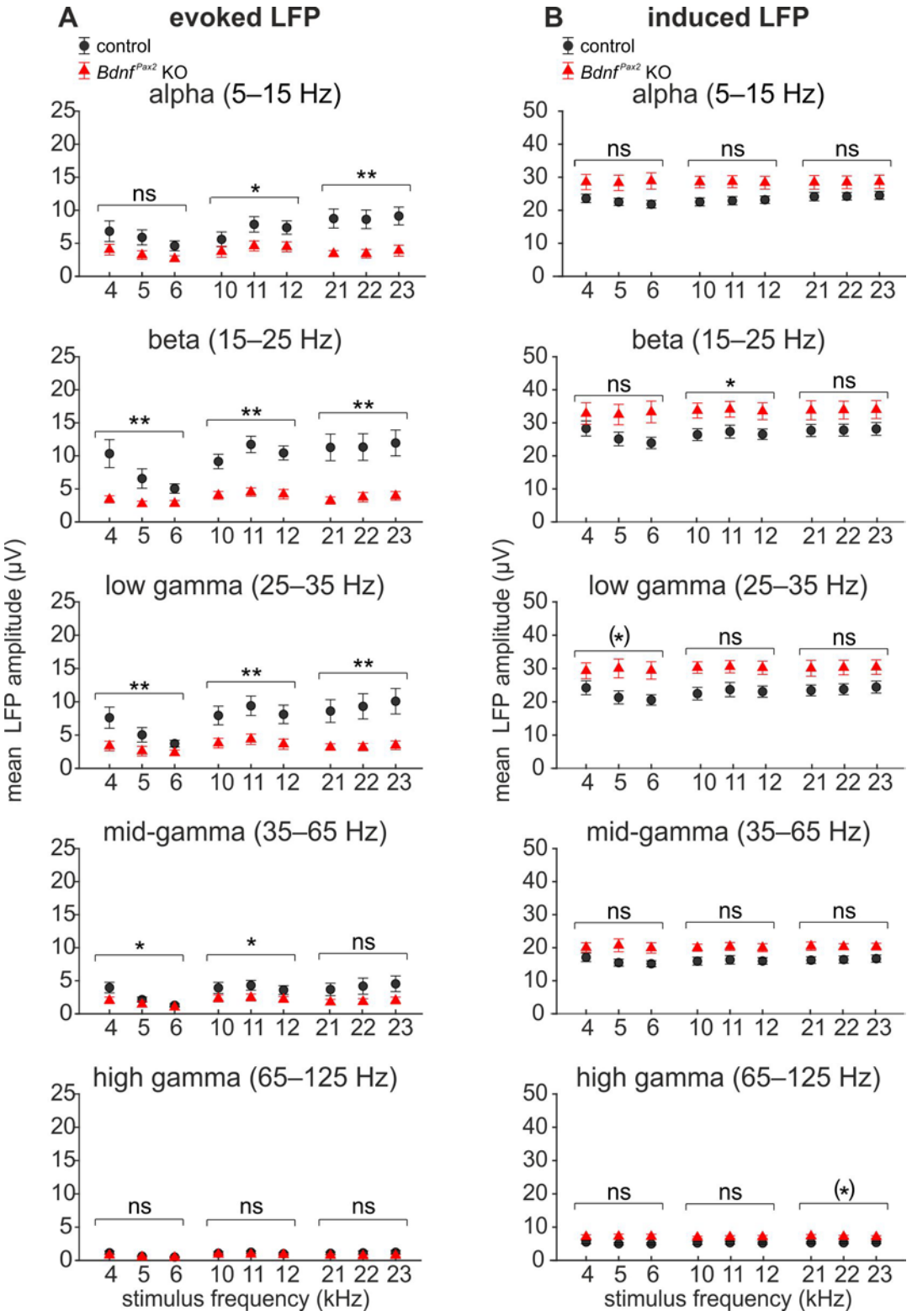

Figure 3.5. *Evoked and induced LFPs. (**A**) Evoked LFP amplitudes in control (black circles) and Bdnf*^{Pax2} *KO mice (red triangles) for the (top to bottom) alpha, beta, low gamma, mid-gamma, and high gamma oscillatory frequency bands (**B**) Induced LFP amplitudes in control (black circles) and Bdnf*^{Pax2} *KO mice (red triangles) for the (top to bottom) alpha, beta, low gamma, mid-gamma, and high gamma oscillatory frequency bands. Mean ± SEM. (*) = p < 0.05 uncorrected for multiple comparisons, * = p < 0.05, ** = p < 0.01, ns = not significant.*

3.1.3 Central Structural Changes in *Bdnf*^{Pax2} KO Mice

Structural changes in the brain of both patients and mouse models of ASD have been reported (for a review, see Varghese et al., 2017). Among these are changes in dendritic spines, which are protrusions from dendrites that form synaptic contacts with neighboring cells (for a review, see Berry & Nedivi, 2017). These complex structures constantly change their size and shape in response to neuronal activity and therefore are critical to synaptic plasticity and memory function (Nimchinsky et al., 2002).

To determine if *Bdnf*^{Pax2} KO mice display central structural changes consistent with an ASD phenotype, we performed Golgi-Cox staining on brains of *Bdnf*^{Pax2} KO mice and littermate controls (**Figure 3.6A**) in order to visualize the dendritic spines (**Figure 3.6B**). Spines were first assessed by their density, defined as the number of protrusions per micrometer, as changes in the density of dendritic spines have been previously reported in ASD patients and mouse models (Varghese et al., 2017). Consistent with this, *Bdnf*^{Pax2} KO mice had a significantly higher spine density in comparison to littermate controls (**Figure 3.6C**, unpaired two-tailed Student's t-test, $t(34) = 3.288$, $p = 0.002$, control: $n = 17$, *Bdnf*^{Pax2} KO: $n = 19$ dendrites).

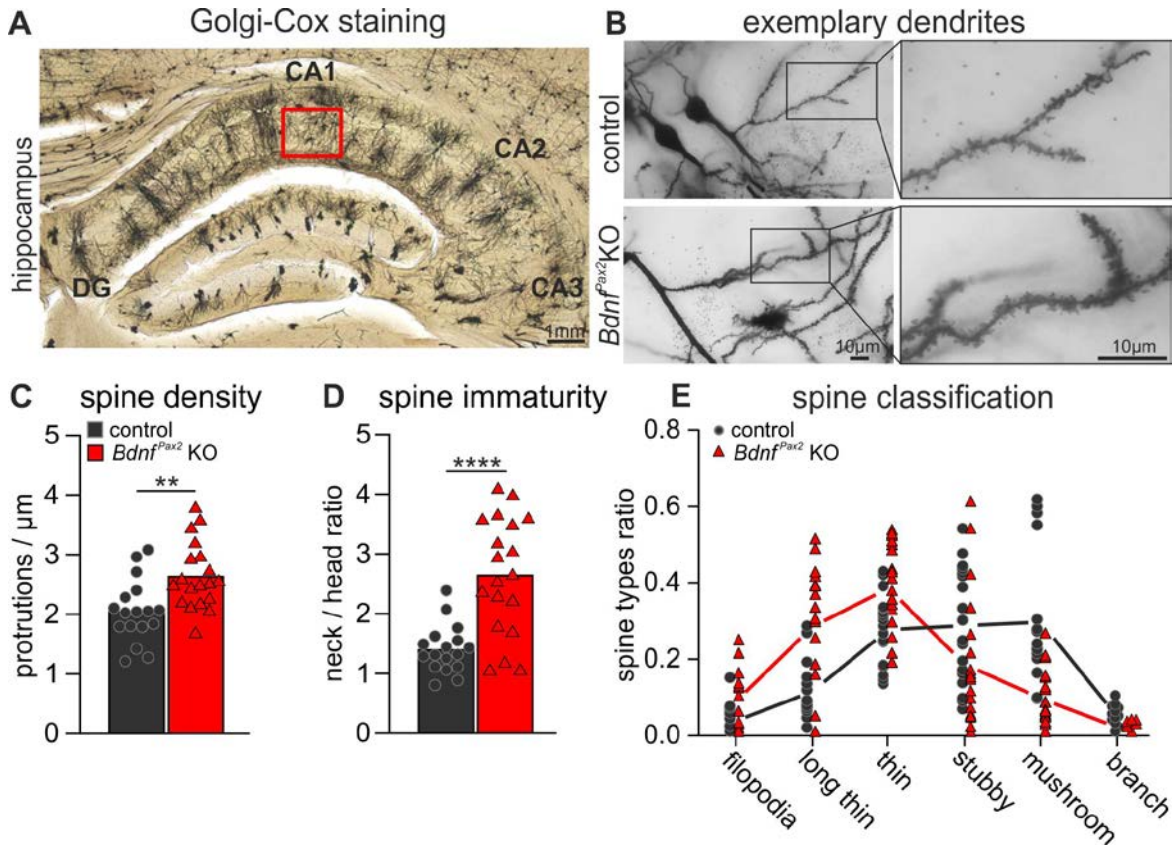

Figure 3.6. *Dendritic spine analysis and classification. (**A**) Exemplary photo of Golgi-Cox staining in the hippocampus, indicating where higher magnification photos were taken in the CA1 region (red box). DG, dentate gyrus. (**B**) Exemplary photos of dendrites from control (top) and Bdnf*^{Pax2} *KO mice (bottom) at 60x magnification (left) and 100x magnification (right). (**C**) Spine density, measured as the number of protrusions per micrometer of control (black circles) and Bdnf*^{Pax2} *KO mice (red triangles). (**D**) Spine immaturity, measured as the neck-to-head ratio, of control and Bdnf*^{Pax2} *KO mice. (**E**) Proportion of the different classes of dendritic spines, ranging from the most immature filopodia-shaped spines to the most mature mushroom- and branch-shaped spines, in control and Bdnf*^{Pax2} *KO mice. Symbols, single dendrites; bar, mean. ** = $p < 0.01$, **** = $p < 0.0001$.*

Dendritic spines can be further classified by their shape and size, which define their functional role. This can be done by measuring the neck-to-head ratio of the spines, with a lower ratio representing more mature dendritic spines and a higher ratio representing more immature, plastic dendritic spines (for a review, see Berry & Nedivi, 2017). A higher proportion of immature spines has been observed in various ASD mouse models (Varghese et al., 2017) and, indeed, *Bdnf*^{Pax2} KO mice had a significantly

higher neck-to-head ratio in comparison to littermate controls (**Figure 3.6D**, unpaired two-tailed Student's t-test, $t(34) = 4.908$, $p < 0.0001$, control: $n = 17$, *Bdnf*^{Pax2} KO: $n = 19$ dendrites). Further, when spines were classified into distinct types (ranging from immature filopodia spines to mature mushroom and branched spines), *Bdnf*^{Pax2} KO mice exhibited a higher proportion of longer, thinner spines in comparison to controls (**Figure 3.6E**). This indicates that *Bdnf*^{Pax2} KO mice have a more immature spine morphology, consistent with observations in other ASD mouse models.

3.1.4 Summary

Taken together, *Bdnf*^{Pax2} KO mice nicely recapitulate several central features observed in ASD patients and mouse models, including a hyperexcitability seen on a molecular and electrophysiological level, differences in neural responses to acoustic stimuli, and structural changes of dendritic spine morphology. When combined with previous behavioral observations in this model (Eckert et al., 2021), it can be remarked that *Bdnf*^{Pax2} KO mice have a phenotype nearly indistinguishable from established ASD models.

3.2 Investigating the Origin of the *Bdnf*^{Pax2} KO Phenotype

The phenotype of *Bdnf*^{Pax2} KO mice closely mimics other models of ASD on very nearly every level, from their behavior (Eckert et al., 2021) to their auditory processing (**Figure 3.1**), and even to their protein expression, cortical responses, and neuronal microstructure (section 3.1). The reason for this, however, is as of yet unclear, as no gene correlated with ASD was deleted in this model.

3.2.1 ASSRs Suggest a Subcortical Origin of the Central Phenotype

To first determine the source of the diminished evoked LFP amplitude in response to acoustic stimuli in *Bdnf*^{Pax2} KO mice, we measured the ASSR in response to amplitude-modulated stimuli. ASSRs reflect the summation of phase-locked activity of multiple neural generators throughout the auditory system, from the cochlea to the AC (Lu et al., 2022). In humans, the response to lower modulation frequencies (below 40 Hz) has been shown to be primarily generated by cortical components, while the response to higher modulation frequencies (above 100 Hz) has been shown to be primarily generated by subcortical components (Lu et al., 2022). Thus, by varying the modulation frequency, we can make a very coarse inference as to where the deficit originates from (i.e., whether cortical or subcortical).

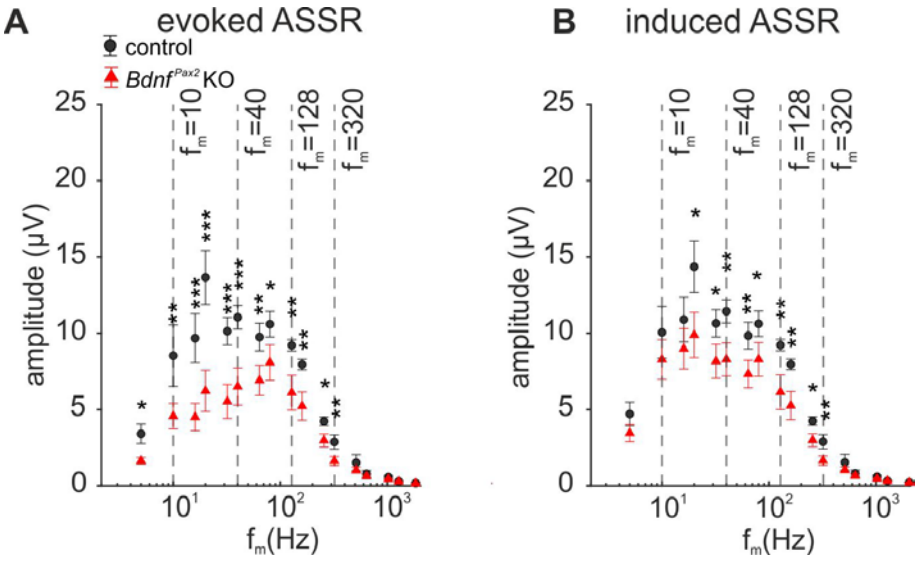

Figure 3.7. *Evoked and induced ASSRs. (**A**) Evoked ASSR amplitude in control (black circles) and Bdnf*^{Pax2} *KO mice (red triangles). (**B**) Induced ASSR amplitude in control and Bdnf*^{Pax2} *KO mice. Mean ± SEM. * = $p < 0.05$, ** = $p < 0.01$, *** = $p < 0.001$.*

Thus, we recorded the ASSR in response to an 11 kHz carrier frequency amplitude-modulated from 5 to 2048 Hz in *Bdnf*^{Pax2} KO mice and littermate controls. Responses were further divided into evoked

(i.e., phase-locked) and induced (i.e., not phase-locked) responses. *Bdnf*^{Pax2} KO mice exhibited a significantly lower evoked ASSR in response to tones amplitude-modulated from 5 to 320 Hz in comparison to controls (**Figure 3.7A**, see **Table 3.1** for statistics). In addition, *Bdnf*^{Pax2} KO mice exhibited a significantly lower induced ASSR in response to tones amplitude-modulated from 20 to 320 Hz in comparison to controls (**Figure 3.7B**, see **Table 3.1** for statistics).

Table 3.1. *Statistics for Figure 3.7, evoked and induced ASSRs. Statistical test performed: permutation analysis with false discovery rate. Control: n = 8 mice; Bdnf*^{Pax2} *KO: n = 9 mice.*

Figure 3.7A ***Evoked ASSR***		***Figure 3.7B*** ***Induced ASSR***	
Comparison	***p* value**	**Comparison**	***p* value**
f_m = 5 Hz	0.0108	f_m = 5 Hz	ns
f_m = 10 Hz	0.0063	f_m = 10 Hz	ns
f_m = 16 Hz	0.0007	f_m = 16 Hz	ns
f_m = 20 Hz	0.0005	f_m = 20 Hz	0.0105
f_m = 32 Hz	0.0003	f_m = 32 Hz	0.0195
f_m = 40 Hz	0.0006	f_m = 40 Hz	0.0041
f_m = 64 Hz	0.0062	f_m = 64 Hz	0.0094
f_m = 80 Hz	0.0188	f_m = 80 Hz	0.0207
f_m = 128 Hz	0.0029	f_m = 128 Hz	0.0032
f_m = 160 Hz	0.0024	f_m = 160 Hz	0.0025
f_m = 256 Hz	0.0129	f_m = 256 Hz	0.0126
f_m = 320 Hz	0.0062	f_m = 320 Hz	0.0070
f_m = 512 Hz	ns	f_m = 512 Hz	ns
f_m = 640 Hz	ns	f_m = 640 Hz	ns
f_m = 1024 Hz	ns	f_m = 1024 Hz	ns
f_m = 1280 Hz	ns	f_m = 1280 Hz	ns
f_m = 2048 Hz	ns	f_m = 2048 Hz	ns

The fact that *Bdnf*^{Pax2} KO mice have smaller responses to both lower (below 40 Hz) and higher (above 100 Hz) modulation frequencies suggests that there is already a deficit at the subcortical level which is exacerbated at the cortical level by an insufficient summation of phase-locked activity along the ascending pathway.

3.2.2 Auditory Nerve Function in *Bdnf*^{Pax2} KO Mice

The pattern of deficits in the ASSRs points to a subcortical deficit that is intensified higher in the auditory system. Other hearing measurements performed in *Bdnf*^{Pax2} KO mice indicate deficits throughout the central and peripheral auditory system, all the way down to the level of the auditory nerve (**Figure 3.1E**). As the auditory nerve is the first synapse of the auditory system, it was hypothesized that it could be the first dysfunctional structure that drives the auditory response deficits throughout the system. Thus, we decided to look more closely at the auditory nerve function.

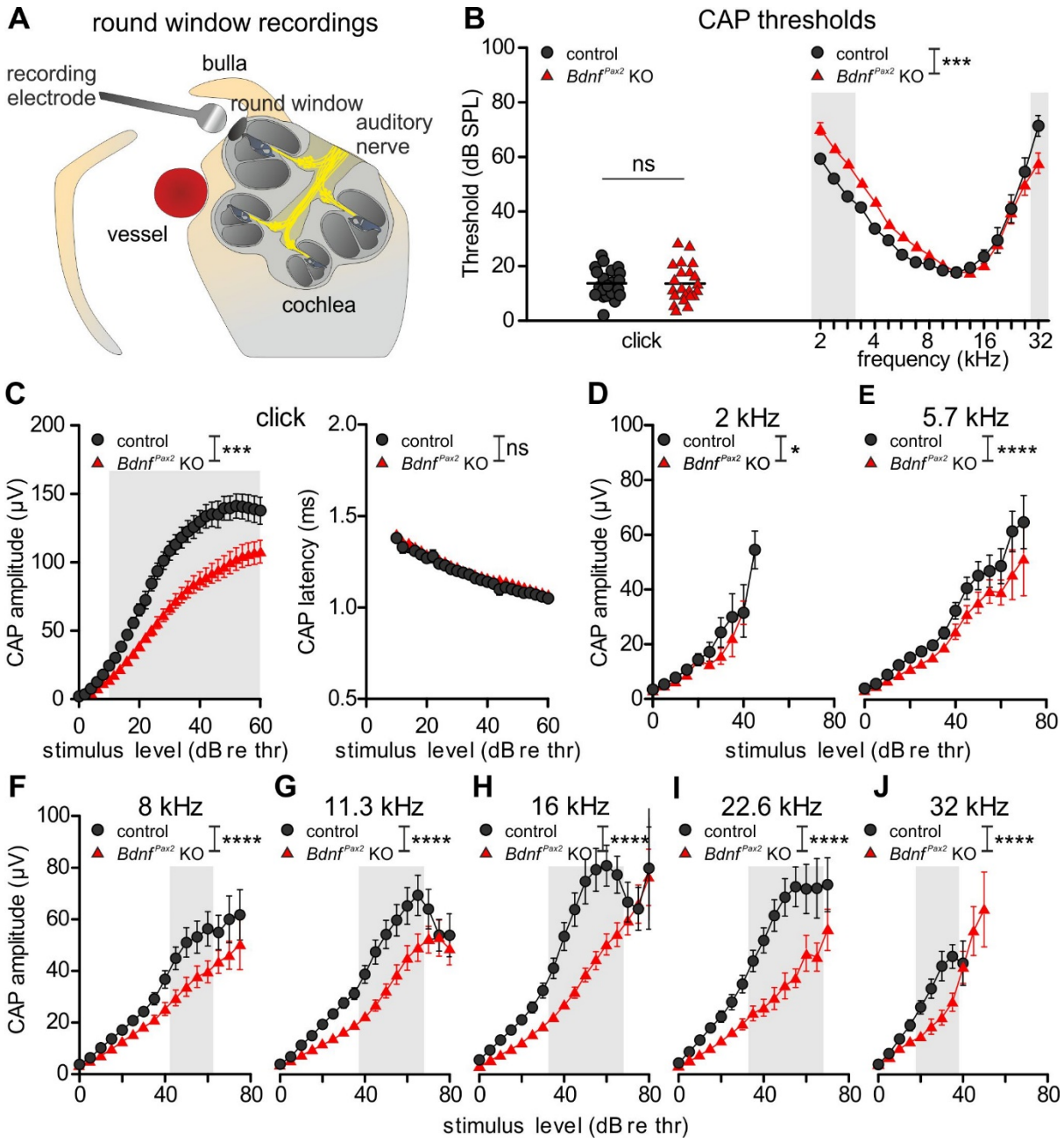

Figure 3.8. *CAP recordings.* ***(A)*** *Schematic of round window recordings depicting the recording electrode placed near the membrane of the round window.* ***(B)*** *CAP thresholds of control (black circles) and Bdnf^{Pax2} KO mice (red triangles) in response to click (left) and pure-tone stimuli (right), with the gray area indicating the frequencies for which the post hoc test was significant.* ***(C)*** *CAP amplitude (left) and latency (right) in response to click stimuli of control and Bdnf^{Pax2} KO mice, with the gray area indicating the stimulus levels for which the post hoc test was significant.* ***(D-J)*** *CAP amplitude in response to pure-tone stimuli of 2 kHz* ***(D)****, 5.7 kHz* ***(E)****, 8 kHz* ***(F)****, 11.3 kHz* ***(G)****, 16 kHz* ***(H)****, 22.6 kHz* ***(I)****, and 32 kHz* ***(J)*** *in control and Bdnf^{Pax2} KO mice, with the gray area indicating the stimulus levels for which the post hoc test was significant. Mean ± SEM. * = p < 0.05, *** = p < 0.001, **** = p < 0.0001, ns = not significant.*

To do so, we measured the CAP from an electrode placed near the round window membrane of anesthetized *Bdnf^{Pax2}* KO and control mice (**Figure 3.8A**) in response to click and pure-tone stimuli. Thresholds in response to click stimuli did not differ between *Bdnf^{Pax2}* KO and control mice, but thresholds in response to pure-tone frequencies were significantly higher in *Bdnf^{Pax2}* KO mice compared to controls, particularly in the low and high frequency ranges (**Figure 3.8B**, click: unpaired two-tailed Student's t-test, $t(42) = 0.05$, $p = 0.96$, control: $n = 21$, *Bdnf^{Pax2}* KO: $n = 23$ ears; pure-tone: 2-way ANOVA, $F(1, 1155) = 12.85$, $p = 0.0004$, Bonferroni's multiple comparisons test, control: $n = 21$, *Bdnf^{Pax2}* KO: $n = 23$ ears).

Bdnf^{Pax2} KO mice also exhibited a significantly lower CAP amplitude in response to click stimuli of increasing intensity in comparison to controls, though the latency did not differ between the genotypes (**Figure 3.8C**, amplitude: MANOVA, $F(1, 37) = 13.43$, $p = 0.0008$, Bonferroni's multiple comparisons test, control: $n = 21$, *Bdnf*^{Pax2} KO: $n = 23$ ears; latency: MANOVA, $F(1, 40) = 0.267$, $p = 0.61$, Bonferroni's multiple comparisons test, control: $n = 21$, *Bdnf*^{Pax2} KO: $n = 23$ ears).

In response to pure-tone stimuli, *Bdnf*^{Pax2} KO mice exhibited a significantly lower CAP amplitude compared to controls in response to 2–32 kHz stimuli (**Figure 3.8D–J**, 2 kHz: 2-way ANOVA, $F(1,249) = 4.72$, $p = 0.03$, Bonferroni's multiple comparisons test, control: $n = 21$, *Bdnf*^{Pax2} KO: $n = 23$ ears; 5.7 kHz: 2-way ANOVA, $F(1,537) = 28.84$, $p < 0.0001$, Bonferroni's multiple comparisons test, control: $n = 21$, *Bdnf*^{Pax2} KO: $n = 23$ ears; 8 kHz: 2-way ANOVA, $F(1,594) = 50.74$, $p < 0.0001$, Bonferroni's multiple comparisons test, control: $n = 21$, *Bdnf*^{Pax2} KO: $n = 23$ ears; 11.3 kHz: 2-way ANOVA, $F(1,639) = 74.26$, $p < 0.0001$, Bonferroni's multiple comparisons test, control: $n = 21$, *Bdnf*^{Pax2} KO: $n = 23$ ears; 16 kHz: 2-way ANOVA, $F(1,614) = 107.24$, $p < 0.0001$, Bonferroni's multiple comparisons test, control: $n = 21$, *Bdnf*^{Pax2} KO: $n = 23$ ears; 22.6 kHz: 2-way ANOVA, $F(1,464) = 148.59$, $p < 0.0001$, Bonferroni's multiple comparisons test, control: $n = 21$, *Bdnf*^{Pax2} KO: $n = 23$ ears; 32 kHz: 2-way ANOVA, $F(1,256) = 37.84$, $p < 0.0001$, Bonferroni's multiple comparisons test, control: $n = 21$, *Bdnf*^{Pax2} KO: $n = 23$ ears).

Taken together, this suggests that *Bdnf*^{Pax2} KO mice have a profound dysfunction in their auditory nerve response.

3.2.3 Specific Dysfunction of High-SR Fibers in *Bdnf*^{Pax2} KO Mice

As the auditory nerve is composed of fibers with different SRs and response thresholds that give them different physiological roles in sound processing (see section 1.1.1), we wanted to take a closer look to determine if there was a differential impairment in the auditory nerve fiber classes. The functional proportion of high-SR fibers to low-SR fibers can be estimated by measuring PSTRs. PSTRs have an envelope shape, consisting of a fast-onset peak followed by a rapid adaptation and finally a steady-state response until the stimulus ends. The ratio of the peak to the plateau has previously been shown to predict the functional proportion of high- to low-SR fibers (Huet et al., 2022).

Bdnf^{Pax2} KO mice did not differ from controls in their peak-to-plateau ratio in response to noise band stimuli with center frequencies of 5.7–11 kHz (**Figure 3.9A–C**, 5.7 kHz: 2-way ANOVA, $F(1,168) = 1.29$, $p = 0.29$, control: $n = 15$, *Bdnf*^{Pax2} KO: $n = 16$ ears; 8 kHz: 2-way ANOVA, $F(1,177) = 1.01$, $p = 0.40$, control: $n = 14$, *Bdnf*^{Pax2} KO: $n = 18$ ears; 11 kHz: 2-way ANOVA, $F(1,203) = 0.37$, $p = 0.66$, control: $n = 17$, *Bdnf*^{Pax2} KO: $n = 19$ ears). However, *Bdnf*^{Pax2} KO mice had significantly lower peak-to-plateau ratios in comparison to controls in response to higher frequency stimuli with center frequencies of 16–22.6 kHz (**Figure 3.9D,E**, 16 kHz: 2-way ANOVA, $F(1,184) = 11.5$, $p = 0.0009$, Bonferroni's multiple comparisons test, control: $n = 17$, *Bdnf*^{Pax2} KO: $n = 19$ ears; 22.6 kHz: 2-way ANOVA, $F(1,95) = 8.15$, $p = 0.005$, Bonferroni's multiple comparisons test, control: $n = 13$, *Bdnf*^{Pax2} KO: $n = 17$ ears). When the peak-to-plateau ratio was compared at 30 dB relative to threshold for all measured frequencies, *Bdnf*^{Pax2} KO mice exhibited an overall lower peak-to-plateau ratio (**Figure 3.9F**, 2-way ANOVA, $F(1,140) = 4.97$, $p = 0.027$, Bonferroni's multiple comparisons test, control: $n = 14$, *Bdnf*^{Pax2} KO: $n = 19$ ears).

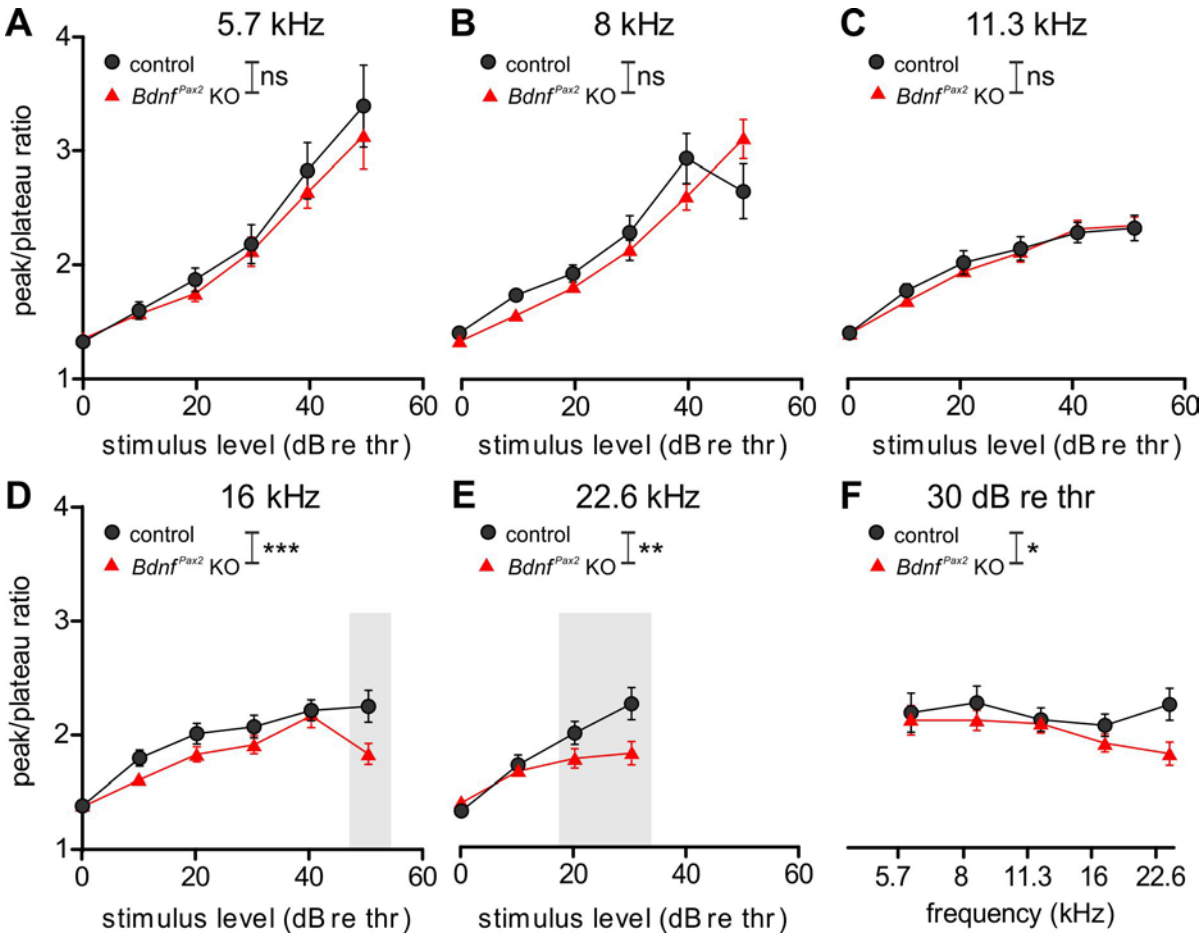

Figure 3.9. *PSTR measurements. (**A-E**) Peak-to-plateau ratio of control (black circles) and Bdnf^{Pax2} KO mice (red triangles) in response to noise stimuli with a center frequency of 5.7 kHz (**A**), 8 kHz (**B**), 11.3 kHz (**C**), 16 kHz (**D**), and 22.6 kHz (**E**), with the gray area indicating stimulus levels for which the post hoc test was significant. (**F**) Peak-to-plateau ratio compared at 30 dB relative to threshold for all measured frequencies of control and Bdnf^{Pax2} KO mice. Mean ± SEM. * = p < 0.05, ** = p < 0.01, *** = p < 0.001, ns = not significant.*

Taken together, this suggests that *Bdnf^{Pax2}* KO mice have a lower proportion of functional high-SR fibers in comparison to controls, possibly indicating that their response characteristics did not fully mature.

3.2.4 Dysfunction of MOC Efferent Fibers in *Bdnf^{Pax2}* KO Mice

The mature response of high-SR fibers develops later than that of low-SR fibers and the emergence of their mature response has been hypothesized to be responsible for the lowering of the hearing threshold and the increase in temporal acuity that occurs with auditory experience (Knipper et al., 2021). The functional maturation of high-SR fibers has been speculated to depend on inhibitory efferent feedback prior to hearing onset. In particular, MOC efferents, which form a transient synapse with IHCs that disappears with hearing onset by P12, may play a role in the development of high-SR fibers (Knipper et al., 2021). We therefore measured the MOC efferent function in adult *Bdnf^{Pax2}* KO mice to determine the strength of these connections (**Figure 3.9**).

In adult mice, MOC efferents modulate OHC electromotility through a rapid (~100 ms) adaptation process (Kujawa & Liberman, 2001; Liberman et al., 1996). This was measured by presenting phase-varied primaries (Dalhoff et al., 2015; Whitehead et al., 1996) and recording and averaging the DPOAE 2*f1–f2 amplitudes, then subtracting the steady-state response from the maximum amplitude (**Figure 3.10A**). *Bdnf*^{Pax2} KO mice exhibited a trend towards smaller maximum DPOAE amplitudes (**Figure 3.10B**, unpaired two-tailed Student's t-test, $t(24) = 1.825$, $p = 0.080$, control: $n = 12/6$, *Bdnf*^{Pax2} KO: $n = 14/7$ ears/mice) and a significantly smaller amplitude adaptation in comparison to controls (**Figure 3.10C**, Mann-Whitney U test, $U = 43$, $p = 0.036$, control: $n = 12/6$, *Bdnf*^{Pax2} KO: $n = 14/7$ ears/mice).

This indicates that MOC efferents are less able to suppress OHC motility in *Bdnf*^{Pax2} KO mice and that their efferent system was weaker overall. It is possible that during development, a lack of sufficient inhibition from efferents may have stunted the maturation of high-SR fibers.

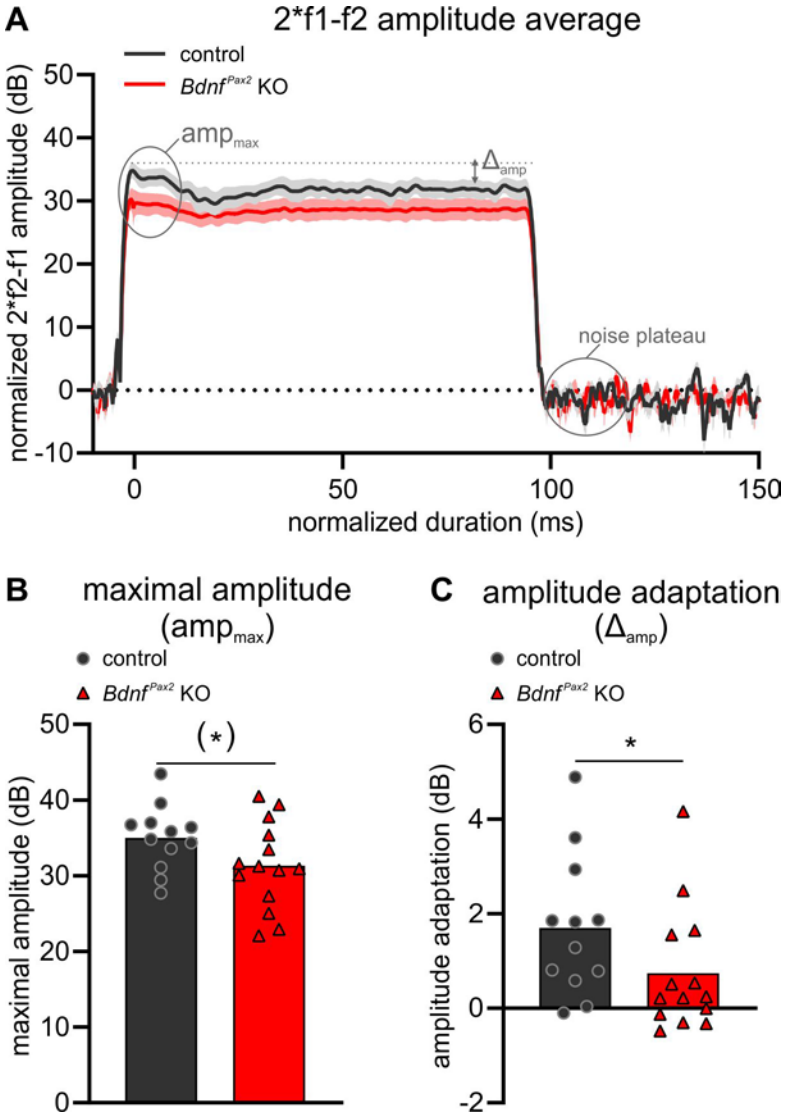

Figure 3.10. *MOC efferent adaptation. **(A)** Time course of the average DPOAE signal from control (black) and Bdnf*^{Pax2} *KO mice (red). The maximum DPOAE amplitude (amp*$_{max}$*), amplitude adaptation (Δ*$_{amp}$*), and noise plateau are indicated. **(B)** Maximal DPOAE amplitude of control (black circles) and Bdnf*^{Pax2} *KO mice (red triangles). **(B)** Amplitude adaptation of control and Bdnf*^{Pax2} *KO mice. Symbols, ears; bars, mean. (*) = p < 0.08, * = p < 0.05.*

3.2.5 Summary

Taken together, the data indicate that the central aspects of the phenotype of *Bdnf*^{Pax2} KO mice are driven by an immaturity in the periphery. Specifically, the PSTR results indicate that high-SR fibers remain in an immature state (**Figure 3.9**), possibly as a result of insufficient inhibitory feedback from efferents. The under-responsiveness of high-SR fibers indicates that *Bdnf*^{Pax2} KO mice have lower temporal resolution starting at the first synapse of the system, a deficit which seems to be exacerbated along the ascending pathway.

3.3 Treatment of *Bdnf*^{Pax2} KO Mice Using a Cognitive Stimulator

Though *Bdnf*^{Pax2} KO mice had functional deficits in their peripheral auditory processing, these deficits compounded on one another, resulting in secondary deficits in more central processing (**Figure 3.7**). We therefore decided to employ a pharmaceutical approach that specifically targeted the more central phenotype by treating mice with a PDE9i. This cGMP-stimulating drug is considered a "cognitive stimulator" for its ability to boost LTP and improve performance on cognitive tests in rodents (Hutson

et al., 2011; Kleiman et al., 2012; Kroker et al., 2014; Kroker et al., 2012; van der Staay et al., 2008). Though most research regarding PDE9i revolves around its effect on memory function, we recently demonstrated that it also increases PV expression in the hippocampus and has a protective effect on hearing function (Savitska et al., 2022). Thus, the PDE9i has the potential to improve both the central and peripheral phenotype of *Bdnf*^{Pax2} KO mice.

3.3.1 Effect of PDE9i Treatment on Corticosterone Levels

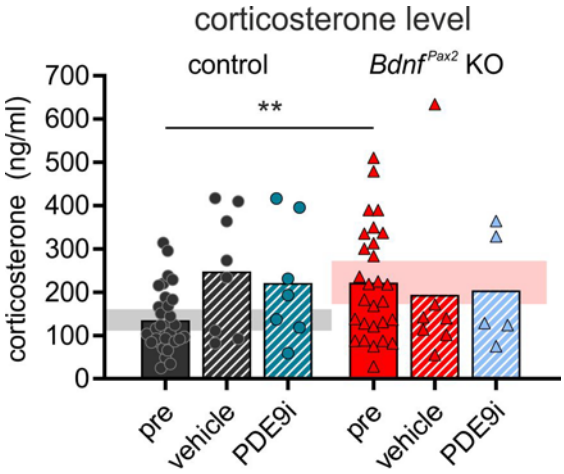

Figure 3.11. *Corticosterone level. Corticosterone level in control (circles) and Bdnf*^{Pax2} *KO mice (triangles) before (solid bars) and after treatment (striped bars) with a vehicle (black or red) or PDE9i (teal or light blue). Shaded areas indicate 95% confidence interval of the respective pre-condition. Symbols, animals; bars, mean. ** = p < 0.01.*

A ten-day injection of either a vehicle or PDE9i has previously been reported to be a stressful event in older mice, shown by increased blood corticosterone levels after treatment (Savitska et al., 2022). To determine if this injection period is also stressful in the younger mice used in the present study, we measured the blood corticosterone level before and after treatment with the vehicle or PDE9i.

Prior to treatment, *Bdnf*^{Pax2} KO mice had significantly higher corticosterone levels in comparison to controls (**Figure 3.11**, unpaired two-tailed Student's t-test, $t(59) = 3.336$, $p = 0.0015$, control: $n = 33$, *Bdnf*^{Pax2} KO: $n = 27$ mice), as previously reported (Eckert et al., 2021). Additionally, after treatment with both a vehicle and PDE9i, control mice exhibited increased corticosterone levels, with mean values falling outside the 95% confidence interval of the pre-condition (**Figure 3.11**, gray shaded area). On the other hand, *Bdnf*^{Pax2} KO mice did not experience an increase in corticosterone levels after treatment with either the vehicle or the PDE9i, with mean values falling within the 95% confidence interval of the pre-condition (**Figure 3.11**, pink shaded area).

This confirms that even in a cohort of young mice, a ten-day injection of either vehicle or PDE9i is a stressful event for control mice. This also indicates that *Bdnf*^{Pax2} KO mice may have an altered stress response, with a high baseline corticosterone level that did not further increase after the ten-day injection.

3.3.2 Effect of PDE9i Treatment on Hearing Function

Higher stress levels have long been known to elevate hearing thresholds (Horner, 2003) and lower ABR wave amplitudes in mice (Savitska et al., 2022). PDE9i treatment was also previously shown to protect against a stress-induced deterioration of hearing function (Savitska et al., 2022). We therefore measured the hearing function of *Bdnf*^{Pax2} KO and control mice before and after treatment with the vehicle or PDE9i to determine not only whether the stress response impacts hearing function in younger animals but also whether the PDE9i can influence both the stress-induced hearing changes and the hearing phenotype of *Bdnf*^{Pax2} KO mice.

We measured the hearing thresholds before and after treatment. Interestingly, both control mice and *Bdnf*^{Pax2} KO mice—which did not have an elevated corticosterone level after treatment—had significantly higher click thresholds after vehicle treatment (**Figure 3.12A**, control: paired two-tailed Student's t-test, $t(15) = 2.98$, $p = 0.0094$, $n = 16/8$ ears/mice; *Bdnf*^{Pax2} KO: paired two-tailed Student's t-test, $t(15) = 2.29$, $p = 0.037$, $n = 16/8$ ears/mice). Upon treatment with PDE9i, control mice did not show this stress-induced elevation of click thresholds, but the click thresholds of *Bdnf*^{Pax2} KO mice remained elevated after PDE9i treatment (**Figure 3.12A**, control: paired two-tailed Student's t-test, $t(15) = 0.978$, $p = 0.34$, $n = 16/8$ ears/mice; *Bdnf*^{Pax2} KO: paired two-tailed Student's t-test, $t(13) =$

3.097, $p = 0.0085$, $n = 14/7$ ears/mice). This indicates that both the control and *Bdnf*^{Pax2} KO mice have a hearing threshold elevation induced by the ten-day injection, which can be prevented upon treatment with the PDE9i only in control mice.

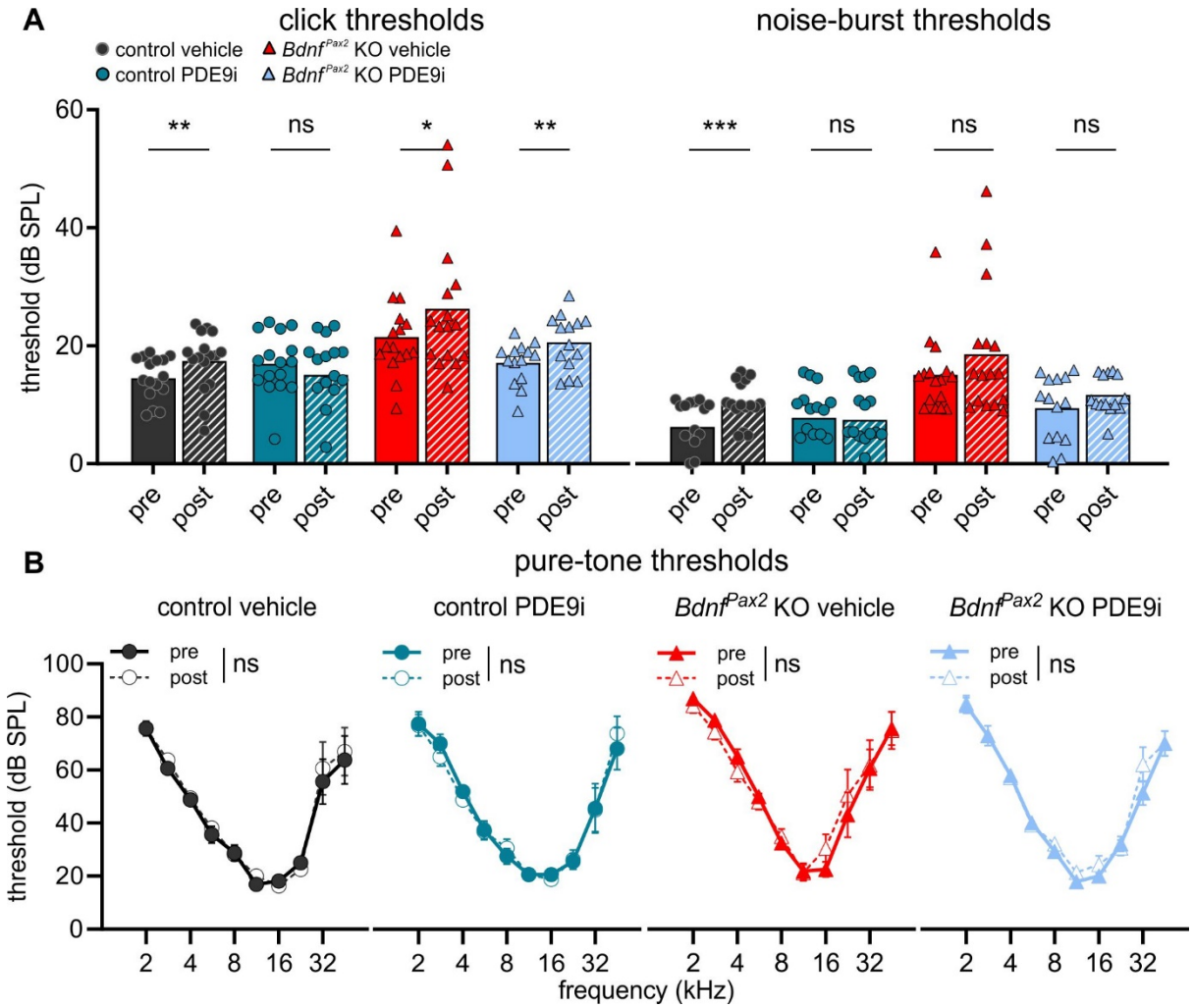

Figure 3.12. *Hearing thresholds before and after treatment with a vehicle or PDE9i. (**A**) Hearing thresholds in response to click (left) and noise-burst stimuli (right) in control (circles) and Bdnf*^{Pax2} *KO mice (triangles) before (solid bars) and after (striped bars) treatment with a vehicle (black or red) or PDE9i (teal or light blue). Symbols, ears; bars, mean. (**B**) Hearing thresholds in response to pure-tone stimuli in control mice before (solid line, filled symbols) and after (dotted line, open symbols) treatment with a vehicle (1*st *panel) or PDE9i (2*nd *panel), and in Bdnf*^{Pax2} *KO mice before and after treatment with a vehicle (3*rd *panel) or PDE9i (4*th *panel). Mean ± SEM. * = p < 0.05, ** = p < 0.01, *** = p < 0.001, ns = not significant.*

When hearing thresholds were measured in response to noise-burst stimuli after vehicle treatment, control mice still had a significantly higher hearing threshold, while *Bdnf*^{Pax2} KO mice showed only a non-significant threshold increase (**Figure 3.12A**, control: paired two-tailed Student's t-test, $t(15) = 4.679$, $p = 0.0003$, $n = 16/8$ ears/mice; *Bdnf*^{Pax2} KO: paired two-tailed Student's t-test, $t(15) = 1.535$, $p = 0.15$, $n = 16/8$ ears/mice). Neither control nor *Bdnf*^{Pax2} KO mice showed significant differences in their sensitivity to noise-burst stimuli after PDE9i treatment (**Figure 3.12A**, control: paired two-tailed Student's t-test, $t(15) = 0.1729$, $p = 0.87$, $n = 16/8$ ears/mice; *Bdnf*^{Pax2} KO: paired two-tailed Student's t-test, $t(13) = 1.437$, $p = 0.17$, $n = 14/7$ ears/mice).

When hearing thresholds were measured in response to pure-tone stimuli, no significant differences were observed after either vehicle or PDE9i treatment in control or *Bdnf*^{Pax2} KO mice (**Figure 3.12B**, control vehicle: 2-way ANOVA, $F(1,140) = 0.3672$, $p = 0.55$, $n = 8$; control PDE9i: 2-way ANOVA, $F(1,140) = 0.0118$, $p = 0.91$, $n = 8$; *Bdnf*^{Pax2} KO vehicle: 2-way ANOVA, $F(1,139) = 0.0277$, $p = 0.87$, $n = 8$; *Bdnf*^{Pax2} KO PDE9i: 2-way ANOVA, $F(1,120) = 1.708$, $p = 0.19$, $n = 7$).

We previously showed in older mice that the auditory nerve function, measured through ABR wave I, was vulnerable to damage from stress and could be subsequently recovered with the PDE9i (Savitska et al., 2022). We therefore measured the ABR wave I amplitude before and after treatment and calculated the delta (i.e., the post-treatment amplitude minus the pre-treatment amplitude) to allow for a direct comparison of the vehicle-treated animals with the PDE9i-treated animals.

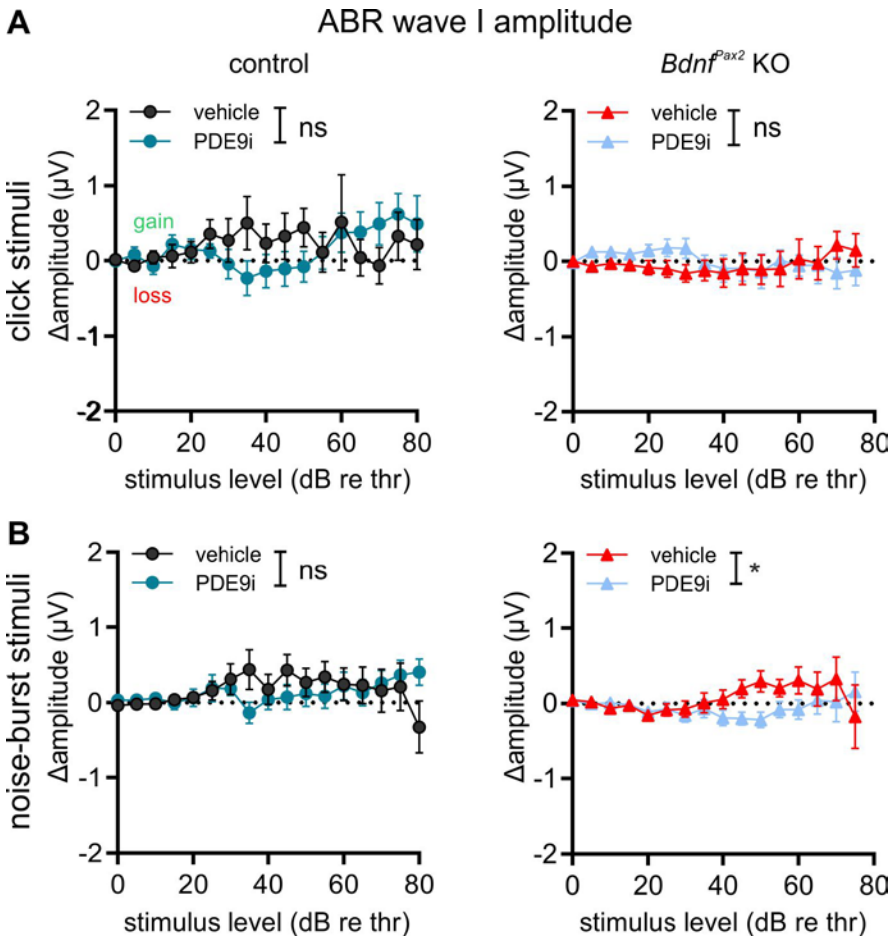

Figure 3.13. *ABR wave I amplitude delta after treatment with a vehicle or PDE9i. (**A**) Amplitude delta of control (left) and Bdnf^{Pax2} KO mice (right) treated with vehicle (black or red) versus PDE9i (teal or light blue) in response to click stimuli. (**B**) Amplitude delta of control (left) and Bdnf^{Pax2} KO mice (right) treated with vehicle versus PDE9i in response to noise-burst stimuli. Mean ± SEM. * = $p < 0.05$, ns = not significant.*

In response to click stimuli, no differences were observed in the ABR wave I amplitude delta in either control or *Bdnf*^{Pax2} KO mice (**Figure 3.13A**, control: 2-way ANOVA, $F(1,356) = 0.4432$, $p = 0.51$, vehicle: $n = 14/7$, PDE9i: n = 14/7 ears/mice; *Bdnf*^{Pax2} KO: 2-way ANOVA, $F(1,336) = 0.7550$, $p = 0.39$, vehicle: $n = 14/7$, PDE9i: n = 12/6 ears/mice). In response to noise-burst stimuli, no significant differences between the treatment conditions were observed in control mice, but *Bdnf*^{Pax2} KO mice treated with the PDE9i had a significantly lower ABR wave I amplitude delta in comparison to those treated with the vehicle (**Figure 3.13B**, control: 2-way ANOVA, $F(1,373) = 0.2633$, $p = 0.61$, vehicle: $n = 14/7$, PDE9i: n = 14/7 ears/mice; *Bdnf*^{Pax2} KO: 2-way ANOVA, $F(1,322) = 5.570$, $p = 0.0189$, vehicle: $n = 14/7$, PDE9i: n = 12/6 ears/mice). This suggests not only that the stress-induced threshold loss is not translated into a loss of sound processing later on in the auditory system, but also that the PDE9i may have a slightly negative effect on *Bdnf*^{Pax2} KO mice.

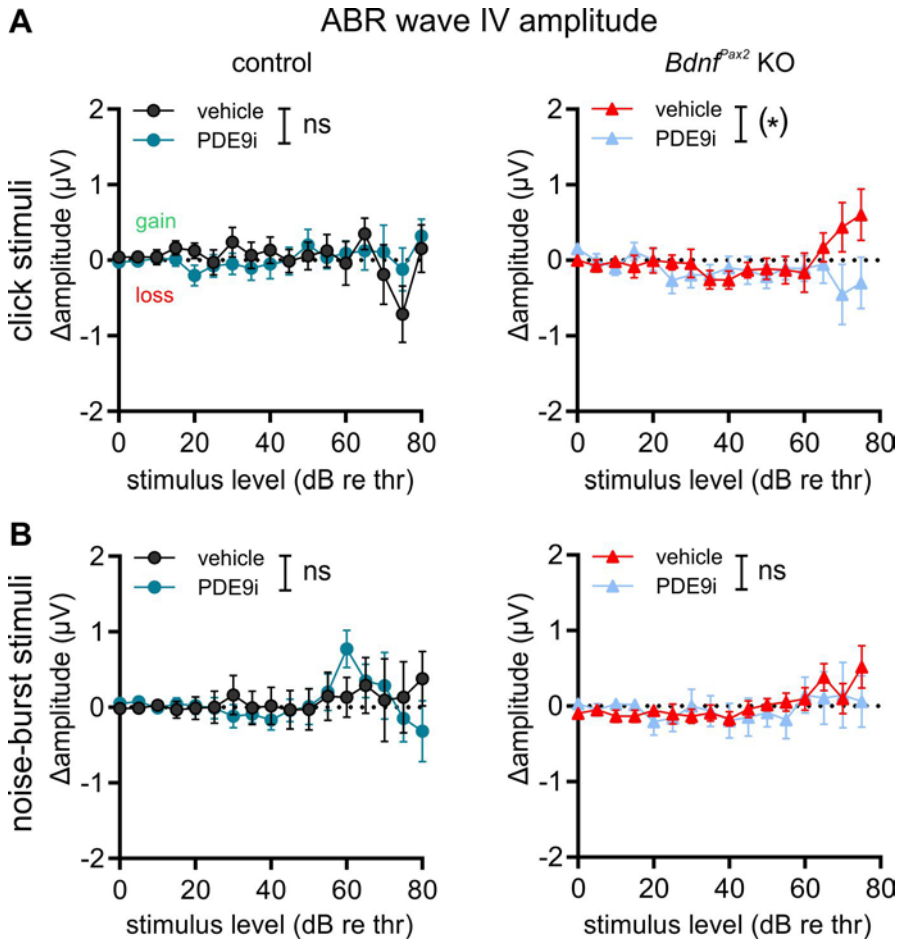

Figure 3.14. *ABR wave IV amplitude delta after treatment with a vehicle or PDE9i. (**A**) Amplitude delta of control (left) and Bdnf^{Pax2} KO mice (right) treated with vehicle (black or red) versus PDE9i (teal or light blue) in response to click stimuli. (**B**) Amplitude delta of control (left) and Bdnf^{Pax2} KO mice (right) treated with vehicle versus PDE9i in response to noise-burst stimuli. Mean ± SEM. (*) = $p < 0.08$, ns = not significant.*

To determine how the vehicle or PDE9i treatment affects structures later in the ascending pathway, we analyzed the ABR wave IV amplitude and calculated the delta. In response to click stimuli, no significant differences between the treatment conditions were observed in control mice, but *Bdnf*^{Pax2} KO mice treated with the PDE9i again trended towards lower ABR wave IV amplitude delta in comparison to those treated with the vehicle (**Figure 3.14A**, control: 2-way ANOVA, $F(1,339) = 0.0583$, $p = 0.81$, vehicle: n = 14/7, PDE9i: n = 14/7 ears/mice; *Bdnf*^{Pax2} KO: 2-way ANOVA, $F(1,302) = 3.516$, $p = 0.062$, vehicle: n = 14/7, PDE9i: n = 12/6 ears/mice). In response to noise-burst stimuli, however, no significant differences between the treatment conditions were observed in either control or *Bdnf*^{Pax2} KO mice (**Figure 3.14B**, control: 2-way ANOVA, $F(1,353) = 0.0590$, $p = 0.81$, vehicle: n = 14/7, PDE9i: n = 14/7 ears/mice; *Bdnf*^{Pax2} KO: 2-way ANOVA, $F(1,300) = 0.4477$, $p = 0.50$, vehicle: n = 14/7, PDE9i: n = 12/6 ears/mice).

Taken together, stress had only a minimal effect on the hearing function in younger mice, limited to a slight elevation in hearing thresholds, which was recovered in control mice upon treatment with a PDE9i. Conversely, in *Bdnf*^{Pax2} KO mice, the PDE9i appeared to have a mildly adverse effect on hearing function along the ascending auditory pathway.

3.3.3 Effect of PDE9i Treatment on Memory Function

Hearing and memory are, as previously detailed (see section 1.1), tightly coupled processes. It was previously shown that when mice had less auditory input (i.e., due to noise damage or aging), they also had less hippocampal output (Manohar et al., 2022; Matt et al., 2018; Savitska et al., 2022), and that PDE9i treatment could preserve both of these processes (Savitska et al., 2022).

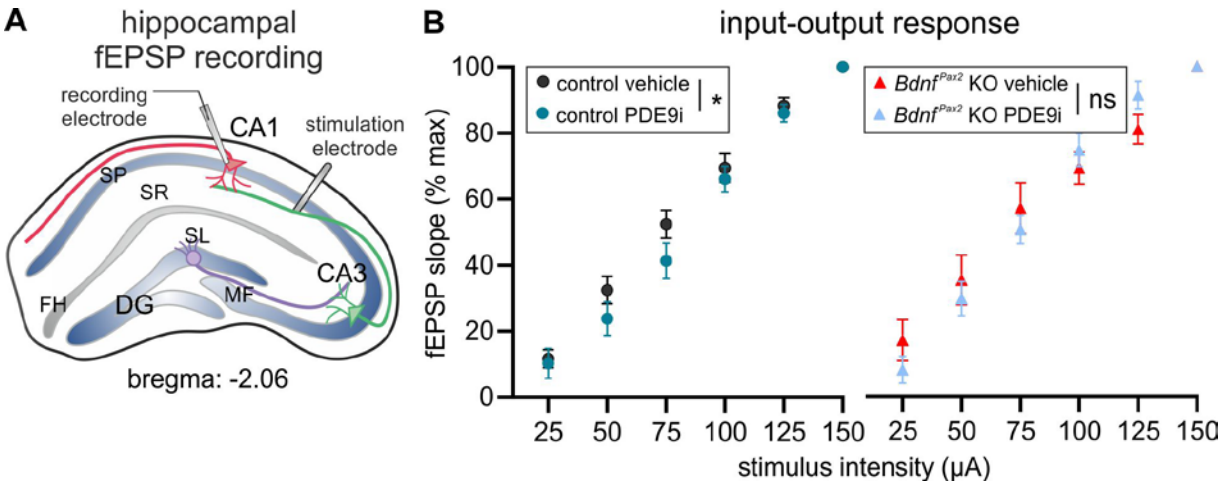

Figure 3.15. *Input-output response after treatment with a vehicle or PDE9i. (**A**) Schematic of hippocampal fEPSP recording showing the stimulation electrode placed in the Schaffer's collaterals and the recording electrode placed in the dendrites of CA1 pyramidal neurons. DG, dentate gyrus; FH, fissura hippocampalis; MF, mossy fibers; SL, stratum lucidum; SP, stratum pyramidale; SR, stratum radiatum. (**B**) Input-output response of control (left) and Bdnf^{Pax2} KO mice (right) treated with vehicle (black or red) versus PDE9i (teal or light blue). Mean ± SEM. * = $p < 0.05$, ns = not significant.*

We therefore assessed hippocampal function by measuring field excitatory postsynaptic potentials (fEPSPs) in hippocampal brain slices from control and *Bdnf*^{Pax2} KO mice after treatment with either a vehicle or PDE9i. For fEPSP recordings, a stimulation electrode was placed in the axons of CA3 Schaffer's collaterals and a recording electrode was placed in the CA1 pyramidal neuron dendrites, which form synaptic contacts with CA3 neurons (**Figure 3.15A**). First, basal synaptic transmission was

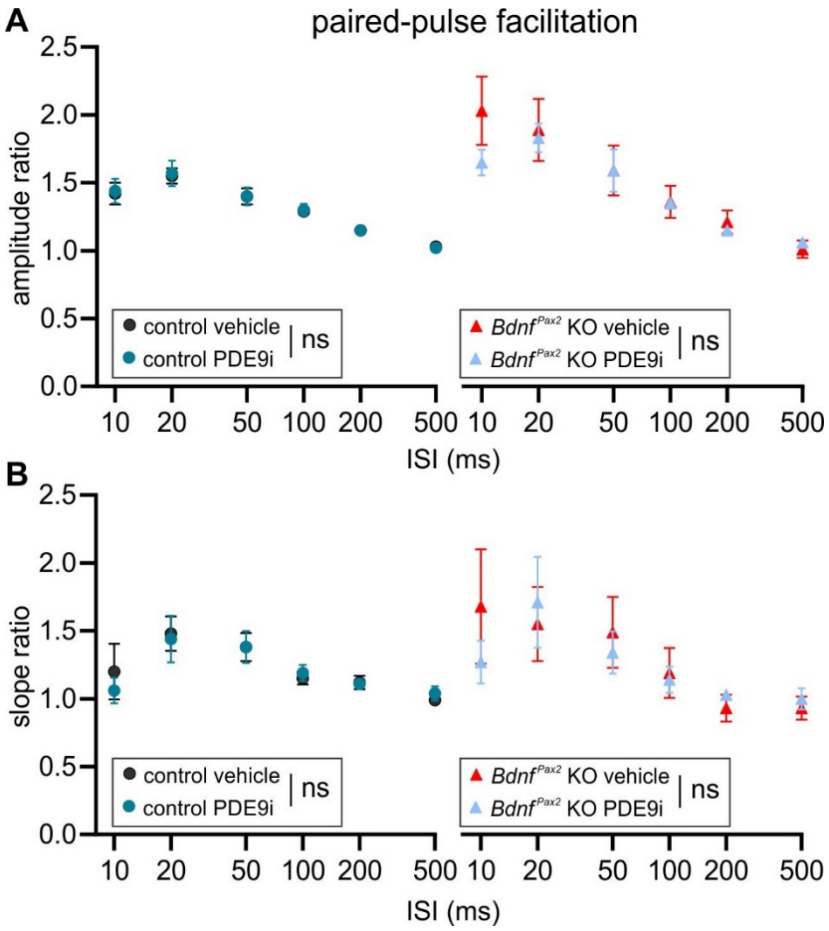

Figure 3.16. *Paired-pulse facilitation after treatment with a vehicle or PDE9i. (**A**) Paired-pulse amplitude ratio of control (left) and Bdnf^{Pax2} KO mice (right) treated with vehicle (black or red) versus PDE9i (teal or light blue). (**B**) Paired-pulse slope ratio of control (left) and Bdnf^{Pax2} KO mice (right) treated with vehicle versus PDE9i. Mean ± SEM. ns = not significant.*

assessed by measuring the input-output relationship of fEPSPs. Control mice treated with the PDE9i had a significantly lower fEPSP slope in comparison to those treated with the vehicle, indicating that a higher stimulus intensity is required to elicit the same fEPSP slope (**Figure 3.15B**, 2-way ANOVA, $F(1,192) = 4.347$, $p = 0.038$, vehicle: $n = 17/7$, PDE9i: n = 17/6 slices/mice). No changes were observed in the input-output relationship of *Bdnf*^{Pax2} KO mice (**Figure 3.15B**, 2-way ANOVA, $F(1,132) = 0.0990$, $p = 0.75$, vehicle: $n = 12/6$, PDE9i: n = 12/6 slices/mice).

To investigate the short-term plasticity, paired-pulse facilitation, in which two stimuli are presented at varying interstimulus intervals, was measured in hippocampal brain slices from vehicle- and PDE9i-treated control and *Bdnf*^{Pax2} KO mice. No significant differences were observed in the paired-pulse amplitude ratio between treatment groups in either control or *Bdnf*^{Pax2} KO mice (**Figure 3.16A**, control: 2-way ANOVA, $F(1,192) = 0.0404$, $p = 0.84$, vehicle: $n = 17/7$, PDE9i: n = 17/6 slices/mice; *Bdnf*^{Pax2} KO: 2-way ANOVA, $F(1,132) = 0.9526$, $p = 0.33$, vehicle: $n = 12/6$, PDE9i: n = 12/6 slices/mice). Additionally, no significant differences were observed in the paired-pulse slope ratio between treatment groups in either control or *Bdnf*^{Pax2} KO mice (**Figure 3.16B**, control: 2-way ANOVA, $F(1,192) = 0.0732$, $p = 0.79$, vehicle: $n = 17/7$, PDE9i: n = 17/6 slices/mice; *Bdnf*^{Pax2} KO: 2-way ANOVA, $F(1,132) = 0.1419$, $p = 0.71$, vehicle: $n = 12/6$, PDE9i: n = 12/6 slices/mice). This suggests that the short-term plasticity is not affected by either vehicle or PDE9i treatment, confirming previous observations (Savitska et al., 2022).

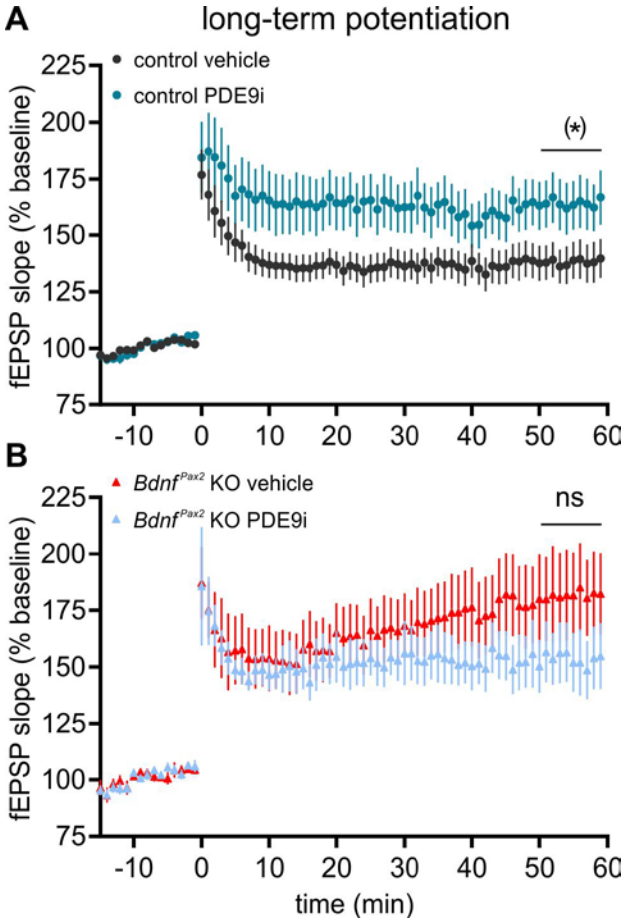

Figure 3.17. *LTP after treatment with a vehicle or PDE9i. fEPSP slope of the baseline recording and for 60 minutes following tetanic stimulation of control (**A**) and Bdnf*^{Pax2} *KO mice (**B**) treated with vehicle (black or red) versus PDE9i (teal or light blue). Mean ± SEM. (*) = p < 0.08, ns = not significant.*

We then measured LTP by applying a high frequency tetanic stimulation to hippocampal brain slices from vehicle- and PDE9i-treated control and *Bdnf*^{Pax2} KO mice. LTP has been regarded as a cellular model of memory formation, measuring a persistent strengthening of synaptic connections that occurs after activity (for a review, see Nicoll, 2017).

To assess LTP, the baseline fEPSP was measured for 15 minutes, then a tetanic stimulation was applied (1 s, 100 Hz), and the fEPSPs were recorded for the following hour. The fEPSP slope of the last ten minutes of the 60-minute recording was averaged and compared as a percentage from the 15-minute baseline measurement. Control mice treated with the PDE9i had a trend towards higher LTP in comparison to those treated with the vehicle (**Figure 3.17A**, unpaired two-tailed Student's t-test, $t(32) = 1.890$, $p = 0.0678$, vehicle: $n = 17/7$, PDE9i: $n = 17/6$ slices/mice), confirming previous observations (Kroker et al., 2012). On the other hand, *Bdnf*^{Pax2} KO mice treated with the PDE9i had a slightly but non-significantly lower LTP than those treated with the vehicle (**Figure 3.17B**, unpaired two-tailed Student's t-test, $t(22) = 1.222$, $p = 0.23$, vehicle: $n = 12/6$, PDE9i: $n = 12/6$ slices/mice).

3.3.4 cGMP Generator Expression Levels in *Bdnf*^{Pax2} KO Mice

One possible explanation as to why the PDE9i did not have the expected beneficial effect on the phenotype of *Bdnf*^{Pax2} KO mice is that the cGMP pathway in these mice is already altered. We therefore decided to examine one of the upstream components of the cGMP pathway, nitric oxide–sensitive guanylyl cyclase (NO-GC). NO-GC is a soluble receptor that binds nitric oxide and produces cGMP (Friebe & Koesling, 2003). We therefore decided to examine the expression levels of NO-GC in untreated *Bdnf*^{Pax2} KO mice. To this end, we performed in situ hybridization on brains of *Bdnf*^{Pax2} KO mice and littermate controls. The NO-GC mRNA expression level was measured from images taken from the AC and from hippocampal dentate gyrus, CA3, and CA1 regions, which comprise the trisynaptic circuit (Fröhlich, 2016). As the AC projects to the entorhinal cortex (Billig et al., 2022; Munoz-Lopez et al., 2010), which subsequently projects to the dentate gyrus and begins the trisynaptic circuit, we measured the NO-GC mRNA expression levels along this pathway to determine if and where altered cGMP generator expression levels may contribute to PDE9i responsiveness.

Images were taken from layers III and IV of the AC (**Figure 3.18A**), as layer IV receives bottom-up input from the auditory thalamus and layer III then projects to other cortical regions, such as the entorhinal cortex (Billig et al., 2022; Munoz-Lopez et al., 2010). In layers III and IV of the AC, *Bdnf*^{Pax2} KO mice did not significantly differ from controls in their NO-GC mRNA expression levels (**Figure 3.18B,C,** unpaired two-tailed Student's t-test, $t(7) = 0.2928$, $p = 0.7782$, control: $n = 4$, *Bdnf*^{Pax2} KO: $n = 5$ mice).

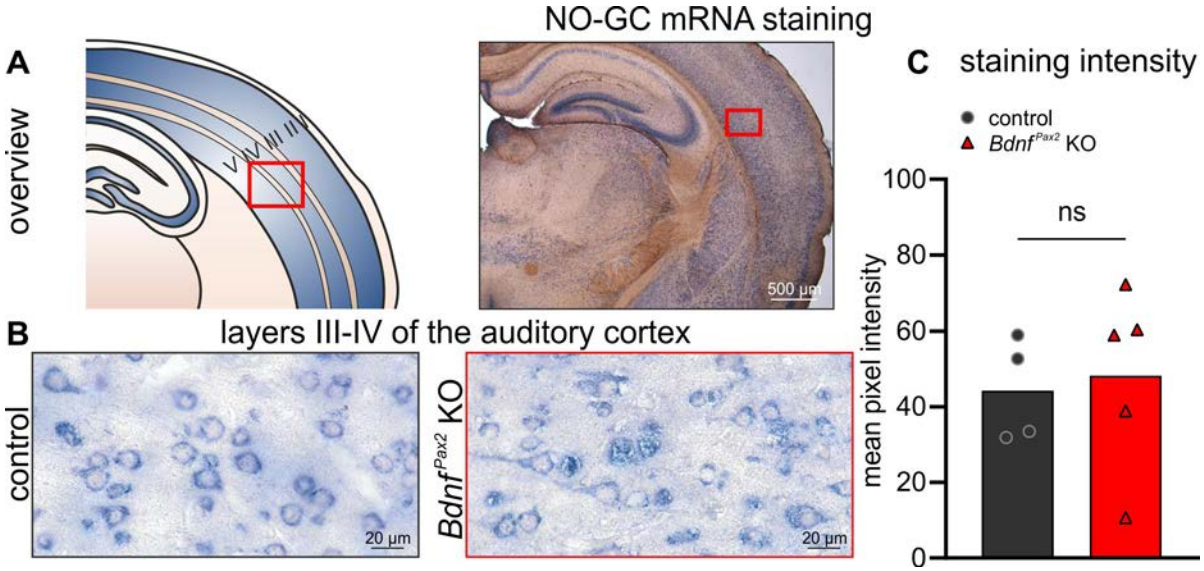

Figure 3.18. *NO-GC mRNA expression in layers III-IV of the AC.* ***(A)*** *Schematic and overview photo (2x magnification) of the AC showing the region in which images were taken (red boxes) with respect to the cortical layers.* ***(B)*** *Exemplary photos from control (left) and Bdnf*^{Pax2} *KO mice (right).* ***(C)*** *Staining intensity of control (black circles) and Bdnf*^{Pax2} *KO mice (red triangles). Symbols, animals; bars, mean. ns = not significant.*

Next, we examined the NO-GC mRNA expression levels in the granule cell layer of the dentate gyrus region of the hippocampus (**Figure 3.19A**). In this region, *Bdnf*^{Pax2} KO mice did not significantly differ from controls in their NO-GC mRNA expression levels (**Figure 3.19B,C,** unpaired two-tailed Student's t-test, $t(7) = 0.3368$, $p = 0.7462$, control: $n = 4$, *Bdnf*^{Pax2} KO: $n = 5$ mice).

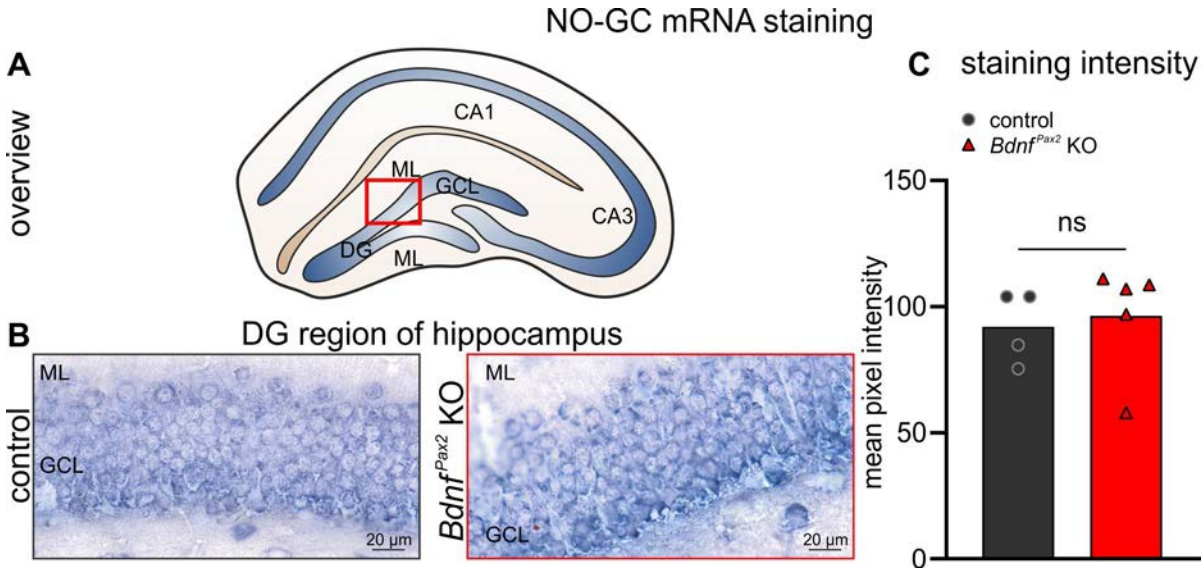

Figure 3.19. *NO-GC mRNA expression in the dentate gyrus region of the hippocampus. (**A**) Schematic of the hippocampus showing the region in which images were taken (red box). (**B**) Exemplary photos from control (left) and Bdnf^{Pax2} KO mice (right). (**C**) Staining intensity of control (black circles) and Bdnf^{Pax2} KO mice (red triangles). Symbols, animals; bars, mean. ns = not significant. DG, dentate gyrus; GCL, granule cell layer; ML, molecular layer.*

We then examined the NO-GC mRNA expression level in the CA3 region of the hippocampus, taking images from the stratum pyramidale (**Figure 3.20A**). In this region, *Bdnf*^{Pax2} KO mice did not significantly differ from controls in their NO-GC mRNA expression levels (**Figure 3.20B,C,** unpaired two-tailed Student's t-test, $t(7) = 0.1744$, $p = 0.8665$, control: $n = 4$, *Bdnf*^{Pax2} KO: $n = 5$ mice).

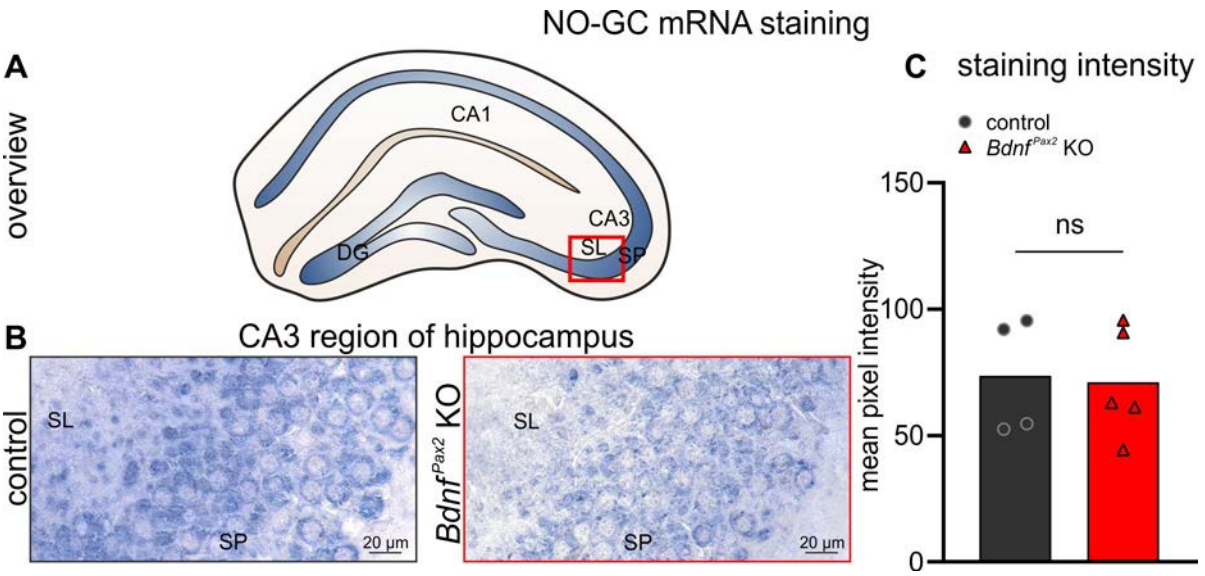

Figure 3.20. *NO-GC mRNA expression in the CA3 region of the hippocampus. (**A**) Schematic of the hippocampus showing the region in which images were taken (red box). (**B**) Exemplary photos from control (left) and Bdnf^{Pax2} KO mice (right). (**C**) Staining intensity of control (black circles) and Bdnf^{Pax2} KO mice (red triangles). Symbols, animals; bars, mean. ns = not significant. DG, dentate gyrus; SP, stratum pyramidale; SL, stratum lucidum.*

Finally, to determine the NO-GC mRNA expression level in the CA1 region of the hippocampus, images were taken from the stratum pyramidale (**Figure 3.21A**). In this region, *Bdnf*^{Pax2} KO mice exhibited significantly higher NO-GC mRNA expression levels in comparison to littermate controls (**Figure 3.21B,C**, unpaired two-tailed Student's t-test, $t(7) = 2.714$, $p = 0.0300$, control: $n = 4$, *Bdnf*^{Pax2} KO: $n = 5$ mice).

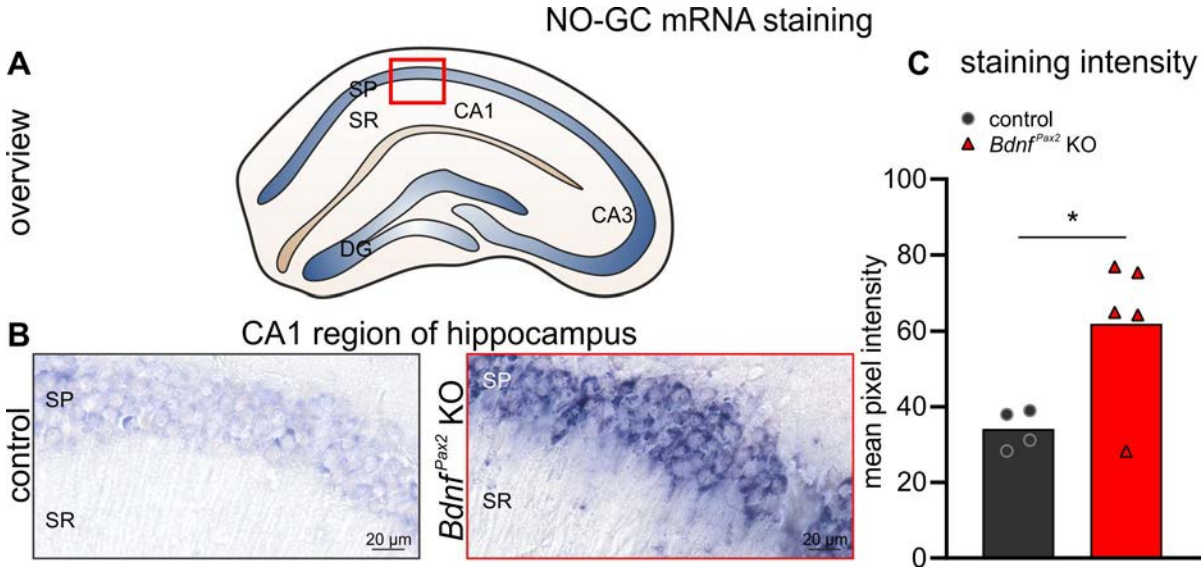

Figure 3.21. *NO-GC mRNA expression in the CA1 region of the hippocampus. (**A**) Schematic of the hippocampus showing the region in which images were taken (red box). (**B**) Exemplary photos from control (left) and Bdnf*^{Pax2} *KO mice (right). (**C**) Staining intensity of control (black circles) and Bdnf*^{Pax2} *KO mice (red triangles). Symbols, animals; bars, mean. * = $p < 0.05$. DG, dentate gyrus; SP, stratum pyramidale; SR, stratum radiatum.*

The pattern of NO-GC mRNA expression levels indicates that the cGMP pathway is altered in the CA1 region of the hippocampus, though it may be unchanged in other regions of the hippocampus and in the AC. As NO-GC is a cGMP generator, these results suggest that more cGMP may be produced in the CA1 region of the hippocampus.

3.3.5 Summary

Taken together, this suggests that younger mice are more resilient to stressful situations, exemplified by the fact that control mice only showed a stress-induced threshold elevation, but the function of higher-level auditory structures remained intact. Additionally, the PDE9i had only minimal effects on control mice, rescuing the slightly elevated hearing thresholds and increasing LTP. *Bdnf*^{Pax2} KO mice also exhibited a slight elevation of hearing thresholds after treatment with both vehicle and PDE9i, despite an unchanged corticosterone level. Unlike in controls however, the worsening of hearing thresholds could not be rescued upon treatment with the PDE9i. Further, the PDE9i had a mildly adverse effect on the hearing function and slightly decreased the LTP. This unexpected detrimental effect of the PDE9i in *Bdnf*^{Pax2} KO mice may be due to their already-altered cGMP pathway in the CA1 region of the hippocampus.

3.4 Treatment of *Bdnf*^{Pax2} KO Mice Using Acoustic Enrichment

As the central ASD phenotype of *Bdnf*^{Pax2} KO mice is likely driven by the periphery and a treatment primarily targeting the central phenotype could not recover the phenotype, we decided to use a treatment that instead targets the peripheral dysfunction. Namely, we exposed control and *Bdnf*^{Pax2} KO mice to a one-time acoustic enrichment—a 10 kHz tone presented at 80 dB SPL for 40 minutes, henceforth referred to as "80 dB"—and measured the hearing, memory function, and behavior two weeks later. This protocol has previously been shown to result in an increased number of IHC ribbons, higher amplitude ABR waves, higher LTP, and improved performance on a cognitive test in another mouse

line two weeks after exposure (Matt et al., 2018), thus making it an ideal therapeutic approach to try in the *Bdnf*^{Pax2} KO model.

3.4.1 Effect of 80 dB Exposure on Hearing Function

80 dB exposure is considered non-traumatic and should not lead to a permanent threshold shift (Matt et al., 2018). To confirm this in our mice, we measured the hearing thresholds in response to click, noise-burst, and pure-tone stimuli before and two weeks after 80 dB exposure.

Indeed, no threshold changes were observed in response to click stimuli in either control mice exposed to sham or 80 dB, or in *Bdnf*^{Pax2} KO mice exposed to sham or 80 dB (**Figure 3.22A**, left, control sham: Mann-Whitney U test, $U = 354$, $p = 0.539$, $n = 28/14$ mice/ears; control 80 dB: Mann-Whitney U test, $U = 337$, $p = 0.372$, $n = 28/14$ mice/ears; *Bdnf*^{Pax2} KO sham: Mann-Whitney U test, $U = 425.5$, $p = 0.722$, $n = 30/15$ mice/ears; *Bdnf*^{Pax2} KO 80 dB: Mann-Whitney U test, $U = 423.5$, $p = 0.70$, $n = 30/15$ mice/ears). Similarly, no threshold changes were observed in response to noise-burst stimuli in either control mice exposed to sham or 80 dB, or in *Bdnf*^{Pax2} KO mice exposed to sham or 80 dB (**Figure 3.22A**, right, control sham: Mann-Whitney U test, $U = 306.5$, $p = 0.164$, $n = 28/14$ mice/ears; control 80 dB: Mann-Whitney U test, $U = 346$, $p = 0.456$, $n = 28/14$ mice/ears; *Bdnf*^{Pax2} KO sham: Mann-Whitney U test, $U = 382.5$, $p = 0.323$, $n = 30/15$ mice/ears; *Bdnf*^{Pax2} KO 80 dB: Mann-Whitney U test,

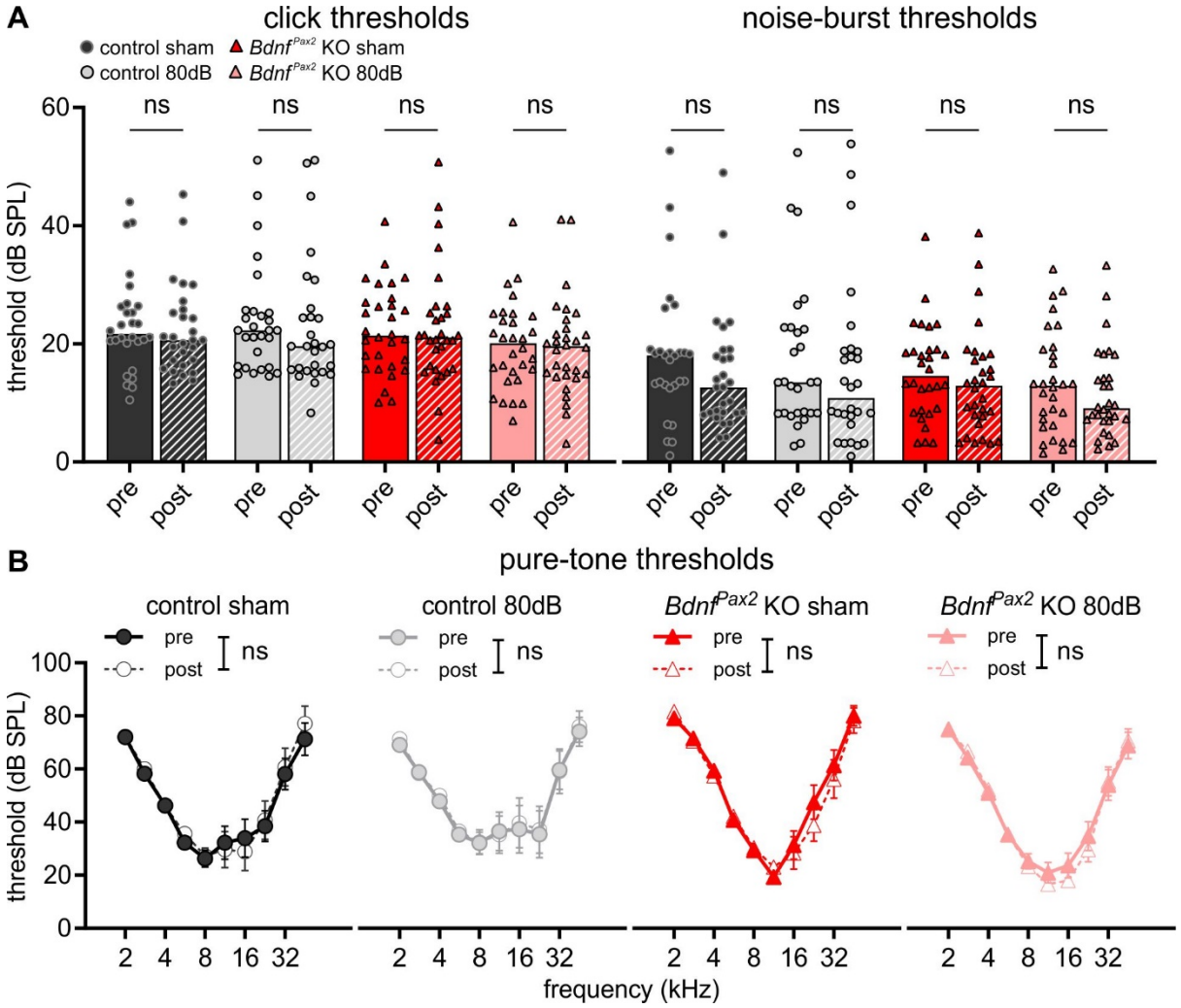

Figure 3.22. *Hearing thresholds after exposure to sham or 80 dB. (**A**) Hearing thresholds in response to click (left) and noise-burst stimuli (right) in control (circles) and Bdnf*^{Pax2} *KO mice (triangles) before (solid bars) and after (striped bars) exposure to sham (black or red) or 80 dB (light gray or pink). Symbols, ears; bars, mean. (**B**) Hearing thresholds in response to pure-tone stimuli in control mice before (solid line, filled symbols) and after (dotted line, open symbols) exposure to sham (1*st *panel) or 80 dB (2*nd *panel), and in Bdnf*^{Pax2} *KO mice before and after exposure to sham (3*rd *panel) or 80 dB (4*th *panel). Mean ± SEM. ns = not significant.*

$U = 400$, $p = 0.465$, $n = 30/15$ mice/ears). Finally, no threshold changes were observed in response to pure-tone stimuli in either control mice exposed to sham or 80 dB, or in *Bdnf*^{Pax2} KO mice exposed to sham or 80 dB (**Figure 3.22B**, control sham: 2-way ANOVA, $F(1,267) = 0.1868$, $p = 0.666$, $n = 15$; control 80 dB: 2-way ANOVA, $F(1,275) = 0.1529$, $p = 0.696$, $n = 16$; *Bdnf*^{Pax2} KO sham: 2-way ANOVA, $F(1,284) = 0.6017$, $p = 0.439$, $n = 16$; *Bdnf*^{Pax2} KO 80 dB: 2-way ANOVA, $F(1,279) = 0.4486$, $p = 0.504$, $n = 15$).

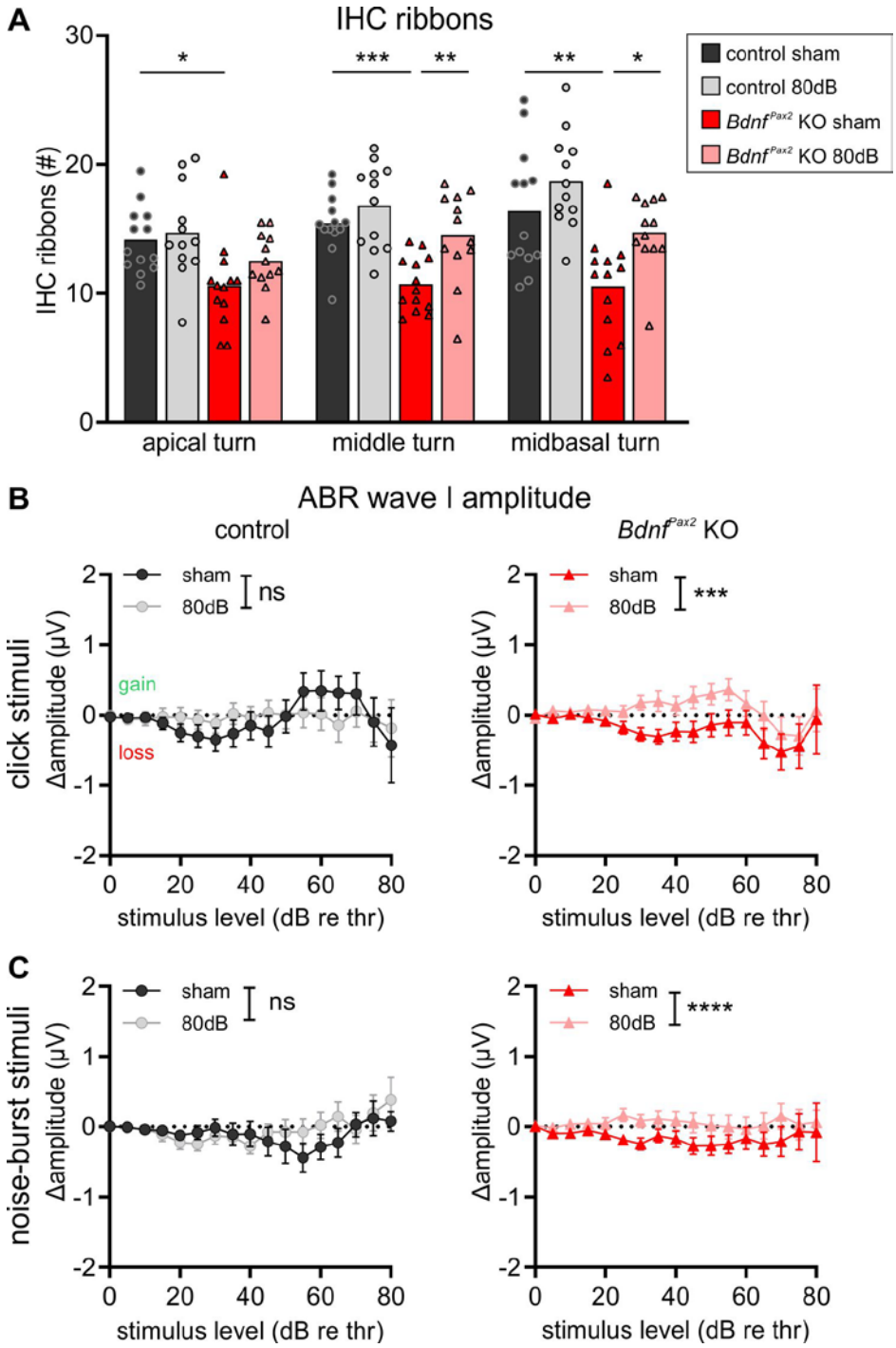

Figure 3.23. *IHC ribbons and ABR wave I after exposure to sham or 80 dB. (**A**) IHC ribbons at the apical, middle, and midbasal cochlear turn of control (circles) and Bdnf*^{Pax2} *KO mice (triangles) exposed to sham (black or red) or 80 dB (light gray or pink). Symbols, cochleae; bars, mean. (**B**) Amplitude delta of control (left) and Bdnf*^{Pax2} *KO mice (right) exposed to sham versus 80 dB in response to click stimuli. (**C**) Amplitude delta of control (left) and Bdnf*^{Pax2} *KO mice (right) exposed to sham versus 80 dB in response to noise-burst stimuli. Mean ± SEM. * = $p < 0.05$, ** = $p < 0.01$, *** = $p < 0.001$, **** = $p < 0.0001$, ns = not significant.*

It has been previously reported that 80 dB exposure increases the number of IHC ribbons—reflecting the active vesicle release sites of the first synapse in the auditory pathway—in the cochlea, particularly in the middle turn (Matt et al., 2018). We therefore stained C-terminal binding protein 2, a critical component of synaptic ribbons, and counted the number of immunopositive dots in the apical, middle, and midbasal cochlear turn of control and *Bdnf*^{Pax2} KO mice exposed to sham or 80 dB.

As previously reported, *Bdnf*^{Pax2} KO mice had fewer IHC ribbons than control mice after sham exposure in the apical, middle, and midbasal turns (**Figure 3.23A**, apical: 1-way ANOVA, $F(3, 46) = 4.745$, $p = 0.0058$, Sidak's multiple comparisons test, control sham: $n = 13$, control 80 dB: $n = 13$,

Bdnf^{Pax2} KO sham: $n = 12$, , *Bdnf*^{Pax2} KO 80 dB: $n = 12$; middle: 1-way ANOVA, $F(3, 46) = 10.54$, $p < 0.0001$, Sidak's multiple comparisons test, control sham: $n = 13$, control 80 dB: $n = 13$, *Bdnf*^{Pax2} KO sham: $n = 12$, , *Bdnf*^{Pax2} KO 80 dB: $n = 12$; midbasal: 1-way ANOVA, $F(3, 46) = 9.560$, $p < 0.0001$, Sidak's multiple comparisons test, control sham: $n = 13$, control 80 dB: $n = 13$, *Bdnf*^{Pax2} KO sham: $n = 12$, *Bdnf*^{Pax2} KO 80 dB: $n = 12$). Surprisingly however, 80 dB exposure resulted in an increase of IHC ribbons in *Bdnf*^{Pax2} KO mice but not in controls in both the middle (**Figure 3.23A**) and midbasal turn (**Figure 3.23A**).

As the number of IHC ribbons determines the auditory nerve fiber discharge rate (Buran et al., 2010; Kujawa & Liberman, 2009), one would expect these observations to also be reflected in functional measurements of the auditory nerve, such as the ABR wave I amplitude. We therefore measured the ABR wave I amplitude before and after exposure and calculated the delta (i.e., the post-exposure amplitude minus the pre-exposure amplitude) to allow for a direct comparison of the sham-exposed animals with the 80 dB–exposed animals.

As expected from the IHC ribbon counts, no differences were observed in the ABR wave I delta in control mice in response to click stimuli, but *Bdnf*^{Pax2} KO mice exposed to 80 dB had a significantly higher ABR wave I delta in comparison to those exposed to sham, reflecting a higher ABR wave I amplitude after exposure (**Figure 3.23B**, control: 2-way ANOVA, $F(1,724) = 0.3951$, $p = 0.5298$, sham: $n = 27/14$, 80 dB: $n = 27/14$ ears/mice; *Bdnf*^{Pax2} KO: 2-way ANOVA, $F(1,846) = 13.91$, $p = 0.0002$, Sidak's multiple comparisons test, sham: $n = 30/15$, 80 dB: $n = 32/16$ ears/mice). Likewise, in response to noise-burst stimuli, no differences were observed in ABR wave I delta in control mice, but *Bdnf*^{Pax2} KO mice exposed to 80 dB had a significantly higher delta in comparison to those exposed to sham (**Figure 3.23C**, control: 2-way ANOVA, $F(1,710) = 1.289$, $p = 0.2566$, sham: $n = 27/14$, 80 dB: $n = 27/14$ ears/mice; *Bdnf*^{Pax2} KO: 2-way ANOVA, $F(1,776) = 18.76$, $p < 0.0001$, Sidak's multiple comparisons test, sham: $n = 30/15$, 80 dB: $n = 28/14$ ears/mice).

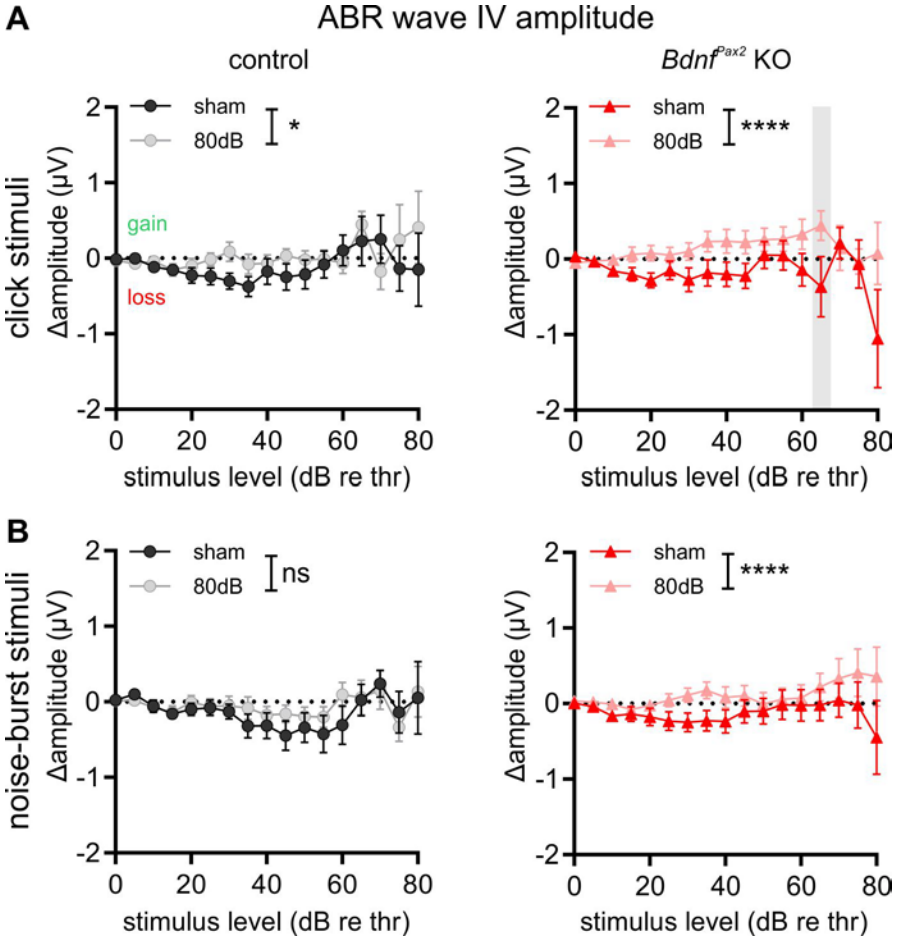

Figure 3.24. *ABR wave IV after exposure to sham or 80 dB. (**A**) Amplitude delta of control (left) and Bdnf*^{Pax2} *KO mice (right) exposed to sham (black or red) versus 80 dB (light gray or pink) in response to click stimuli. (**B**) Amplitude delta of control (left) and Bdnf*^{Pax2} *KO mice (right) exposed to sham versus 80 dB in response to noise-burst stimuli. Mean ± SEM. * = p < 0.05, **** = p < 0.0001, ns = not significant*

To determine if the increase of activity was propagated along the ascending auditory pathway, we measured the ABR wave IV amplitude before and after exposure and calculated the delta as described above. Surprisingly, control mice exposed to 80 dB exhibited a slightly but

significantly higher ABR wave IV delta in response to click stimuli in comparison to those exposed to sham (**Figure 3.24A**, 2-way ANOVA, $F(1,711) = 5.610$, $p = 0.0181$, Sidak's multiple comparisons test, sham: $n = 27/14$, 80 dB: $n = 27/14$ ears/mice). As expected from the higher ABR wave I amplitude, *Bdnf*^{Pax2} KO mice exposed to 80 dB had a significantly higher ABR wave IV delta in response to click stimuli in comparison to those exposed to sham (**Figure 3.24A**, 2-way ANOVA, $F(1,775) = 25.11$, $p < 0.0001$, Sidak's multiple comparisons test, sham: $n = 29/15$, 80 dB: $n = 32/16$ ears/mice). In response to noise-burst stimuli, no differences between the exposure conditions were observed in ABR wave IV delta in control mice, but *Bdnf*^{Pax2} KO mice exposed to 80 dB had a significantly higher delta in comparison to those exposed to sham, indicating a higher ABR wave IV amplitude after 80 dB exposure (**Figure 3.24B**, control: 2-way ANOVA, $F(1,689) = 2.156$, $p = 0.1425$, sham: $n = 27/14$, 80 dB: $n = 27/14$ ears/mice; *Bdnf*^{Pax2} KO: 2-way ANOVA, $F(1,751) = 18.42$, $p < 0.0001$, Sidak's multiple comparisons test, sham: $n = 28/14$, 80 dB: $n = 27/14$ ears/mice). This suggests that the increased activity in the early auditory pathway (ABR wave I) of 80 dB–exposed *Bdnf*^{Pax2} KO mice is indeed able to propagate to higher order structures.

To determine if this increased activity in the auditory system also translates to an improvement in temporal sound coding, we measured the ASSRs in control and *Bdnf*^{Pax2} KO mice exposed to sham or 80 dB. ASSRs are responses to amplitude-modulated stimuli, in which the measured signal reflects the discharge of neurons that are phase-locked to the modulation frequency (Lin et al., 2009). Thus, we measured the ASSRs in response to amplitude-modulated stimuli of increasing loudness and increasing modulation depth before and after exposure and calculated the delta (i.e., the post-exposure SNR minus the pre-exposure SNR).

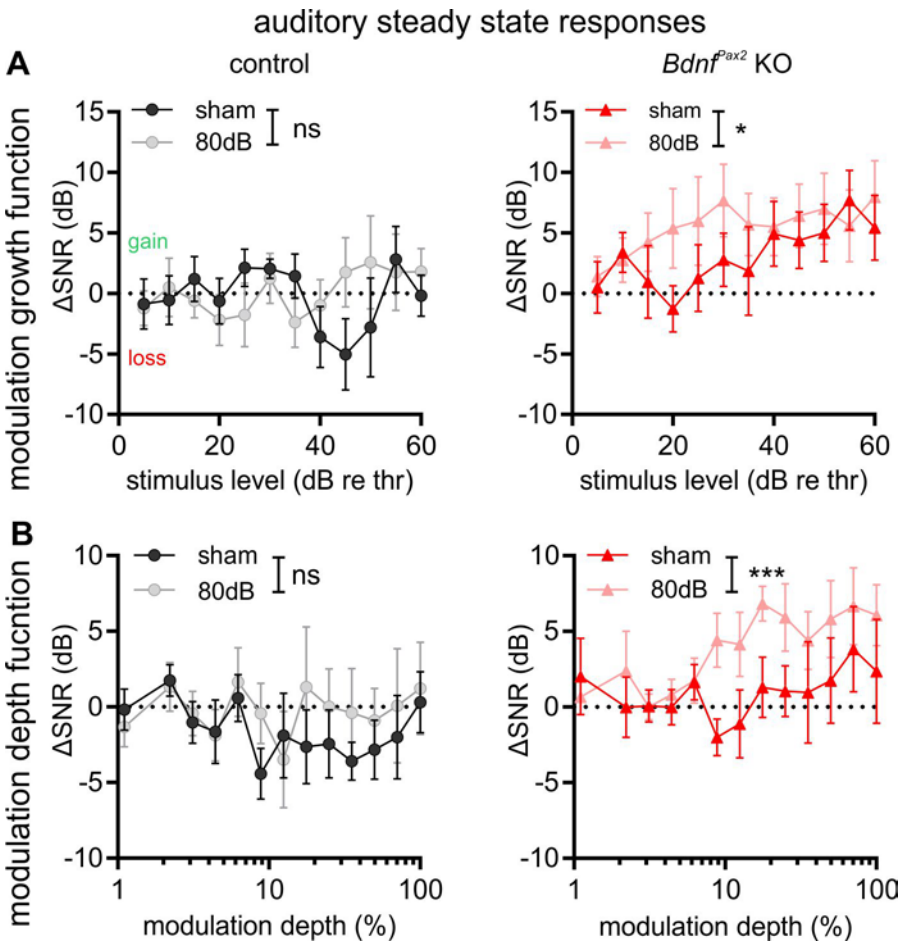

Figure 3.25. *ASSRs after exposure to sham or 80 dB. (**A**) Modulation growth function SNR delta of control (left) and Bdnf*^{Pax2} *KO mice (right) exposed to sham (black or red) versus 80 dB (light gray or pink). (**B**) Modulation depth function SNR delta of control (left) and Bdnf*^{Pax2} *KO mice (right) exposed to sham versus 80 dB. Mean ± SEM. (*) = p < 0.08, * = p < 0.05, *** = p < 0.001, ns = not significant.*

In control mice, no differences between exposure conditions were observed in response to amplitude-modulated tones of increasing loudness, but *Bdnf*^{Pax2} KO mice exposed to 80 dB had a significantly higher SNR delta in comparison to those exposed to sham (**Figure 3.25A**, control: 2-way ANOVA, $F(1,204) = 0.151$, $p = 0.6980$, sham: $n = 10$, 80 dB: $n = 9$; *Bdnf*^{Pax2} KO: 2-way ANOVA, $F(1,228) = 4.919$, $p = 0.0275$, Sidak's multiple comparisons test, sham: $n = 11$, 80 dB: $n = 10$). In response to amplitude-modulated tones of increasing modulation depths, no differences between exposure conditions

were observed in control mice, while *Bdnf*^{Pax2} KO mice exposed to 80 dB had a significantly higher SNR delta in comparison to those exposed to sham (**Figure 3.25B**, control: 2-way ANOVA, $F(1,197) = 2.741$, $p = 0.0994$, sham: $n = 10$, 80 dB: $n = 9$; *Bdnf*^{Pax2} KO: 2-way ANOVA, $F(1,153) = 14.12$, $p = 0.0002$, Sidak's multiple comparisons test, sham: $n = 10$, 80 dB: $n = 9$).

Taken together, this suggests that 80 dB exposure is able to at least partially recover the hearing phenotype of *Bdnf*^{Pax2} KO mice along the ascending auditory pathway, starting from the IHC ribbons, translating into a functional increase in ABR wave amplitude, and finally improving the temporal sound coding.

3.4.2 Effect of 80 dB Exposure on Memory Function

The beneficial effects of 80 dB exposure in the auditory system have been previously shown to lead to an improvement of memory function (Matt et al., 2018). This at first somewhat surprising result makes sense if we consider that the auditory system provides a major source of input to the hippocampus (for a review, see Billig et al., 2022). We therefore studied whether 80 dB sound exposure could recover both the hearing phenotype (see section 3.4.1) and the behavioral phenotype of *Bdnf*^{Pax2} KO mice.

To this end, we assessed memory function of control and *Bdnf*^{Pax2} KO mice by performing the novel object recognition test. In the first day of this two-day behavioral test, mice were placed in a chamber with two identical objects and allowed to explore for ten minutes. On the second day, mice were placed in the same chamber for ten minutes, but one of the objects was replaced by a novel object (**Figure 3.26A**). If mice learned and recognized the familiar object, their natural propensity towards novelty resulted in them spending more time interacting with the novel object as opposed to the familiar one (Lueptow, 2017).

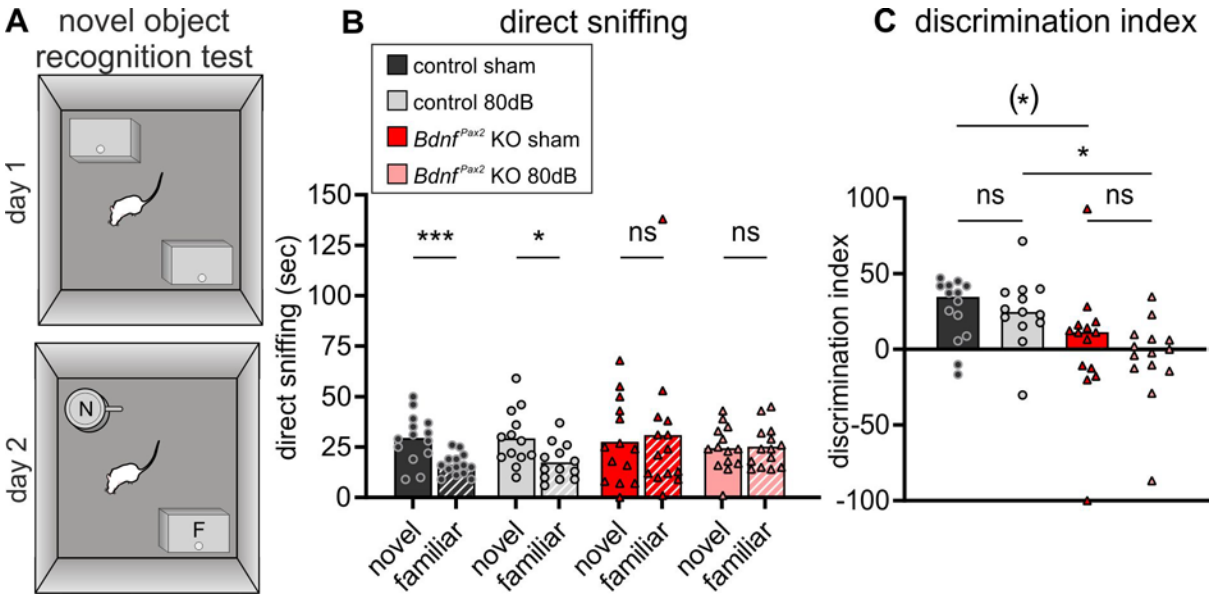

Figure 3.26. *Novel object recognition test after exposure to sham or 80 dB. (**A**) Schematic of novel object recognition test showing the learning phase (day 1), in which the mouse is allowed to explore two identical objects, and the test phase (day 2), in which one of the prior, familiar objects ("F") has been replaced with a novel object ("N"). (**B**) Direct sniffing of the novel (solid bars) versus the familiar object (striped bars) in control mice treated with sham (black circles) or 80 dB (light gray circles) and in Bdnf*^{Pax2} *KO mice treated with sham (red triangles) or 80 dB (pink triangles). Symbols, animals; bars, mean. (**C**) Discrimination index of control and Bdnf*^{Pax2} *KO mice treated with sham or 80 dB. Symbols, animals; bars, median. (*) = $p < 0.08$, * = $p < 0.05$, *** = $p < 0.001$, ns = not significant.*

We therefore analyzed the time the mice spent sniffing each object. As expected, control mice spent significantly more time sniffing the novel object as compared to the familiar object after both sham and 80 dB exposure (**Figure 3.26B**, sham: unpaired two-tailed Student's t-test, $t(26) = 3.77$, $p = 0.0008$, $n = 14$; 80 dB: unpaired two-tailed Student's t-test, $t(24) = 2.617$, $p = 0.0151$, $n = 13$). On the other hand, *Bdnf*^{Pax2} KO mice exposed to sham did not show any preference towards either the novel or familiar

object, and this phenotype was unaffected by 80 dB exposure (**Figure 3.26B**, sham: unpaired two-tailed Student's t-test, $t(26) = 0.309$, $p = 0.7598$, $n = 14$; 80 dB: unpaired two-tailed Student's t-test, $t(26) = 0.1947$, $p = 0.8471$, $n = 14$).

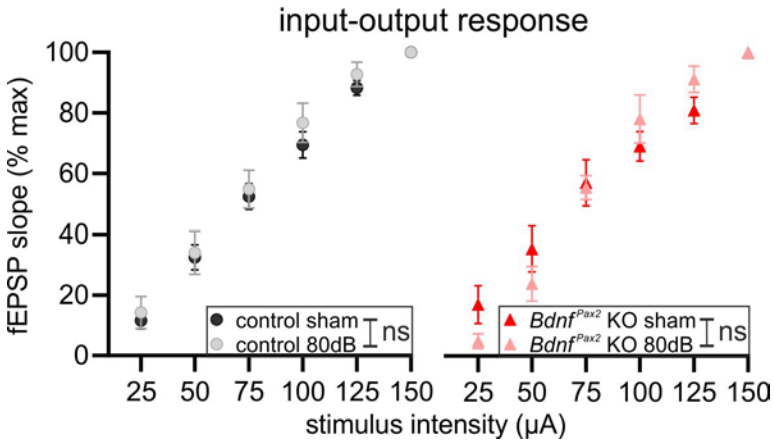

Figure 3.27. *Input-output response of hippocampal fEPSP slope after exposure to sham or 80 dB. Input-output response of control (left) and Bdnf^{Pax2} KO mice (right) exposed to sham (black or red) versus 80 dB (light gray or pink). Mean ± SEM. ns = not significant.*

In order to directly compare the exposure groups, a discrimination index was calculated, which considers the relative time the mice spent sniffing the novel object. A positive discrimination index indicates more time spent sniffing the novel object, while a negative discrimination index indicates more time spent sniffing the familiar object. Accordingly, control mice exposed to sham trended towards a higher discrimination index in comparison to *Bdnf*^{Pax2} KO mice exposed to sham (**Figure 3.26C**). Additionally, control mice exposed to 80 dB had a significantly higher discrimination index in comparison to *Bdnf*^{Pax2} KO mice exposed to 80 dB (**Figure 3.26C**). Finally, controls exposed to sham or 80 dB and *Bdnf*^{Pax2} KO mice exposed to sham or 80 dB did not differ in their discrimination index (**Figure 3.26C**, Kruskal-Wallis test, $H(3) = 15.17$, $p = 0.0017$, Dunn's multiple comparisons test, control sham: $n = 14$, control 80 dB: $n = 13$, *Bdnf*^{Pax2} KO sham: $n = 14$, *Bdnf*^{Pax2} KO 80 dB: $n = 14$). This indicates that the memory function of neither control nor *Bdnf*^{Pax2} KO mice benefited from 80 dB in their memory function.

To test if this effect was truly due to memory function and not simply an issue of motivation, we assessed hippocampal function by measuring fEPSPs in hippocampal brain slices from control and *Bdnf*^{Pax2} KO mice after exposure to either sham or 80 dB. First, basal synaptic transmission was assessed by measuring the input-output relationship of fEPSPs. No differences between exposure conditions were observed in either control or *Bdnf*^{Pax2} KO mice (**Figure 3.27**, control: 2-

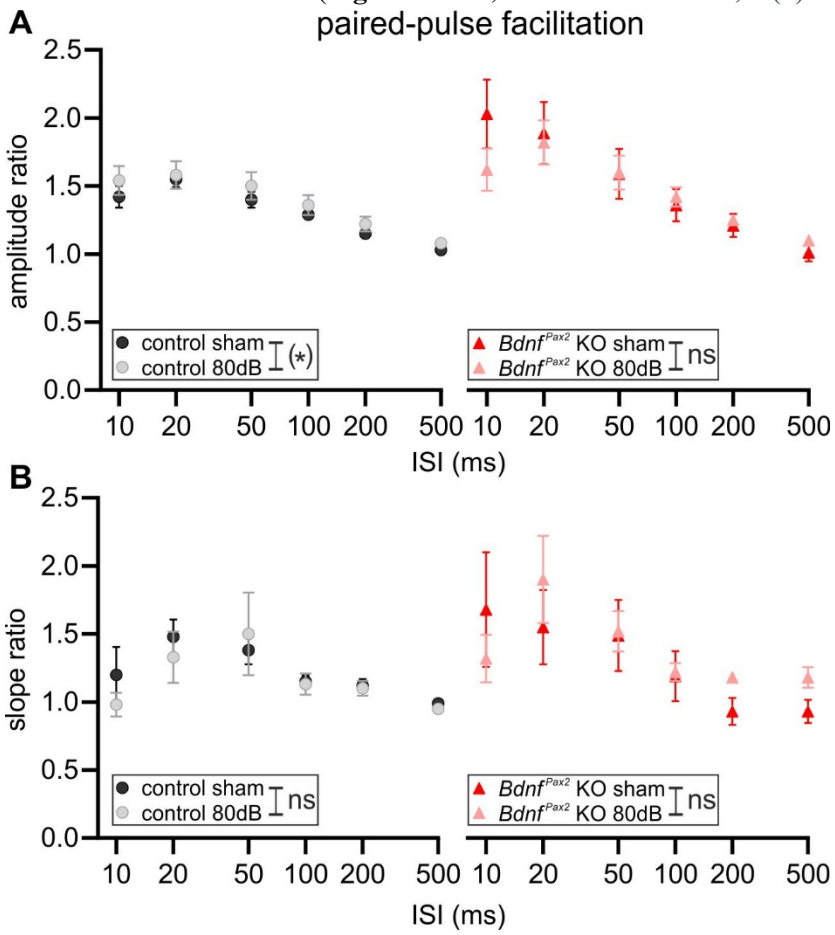

Figure 3.28. *Paired-pulse facilitation after exposure to sham or 80 dB. (**A**) Paired-pulse amplitude ratio of control (left) and Bdnf^{Pax2} KO mice (right) exposed to sham (black or red) versus 80 dB (light gray or pink). (**B**) Paired-pulse slope ratio of control (left) and Bdnf^{Pax2} KO mice (right) exposed to sham versus 80 dB. Mean ± SEM. (*) = $p < 0.08$, ns = not significant.*

way ANOVA, $F(1,156) = 1.532$, $p = 0.2176$, sham: $n = 17/7$, 80 dB: $n = 11/6$ slices/mice; $Bdnf^{Pax2}$ KO: 2-way ANOVA, $F(1,138) = 0.0997$, $p = 0.7527$, sham: $n = 12/6$, 80 dB: $n = 13/7$ slices/mice). This suggests that basal synaptic transmission remained intact after exposure.

After the basal synaptic transmission, we investigated the effect on short-term plasticity by performing paired-pulse facilitation in hippocampal brain slices from sham- or 80 dB–exposed control and $Bdnf^{Pax2}$ KO mice. Control mice exposed to 80 dB trended towards a slightly higher paired-pulse amplitude ratio in comparison to those exposed to sham, but no differences were observed in the paired-pulse amplitude ratio of $Bdnf^{Pax2}$ KO mice exposed to sham or 80 dB (**Figure 3.28A**, control: 2-way ANOVA, $F(1,156) = 3.882$, $p = 0.0506$, sham: $n = 17/7$, 80 dB: $n = 11/6$ slices/mice; $Bdnf^{Pax2}$ KO: 2-way ANOVA, $F(1,138) = 0.3254$, $p = 0.5693$, sham: $n = 12/6$, 80 dB: $n = 13/7$ slices/mice). In the paired-pulse slope ratio, however, no significant differences were observed between exposure groups in either control or $Bdnf^{Pax2}$ KO mice (**Figure 3.28B**, control: 2-way ANOVA, $F(1,156) = 0.5147$, $p = 0.4742$, sham: $n = 17/7$, 80 dB: $n = 11/6$ slices/mice; $Bdnf^{Pax2}$ KO: 2-way ANOVA, $F(1,138) = 0.5747$, $p = 0.4497$, sham: $n = 12/6$, 80 dB: $n = 13/7$ slices/mice). Overall, this suggests that 80 dB exposure had minimal impact on the presynapse.

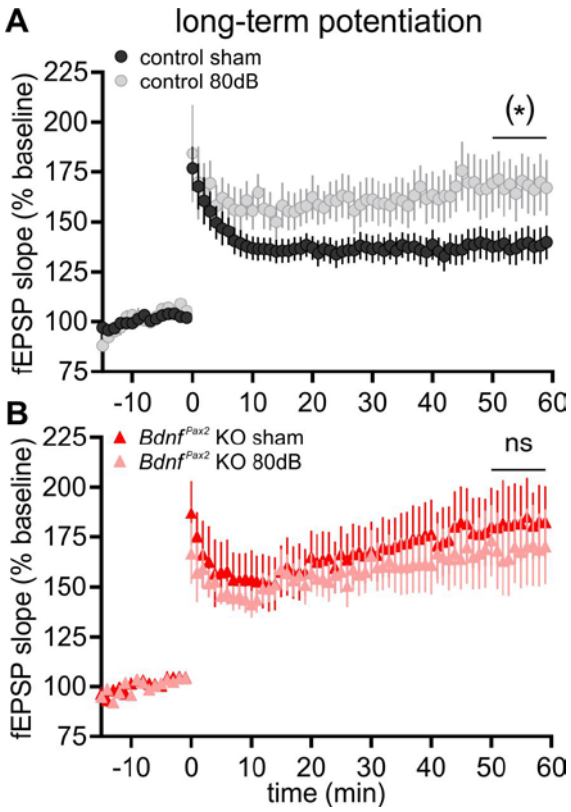

Figure 3.29. *LTP after exposure to sham or 80 dB. fEPSP slope of the 15-minute baseline recording and for 60 minutes following tetanic stimulation of control (**A**) and $Bdnf^{Pax2}$ KO mice (**B**) exposed to sham (black or red) versus 80 dB (light gray or pink). Mean ± SEM. (*) = $p < 0.08$, ns = not significant.*

At the end of the recordings, we investigated the exposure effect on LTP by applying a high frequency stimulation (1 s, 100 Hz) to hippocampal brain slices from control and $Bdnf^{Pax2}$ KO mice after exposure to either sham or 80 dB.

Control mice exposed to 80 dB had a trend towards higher LTP in comparison to those exposed to sham (**Figure 3.29A**, unpaired two-tailed Student's t-test, $t(26) = 2.047$, $p = 0.0509$, sham: $n = 17/7$, 80 dB: $n = 11/6$ slices/mice). On the other hand, $Bdnf^{Pax2}$ KO mice exposed to sham or 80 dB did not differ in their LTP (**Figure 3.29B**, unpaired two-tailed Student's t-test, $t(23) = 0.4925$, $p = 0.6270$, sham: $n = 12/6$, 80 dB: $n = 13/7$ slices/mice).

3.4.3 Effect of 80 dB Exposure on Social Behavior

The disinterested social behavior of $Bdnf^{Pax2}$ KO mice was one of the most striking features of their phenotype in its resemblance to ASD (Eckert et al., 2021). Though the effect of 80 dB exposure on social behavior has not yet been examined, other protocols of environmental enrichment were shown to increase social interaction in various mouse models of ASD (Clipperton-Allen et al., 2021; Queen et al., 2020; Xiao, 2017; Yamaguchi et al., 2017). We therefore tested whether 80 dB exposure had similar beneficial effects on the social behavior of $Bdnf^{Pax2}$ KO mice.

To this end, we performed Crawley's three-chamber sociability test (Silverman et al., 2010) in control and $Bdnf^{Pax2}$ KO mice exposed to sham or 80 dB. In this behavioral experiment, the mouse was initially placed in the middle chamber of a three-chamber box, with the two outer chambers blocked. It was allowed five minutes to acclimate to the new environment before the doors to the outer chambers were removed. Both of the outer chambers contained a wire cup, inside one of which was a "stranger" mouse (**Figure 3.30A**).

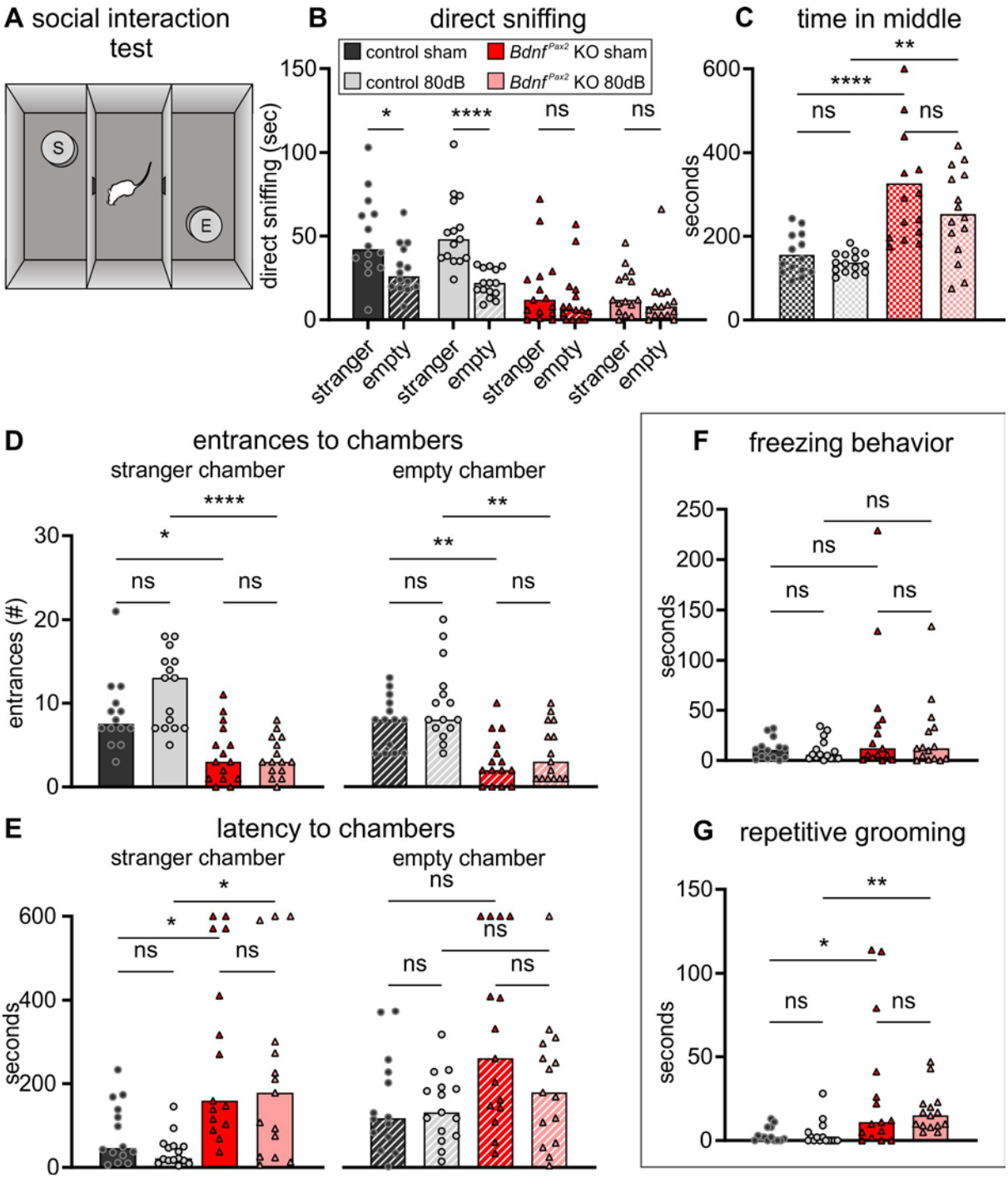

Figure 3.30. *Social and autism-like behavior after exposure to sham or 80 dB. (**A**) Schematic of Crawley's three-chamber sociability test, showing the mouse in a three-chamber box in which one of the outer chambers contains a "stranger" mouse ("S") and the other contains an empty cup ("E"). (**B**) Direct sniffing of the stranger mouse (solid bars) versus the empty cup (striped bars) in control mice exposed to sham (black circles) or 80 dB (light gray circles) and in Bdnf^{Pax2} KO mice exposed to sham (red triangles) or 80 dB (pink triangles). (**C**) Time spent in the middle chamber by control and Bdnf^{Pax2} KO mice exposed to sham or 80 dB. Symbols, animals; bars, mean. (**D**) Number of entrances to the stranger chamber (left) and the empty chamber (right) by control and Bdnf^{Pax2} KO mice exposed to sham or 80 dB. (**E**) Latency of entrance to the stranger chamber (left) and the empty chamber (right) by control and Bdnf^{Pax2} KO mice exposed to sham or 80 dB. (**F**) Time spent freezing by control and Bdnf^{Pax2} KO mice exposed to sham or 80 dB. (**G**) Time spent grooming by control and Bdnf^{Pax2} KO mice exposed to sham or 80 dB. Symbols, animals; bars, median. * = $p < 0.05$, ** = $p < 0.01$, *** = $p < 0.001$, **** = $p < 0.0001$, ns = not significant.*

We first analyzed the time mice spent sniffing each cup, as the innate social instincts of mice will result in their spending more time interacting with the stranger mouse rather than the empty cup. Indeed, control mice spent more time sniffing the stranger mouse compared to the empty cup after exposure to

sham or 80 dB (**Figure 3.30B**, sham: unpaired two-tailed Student's t-test, $t(26) = 2.493$, $p = 0.0194$, $n = 14$; 80 dB: unpaired two-tailed Student's t-test, $t(26) = 5.217$, $p < 0.0001$, $n = 15$). On the other hand, *Bdnf*^{Pax2} KO mice did not show a preference for the stranger mouse after exposure to either sham or 80 dB (**Figure 3.30B**, sham: Mann-Whitney U test, $U = 90.5$, $p = 0.3697$, $n = 15$; 80 dB: Mann-Whitney U test, $U = 77$, $p = 0.1446$, $n = 15$).

This experiment can also be used to evaluate the exploratory behavior of mice by quantifying the amount of time mice spent in each chamber. Control mice exposed to sham or 80 dB spent significantly less time in the empty middle chamber in comparison to *Bdnf*^{Pax2} KO mice exposed to sham or 80 dB, respectively. In both genotypes, this behavior was not affected by sham or 80 dB exposure (**Figure 3.30C**, 1-way ANOVA, $F(3, 55) = 12.41$, $p < 0.0001$, Sidak's multiple comparisons test, control sham: $n = 14$, control 80 dB: $n = 15$, *Bdnf*^{Pax2} KO sham: $n = 15$, *Bdnf*^{Pax2} KO 80 dB: $n = 15$).

The exploratory behavior was also quantified by analyzing the number of times mice entered each chamber. Control mice exposed to sham or 80 dB entered the chamber with the stranger mouse significantly more times than *Bdnf*^{Pax2} KO mice exposed to sham or 80 dB, respectively. In both genotypes, this behavior was not affected by sham or 80 dB exposure (**Figure 3.30D**, Kruskal-Wallis test, $H(3) = 28.09$, $p < 0.0001$, Dunn's multiple comparisons test, control sham: $n = 14$, control 80 dB: $n = 15$, *Bdnf*^{Pax2} KO sham: $n = 15$, *Bdnf*^{Pax2} KO 80 dB: $n = 15$). Control mice exposed to sham or 80 dB also entered the chamber with the empty cup significantly more times than *Bdnf*^{Pax2} KO mice exposed to sham or 80 dB, respectively. In both genotypes, this behavior was not affected by sham or 80 dB exposure (**Figure 3.30D**, Kruskal-Wallis test, $H(3) = 23.1$, $p < 0.0001$, Dunn's multiple comparisons test, control sham: $n = 14$, control 80 dB: $n = 15$, *Bdnf*^{Pax2} KO sham: $n = 15$, *Bdnf*^{Pax2} KO 80 dB: $n = 15$).

Finally, exploratory behavior can be assessed by analyzing the time it takes for mice to enter each chamber. Control mice exposed to sham or 80 dB waited significantly less to enter the chamber with the stranger mouse in comparison to *Bdnf*^{Pax2} KO mice exposed to sham or 80 dB, respectively. In both genotypes, the exposure condition did not affect this behavior (**Figure 3.30E**, Kruskal-Wallis test, $H(3) = 19.56$, $p = 0.0002$, Dunn's multiple comparisons test, control sham: $n = 14$, control 80 dB: $n = 15$, *Bdnf*^{Pax2} KO sham: $n = 15$, *Bdnf*^{Pax2} KO 80 dB: $n = 15$). Conversely, no significant differences were found between either genotype or exposure condition in the latency to enter the chamber containing the empty cup (**Figure 3.30E**, Kruskal-Wallis test, $H(3) = 6.486$, $p = 0.090$, control sham: $n = 14$, control 80 dB: $n = 15$, *Bdnf*^{Pax2} KO sham: $n = 15$, *Bdnf*^{Pax2} KO 80 dB: $n = 15$). This indicated that control mice preferentially entered the chamber with the stranger mouse first, while *Bdnf*^{Pax2} KO mice both waited longer to enter either chamber and did not show a preference as to which chamber they entered first.

Taken together, this suggests that *Bdnf*^{Pax2} KO mice are less social and exploratory than control mice. Further, 80 dB exposure does not appear to influence social or exploratory behavior in either control or *Bdnf*^{Pax2} KO mice.

During the social experiments, so-called "autism-like" behaviors (Eckert et al., 2021) were analyzed; this consisted of freezing (used as a metric for stress) and repetitive grooming (used as a metric for stereotypic behavior). Unlike previous reports (Eckert et al., 2021), in the present study, no differences were observed in freezing behavior between the genotypes or exposure conditions (**Figure 3.30F**, Kruskal-Wallis test, $H(3) = 1.787$, $p = 0.6178$, control sham: $n = 14$, control 80 dB: $n = 15$, *Bdnf*^{Pax2} KO sham: $n = 15$, *Bdnf*^{Pax2} KO 80 dB: $n = 15$). However, *Bdnf*^{Pax2} KO mice exposed to sham or 80 dB spent significantly more time grooming than control mice exposed to sham or 80 dB, respectively. In both genotypes, this behavior was not affected by sham or 80 dB exposure (**Figure 3.30G**, Kruskal-Wallis test, $H(3) = 19.79$, $p = 0.0002$, Dunn's multiple comparisons test, control sham: $n = 14$, control 80 dB: $n = 15$, *Bdnf*^{Pax2} KO sham: $n = 15$, *Bdnf*^{Pax2} KO 80 dB: $n = 15$).

Altogether, this suggests that the central phenotype as a whole—consisting of memory, social behavior, and autism-like behaviors—is unaffected by 80 dB.

3.4.4 Summary

Taken together, these results suggest that 80 dB exposure can recover the more peripheral aspects of the phenotype of *Bdnf*^{Pax2} KO mice, such as the hearing function, but it fails to recover central processes, such as the memory and behavior. It therefore appears that 80 dB exposure is able to improve the quality of responses to sensory information in a bottom-up manner without improving the more central integration of this sensory information which would lead to an improvement in the memory and behavior.

3.5 A Note on Sex Differences

It should be noted that all experiments in the present work used both male and female mice, which is not always the case in the field of neuroscience and biomedical research, where studies using male mice outnumber those using female mice at a rate of 5.5 to 1 (Beery & Zucker, 2011). This has been justified by the assumption that, due to the estrous cycle, female animals yield more variable results than male animals (Wizemann & Pardue, 2001). The systematic exclusion of females from studies has public health implications when diseases or treatment approaches are only studied in male animals. We therefore consciously decided to analyze if sex differences exist both in untreated *Bdnf*^{Pax2} KO mice and in the effects of the two treatment approaches used—80 dB exposure and PDE9i.

3.5.1 Sex Differences in Hearing Function of Untreated *Bdnf*^{Pax2} KO Mice

Though the *Bdnf*^{Pax2} KO mouse model has been in use since at least 2012, sex differences in the phenotype have never been examined. As we propose that this mouse has a phenotype reminiscent of ASD, and ASD is four times more prevalent in males than in females (*Diagnostic and statistical manual of mental disorders (5th ed.)*, 2013; Fombonne, 2009; Werling & Geschwind, 2013), we now decided to examine whether sex differences exist in the phenotype of *Bdnf*^{Pax2} KO mice.

We therefore analyzed sex differences in each experiment detailed in the present work. However, due to the limited *n*-number per group that arose when splitting by sex, statistical power was sufficient only for hearing measurements.

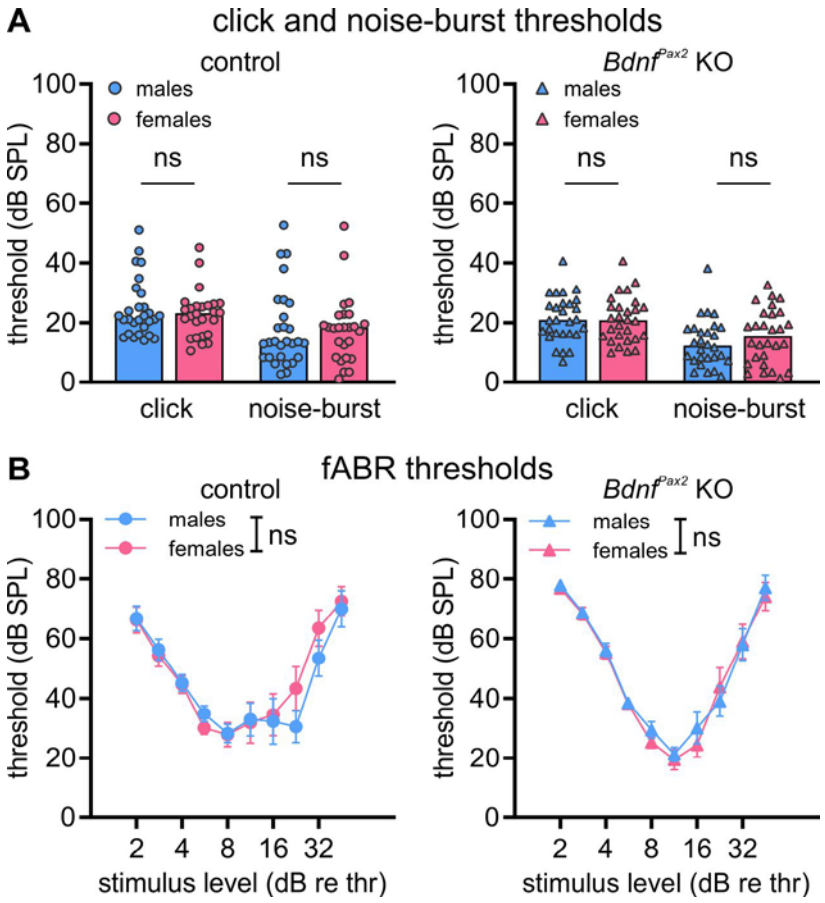

Figure 3.31. *Sex differences in hearing thresholds of untreated control and Bdnf*^{Pax2} *KO mice. **(A)** Hearing thresholds of male (blue) and female (pink) control (left, circles) and Bdnf*^{Pax2} *KO mice (right, triangles) in response to click (left) and noise-burst stimuli (right). Symbols, ears; bar, median. **(B)** Hearing thresholds of male and female control and Bdnf*^{Pax2} *KO mice in response to pure-tone stimuli. Mean ± SEM. ns = not significant.*

We first examined if untreated *Bdnf*^{Pax2} KO and control mice exhibited sex differences in their hearing thresholds. To this end, the data from **Figure 3.1B,C** were split by the sex of the mice and replotted in **Figure 3.31**. Male and female control mice did not exhibit significant differences in their hearing threshold in response to click or noise-burst stimuli (**Figure 3.31A**, left panel, click: Mann-Whitney U test, $U = 362.5$, $p = 0.9829$, males: $n = 28/14$, females: $n = 26/13$ ears/mice; noise-burst: Mann-Whitney U test, $U = 333$, $p = 0.6003$, males: $n = 28/14$, females: $n = 26/13$ ears/mice). Male and female *Bdnf*^{Pax2} KO mice also did not exhibit significant differences in their hearing threshold in response to click or noise-burst stimuli (**Figure 3.31A**, right panel, click: Mann-Whitney U test, $U = 373$, $p = 0.7636$, males: $n = 28/14$, females: $n = 28/14$ ears/mice; noise-burst: Mann-Whitney U test, $U = 328.5$, $p = 0.3026$, males: $n = 28/14$, females: $n = 28/14$ ears/mice). Accordingly, male and female control mice also did not exhibit statistically significant differences in their hearing threshold in response to pure-tone stimuli (**Figure 3.31B**, left panel, circles, 2-way ANOVA, $F(1,301) = 0.6636$, $p = 0.4159$, males: $n = 18$, females: $n = 17$ mice). Male and female *Bdnf*^{Pax2} KO mice also did not exhibit statistically significant differences in their hearing threshold in response to pure-tone stimuli (**Figure 3.31B**, right panel, triangles, 2-way ANOVA, $F(1,303) = 0.4750$, $p = 0.4912$, males: $n = 17$, females: $n = 16$ mice).

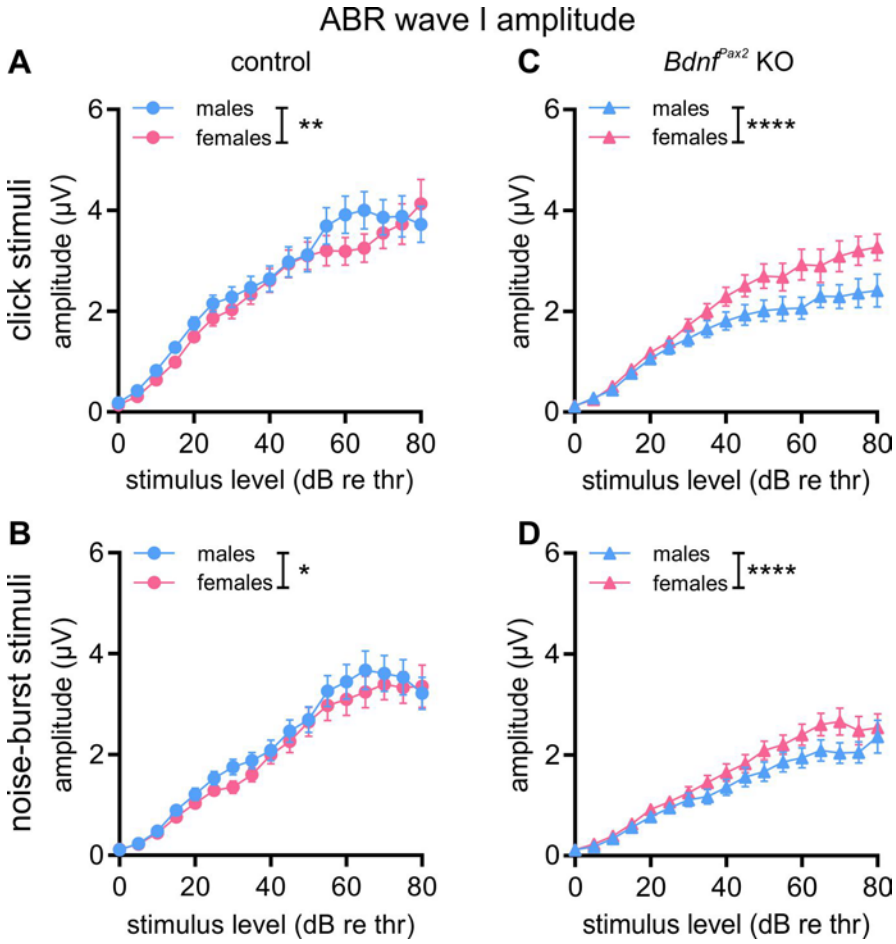

Figure 3.32. *Sex differences in ABR wave I amplitude of untreated control and Bdnf*^{Pax2} *KO mice. (**A**) ABR wave I amplitude of male (blue) and female (pink) control mice (circles) in response to click stimuli. (**B**) ABR wave I amplitude of male and female control mice in response to noise-burst stimuli. (**C**) ABR wave I amplitude of male and female Bdnf*^{Pax2} *KO mice (triangles) in response to click stimuli. (**D**) ABR wave I amplitude of male and female Bdnf*^{Pax2} *KO mice (triangles) in response to noise-burst stimuli. Mean ± SEM. * = $p < 0.05$, ** = $p < 0.01$, **** = $p < 0.0001$.*

We next analyzed whether untreated *Bdnf*^{Pax2} KO and control mice exhibited sex differences in their ABR wave I amplitude by splitting the data from **Figure 3.1E** by the sex of the mice and replotting them in **Figure 3.32**. Male control mice exhibited a slightly but significantly higher ABR wave I amplitude in comparison to female control mice in response to click and noise-burst stimuli (**Figure 3.32A,B**, click: 2-way ANOVA, $F(1,809) = 7.060$, $p = 0.0080$, males: $n = 28/14$, females: $n = 30/15$

ears/mice; noise-burst: 2-way ANOVA, $F(1,809) = 5.523$, $p = 0.019$, males: $n = 28/14$, females: $n = 30/15$ ears/mice). However, male *Bdnf*^{Pax2} KO mice exhibited a significantly lower ABR wave I amplitude in comparison to female *Bdnf*^{Pax2} KO mice in response to both click and noise-burst stimuli (**Figure 3.32C,D**, click: 2-way ANOVA, $F(1,914) = 33.25$, $p < 0.0001$, males: $n = 28/14$, females: $n = 34/17$ ears/mice; noise-burst: 2-way ANOVA, $F(1,884) = 18.99$, $p < 0.0001$, males: $n = 28/14$, females: $n = 34/17$ ears/mice).

To determine if the sex differences observed in ABR wave I were also reflected in the activity of structures higher in the auditory system, we analyzed the ABR wave IV amplitude by splitting the data from **Figure 3.1F** by the sex of the mice and replotting them in **Figure 3.33**. In their ABR wave IV, untreated male controls actually exhibited a slightly but significantly lower amplitude in comparison to female controls in response to click and noise-burst stimuli (**Figure 3.33A,B**, click: 2-way ANOVA, $F(1,818) = 7.495$, $p = 0.0063$, males: $n = 28/14$, females: $n = 30/15$ ears/mice; noise-burst: 2-way ANOVA, $F(1,791) = 7.039$, $p = 0.0081$, males: $n = 28/14$, females: $n = 30/15$ ears/mice). On the other hand, untreated male *Bdnf*^{Pax2} KO mice exhibited significantly lower ABR wave IV amplitude in comparison to female *Bdnf*^{Pax2} KO mice in response to click and noise-burst stimuli (**Figure 3.33C,D**, click: 2-way ANOVA, $F(1,872) = 47.18$, $p < 0.0001$, males: $n = 28/14$, females: $n = 34/17$ ears/mice; noise-burst: 2-way ANOVA, $F(1,888) = 27.74$, $p < 0.0001$, males: $n = 28/14$, females: $n = 34/17$ ears/mice).

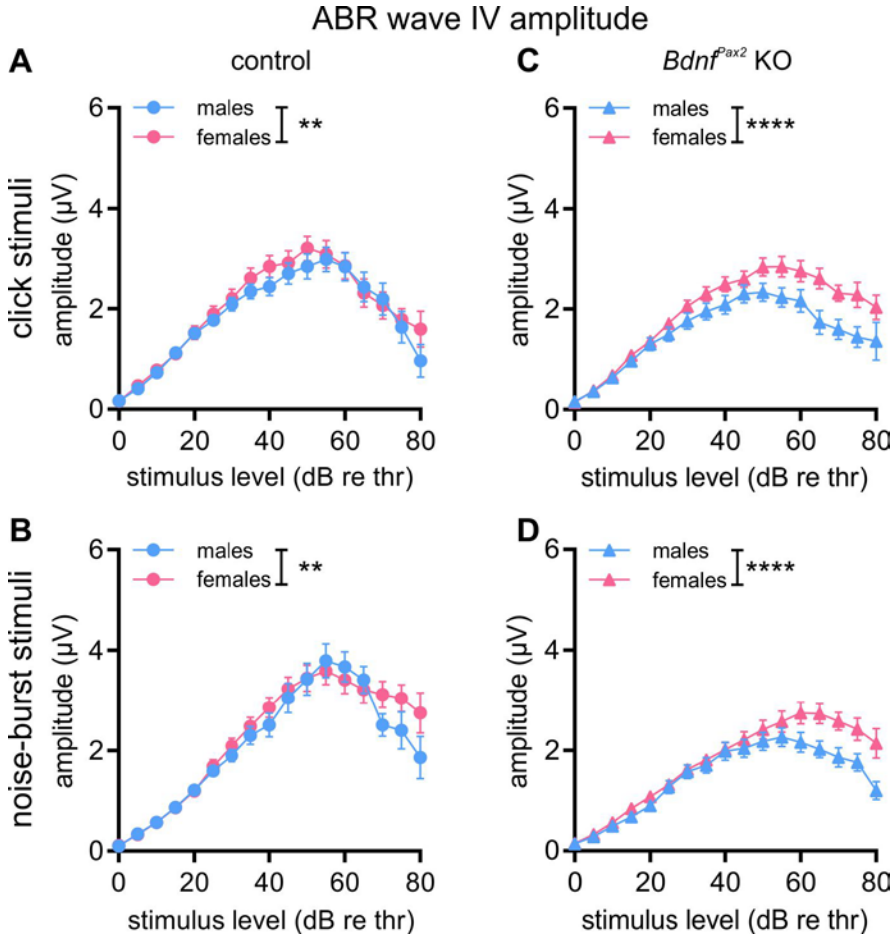

Figure 3.33. *Sex differences in ABR wave IV amplitude of untreated control and Bdnf*^{Pax2} *KO mice. (**A**) ABR wave IV amplitude of male (blue) and female (pink) control mice (circles) in response to click stimuli. (**B**) ABR wave IV amplitude of male and female control mice in response to noise-burst stimuli. (**C**) ABR wave IV amplitude of male and female Bdnf*^{Pax2} *KO mice (triangles) in response to click stimuli. (**D**) ABR wave IV amplitude of male and female Bdnf*^{Pax2} *KO mice (triangles) in response to noise-burst stimuli. Mean ± SEM. ** = p < 0.01, **** = p < 0.0001.*

Finally, to determine if the sex differences in the ABR wave amplitudes also affect the processing of more complex stimuli (i.e., amplitude-modulated stimuli), we analyzed the ASSRs of untreated mice by splitting the data from **Figure 3.1H,I** by the sex of the mice and replotting them in **Figure 3.34**. Male control mice did not significantly differ from female control mice in their modulation growth function but showed a slightly lower SNR in their modulation depth function (**Figure 3.34A,B**, modulation growth: 2-way ANOVA, $F(1,217) = 2.951$, $p = 0.0873$, males: $n = 9$, females: $n = 10$ mice; modulation depth: 2-way ANOVA, $F(1,221) = 6.078$, $p = 0.0145$, males: $n = 9$, females: $n = 10$ mice). In contrast, male *Bdnf*^{Pax2} KO mice had a significantly lower SNR in comparison to female *Bdnf*^{Pax2} KO mice in their modulation growth and modulation depth functions (**Figure 3.34C,D**, modulation growth: 2-way ANOVA, $F(1,247) = 13.36$, $p = 0.0003$, males: $n = 10$, females: $n = 11$ mice; modulation depth: 2-way ANOVA, $F(1,221) = 6.425$, $p = 0.0119$, males: $n = 9$, females: $n = 10$ mice).

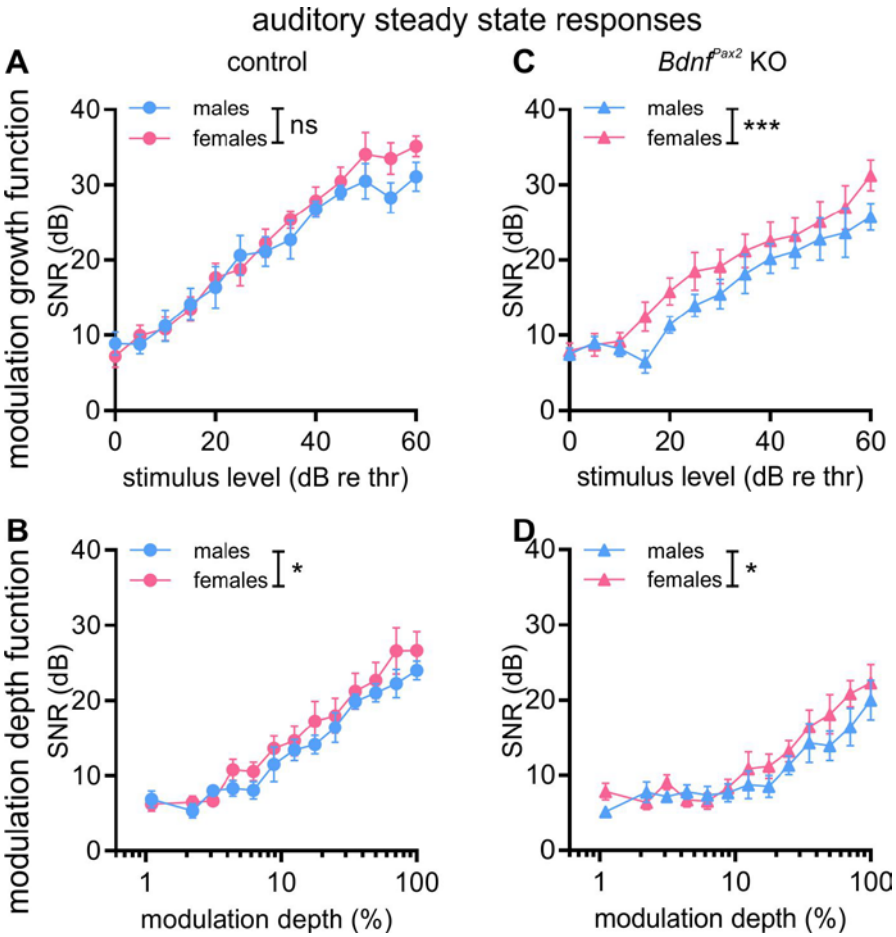

Figure 3.34. *Sex differences in ASSRs of untreated control and Bdnf*^{Pax2} *KO mice. (**A**) Modulation growth function of male (blue) and female (pink) control mice (circles). (**B**) Modulation depth function of male and female control mice. (**C**) Modulation growth function of male and female Bdnf*^{Pax2} *KO mice (triangles). (**D**) Modulation depth function of male and female Bdnf*^{Pax2} *KO mice. Mean ± SEM. * = p < 0.05, *** = p < 0.001, ns = not significant.*

Taken together, despite the minor differences between male and female control mice, the small magnitude of these differences and the fact that they are not consistent suggests that control mice do not have any meaningful sex differences in their hearing function. On the other hand, male *Bdnf*^{Pax2} KO mice may have a more severe phenotype than females, reflected in lower amplitude ABR waves and poorer temporal sound coding, which is reminiscent of the higher rate of ASD diagnosis in males compared to females.

3.5.2 Sex Differences in Hearing Function after PDE9i Treatment

Whether sex differences exist in the response to treatment with the specific PDE9i used in the present work—BAY 73-6691—has never been examined. Of all the animal studies published thus far that used

BAY 73-6691, ten used exclusively male animals (Almeida et al., 2012; Chen et al., 2024; da Silva et al., 2013; Kroker et al., 2014; Kroker et al., 2012; Li et al., 2016; Liddie et al., 2012; Orru et al., 2013; Prieto et al., 2017; van der Staay et al., 2008), two used exclusively female animals and were specifically studying the development of oocytes (Hanna et al., 2012; Li et al., 2020), one did not report the sex of the animals used (Tajima et al., 2018), and only one study (from our own lab) used both male and female animals but did not analyze for sex differences (Savitska et al., 2022). This underrepresentation of females in early-stage drug development and testing is a critical oversight in the field of pharmaceutical research at large and poses a threat to women's health when considering that, for example, pharmacokinetics and pharmacodynamics can differ in females, thus affecting a drug's efficacy and toxicity (Zucker et al., 2022).

Therefore, although it was outside of the scope of the original study, we analyzed whether there was a sex-dependent effect of PDE9i treatment in control and *Bdnf*^{Pax2} KO mice. Unfortunately, due to the limited *n*-number that arose when splitting treatment groups by sex, statistical power was sufficient only for ABR measurements.

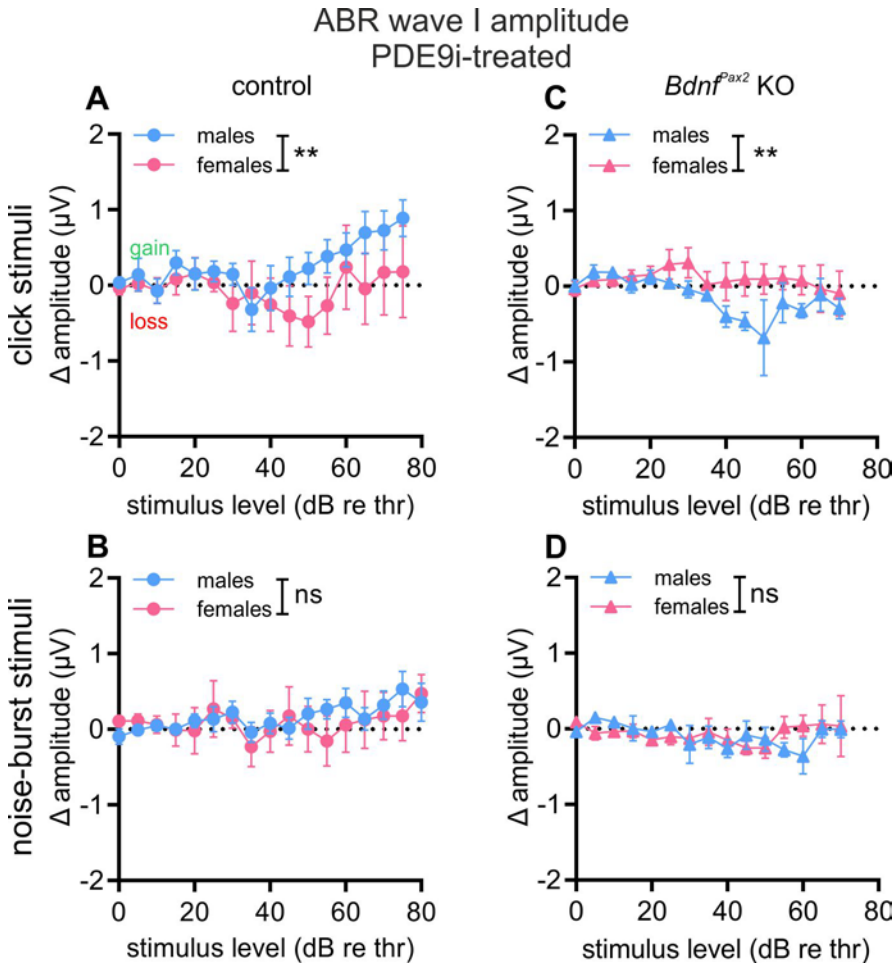

Figure 3.35. *Sex differences in ABR wave I after PDE9i treatment. (**A**) ABR wave I amplitude delta of male (blue) and female (pink) control mice (circles) in response to click stimuli. (**B**) ABR wave I amplitude delta of male and female control mice in response to noise-burst stimuli. (**C**) ABR wave I amplitude delta of male and female Bdnf*^{Pax2} *KO mice (triangles) in response to click stimuli. (**D**) ABR wave I amplitude delta of male and female Bdnf*^{Pax2} *KO mice in response to noise-burst stimuli. Mean ± SEM. ** = $p < 0.01$, ns = not significant.*

ABR wave I amplitude delta was analyzed for sex differences by splitting the data from **Figure 3.13** by the sex of the mice and replotting them in **Figure 3.35**. Surprisingly, male control mice exhibited a significantly higher ABR wave I amplitude delta in comparison to female control mice in response to click but not noise-burst stimuli (**Figure 3.35A,B**, click: 2-way ANOVA, $F(1,159) = 7.826$, $p = 0.0058$, males: $n = 8/4$, females: $n = 6/3$ ears/mice; noise-burst: 2-way ANOVA, $F(1,167) = 0.8150$, $p = 0.3679$,

males: $n = 8/4$, females: $n = 6/3$ ears/mice). Conversely, male *Bdnf*^{Pax2} KO mice exhibited a significantly lower ABR wave I amplitude delta in comparison to female *Bdnf*^{Pax2} KO mice in response to click but not noise-burst stimuli (**Figure 3.35C,D**, click: 2-way ANOVA, $F(1,127) = 7.846$, $p = 0.0059$, males: $n = 4/2$, females: $n = 8/4$ ears/mice; noise-burst: 2-way ANOVA, $F(1,130) = 0.0623$, $p = 0.8032$, males: $n = 4/2$, females: $n = 8/4$ ears/mice). This suggests that the PDE9i may have more pronounced positive effects in male controls and negative effects in male *Bdnf*^{Pax2} KO mice that were masked when the sexes were pooled (**Figure 3.13**).

In order to determine if this sex-dependent effect holds true for the activity in higher order structures along the auditory pathway, the ABR wave IV amplitude delta was analyzed for sex differences by splitting the data from **Figure 3.14** by the sex of the mice and replotting them in **Figure 3.36**. Male control mice again exhibited a significantly higher ABR wave IV amplitude delta in comparison to female control mice in response to click stimuli and a non-significant trend towards a higher delta in response to noise-burst stimuli (**Figure 3.36A,B**, click: 2-way ANOVA, $F(1,152) = 13.38$, $p = 0.0003$, males: $n = 8/4$, females: $n = 6/3$ ears/mice; noise-burst: 2-way ANOVA, $F(1,155) = 3.818$, $p = 0.0525$, males: $n = 8/4$, females: $n = 6/3$ ears/mice). In contrast, male *Bdnf*^{Pax2} KO mice again had a significantly lower ABR wave IV amplitude delta in comparison to female *Bdnf*^{Pax2} KO mice in response to click but not noise-burst stimuli (**Figure 3.36C,D**, click: 2-way ANOVA, $F(1,121) = 6.804$, $p = 0.0102$, males: $n = 4/2$, females: $n = 8/4$ ears/mice; noise-burst: 2-way ANOVA, $F(1,145) = 1.950$, $p = 0.1647$, males: $n = 4/2$, females: $n = 8/4$ ears/mice).

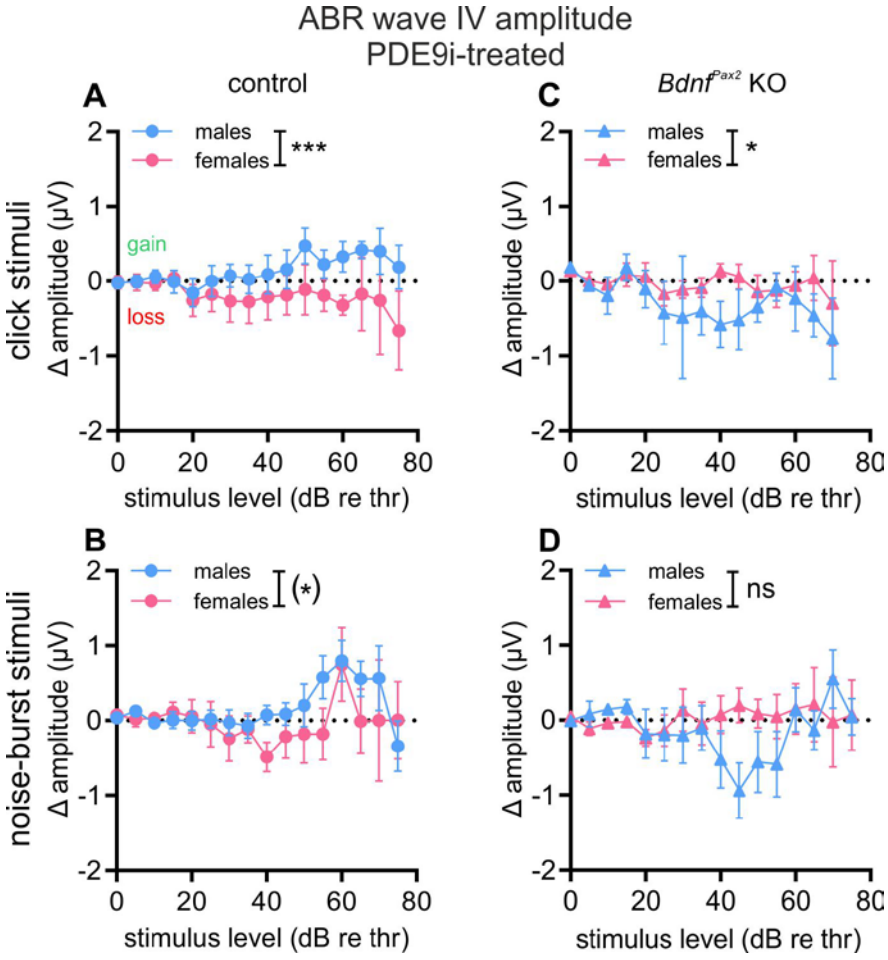

Figure 3.36. *Sex differences in ABR wave IV after PDE9i treatment. (**A**) ABR wave IV amplitude delta of male (blue) and female (pink) control mice (circles) in response to click stimuli. (**B**) ABR wave IV amplitude delta of male and female control mice in response to noise-burst stimuli. (**C**) ABR wave IV amplitude delta of male and female Bdnf*^{Pax2} *KO mice (triangles) in response to click stimuli. (**D**) ABR wave IV amplitude delta of male and female Bdnf*^{Pax2} *KO mice in response to noise-burst stimuli. Mean ± SEM. (*) = p < 0.08, * = p < 0.05, ** = p < 0.01, ns = not significant.*

Taken together, these results suggest that the PDE9i has a significantly more pronounced effect on males in comparison to females. Interestingly, this holds true for both the beneficial effect in the control mice and the adverse effect in *Bdnf*^{Pax2} KO mice.

3.5.3 Sex Differences in Hearing Function after 80 dB Exposure

80 dB exposure was used in a previous study from our lab that used both male and female mice but did not examine sex differences (Matt et al., 2018). Here, we also analyzed for sex-dependent effects of 80 dB exposure in control and *Bdnf*^{Pax2} KO mice. Similar to the PDE9i, this analysis was outside of the scope of the original study, leading to a limited *n*-number when splitting exposure groups by sex. Thus, statistical power was sufficient only for ABR measurements.

ABR wave I amplitude delta was analyzed for sex differences by splitting the data from **Figure 3.23** by the sex of the mice and replotting them in **Figure 3.37**. Male and female control mice did not differ in their ABR wave I amplitude delta in response to click or noise-burst stimuli (**Figure 3.37A,B**, click: 2-way ANOVA, $F(1,327) = 0.3299$, $p = 0.5661$, males: $n = 14/7$, females: $n = 14/7$ ears/mice; noise-burst: 2-way ANOVA, $F(1,334) = 0.0097$, $p = 0.9217$, males: $n = 14/7$, females: $n = 14/7$ ears/mice). Similarly, male and female *Bdnf*^{Pax2} KO mice did not differ in their ABR wave I amplitude delta in response to click or noise-burst stimuli (**Figure 3.37C,D**, click: 2-way ANOVA, $F(1,403) = 0.5290$, $p = 0.4675$, males: $n = 16/8$, females: $n = 16/8$ ears/mice; noise-burst: 2-way ANOVA, $F(1,390) = 0.5351$, $p = 0.4649$, males: $n = 16/8$, females: $n = 16/8$ ears/mice).

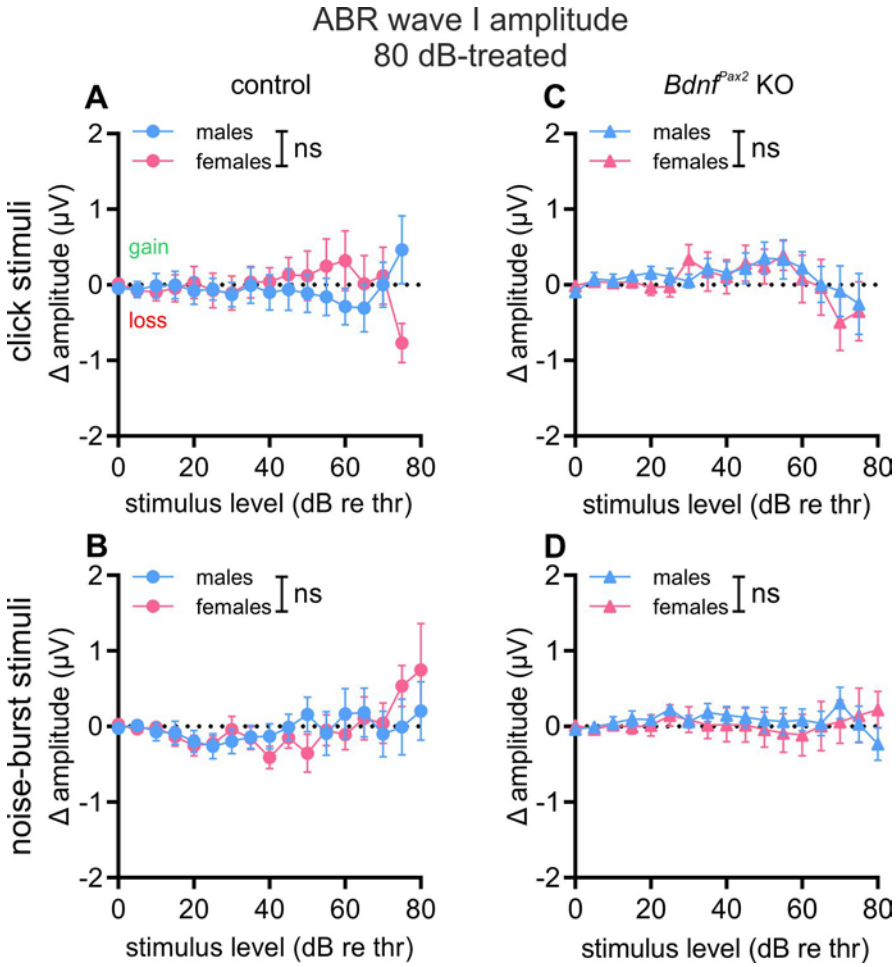

Figure 3.37. *Sex differences in ABR wave I after 80 dB exposure. (**A**) ABR wave I amplitude delta of male (blue) and female (pink) control mice (circles) in response to click stimuli. (**B**) ABR wave I amplitude delta of male and female control mice in response to noise-burst stimuli. (**C**) ABR wave I amplitude delta of male and female Bdnf*^{Pax2} *KO mice (triangles) in response to click stimuli. (**D**) ABR wave I amplitude delta of male and female Bdnf*^{Pax2} *KO mice in response to noise-burst stimuli. Mean ± SEM. ns = not significant.*

To determine if that also held true for ABR wave IV, the amplitude delta data from **Figure 3.24** was split by the sex of the mice and replotted in **Figure 3.38**. Indeed, male and female control mice did not differ in their ABR wave IV amplitude delta in response to click or noise-burst stimuli (**Figure 3.38A,B**, click: 2-way ANOVA, $F(1,326) = 1.719$, $p = 0.1907$, males: $n = 14/7$, females: $n = 14/7$ ears/mice; noise-burst: 2-way ANOVA, $F(1,312) = 0.2543$, $p = 0.6144$, males: $n = 14/7$, females: $n = 14/7$ ears/mice). However, male *Bdnf*^{Pax2} KO mice exhibited a slightly higher ABR wave IV amplitude delta compared to females in response to click but not noise-burst stimuli (**Figure 3.38C,D**, click: 2-way ANOVA, $F(1,382) = 5.944$, $p = 0.0152$, males: $n = 16/8$, females: $n = 16/8$ ears/mice; noise-burst: 2-way ANOVA, $F(1,396) = 0.7527$, $p = 0.2861$, males: $n = 16/8$, females: $n = 16/8$ ears/mice).

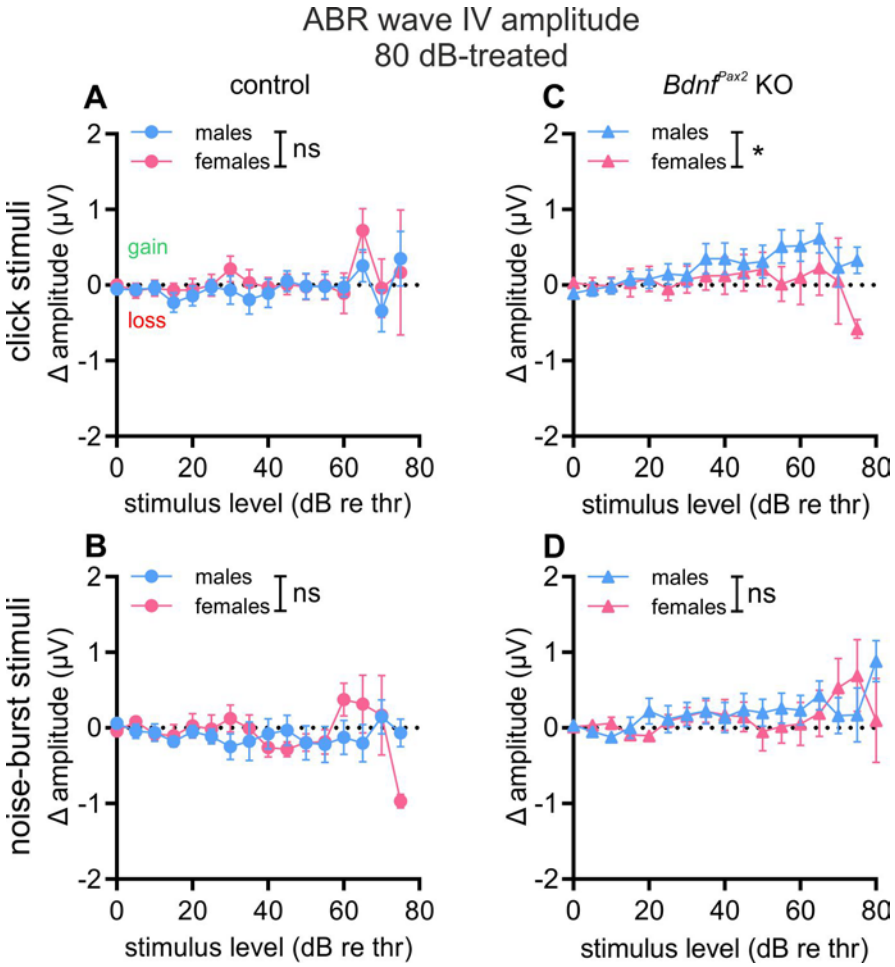

Figure 3.38. *Sex differences in ABR wave IV after 80 dB exposure. (**A**) ABR wave I amplitude delta of male (blue) and female (pink) control mice (circles) in response to click stimuli. (**B**) ABR wave IV amplitude delta of male and female control mice in response to noise-burst stimuli. (**C**) ABR wave IV amplitude delta of male and female Bdnf*^{Pax2} *KO mice (triangles) in response to click stimuli. (**D**) ABR wave IV amplitude delta of male and female Bdnf*^{Pax2} *KO mice in response to noise-burst stimuli. Mean ± SEM. * = $p < 0.05$, ns = not significant.*

Overall, these results suggest that the response to 80 dB exposure does not profoundly differ between male and female control or *Bdnf*^{Pax2} KO mice.

3.5.4 Summary

In conclusion, we could show that male *Bdnf*^{Pax2} KO mice have a more pronounced phenotype—at least for hearing measures—in comparison to female *Bdnf*^{Pax2} KO mice. While the effects of 80 dB exposure did not differ between the sexes in controls or *Bdnf*^{Pax2} KO mice, these results indicate that the PDE9i used in this study may only affect males, both positively in control mice and negatively in *Bdnf*^{Pax2} KO mice. Despite a very limited *n*-number leading to the inability to statistically analyze most of the data for sex differences, the results obtained from hearing measurements nevertheless provide an important starting point that may allow for more in-depth research about this in the future.

4 DISCUSSION

In this work, we proposed a model in which ASD symptoms could result from a stunted development in the peripheral auditory system that propagates along the ascending pathway and leaves the entire system in an immature state, affecting sensory integration and subsequent higher-level, cognitive processes (see section 1.3.2). After confirming a central ASD phenotype in the *Bdnf*^{Pax2} KO mouse model (section 3.1), we found evidence that their specific phenotype may originate from a persisting immaturity of high-SR fibers, possibly due to insufficient shaping by efferents during development (section 3.2). This discovery has wider-reaching implications for the field of developmental disorders, suggesting that immaturity of a peripheral structure alone can have effects that cascade up the system and end up affecting central processes.

We subsequently used two complementary treatment approaches to examine whether these processes could be recovered in adult mice: a top-down pharmaceutical approach that primarily targeted the cognitive phenotype (PDE9i, section 3.3) and a bottom-up enrichment approach that primarily targeted the peripheral sensory deficits (80 dB, section 3.4). While the PDE9i had a small adverse effect on the hearing function of *Bdnf*^{Pax2} KO mice that was more pronounced in males (section 3.5), 80 dB was able to bring their hearing phenotype closer to the physiological state. Nevertheless, neither treatment approach was able to recover cognitive aspects of the phenotype, perhaps suggesting that while the peripheral deficits that give rise to the central phenotype can be recovered in adulthood, the central phenotype itself cannot be. This necessitates an early intervention strategy targeting the original peripheral deficits in developmental disorders such as ASD.

4.1 CENTRAL PHENOTYPE OF *BDNF*^{PAX2} KO MICE IS CONSISTENT WITH ASD

It was previously shown that *Bdnf*^{Pax2} KO mice exhibit some characteristics consistent with an ASD phenotype (Eckert et al., 2021). This initial observation was quite surprising given the fact that no gene known to be associated with ASD was deleted in this model. In this work, we therefore aimed to extend that line of questioning to determine whether the *Bdnf*^{Pax2} KO mouse model could be useful to later study a possible novel pathogenic mechanism underlying ASD. An ASD phenotype in *Bdnf*^{Pax2} KO mice was determined by combining previous work (Eckert et al., 2021) with the present study, allowing us to recapitulate many aspects of an ASD phenotype in this model, including the core features, several associated symptoms, a similar hearing phenotype, and finally a common dysfunction of the neural circuitry.

The initial observation of disinterested social behavior in *Bdnf*^{Pax2} KO mice—one of the two core symptoms of ASD (*Diagnostic and statistical manual of mental disorders (5th ed.)*, 2013)—prompted us to examine this phenotype in more depth (Eckert et al., 2021). In the present study, we replicated these findings, demonstrating that *Bdnf*^{Pax2} KO mice spent less time interacting with other mice in comparison to controls (**Figure 3.30**). The second core symptom of ASD, restricted or repetitive behavior patterns (*Diagnostic and statistical manual of mental disorders (5th ed.)*, 2013), was also first observed by Eckert et al. (2021) and replicated here, in which *Bdnf*^{Pax2} KO mice spent significantly more time repetitively grooming themselves in comparison to controls (**Figure 3.30**).

In addition, both Eckert et al. (2021) and the present work documented several associated features of ASD in *Bdnf*^{Pax2} KO mice, including learning and memory deficits and anxiety. In the present study, learning and memory deficits were seen in a new context. Previously, Eckert et al. (2021) used a multiple-T maze to demonstrate that *Bdnf*^{Pax2} KO mice had deficits in spatial learning. In the present study, however, we could show that *Bdnf*^{Pax2} KO mice had learning and memory deficits independent of spatial navigation by using the novel object recognition test. In this test, *Bdnf*^{Pax2} KO mice did not display the typical preference for the novel object in comparison to the familiar one they had interacted

with the day before (**Figure 3.26**), indicating that they had deficits in either learning the object or retrieving the memory of it. Furthermore, their abnormal LTP levels confirmed that this behavioral result was due to learning/memory deficits as opposed to lack of intrinsic motivation (**Figure 3.29**).

It is only with these more recent observations of the behavioral phenotype in *Bdnf*^{Pax2} KO mice that we can view their hearing phenotype in a new light. Because *Bdnf*^{Pax2} KO mice were originally generated to study the effect of BDNF in the adult auditory system, their hearing phenotype has been extensively described in several publications (Chumak et al., 2016; Eckert et al., 2021; Zuccotti et al., 2012). Replicating the results from those publications, we here showed that *Bdnf*^{Pax2} KO mice had normal hearing sensitivity (i.e., thresholds) but impaired sound processing along the ascending auditory pathway, starting at the level of the auditory nerve (**Figure 3.1**). Further, *Bdnf*^{Pax2} KO mice exhibited smaller ASSRs, indicating a deficit in temporal sound coding (**Figure 3.1**). This phenotype is generally consistent with ASD patients and associated animal models, which have, on the whole, normal hearing thresholds but lower amplitude and slower ABR waves and auditory processing disorders (Ocak et al., 2018; Wilde et al., 2022).

In the present work we could also measure the cortical response to acoustic stimuli for the first time by measuring the LFP through EEG. We found that *Bdnf*^{Pax2} KO mice had lower evoked activity (phase-locked to stimulus, reflecting bottom-up sensory processing) that was partially accompanied by increased induced activity (not phase-locked to stimulus, reflecting integration of sensory input with ongoing activity; **Figure 3.5**). The same pattern of decreased evoked activity and increased induced activity was observed in patients with Fragile X syndrome, the leading monogenic cause of ASD (e.g., Ethridge et al., 2017; Wang et al., 2017), and associated mouse models (e.g., Holley et al., 2022; Jonak et al., 2020; Lovelace et al., 2018).

However, while the hearing phenotype in *Bdnf*^{Pax2} KO mice indeed replicates *some* observations in other ASD models, it is important to note that the neural responses to acoustic stimuli in both patients with ASD and associated mouse models are extremely variable (Wilde et al., 2022). For example, while several studies using the mouse model for Fragile X syndrome reported lower stimulus-evoked LFPs, as described above, other studies using different ASD mouse models conversely reported unchanged or even higher stimulus-evoked LFPs (e.g., Barnes et al., 2015; Engineer et al., 2015; Jonak et al., 2020). The same is true for the activity in specific oscillatory frequency bands (e.g., Barnes et al., 2015; Goffin et al., 2011; Jonak et al., 2020) and even ABR wave amplitudes and latencies (e.g., Rotschafer et al., 2015; Scott et al., 2018). This heterogeneity in auditory responses is extensively reviewed by Wilde et al. (2022), but it is not entirely surprising. Because ASD is diagnosed solely on the basis of behavioral symptoms with no universal biological marker, it is an inherently diverse disorder. Furthermore, because the underlying neural circuitry changes that contribute to ASD (e.g., PV-IN dysfunction) occur very early in development, this may allow the brain to develop various compensation mechanisms to attempt to overcome or bypass these changes. Thus, individual differences in how the brain tries to compensate could lead to variability in neural responses across different models and patients.

Despite the variability in some aspects of ASD, other aspects are broadly overlapping. One such aspect that has been extremely well-documented in both ASD patients and associated animal models is a circuit-specific imbalance of excitatory and inhibitory neural activity, primarily resulting from decreased PV-IN expression or function (Contractor et al., 2021). In *Bdnf*^{Pax2} KO mice, this was first observed by Eckert et al. (2021), who found lower PV expression levels in the AC and hippocampus, accompanied by higher expression levels of excitatory molecular markers. The present work was able to confirm those hints of an E/I imbalance on a functional level by recording the spontaneous LFP in the AC, which revealed a higher baseline neural activity in *Bdnf*^{Pax2} KO mice (**Figure 3.3**). Notably, Eckert et al. (2021) found that this E/I imbalance was specific to the auditory system, as they observed normal PV expression levels in the somatosensory cortex and also in the cerebellum, where *Bdnf* is deleted in *Pax2*-expressing cells (Eckert et al., 2021; Rowitch et al., 1999). This suggests that the PV

expression level changes in the hippocampus and AC, and by extension the E/I imbalance there, are not a direct result of the deletion, but rather a secondary effect, supporting the hypothesis of a persisting immaturity in the periphery that cascades along the ascending pathway, as proposed in section 1.3.2.

In addition to phenotypic observations in *Bdnf*^{Pax2} KO mice, we also noted that at least the hearing phenotype was more severe in males (**Figure 3.31–34**), perhaps consistent with the four times higher prevalence of the disorder in human males as compared to females (*Diagnostic and statistical manual of mental disorders (5th ed.)*, 2013). While this was observed in the hearing phenotype of *Bdnf*^{Pax2} KO mice, the behavioral and EEG data could not be statistically analyzed for sex differences due to a limited *n*-number arising when splitting the groups by sex. However, this would be an interesting avenue to pursue in future work.

Given the fact that *Bdnf*^{Pax2} KO mice exhibit both core symptoms of ASD, several associated symptoms, and an underlying dysfunction in neural circuitry strongly implicated in ASD patients and mouse models, we can conclude that this model is indeed useful in studying ASD. This then led us to ask where and how this ASD phenotype arose in *Bdnf*^{Pax2} KO mice.

4.2 ASD Phenotype in *Bdnf*^{Pax2} KO Mice Originates from Periphery

Because no genes known to be associated with ASD were deleted in *Bdnf*^{Pax2} KO mice, and the deletion of *Bdnf* was carried out primarily in the auditory periphery, we hypothesized that the immaturity in the auditory periphery cascaded along ascending pathways and prevented central processes from following their normal developmental trajectory, eventually resulting in an ASD phenotype (see section 1.3.2). To gain an initial insight into this, we measured the ASSR in response to amplitude-modulated tones in the AC, reflecting the summed activity of structures along the ascending pathway. By varying the modulation frequency, we were able to disseminate responses generated primarily by cortical structures (in response to lower modulation frequencies) from responses generated primarily by subcortical structures (in response to higher modulation frequencies; Lu et al., 2022). We were thereby able to determine that *Bdnf*^{Pax2} KO mice had a deficit in their subcortical responses that was amplified in their cortical responses (**Figure 3.7**).

Since it has been shown many times that *Bdnf*^{Pax2} KO mice exhibit deficits in response to acoustic stimuli throughout the ascending pathway, it was hypothesized that this could be driven by the first dysfunctional structure in the pathway. Specifically, the lower ABR wave I amplitude in *Bdnf*^{Pax2} KO mice indicated deficits at the first synapse of the system (**Figure 3.1**). We therefore measured the CAP to assess the auditory nerve activity more specifically, and we confirmed a profound deficit in the auditory nerve function of *Bdnf*^{Pax2} KO mice (**Figure 3.8**). To determine if a specific class of auditory nerve fibers contributed to its overall response deficit, we measured the PSTR in *Bdnf*^{Pax2} KO mice. The results indicated that *Bdnf*^{Pax2} KO mice had a specific deficit in high-SR fibers (**Figure 3.9**), the class of fibers that contributes to high temporal resolution by coding the onset of stimuli (Bharadwaj et al., 2014), possibly driving temporal sound coding deficits later in the ascending pathway, as observed in the ASSR (**Figure 3.1**, **Figure 3.7**).

The differentiation of low-SR fibers from high-SR fibers was previously shown to be dependent on spontaneous activity of the IHC prior to hearing onset (Shrestha et al., 2018), while the mature firing characteristics of high-SR fibers emerged only with sensory experience (Grant et al., 2010). This suggests that high-SR fiber maturation is dependent upon activity both before and after hearing onset in a process that may be mediated by efferent fiber activity. MOC efferents form a transient synapse with IHCs prior to hearing onset, modulating their activity until P12 (Bulankina & Moser, 2012; Glowatzki & Fuchs, 2000). To examine whether aberrant MOC efferent activity could have contributed to the deficits in high-SR fiber responses, we measured the MOC efferent-mediated suppression of OHC activity and found that *Bdnf*^{Pax2} KO mice had significantly weaker MOC activity in comparison to

controls (**Figure 3.10**), perhaps indicating an overall weaker efferent system that may have prevented proper maturation of high-SR fibers.

Taken together, this suggests that the ASD phenotype in *Bdnf*^{Pax2} KO mice is driven by impaired activity in the periphery that cascades along the ascending pathway. Specifically, we speculate that insufficient inhibitory feedback from efferents prior to hearing onset leads to a persisting immaturity of high-SR fibers, which results in their under-responsiveness. This would not only affect the hearing function of *Bdnf*^{Pax2} KO mice, but also the maturation of their ascending pathway in general, eventually leading to more central and cognitive deficits.

This cascading mechanism may also be an underlying cause of ASD phenotypes in other models. While it has long been thought that disorders affecting cognitive processes, such as ASD, result from deficits in the central nervous system, it is still unclear when and how such a dysfunction would occur. It was previously proposed that all or most instances of ASD could be explained by an underlying dysfunction of PV-INs (Contractor et al., 2021), but the present results demonstrated that a peripheral sensory dysfunction can lead to at least two of the central PV-IN changes that were proposed as evidence for this hypothesis. In particular, *Bdnf*^{Pax2} KO mice exhibited (1) less PV expression in the cortex (Eckert et al., 2021) and hippocampus (**Figure 3.2**) and (2) higher spontaneous gamma activity (**Figure 3.3**). These observations suggest that PV-IN dysfunction, previously proposed to be an underlying neural mechanism of ASD, may instead be a secondary result of an underlying peripheral immaturity.

There is also evidence that this model may not be exclusive to a maturational disruption of a structure in the auditory system. In the somatosensory system it has also been shown that decreased activity in a specific fiber class from early in development leads to an ASD phenotype (Huzard et al., 2022). The fact that a similar observation has been made in another sensory system indeed supports the model that development of primary sensory processing is a prerequisite for development of higher-level integrative and cognitive processes, and a lack thereof may lead to wider-reaching developmental disorders. However, while this data does show an association between a peripheral immaturity and the development of an ASD phenotype, at the moment these results are still correlational and must therefore be validated in other models.

The ideal model to test if peripheral developmental deficits are causally linked to ASD would be one in which a gene specific to high-SR fibers that enables their function is knocked out early in development, but this may not be technically possible. Genes that are differentially expressed in high- and low-SR fibers later in development (P25–27), are more ubiquitously expressed early on (P0.5; Shrestha et al., 2018). Thus, deleting one of these genes would have to be under tight temporal control—early enough that high-SR fibers do not develop but late enough that low-SR fibers are not affected. Another complication arises when considering that the identified differentially expressed genes (Shrestha et al., 2018) are not necessarily restricted to the cochlea, so their deletion may also lead to unintended consequences. Thus, finding a specific marker that will enable a genetic ablation of high-SR fiber function remains a challenge.

To validate our model then, we need another, more subtle approach. One option could be to perturb either the generation or the shaping of IHC-afferent synapse activity, which is mediated by supporting cells and efferent fibers, respectively (Glowatzki & Fuchs, 2000; Tritsch et al., 2007). In fact, mutant mice with disrupted spontaneous IHC activity (Kersbergen et al., 2022; Tritsch et al., 2007) and mutant mice without functional synapses between efferents and hair cells (Clause et al., 2017; Lauer & May, 2011) were both shown to have hearing phenotypes similar to that of *Bdnf*^{Pax2} KO mice, exhibiting coarser responses to acoustic stimuli and disruptions in temporal sound coding. Both of these genetic modifications may have specifically affected the high-SR fibers as a secondary effect, since activity before and after hearing onset drives their differentiation and the emergence of their mature firing characteristics (Grant et al., 2010; Shrestha et al., 2018). Thus, in light of the results from the present

work, it would be interesting to examine whether either of these mutant mice have a behavioral phenotype consistent with ASD.

4.3 PDE9I CANNOT RECOVER ASD PHENOTYPE IN *BDNF*^{Pax2} KO MICE

In *Bdnf*^{Pax2} KO mice, the more peripheral hearing deficits seemed to accumulate and lead to a profound deficit in central responses (**Figure 3.7**) as well as a cognitive phenotype consistent with ASD. Therefore, a more central, pharmaceutical approach—PDE9i treatment—was used to specifically target the cognitive aspects of the phenotype. PDE9 inhibitors, which increase cGMP levels by inhibiting the enzyme that degrades it, have been regarded as "cognitive stimulators" for their ability to improve learning and memory function (Hutson et al., 2011; Kroker et al., 2014; Kroker et al., 2012; Rosenbrock et al., 2019; van der Staay et al., 2008). Further, PDE9i treatment was recently shown to improve social interaction deficits in a mouse model of ASD (Scarborough et al., 2021).

In control mice, a ten-day injection with both the PDE9i and a vehicle resulted in increased corticosterone levels, indicating that it was a stressful event. This phenomenon was previously observed in a cohort of older mice, where their high stress levels also led to poorer hearing and memory function—a loss that was prevented by PDE9i treatment (Savitska et al., 2022). In the present study, which used a much younger cohort of mice, the injection stress led to a slight elevation of hearing thresholds that could be rescued by PDE9i treatment (**Figure 3.12**). However, other measures of hearing function (ABR wave amplitudes; **Figure 3.13**, **Figure 3.14**) and memory function (LTP; **Figure 3.17**) did not react to the stressful injection. This suggests that the cohort of young mice used in the present study was relatively resilient to stress. Surprisingly, however, control mice also did not greatly benefit from PDE9i treatment, exhibiting only slightly higher LTP levels but no change in ABR wave amplitudes. It was previously suggested by Savitska et al. (2022) that the PDE9i is preventative; thus, it may be the case that in young mice there is simply no loss to prevent.

However, there are indications that cGMP signaling may differ based on sex, at least in the cardiovascular system (Stehle et al., 2023; Vermeersch et al., 2009). These sex differences also have implications for pharmaceutical treatments, as a phase IV clinical trial found that inhibition of PDE5 improved a measure of cardiac function only in male patients (Pofi et al., 2022). We therefore also analyzed whether the PDE9i also had sex-dependent effects on hearing function and found that, while the PDE9i improved hearing function in male controls, females did not benefit from it (**Figure 3.35**, **Figure 3.36**). When combined with the evidence from the cardiovascular system, this indicates that cGMP-stimulating drugs may be less beneficial for females, highlighting the importance of using female animals in early-stage pharmaceutical research, particularly for diseases where sex differences are already known to exist, such as cardiovascular diseases (Humphries et al., 2017) or ASD (Ochoa-Lubinoff et al., 2023).

A sex-dependent effect was also observed in the response of *Bdnf*^{Pax2} KO mice to PDE9i treatment. When the data from males and females were pooled, PDE9i treatment had a mildly adverse effect on hearing (i.e., ABR wave amplitude; **Figure 3.13**, **Figure 3.14**) and memory function (i.e., LTP; **Figure 3.17**). However, when that data was split by sex, it became clear that the more negative effect of the PDE9i also came primarily from the male mice (**Figure 3.35** and **Figure 3.36**). The fact that PDE9i was damaging to *Bdnf*^{Pax2} KO mice was entirely unexpected and may be explained by two main factors.

The first and perhaps most obvious explanation as to the negative effects of PDE9i treatment in *Bdnf*^{Pax2} KO mice is simply that increasing cGMP levels via inhibition of PDE9 was the wrong pharmaceutical target. In untreated *Bdnf*^{Pax2} KO mice, we examined the mRNA expression levels of the cGMP generator NO-GC and found that its expression levels in the CA1 region of the hippocampus were already high (**Figure 3.21**). However, the implications of this finding are unclear. When NO-GC is activated by nitric oxide, it converts guanosine triphosphate into cGMP (Hobbs, 1997); thus, we would intuitively expect higher NO-GC levels to reflect more cGMP production, but it is also possible

that increased NO-GC levels are a compensatory mechanism to try to overcome less cGMP production from other cGMP generators. In addition, it has been demonstrated that PDE9 inhibitors regulate cGMP levels in a way that is independent from nitric oxide (Harms et al., 2019; Lee et al., 2015). Thus, higher NO-GC levels alone would not explain the negative effects of the PDE9i on *Bdnf*^{Pax2} KO mice. This could be elucidated by crossing *Bdnf*^{Pax2} KO mice with mice expressing a cGMP biosensor that would enable the measurement of intracellular cGMP levels (Thunemann et al., 2013).

An alternate possibility is that because the PDE9i is a "central," top-down treatment, it cannot recover the phenotype of *Bdnf*^{Pax2} KO mice as the underlying issue is peripheral, and the central effects are just a secondary result from a stunted developmental cascade. One could argue that the assumption that the PDE9i is a "central" treatment may be misplaced, as PDE9A is also expressed in the cochlea (Marchetta, Mohrle, et al., 2020). Indeed, Savitska et al. (2022) acknowledged that it was unclear whether the PDE9i-induced preservation of hearing and memory processes was a result of protection against hearing loss (bottom-up) or against hippocampal degeneration (top-down). However, the present work demonstrates a more pronounced effect of the PDE9i on the LTP than on the auditory responses, suggesting that it indeed works in a top-down manner, first affecting hippocampal function which subsequently affects the hearing.

Thus, we may ask the question, what in particular prevents a beneficial top-down effect of PDE9i? It was previously shown in older mice that an altered (in that case, blunted) stress response prevented any therapeutic effect of PDE9i (Savitska et al., 2022). *Bdnf*^{Pax2} KO mice also exhibited an altered stress response, with higher baseline levels of corticosterone that did not respond to the stressful vehicle injection (**Figure 3.11**). The altered stress response could result directly from deletion of *Bdnf*, as glucocorticoids and BDNF interact to suppress each other (Tsimpolis et al., 2024). However, BDNF levels in the cortex and hippocampus of *Bdnf*^{Pax2} KO mice are normal (Eckert et al., 2021), suggesting a more indirect effect of the deletion on the stress response. This indirect effect may nevertheless occur through the hippocampus, which, despite its normal BDNF expression levels, was shown to remain functionally immature, measured by higher LTP levels that were similar to those observed in young animals (Eckert et al., 2021). The hippocampus normally suppresses the activity of the hypothalamic-pituitary-adrenal axis that produces glucocorticoids and mediates the response to stressful situations (Cole et al., 2022; de Kloet et al., 2019; Manohar et al., 2022). Thus, the hippocampal dysfunction/immaturity of *Bdnf*^{Pax2} KO mice which occurs secondarily to the peripheral sensory immaturity may lead to an overactive hypothalamic-pituitary-adrenal axis that produces more glucocorticoids. This would explain the elevated corticosterone levels in untreated *Bdnf*^{Pax2} KO mice and could result in different effects of PDE9i treatment.

Taken together, this suggests that the PDE9i is not a promising treatment for *Bdnf*^{Pax2} KO mice and may indicate that developmental disorders resulting from peripheral immaturity may not benefit from any central treatment.

4.4 80 dB Recovers Hearing Phenotype of *Bdnf*^{Pax2} KO Mice

Thus far, we demonstrated that the phenotype of *Bdnf*^{Pax2} KO mice could originate from an immaturity in the peripheral auditory system, and we further showed that the central PDE9i treatment offered no therapeutic benefit in *Bdnf*^{Pax2} KO mice. Therefore, a complementary treatment primarily targeting the peripheral hearing phenotype of the *Bdnf*^{Pax2} KO mice was used. This protocol, termed "80 dB", consisted of a one-time exposure for 40 minutes to a 10 kHz stimulus at 80 dB SPL.

The 80 dB exposure used in the present study is conceptually similar to protocols of environmental enrichment, in that the external environment is modulated to stimulate the system and increase or improve neural activity. Environmental enrichment has also been used in various animal models of ASD and was shown to increase sociability and decrease stereotypic behaviors (for a review, see Caires & Bossolani-Martins, 2023). While sensory-specific forms of enrichment are not unheard of and

protocols exist for each sensory system (e.g., olfactory: Woo et al., 2023; visual: Baroncelli et al., 2012; somatosensory/motor: Baroncelli et al., 2012; Kondo et al., 2016), they are, on the whole, much more long-term than our one-time 80 dB exposure protocol. However, despite differences in how and for how long the enriching stimulus is presented, both environmental enrichment and 80 dB exposure have been shown to improve learning and memory function in control mice (Alwis & Rajan, 2014; Matt et al., 2018). Furthermore, 80 dB was previously reported to increase ABR wave amplitudes (Matt et al., 2018), consistent with findings for auditory-specific enrichment protocols (Oliver et al., 2011).

However, in contrast to previous results using 80 dB, the control mice used in the present study did not benefit from 80 dB exposure in their hearing function, as measured by ABR wave amplitude (**Figure 3.23**, **Figure 3.24**) and ASSR (**Figure 3.25**), or in their memory function, as measured by hippocampal LTP (**Figure 3.29**) and the novel object recognition test (**Figure 3.26**). The fact that 80 dB exposure had no beneficial effect on control mice was quite surprising, as the efficacy of this protocol in control mice was previously demonstrated by Matt et al. (2018). This prompted us to examine what differences could have contributed to the different outcomes of these two studies. The age of the mice used was similar, with Matt et al. (2018) using mice between 2 and 3 months and the average age of control mice in the present study being 3.3 months. A sex-dependent effect is also unlikely, as both studies used male and female mice, and 80 dB did not exhibit sex-dependent effects in auditory measures in the present study (see section 3.5.3). Further, the hearing function of control mice in both studies was similar, with comparable thresholds (~7 dB difference) and control mice in the present study exhibiting a higher ABR wave I amplitude (~1 µV difference) but a similar ABR wave IV amplitude (~4 µV; Marchetta, Savitska, et al., 2020; Matt et al., 2018). The only obvious difference therefore was the background of the mouse strains, with the mice used by Matt et al. (2018) having a mixed background and the *Bdnf*^{Pax2} line having an NMRI background. Indeed, it has been shown that there are strain-dependent differences in, for example, plasticity-related proteins (Pollak et al., 2005), LTP, and memory function (Nguyen et al., 2000) that may impact adaptive responses to enriching stimuli. Strain-specific differences have also been observed in more general environmental enrichment protocols (for a review, see Bayne, 2018).

In contrast to control mice, *Bdnf*^{Pax2} KO mice did benefit from 80 dB exposure to some extent, with an increased number of IHC ribbons that was functionally reflected in a higher ABR wave I amplitude (**Figure 3.23**). This increased activity propagated through the auditory system, resulting in a higher ABR wave IV amplitude (**Figure 3.24**) and a higher SNR in response to amplitude-modulated stimuli (**Figure 3.25**), reflecting improved temporal sound coding. However, 80 dB exposure did not have any effect on the cognitive phenotype of *Bdnf*^{Pax2} KO mice, leaving the social behavior (**Figure 3.30**), learning, and memory functions still impaired (**Figure 3.26**, **Figure 3.29**).

As proposed for the effects of the PDE9i, it is possible that the altered stress response of *Bdnf*^{Pax2} KO mice interfered with their adaptive responses to enriching stimuli, such as 80 dB. It was previously suggested that 80 dB may exert its effects through a feedback loop that relies on interactions between glucocorticoids and activity-driven BDNF (Matt et al., 2018). This interaction was suggested to drive an increase in vGlut1 expression along the ascending auditory pathway, leading to a long-term strengthening of synapses that increased auditory responsiveness two weeks after exposure. This activity increase was also shown to propagate along the ascending pathway to the hippocampus, resulting in long-term adjustments in the local E/I balance (Matt et al., 2018).

While the BDNF-mediated aspect of this proposed mechanism of action for 80 dB may still function in *Bdnf*^{Pax2} KO mice—as BDNF is only deleted in a subset of INs in some brainstem regions—the glucocorticoid-mediated aspect may be affected by their altered stress response. The high baseline corticosterone levels observed in *Bdnf*^{Pax2} KO mice (**Figure 3.11**) could interfere with an effect of any additional glucocorticoid release (i.e., upon 80 dB exposure), thereby preventing the upregulation of vGlut1 along ascending pathways. Speaking against this view, however, is the fact that *Bdnf*^{Pax2} KO mice indeed showed a functional increase in the responses of the ascending auditory pathway (**Figure**

3.23–25). This would suggest that either the effects of the glucocorticoid-mediated actions in response to 80 dB are not impaired in *Bdnf*^{Pax2} KO mice, despite their high baseline corticosterone levels, or that BDNF (and by extension vGlut1) can be upregulated independent of glucocorticoids.

Interestingly, the mechanism proposed by Matt et al. (2018) for 80 dB is similar to what has been proposed for more general environmental enrichment. It is thought that environmental enrichment leads to improvements in behavior and cognitive performance through a long-term enhancement of synaptic transmission that changes the balance of excitatory and inhibitory activity in cortical circuits (Alwis & Rajan, 2014). Notably, environmental enrichment has been shown to lead to upregulations of both activity-driven *Bdnf* transcripts (Costa et al., 2023; Gomez-Pinilla et al., 2011; Kuzumaki et al., 2011) and vGlut1 expression levels (Mainardi et al., 2010). In fact, even a brief exposure (22 hours) to an enriched environment increased vGlut1 expression levels, along with other excitatory markers, in the hippocampus and prefrontal cortex (Pintori et al., 2024). These findings underscore that, despite the differences between general environmental enrichment and 80 dB in both the specificity and duration of exposure, they operate by very similar mechanisms.

One notable aspect of the use of environmental enrichment in ASD models is that it is much more effective in reversing the phenotype when given in early postnatal development (for a review, see Caires & Bossolani-Martins, 2023). This has been shown using a variety of enrichment protocols and is consistent across several different ASD models (e.g., Campolongo et al., 2018; Favre et al., 2015; Oddi et al., 2015; Pietropaolo et al., 2014; Schneider et al., 2006; Yamaguchi et al., 2017; Yang et al., 2011). In these studies, environmental enrichment paradigms were started in rodents between P14 and P28, at which point, sensory systems are undergoing a critical period of strong experience-driven plasticity (Ferrer & De Marco Garcia, 2022). It may be that this critical period plasticity allows for environmental enrichment to modify the underlying neural deficits that lead to ASD. Thus, an ASD phenotype caused by a persisting immaturity in the sensory periphery, as we propose is the case for *Bdnf*^{Pax2} KO mice, may be particularly susceptible to treatment targeting these deficits not in adulthood, but during the critical period. It is therefore possible that exposure to 80 dB in the early postnatal period of *Bdnf*^{Pax2} KO mice could have the potential to more specifically target and reverse the underlying circuitry changes leading to their ASD phenotype.

This suggests that, in cases of developmental disorders associated with an underlying sensory immaturity, an early intervention strategy (i.e., during the critical period) that targets the underlying peripheral deficits may be the only option to restore the more central effects of the phenotype—preventing them before they can fully set in.

4.5 Conclusion & Outlook

In conclusion, we demonstrated that *Bdnf*^{Pax2} KO mice display a phenotype consistent with ASD on a behavioral, functional, structural, and molecular level. This phenotype arises in spite of the fact that no genes known to be associated with ASD were deleted in this model. We therefore searched for the underlying disease mechanism and found evidence that a persisting immaturity of high-SR auditory nerve fibers may drive dysfunctional responses throughout the ascending pathway and prevent proper development of cognitive responses, eventually leading to a phenotype that resembles ASD. To validate this putative underlying mechanism, we propose to examine the cognitive phenotype in two models with genetic modifications affecting either the early spontaneous activity in IHCs or the synapses between efferents and hair cells, as these may affect the maturation of high-SR fiber responses more specifically than in the *Bdnf*^{Pax2} KO model.

The search for effective treatments or therapies for ASD has been hindered by the fact that the disease mechanism has thus far remained elusive. Thus, having here identified the underlying neural mechanism in our model, we used two complementary treatment approaches in adult mice targeted to nudge the phenotype back towards the physiological state. The first treatment approach was a top-down

pharmaceutical approach using a PDE9i, which has been shown in other studies to improve hearing, memory function, and socialization deficits by increasing cGMP levels. However, this drug yielded no therapeutic benefit for *Bdnf*^{Pax2} KO mice and even had a mildly adverse effect. We propose that this unexpected adverse effect was due to an altered stress response in *Bdnf*^{Pax2} KO mice which arises as another central secondary consequence of the underlying peripheral deficits. However, we cannot rule out that the adverse effects may instead be due to altered cGMP signaling in these mice; this could be confirmed by crossing *Bdnf*^{Pax2} KO mice with mice expressing a cGMP biosensor and measuring the intracellular cGMP levels.

As the treatment targeting the central aspects of the *Bdnf*^{Pax2} KO phenotype was ineffective, we then used a complementary treatment approach that targeted the underlying peripheral deficits. This bottom-up, sensory specific enrichment paradigm, termed "80 dB," was able to recover the hearing deficits of *Bdnf*^{Pax2} KO mice but not the cognitive aspects of the phenotype. However, 80 dB exposure was performed only in adult mice, and it has been shown that environmental enrichment paradigms are more effective in improving ASD symptoms when given early in postnatal development. Thus, repeating this protocol in younger mice may have the potential to recover the cognitive phenotype in addition to the hearing phenotype.

Taken together, this suggests that an underlying peripheral, sensory deficit may contribute to the generation of developmental disorders, and that the only viable treatment option for those disorders may be one given early in development that targets underlying peripheral deficits.

ABBREVIATIONS

ABR, auditory brainstem response

AC, auditory cortex

ASD, autism spectrum disorder

ASSR, auditory steady state response

***Bdnf*/BDNF**, brain-derived neurotrophic factor

CA, cornu Ammonis

CAP, compound action potential

cGMP, cyclic guanosine monophosphate

DPOAE, distortion product of otoacoustic emissions

E, embryonic day

EEG, electroencephalography

E/I, excitation-inhibition

ERP, event related potential

fEPSP, field excitatory postsynaptic potential

GABA, γ-Aminobutyric acid

i, inhibitor

IC, inferior colliculus

IHC, inner hair cell

IN, interneuron

LFP, local field potential

LOC, lateral olivocochlear

LTP, long-term potentiation

MOC, medial olivocochlear

NO-GC, nitric oxide–sensitive guanylyl cyclase

OHC, outer hair cell

P, postnatal day

Pax2, paired box gene 2

PBS, phosphate buffered saline

PCR, polymerase chain reaction

PDE, phosphodiesterase

PSTR, peristimulus time response

PV, parvalbumin

SGN, spiral ganglion neuron

SNR, signal-to-noise ratio

SPL, sound pressure level

SR, spontaneous firing rate

vGlut1, vesicular glutamate transporter 1

LIST OF FIGURES

REFERENCES

Almeida, C. B., Scheiermann, C., Jang, J. E., Prophete, C., Costa, F. F., Conran, N., & Frenette, P. S. (2012). Hydroxyurea and a cGMP-amplifying agent have immediate benefits on acute vaso-occlusive events in sickle cell disease mice. *Blood*, *120*(14), 2879-2888. https://doi.org/10.1182/blood-2012-02-409524

Alwis, D. S., & Rajan, R. (2014). Environmental enrichment and the sensory brain: the role of enrichment in remediating brain injury. *Front Syst Neurosci*, *8*, 156. https://doi.org/10.3389/fnsys.2014.00156

Andreeva, S. G., Dikkes, P., Epstein, P. M., & Rosenberg, P. A. (2001). Expression of cGMP-specific phosphodiesterase 9A mRNA in the rat brain. *J Neurosci*, *21*(22), 9068-9076. https://doi.org/10.1523/JNEUROSCI.21-22-09068.2001

Antoine, M. W., Langberg, T., Schnepel, P., & Feldman, D. E. (2019). Increased Excitation-Inhibition Ratio Stabilizes Synapse and Circuit Excitability in Four Autism Mouse Models. *Neuron*, *101*(4), 648-661 e644. https://doi.org/10.1016/j.neuron.2018.12.026

Babola, T. A., Li, S., Gribizis, A., Lee, B. J., Issa, J. B., Wang, H. C., Crair, M. C., & Bergles, D. E. (2018). Homeostatic Control of Spontaneous Activity in the Developing Auditory System. *Neuron*, *99*(3), 511-524 e515. https://doi.org/10.1016/j.neuron.2018.07.004

Banerjee, A., Rikhye, R. V., Breton-Provencher, V., Tang, X., Li, C., Li, K., Runyan, C. A., Fu, Z., Jaenisch, R., & Sur, M. (2016). Jointly reduced inhibition and excitation underlies circuit-wide changes in cortical processing in Rett syndrome. *Proc Natl Acad Sci U S A*, *113*(46), E7287-E7296. https://doi.org/10.1073/pnas.1615330113

Barnes, S. A., Pinto-Duarte, A., Kappe, A., Zembrzycki, A., Metzler, A., Mukamel, E. A., Lucero, J., Wang, X., Sejnowski, T. J., Markou, A., & Behrens, M. M. (2015). Disruption of mGluR5 in parvalbumin-positive interneurons induces core features of neurodevelopmental disorders. *Mol Psychiatry*, *20*(10), 1161-1172. https://doi.org/10.1038/mp.2015.113

Baroncelli, L., Bonaccorsi, J., Milanese, M., Bonifacino, T., Giribaldi, F., Manno, I., Cenni, M. C., Berardi, N., Bonanno, G., Maffei, L., & Sale, A. (2012). Enriched experience and recovery from amblyopia in adult rats: impact of motor, social and sensory components. *Neuropharmacology*, *62*(7), 2388-2397. https://doi.org/10.1016/j.neuropharm.2012.02.010

Bayne, K. (2018). Environmental enrichment and mouse models: Current perspectives. *Animal Model Exp Med*, *1*(2), 82-90. https://doi.org/10.1002/ame2.12015

Beery, A. K., & Zucker, I. (2011). Sex bias in neuroscience and biomedical research. *Neurosci Biobehav Rev*, *35*(3), 565-572. https://doi.org/10.1016/j.neubiorev.2010.07.002

Behar, T. N., Dugich-Djordjevic, M. M., Li, Y. X., Ma, W., Somogyi, R., Wen, X., Brown, E., Scott, C., McKay, R. D., & Barker, J. L. (1997). Neurotrophins stimulate chemotaxis of embryonic cortical neurons. *Eur J Neurosci*, *9*(12), 2561-2570. https://doi.org/10.1111/j.1460-9568.1997.tb01685.x

Bellis, T. J. (2011). *Assessment and management of central auditory processing disorders in the educational setting: From science to practice*. Plural Publishing.

Ben-Ari, Y., & Spitzer, N. C. (2010). Phenotypic checkpoints regulate neuronal development. *Trends Neurosci*, *33*(11), 485-492. https://doi.org/10.1016/j.tins.2010.08.005

Berry, K. P., & Nedivi, E. (2017). Spine Dynamics: Are They All the Same? *Neuron*, *96*(1), 43-55. https://doi.org/10.1016/j.neuron.2017.08.008

Berryer, M. H., Chattopadhyaya, B., Xing, P., Riebe, I., Bosoi, C., Sanon, N., Antoine-Bertrand, J., Levesque, M., Avoli, M., Hamdan, F. F., Carmant, L., Lamarche-Vane, N., Lacaille, J. C., Michaud, J. L., & Di Cristo, G. (2016). Decrease of SYNGAP1 in GABAergic cells impairs inhibitory synapse connectivity, synaptic inhibition and cognitive function. *Nat Commun*, *7*, 13340. https://doi.org/10.1038/ncomms13340

Berzhanskaya, J., Phillips, M. A., Shen, J., & Colonnese, M. T. (2016). Sensory hypo-excitability in a rat model of fetal development in Fragile X Syndrome. *Sci Rep*, *6*, 30769. https://doi.org/10.1038/srep30769

Bharadwaj, H. M., Verhulst, S., Shaheen, L., Liberman, M. C., & Shinn-Cunningham, B. G. (2014). Cochlear neuropathy and the coding of supra-threshold sound. *Front Syst Neurosci*, *8*, 26. https://doi.org/10.3389/fnsys.2014.00026

Bickford, P. C., & Wear, K. D. (1995). Restoration of sensory gating of auditory evoked response by nicotine in fimbria-fornix lesioned rats. *Brain Res*, *705*(1-2), 235-240. https://doi.org/10.1016/0006-8993(95)01157-9

Billig, A. J., Lad, M., Sedley, W., & Griffiths, T. D. (2022). The hearing hippocampus. *Prog Neurobiol*, *218*, 102326. https://doi.org/10.1016/j.pneurobio.2022.102326

Brandwein, A. B., Foxe, J. J., Butler, J. S., Frey, H. P., Bates, J. C., Shulman, L. H., & Molholm, S. (2015). Neurophysiological indices of atypical auditory processing and multisensory integration are associated with symptom severity in autism. *J Autism Dev Disord*, *45*(1), 230-244. https://doi.org/10.1007/s10803-014-2212-9

Bulankina, A. V., & Moser, T. (2012). Neural circuit development in the mammalian cochlea. *Physiology (Bethesda)*, *27*(2), 100-112. https://doi.org/10.1152/physiol.00036.2011

Buran, B. N., Strenzke, N., Neef, A., Gundelfinger, E. D., Moser, T., & Liberman, M. C. (2010). Onset coding is degraded in auditory nerve fibers from mutant mice lacking synaptic ribbons. *J Neurosci*, *30*(22), 7587-7597. https://doi.org/10.1523/JNEUROSCI.0389-10.2010

Burkard, R. F., Eggermont, J. J., & Don, M. (2007). *Auditory evoked potentials: basic principles and clinical application*. Lippincott Williams & Wilkins.

Buzsaki, G., & Wang, X. J. (2012). Mechanisms of gamma oscillations. *Annu Rev Neurosci*, *35*, 203-225. https://doi.org/10.1146/annurev-neuro-062111-150444

Caires, C. R. S., & Bossolani-Martins, A. L. (2023). Which form of environmental enrichment is most effective in rodent models of autism? *Behav Processes*, *211*, 104915. https://doi.org/10.1016/j.beproc.2023.104915

Calis, D., Hess, M., Marchetta, P., Singer, W., Modro, J., Nelissen, E., Prickaerts, J., Sandner, P., Lukowski, R., Ruth, P., Knipper, M., & Ruttiger, L. (2023). Acute deletion of the central MR/GR steroid receptor correlates with changes in LTP, auditory neural gain, and GC-A cGMP signaling. *Front Mol Neurosci*, *16*, 1017761. https://doi.org/10.3389/fnmol.2023.1017761

Campolongo, M., Kazlauskas, N., Falasco, G., Urrutia, L., Salgueiro, N., Hocht, C., & Depino, A. M. (2018). Sociability deficits after prenatal exposure to valproic acid are rescued by early social enrichment. *Mol Autism*, *9*, 36. https://doi.org/10.1186/s13229-018-0221-9

Canetta, S., Bolkan, S., Padilla-Coreano, N., Song, L. J., Sahn, R., Harrison, N. L., Gordon, J. A., Brown, A., & Kellendonk, C. (2016). Maternal immune activation leads to selective functional deficits in offspring parvalbumin interneurons. *Mol Psychiatry*, *21*(7), 956-968. https://doi.org/10.1038/mp.2015.222

Cardin, J. A., Carlen, M., Meletis, K., Knoblich, U., Zhang, F., Deisseroth, K., Tsai, L. H., & Moore, C. I. (2009). Driving fast-spiking cells induces gamma rhythm and controls sensory responses. *Nature*, *459*(7247), 663-667. https://doi.org/10.1038/nature08002

Cheaha, D., & Kumarnsit, E. (2015). Alteration of spontaneous spectral powers and coherences of local field potential in prenatal valproic acid mouse model of autism. *Acta Neurobiol Exp (Wars)*, *75*(4), 351-363. https://doi.org/10.55782/ane-2015-2040

Chen, Q., Deister, C. A., Gao, X., Guo, B., Lynn-Jones, T., Chen, N., Wells, M. F., Liu, R., Goard, M. J., Dimidschstein, J., Feng, S., Shi, Y., Liao, W., Lu, Z., Fishell, G., Moore, C. I., & Feng, G. (2020). Dysfunction of cortical GABAergic neurons leads to sensory hyper-reactivity in a Shank3 mouse model of ASD. *Nat Neurosci*, *23*(4), 520-532. https://doi.org/10.1038/s41593-020-0598-6

Chen, X., Delic, D., Cao, Y., Zhang, Z., Wu, H., Hasan, A. A., Gaballa, M. M. S., Yin, L., Kramer, B. K., Klein, T., Shi, X., He, B., Shen, L., & Hocher, B. (2024). Renal and cardiac effects of the PDE9 inhibitor BAY 73-6691 in 5/6 nephrectomized rats. *Pflugers Arch*, *476*(5), 755-767. https://doi.org/10.1007/s00424-024-02915-2

Chen, Z., Li, X., Zhou, J., Yuan, B., Yu, B., Tong, D., Cheng, C., Shao, Y., Xia, S., Zhang, R., Lyu, J., Yu, X., Dong, C., Zhou, W. H., & Qiu, Z. (2017). Accumulated quiescent neural stem cells in adult hippocampus of the mouse model for the MECP2 duplication syndrome. *Sci Rep*, *7*, 41701. https://doi.org/10.1038/srep41701

Chumak, T., Ruttiger, L., Lee, S. C., Campanelli, D., Zuccotti, A., Singer, W., Popelar, J., Gutsche, K., Geisler, H. S., Schraven, S. P., Jaumann, M., Panford-Walsh, R., Hu, J., Schimmang, T., Zimmermann, U., Syka, J., & Knipper, M. (2016). BDNF in Lower Brain Parts Modifies Auditory Fiber Activity to Gain Fidelity but Increases the Risk for Generation of Central Noise After Injury. *Mol Neurobiol*, *53*(8), 5607-5627. https://doi.org/10.1007/s12035-015-9474-x

Clause, A., Lauer, A. M., & Kandler, K. (2017). Mice Lacking the Alpha9 Subunit of the Nicotinic Acetylcholine Receptor Exhibit Deficits in Frequency Difference Limens and Sound Localization. *Front Cell Neurosci*, *11*, 167. https://doi.org/10.3389/fncel.2017.00167

Clipperton-Allen, A. E., Zhang, A., Cohen, O. S., & Page, D. T. (2021). Environmental Enrichment Rescues Social Behavioral Deficits and Synaptic Abnormalities in Pten Haploinsufficient Mice. *Genes (Basel)*, *12*(9). https://doi.org/10.3390/genes12091366

Cole, A. B., Montgomery, K., Bale, T. L., & Thompson, S. M. (2022). What the hippocampus tells the HPA axis: Hippocampal output attenuates acute stress responses via disynaptic inhibition of CRF+ PVN neurons. *Neurobiol Stress*, *20*, 100473. https://doi.org/10.1016/j.ynstr.2022.100473

Contractor, A., Ethell, I. M., & Portera-Cailliau, C. (2021). Cortical interneurons in autism. *Nat Neurosci*, *24*(12), 1648-1659. https://doi.org/10.1038/s41593-021-00967-6

Cooper, B. G., Miya, D. Y., & Mizumori, S. J. (1998). Superior colliculus and active navigation: role of visual and non-visual cues in controlling cellular representations of space. *Hippocampus*, *8*(4), 340-372. https://doi.org/10.1002/(SICI)1098-1063(1998)8:4<340::AID-HIPO4>3.0.CO;2-L

Costa, G. A., de Gusmao Taveiros Silva, N. K., Marianno, P., Chivers, P., Bailey, A., & Camarini, R. (2023). Environmental Enrichment Increased Bdnf Transcripts in the Prefrontal Cortex: Implications for an Epigenetically Controlled Mechanism. *Neuroscience*, *526*, 277-289. https://doi.org/10.1016/j.neuroscience.2023.07.001

da Silva, F. H., Pereira, M. N., Franco-Penteado, C. F., De Nucci, G., Antunes, E., & Claudino, M. A. (2013). Phosphodiesterase-9 (PDE9) inhibition with BAY 73-6691 increases corpus cavernosum relaxations mediated by nitric oxide-cyclic GMP pathway in mice. *Int J Impot Res*, *25*(2), 69-73. https://doi.org/10.1038/ijir.2012.35

Dalhoff, E., Zelle, D., & Gummer, A. W. (2015). Ipsilateral medial olivocochlear reflex adaptation of the primary-source DPOAE component measured with pulsed tones. AIP Conference Proceedings,

de Kloet, E. R., de Kloet, S. F., de Kloet, C. S., & de Kloet, A. D. (2019). Top-down and bottom-up control of stress-coping. *J Neuroendocrinol*, *31*(3), e12675. https://doi.org/10.1111/jne.12675

Delorme, A., & Makeig, S. (2004). EEGLAB: an open source toolbox for analysis of single-trial EEG dynamics including independent component analysis. *J Neurosci Methods*, *134*(1), 9-21. https://doi.org/10.1016/j.jneumeth.2003.10.009

Denaxa, M., Neves, G., Rabinowitz, A., Kemlo, S., Liodis, P., Burrone, J., & Pachnis, V. (2018). Modulation of Apoptosis Controls Inhibitory Interneuron Number in the Cortex. *Cell Rep*, *22*(7), 1710-1721. https://doi.org/10.1016/j.celrep.2018.01.064

Diagnostic and statistical manual of mental disorders (5th ed.). (2013). American Psychiatric Association. https://doi.org/https://doi.org/10.1176/appi.books.9780890425596

Dolen, G., Osterweil, E., Rao, B. S., Smith, G. B., Auerbach, B. D., Chattarji, S., & Bear, M. F. (2007). Correction of fragile X syndrome in mice. *Neuron*, *56*(6), 955-962. https://doi.org/10.1016/j.neuron.2007.12.001

Dressler, G. R., Deutsch, U., Chowdhury, K., Nornes, H. O., & Gruss, P. (1990). Pax2, a new murine paired-box-containing gene and its expression in the developing excretory system. *Development*, *109*(4), 787-795. https://doi.org/10.1242/dev.109.4.787

Eckert, P., Marchetta, P., Manthey, M. K., Walter, M. H., Jovanovic, S., Savitska, D., Singer, W., Jacob, M. H., Ruttiger, L., Schimmang, T., Milenkovic, I., Pilz, P. K. D., & Knipper, M. (2021). Deletion of BDNF in Pax2 Lineage-Derived Interneuron Precursors in the Hindbrain Hampers the Proportion of Excitation/Inhibition, Learning, and Behavior. *Front Mol Neurosci*, *14*, 642679. https://doi.org/10.3389/fnmol.2021.642679

Edgar, J. C., Fisk Iv, C. L., Berman, J. I., Chudnovskaya, D., Liu, S., Pandey, J., Herrington, J. D., Port, R. G., Schultz, R. T., & Roberts, T. P. (2015). Auditory encoding abnormalities in children with autism spectrum disorder suggest delayed development of auditory cortex. *Mol Autism*, *6*, 69. https://doi.org/10.1186/s13229-015-0065-5

Engineer, C. T., Rahebi, K. C., Borland, M. S., Buell, E. P., Centanni, T. M., Fink, M. K., Im, K. W., Wilson, L. G., & Kilgard, M. P. (2015). Degraded neural and behavioral processing of speech sounds in a rat model of Rett syndrome. *Neurobiol Dis*, *83*, 26-34. https://doi.org/10.1016/j.nbd.2015.08.019

Ergaz, Z., Weinstein-Fudim, L., & Ornoy, A. (2016). Genetic and non-genetic animal models for autism spectrum disorders (ASD). *Reprod Toxicol*, *64*, 116-140. https://doi.org/10.1016/j.reprotox.2016.04.024

Ethridge, L. E., White, S. P., Mosconi, M. W., Wang, J., Pedapati, E. V., Erickson, C. A., Byerly, M. J., & Sweeney, J. A. (2017). Neural synchronization deficits linked to cortical hyper-excitability and auditory hypersensitivity in fragile X syndrome. *Mol Autism*, *8*, 22. https://doi.org/10.1186/s13229-017-0140-1

Fagiolini, M., Fritschy, J. M., Low, K., Mohler, H., Rudolph, U., & Hensch, T. K. (2004). Specific GABAA circuits for visual cortical plasticity. *Science*, *303*(5664), 1681-1683. https://doi.org/10.1126/science.1091032

Favre, M. R., La Mendola, D., Meystre, J., Christodoulou, D., Cochrane, M. J., Markram, H., & Markram, K. (2015). Predictable enriched environment prevents development of hyper-emotionality in the VPA rat model of autism. *Front Neurosci*, *9*, 127. https://doi.org/10.3389/fnins.2015.00127

Ferrer, C., & De Marco Garcia, N. V. (2022). The Role of Inhibitory Interneurons in Circuit Assembly and Refinement Across Sensory Cortices. *Front Neural Circuits*, *16*, 866999. https://doi.org/10.3389/fncir.2022.866999

Fettiplace, R. (2017). Hair Cell Transduction, Tuning, and Synaptic Transmission in the Mammalian Cochlea. *Compr Physiol*, *7*(4), 1197-1227. https://doi.org/10.1002/cphy.c160049

Fiala, J. C. (2005). Reconstruct: a free editor for serial section microscopy. *J Microsc*, *218*(Pt 1), 52-61. https://doi.org/10.1111/j.1365-2818.2005.01466.x

Filice, F., Vorckel, K. J., Sungur, A. O., Wohr, M., & Schwaller, B. (2016). Reduction in parvalbumin expression not loss of the parvalbumin-expressing GABA interneuron subpopulation in genetic parvalbumin and shank mouse models of autism. *Mol Brain*, *9*, 10. https://doi.org/10.1186/s13041-016-0192-8

Fombonne, E. (2009). Epidemiology of pervasive developmental disorders. *Pediatr Res*, *65*(6), 591-598. https://doi.org/10.1203/PDR.0b013e31819e7203

Foss-Feig, J. H., Schauder, K. B., Key, A. P., Wallace, M. T., & Stone, W. L. (2017). Audition-specific temporal processing deficits associated with language function in children with autism spectrum disorder. *Autism Res*, *10*(11), 1845-1856. https://doi.org/10.1002/aur.1820

Fotaki, V., Price, D. J., & Mason, J. O. (2008). Newly identified patterns of Pax2 expression in the developing mouse forebrain. *BMC Dev Biol*, *8*, 79. https://doi.org/10.1186/1471-213X-8-79

Franklin, K. B., & Paxinos, G. (2008). The mouse brain in stereotaxic coordinates, Amsterdam. In: Boston: Elsevier/Academic Press.

Friebe, A., & Koesling, D. (2003). Regulation of nitric oxide-sensitive guanylyl cyclase. *Circ Res*, *93*(2), 96-105. https://doi.org/10.1161/01.RES.0000082524.34487.31

Fröhlich, F. (2016). Microcircuits of the Hippocampus. *Network neuroscience*, 97-109.

Gener, T., Perez-Mendez, L., & Sanchez-Vives, M. V. (2013). Tactile modulation of hippocampal place fields. *Hippocampus*, *23*(12), 1453-1462. https://doi.org/10.1002/hipo.22198

Gerhard, D. (2013). *Neuroscience* (D. Gerhard, Ed. 5 ed.). Yale Journal of Biology and Medicine.

Glowatzki, E., & Fuchs, P. A. (2000). Cholinergic synaptic inhibition of inner hair cells in the neonatal mammalian cochlea. *Science*, *288*(5475), 2366-2368. https://doi.org/10.1126/science.288.5475.2366

Glowatzki, E., & Fuchs, P. A. (2002). Transmitter release at the hair cell ribbon synapse. *Nat Neurosci*, *5*(2), 147-154. https://doi.org/10.1038/nn796

Godavarthi, S. K., Sharma, A., & Jana, N. R. (2014). Reversal of reduced parvalbumin neurons in hippocampus and amygdala of Angelman syndrome model mice by chronic treatment of fluoxetine. *J Neurochem*, *130*(3), 444-454. https://doi.org/10.1111/jnc.12726

Goel, A., Cantu, D. A., Guilfoyle, J., Chaudhari, G. R., Newadkar, A., Todisco, B., de Alba, D., Kourdougli, N., Schmitt, L. M., Pedapati, E., Erickson, C. A., & Portera-Cailliau, C. (2018). Impaired perceptual learning in a mouse model of Fragile X syndrome is mediated by parvalbumin neuron dysfunction and is reversible. *Nat Neurosci*, *21*(10), 1404-1411. https://doi.org/10.1038/s41593-018-0231-0

Goffin, D., Allen, M., Zhang, L., Amorim, M., Wang, I. T., Reyes, A. R., Mercado-Berton, A., Ong, C., Cohen, S., Hu, L., Blendy, J. A., Carlson, G. C., Siegel, S. J., Greenberg, M. E., & Zhou, Z. (2011). Rett syndrome mutation MeCP2 T158A disrupts DNA binding, protein stability and ERP responses. *Nat Neurosci*, *15*(2), 274-283. https://doi.org/10.1038/nn.2997

Gogolla, N., Leblanc, J. J., Quast, K. B., Sudhof, T. C., Fagiolini, M., & Hensch, T. K. (2009). Common circuit defect of excitatory-inhibitory balance in mouse models of autism. *J Neurodev Disord*, *1*(2), 172-181. https://doi.org/10.1007/s11689-009-9023-x

Golshani, P., Goncalves, J. T., Khoshkhoo, S., Mostany, R., Smirnakis, S., & Portera-Cailliau, C. (2009). Internally mediated developmental desynchronization of neocortical network activity. *J Neurosci*, *29*(35), 10890-10899. https://doi.org/10.1523/JNEUROSCI.2012-09.2009

Gomez-Pinilla, F., Zhuang, Y., Feng, J., Ying, Z., & Fan, G. (2011). Exercise impacts brain-derived neurotrophic factor plasticity by engaging mechanisms of epigenetic regulation. *Eur J Neurosci*, *33*(3), 383-390. https://doi.org/10.1111/j.1460-9568.2010.07508.x

Grant, L., Yi, E., & Glowatzki, E. (2010). Two modes of release shape the postsynaptic response at the inner hair cell ribbon synapse. *J Neurosci*, *30*(12), 4210-4220. https://doi.org/10.1523/JNEUROSCI.4439-09.2010

Guinan, J. J., Jr. (2006). Olivocochlear efferents: anatomy, physiology, function, and the measurement of efferent effects in humans. *Ear Hear*, *27*(6), 589-607. https://doi.org/10.1097/01.aud.0000240507.83072.e7

Hanna, C. B., Yao, S., Wu, X., & Jensen, J. T. (2012). Identification of phosphodiesterase 9A as a cyclic guanosine monophosphate-specific phosphodiesterase in germinal vesicle oocytes: a proposed role in the resumption of meiosis. *Fertil Steril*, *98*(2), 487-495 e481. https://doi.org/10.1016/j.fertnstert.2012.05.015

Harms, J. F., Menniti, F. S., & Schmidt, C. J. (2019). Phosphodiesterase 9A in Brain Regulates cGMP Signaling Independent of Nitric-Oxide. *Front Neurosci*, *13*, 837. https://doi.org/10.3389/fnins.2019.00837

Hashemi, E., Ariza, J., Rogers, H., Noctor, S. C., & Martinez-Cerdeno, V. (2017). The Number of Parvalbumin-Expressing Interneurons Is Decreased in the Prefrontal Cortex in Autism. *Cereb Cortex*, *27*(3), 1931-1943. https://doi.org/10.1093/cercor/bhw021

Heil, P., Neubauer, H., Brown, M., & Irvine, D. R. (2008). Towards a unifying basis of auditory thresholds: distributions of the first-spike latencies of auditory-nerve fibers. *Hear Res*, *238*(1-2), 25-38. https://doi.org/10.1016/j.heares.2007.09.014

Heil, P., & Peterson, A. J. (2015). Basic response properties of auditory nerve fibers: a review. *Cell Tissue Res*, *361*(1), 129-158. https://doi.org/10.1007/s00441-015-2177-9

Hobbs, A. J. (1997). Soluble guanylate cyclase: the forgotten sibling. *Trends Pharmacol Sci*, *18*(12), 484-491. https://doi.org/10.1016/s0165-6147(97)01137-1

Holley, A. J., Shedd, A., Boggs, A., Lovelace, J., Erickson, C., Gross, C., Jankovic, M., Razak, K., Huber, K., & Gibson, J. R. (2022). A sound-driven cortical phase-locking change in the Fmr1 KO mouse requires Fmr1 deletion in a subpopulation of brainstem neurons. *Neurobiol Dis*, *170*, 105767. https://doi.org/10.1016/j.nbd.2022.105767

Horner, K. C. (2003). The emotional ear in stress. *Neurosci Biobehav Rev*, *27*(5), 437-446. https://doi.org/10.1016/s0149-7634(03)00071-x

Huet, A., Batrel, C., Dubernard, X., Kleiber, J. C., Desmadryl, G., Venail, F., Liberman, M. C., Nouvian, R., Puel, J. L., & Bourien, J. (2022). Peristimulus Time Responses Predict Adaptation and Spontaneous Firing of Auditory-Nerve Fibers: From Rodents Data to Humans. *J Neurosci*, *42*(11), 2253-2267. https://doi.org/10.1523/JNEUROSCI.0858-21.2022

Humphries, K. H., Izadnegahdar, M., Sedlak, T., Saw, J., Johnston, N., Schenck-Gustafsson, K., Shah, R. U., Regitz-Zagrosek, V., Grewal, J., Vaccarino, V., Wei, J., & Bairey Merz, C. N. (2017). Sex differences in cardiovascular disease - Impact on care and outcomes. *Front Neuroendocrinol*, *46*, 46-70. https://doi.org/10.1016/j.yfrne.2017.04.001

Hussman, J. P. (2001). Suppressed GABAergic inhibition as a common factor in suspected etiologies of autism. *J Autism Dev Disord*, *31*(2), 247-248. https://doi.org/10.1023/a:1010715619091

Hutson, P. H., Finger, E. N., Magliaro, B. C., Smith, S. M., Converso, A., Sanderson, P. E., Mullins, D., Hyde, L. A., Eschle, B. K., Turnbull, Z., Sloan, H., Guzzi, M., Zhang, X., Wang, A., Rindgen, D., Mazzola, R., Vivian, J. A., Eddins, D., Uslaner, J. M., . . . Parmentier-Batteur, S. (2011). The selective phosphodiesterase 9 (PDE9) inhibitor PF-04447943 (6-[(3S,4S)-4-methyl-1-(pyrimidin-2-ylmethyl)pyrrolidin-3-yl]-1-(tetrahydro-2H-pyran-4-yl)-1,5-dihydro-4H-pyrazolo[3,4-d]pyrimidin-4-one) enhances synaptic plasticity and cognitive function in rodents. *Neuropharmacology*, *61*(4), 665-676. https://doi.org/10.1016/j.neuropharm.2011.05.009

Huzard, D., Martin, M., Maingret, F., Chemin, J., Jeanneteau, F., Mery, P. F., Fossat, P., Bourinet, E., & Francois, A. (2022). The impact of C-tactile low-threshold mechanoreceptors on affective touch and social interactions in mice. *Sci Adv*, *8*(26), eabo7566. https://doi.org/10.1126/sciadv.abo7566

Irwin, J., Avery, T., Turcios, J., Brancazio, L., Cook, B., & Landi, N. (2017). Electrophysiological Indices of Audiovisual Speech Perception in the Broader Autism Phenotype. *Brain Sci*, *7*(6). https://doi.org/10.3390/brainsci7060060

Iwai, Y., Fagiolini, M., Obata, K., & Hensch, T. K. (2003). Rapid critical period induction by tonic inhibition in visual cortex. *J Neurosci*, *23*(17), 6695-6702. https://doi.org/10.1523/JNEUROSCI.23-17-06695.2003

Jansen, B. H., & Brandt, M. E. (1991). The effect of the phase of prestimulus alpha activity on the averaged visual evoked response. *Electroencephalogr Clin Neurophysiol*, *80*(4), 241-250. https://doi.org/10.1016/0168-5597(91)90107-9

Janssen, T., Niedermeyer, H. P., & Arnold, W. (2006). Diagnostics of the cochlear amplifier by means of distortion product otoacoustic emissions. *ORL J Otorhinolaryngol Relat Spec*, *68*(6), 334-339. https://doi.org/10.1159/000095275

Jonak, C. R., Lovelace, J. W., Ethell, I. M., Razak, K. A., & Binder, D. K. (2020). Multielectrode array analysis of EEG biomarkers in a mouse model of Fragile X Syndrome. *Neurobiol Dis*, *138*, 104794. https://doi.org/10.1016/j.nbd.2020.104794

Kandel, E., Schwartz, J., Jessell, T., Siegelbaum, S., Hudspeth, A. (2013). *Principles of Neural Science* (E. Kandel, Schwartz, J., Jessell, T., Siegelbaum, S., Hudspeth, A., Ed. 5 ed.). McGraw Hill.

Katz, L. C., & Shatz, C. J. (1996). Synaptic activity and the construction of cortical circuits. *Science*, *274*(5290), 1133-1138. https://doi.org/10.1126/science.274.5290.1133

Kersbergen, C. J., Babola, T. A., Rock, J., & Bergles, D. E. (2022). Developmental spontaneous activity promotes formation of sensory domains, frequency tuning and proper gain in central auditory circuits. *Cell Rep*, *41*(7), 111649. https://doi.org/10.1016/j.celrep.2022.111649

Kissinger, S. T., Wu, Q., Quinn, C. J., Anderson, A. K., Pak, A., & Chubykin, A. A. (2020). Visual Experience-Dependent Oscillations and Underlying Circuit Connectivity Changes Are Impaired in Fmr1 KO Mice. *Cell Rep*, *31*(1), 107486. https://doi.org/10.1016/j.celrep.2020.03.050

Kleiman, R. J., Chapin, D. S., Christoffersen, C., Freeman, J., Fonseca, K. R., Geoghegan, K. F., Grimwood, S., Guanowsky, V., Hajos, M., Harms, J. F., Helal, C. J., Hoffmann, W. E., Kocan, G. P., Majchrzak, M. J., McGinnis, D., McLean, S., Menniti, F. S., Nelson, F., Roof, R., . . . Schmidt, C. J. (2012). Phosphodiesterase 9A regulates central cGMP and modulates responses to cholinergic and monoaminergic perturbation in vivo. *J Pharmacol Exp Ther*, *341*(2), 396-409. https://doi.org/10.1124/jpet.111.191353

Kleppisch, T., & Feil, R. (2009). cGMP signalling in the mammalian brain: role in synaptic plasticity and behaviour. *Handb Exp Pharmacol*(191), 549-579. https://doi.org/10.1007/978-3-540-68964-5_24

Knipper, M., Singer, W., Schwabe, K., Hagberg, G. E., Li Hegner, Y., Ruttiger, L., Braun, C., & Land, R. (2021). Disturbed Balance of Inhibitory Signaling Links Hearing Loss and Cognition. *Front Neural Circuits*, *15*, 785603. https://doi.org/10.3389/fncir.2021.785603

Kondo, M. A., Gray, L. J., Pelka, G. J., Leang, S. K., Christodoulou, J., Tam, P. P., & Hannan, A. J. (2016). Affective dysfunction in a mouse model of Rett syndrome: Therapeutic effects of environmental stimulation and physical activity. *Dev Neurobiol*, *76*(2), 209-224. https://doi.org/10.1002/dneu.22308

Krishnan, K., Wang, B. S., Lu, J., Wang, L., Maffei, A., Cang, J., & Huang, Z. J. (2015). MeCP2 regulates the timing of critical period plasticity that shapes functional connectivity in primary visual cortex. *Proc Natl Acad Sci U S A*, *112*(34), E4782-4791. https://doi.org/10.1073/pnas.1506499112

Kroker, K. S., Mathis, C., Marti, A., Cassel, J. C., Rosenbrock, H., & Dorner-Ciossek, C. (2014). PDE9A inhibition rescues amyloid beta-induced deficits in synaptic plasticity and cognition. *Neurobiol Aging*, *35*(9), 2072-2078. https://doi.org/10.1016/j.neurobiolaging.2014.03.023

Kroker, K. S., Rast, G., Giovannini, R., Marti, A., Dorner-Ciossek, C., & Rosenbrock, H. (2012). Inhibition of acetylcholinesterase and phosphodiesterase-9A has differential effects on hippocampal early and late LTP. *Neuropharmacology*, *62*(5-6), 1964-1974. https://doi.org/10.1016/j.neuropharm.2011.12.021

Kujawa, S. G., & Liberman, M. C. (2001). Effects of olivocochlear feedback on distortion product otoacoustic emissions in guinea pig. *J Assoc Res Otolaryngol*, *2*(3), 268-278. https://doi.org/10.1007/s101620010047

Kujawa, S. G., & Liberman, M. C. (2009). Adding insult to injury: cochlear nerve degeneration after "temporary" noise-induced hearing loss. *J Neurosci*, *29*(45), 14077-14085. https://doi.org/10.1523/JNEUROSCI.2845-09.2009

Kuzumaki, N., Ikegami, D., Tamura, R., Hareyama, N., Imai, S., Narita, M., Torigoe, K., Niikura, K., Takeshima, H., Ando, T., Igarashi, K., Kanno, J., Ushijima, T., Suzuki, T., & Narita, M. (2011). Hippocampal epigenetic modification at the brain-derived neurotrophic factor gene induced by an enriched environment. *Hippocampus*, *21*(2), 127-132. https://doi.org/10.1002/hipo.20775

Kwakye, L. D., Foss-Feig, J. H., Cascio, C. J., Stone, W. L., & Wallace, M. T. (2011). Altered auditory and multisensory temporal processing in autism spectrum disorders. *Front Integr Neurosci*, *4*, 129. https://doi.org/10.3389/fnint.2010.00129

Larsson, M. (2017). Pax2 is persistently expressed by GABAergic neurons throughout the adult rat dorsal horn. *Neurosci Lett*, *638*, 96-101. https://doi.org/10.1016/j.neulet.2016.12.015

Lauer, A. M., & May, B. J. (2011). The medial olivocochlear system attenuates the developmental impact of early noise exposure. *J Assoc Res Otolaryngol*, *12*(3), 329-343. https://doi.org/10.1007/s10162-011-0262-7

Lawrence, Y. A., Kemper, T. L., Bauman, M. L., & Blatt, G. J. (2010). Parvalbumin-, calbindin-, and calretinin-immunoreactive hippocampal interneuron density in autism. *Acta Neurol Scand*, *121*(2), 99-108. https://doi.org/10.1111/j.1600-0404.2009.01234.x

Lazaro, M. T., Taxidis, J., Shuman, T., Bachmutsky, I., Ikrar, T., Santos, R., Marcello, G. M., Mylavarapu, A., Chandra, S., Foreman, A., Goli, R., Tran, D., Sharma, N., Azhdam, M., Dong, H., Choe, K. Y., Penagarikano, O., Masmanidis, S. C., Racz, B., . . . Golshani, P. (2019). Reduced Prefrontal Synaptic Connectivity and Disturbed Oscillatory Population Dynamics in the CNTNAP2 Model of Autism. *Cell Rep*, *27*(9), 2567-2578 e2566. https://doi.org/10.1016/j.celrep.2019.05.006

LeBlanc, J. J., & Fagiolini, M. (2011). Autism: a "critical period" disorder? *Neural Plast*, *2011*, 921680. https://doi.org/10.1155/2011/921680

Lee, D. I., Zhu, G., Sasaki, T., Cho, G. S., Hamdani, N., Holewinski, R., Jo, S. H., Danner, T., Zhang, M., Rainer, P. P., Bedja, D., Kirk, J. A., Ranek, M. J., Dostmann, W. R., Kwon, C., Margulies, K. B., Van Eyk, J. E., Paulus, W. J., Takimoto, E., & Kass, D. A. (2015). Phosphodiesterase 9A controls nitric-oxide-independent cGMP and hypertrophic heart disease. *Nature*, *519*(7544), 472-476. https://doi.org/10.1038/nature14332

Levy, D. A., Hopkins, R. O., & Squire, L. R. (2004). Impaired odor recognition memory in patients with hippocampal lesions. *Learn Mem*, *11*(6), 794-796. https://doi.org/10.1101/lm.82504

Li, J., Bai, L., Liu, Z., & Wang, W. (2020). Dual roles of PDE9a in meiotic maturation of zebrafish oocytes. *Biochem Biophys Res Commun*, *532*(1), 40-46. https://doi.org/10.1016/j.bbrc.2020.08.005

Li, J., Liu, C. N., Wei, N., Li, X. D., Liu, Y. Y., Yang, R., & Jia, Y. J. (2016). Protective effects of BAY 73-6691, a selective inhibitor of phosphodiesterase 9, on amyloid-beta peptides-induced oxidative stress in in-vivo and in-vitro models of Alzheimer's disease. *Brain Res*, *1642*, 327-335. https://doi.org/10.1016/j.brainres.2016.04.011

Liberman, M. C. (1978). Auditory-nerve response from cats raised in a low-noise chamber. *J Acoust Soc Am*, *63*(2), 442-455. https://doi.org/10.1121/1.381736

Liberman, M. C., Puria, S., & Guinan, J. J., Jr. (1996). The ipsilaterally evoked olivocochlear reflex causes rapid adaptation of the 2f1-f2 distortion product otoacoustic emission. *J Acoust Soc Am*, *99*(6), 3572-3584. https://doi.org/10.1121/1.414956

Liddie, S., Anderson, K. L., Paz, A., & Itzhak, Y. (2012). The effect of phosphodiesterase inhibitors on the extinction of cocaine-induced conditioned place preference in mice. *J Psychopharmacol*, *26*(10), 1375-1382. https://doi.org/10.1177/0269881112447991

Lin, Y. H., Ho, H. C., & Wu, H. P. (2009). Comparison of auditory steady-state responses and auditory brainstem responses in audiometric assessment of adults with sensorineural hearing loss. *Auris Nasus Larynx*, *36*(2), 140-145. https://doi.org/10.1016/j.anl.2008.04.009

Livingston, G., Huntley, J., Sommerlad, A., Ames, D., Ballard, C., Banerjee, S., Brayne, C., Burns, A., Cohen-Mansfield, J., Cooper, C., Costafreda, S. G., Dias, A., Fox, N., Gitlin, L. N., Howard, R., Kales, H. C., Kivimaki, M., Larson, E. B., Ogunniyi, A., . . . Mukadam, N. (2020). Dementia prevention, intervention, and care: 2020 report of the Lancet Commission. *Lancet*, *396*(10248), 413-446. https://doi.org/10.1016/S0140-6736(20)30367-6

Livingston, G., Sommerlad, A., Orgeta, V., Costafreda, S. G., Huntley, J., Ames, D., Ballard, C., Banerjee, S., Burns, A., Cohen-Mansfield, J., Cooper, C., Fox, N., Gitlin, L. N., Howard, R., Kales, H. C., Larson, E. B., Ritchie, K., Rockwood, K., Sampson, E. L., . . . Mukadam, N. (2017). Dementia prevention, intervention, and care. *Lancet*, *390*(10113), 2673-2734. https://doi.org/10.1016/S0140-6736(17)31363-6

Lohrke, S., Srinivasan, G., Oberhofer, M., Doncheva, E., & Friauf, E. (2005). Shift from depolarizing to hyperpolarizing glycine action occurs at different perinatal ages in superior olivary complex nuclei. *Eur J Neurosci*, *22*(11), 2708-2722. https://doi.org/10.1111/j.1460-9568.2005.04465.x

Lovelace, J. W., Ethell, I. M., Binder, D. K., & Razak, K. A. (2018). Translation-relevant EEG phenotypes in a mouse model of Fragile X Syndrome. *Neurobiol Dis*, *115*, 39-48. https://doi.org/10.1016/j.nbd.2018.03.012

Lu, H., Mehta, A. H., & Oxenham, A. J. (2022). Methodological considerations when measuring and analyzing auditory steady-state responses with multi-channel EEG. *Curr Res Neurobiol*, *3*, 100061. https://doi.org/10.1016/j.crneur.2022.100061

Lueptow, L. M. (2017). Novel Object Recognition Test for the Investigation of Learning and Memory in Mice. *J Vis Exp*(126). https://doi.org/10.3791/55718

Luhmann, H. J., & Khazipov, R. (2018). Neuronal activity patterns in the developing barrel cortex. *Neuroscience*, *368*, 256-267. https://doi.org/10.1016/j.neuroscience.2017.05.025

Mainardi, M., Landi, S., Gianfranceschi, L., Baldini, S., De Pasquale, R., Berardi, N., Maffei, L., & Caleo, M. (2010). Environmental enrichment potentiates thalamocortical transmission and plasticity in the adult rat visual cortex. *J Neurosci Res*, *88*(14), 3048-3059. https://doi.org/10.1002/jnr.22461

Makeig, S., Westerfield, M., Jung, T. P., Enghoff, S., Townsend, J., Courchesne, E., & Sejnowski, T. J. (2002). Dynamic brain sources of visual evoked responses. *Science*, *295*(5555), 690-694. https://doi.org/10.1126/science.1066168

Manohar, S., Chen, G. D., Ding, D., Liu, L., Wang, J., Chen, Y. C., Chen, L., & Salvi, R. (2022). Unexpected Consequences of Noise-Induced Hearing Loss: Impaired Hippocampal Neurogenesis, Memory, and Stress. *Front Integr Neurosci*, *16*, 871223. https://doi.org/10.3389/fnint.2022.871223

Mao, W., Watanabe, T., Cho, S., Frost, J. L., Truong, T., Zhao, X., & Futai, K. (2015). Shank1 regulates excitatory synaptic transmission in mouse hippocampal parvalbumin-expressing inhibitory interneurons. *Eur J Neurosci*, *41*(8), 1025-1035. https://doi.org/10.1111/ejn.12877

Marchetta, P., Dapper, K., Hess, M., Calis, D., Singer, W., Wertz, J., Fink, S., Hage, S. R., Alam, M., Schwabe, K., Lukowski, R., Bourien, J., Puel, J. L., Jacob, M. H., Munk, M. H. J., Land, R., Ruttiger, L., & Knipper, M. (2024). Dysfunction of specific auditory fibers impacts cortical oscillations, driving an autism phenotype despite near-normal hearing. *FASEB J*, *38*(2), e23411. https://doi.org/10.1096/fj.202301995R

Marchetta, P., Mohrle, D., Eckert, P., Reimann, K., Wolter, S., Tolone, A., Lang, I., Wolters, M., Feil, R., Engel, J., Paquet-Durand, F., Kuhn, M., Knipper, M., & Ruttiger, L. (2020). Guanylyl Cyclase A/cGMP Signaling Slows Hidden, Age- and Acoustic Trauma-Induced Hearing Loss. *Front Aging Neurosci*, *12*, 83. https://doi.org/10.3389/fnagi.2020.00083

Marchetta, P., Savitska, D., Kubler, A., Asola, G., Manthey, M., Mohrle, D., Schimmang, T., Ruttiger, L., Knipper, M., & Singer, W. (2020). Age-Dependent Auditory Processing Deficits after Cochlear Synaptopathy Depend on Auditory Nerve Latency and the Ability of the Brain to Recruit LTP/BDNF. *Brain Sci*, *10*(10). https://doi.org/10.3390/brainsci10100710

Maricich, S. M., & Herrup, K. (1999). Pax-2 expression defines a subset of GABAergic interneurons and their precursors in the developing murine cerebellum. *J Neurobiol*, *41*(2), 281-294. https://doi.org/10.1002/(sici)1097-4695(19991105)41:2<281::aid-neu10>3.0.co;2-5

Marin, O. (2012). Interneuron dysfunction in psychiatric disorders. *Nat Rev Neurosci*, *13*(2), 107-120. https://doi.org/10.1038/nrn3155

Marin, O., & Rubenstein, J. L. (2001). A long, remarkable journey: tangential migration in the telencephalon. *Nat Rev Neurosci*, *2*(11), 780-790. https://doi.org/10.1038/35097509

Martin, C., Beshel, J., & Kay, L. M. (2007). An olfacto-hippocampal network is dynamically involved in odor-discrimination learning. *J Neurophysiol*, *98*(4), 2196-2205. https://doi.org/10.1152/jn.00524.2007

Matt, L., Eckert, P., Panford-Walsh, R., Geisler, H. S., Bausch, A. E., Manthey, M., Muller, N. I. C., Harasztosi, C., Rohbock, K., Ruth, P., Friauf, E., Ott, T., Zimmermann, U., Ruttiger, L., Schimmang, T., Knipper, M., & Singer, W. (2018). Visualizing BDNF Transcript Usage During Sound-Induced Memory Linked Plasticity. *Front Mol Neurosci*, *11*, 260. https://doi.org/10.3389/fnmol.2018.00260

Meddis, R. (2006). Auditory-nerve first-spike latency and auditory absolute threshold: a computer model. *J Acoust Soc Am*, *119*(1), 406-417. https://doi.org/10.1121/1.2139628

Melcher, J. R., & Kiang, N. Y. (1996). Generators of the brainstem auditory evoked potential in cat. III: Identified cell populations. *Hear Res*, *93*(1-2), 52-71. https://doi.org/10.1016/0378-5955(95)00200-6

Meyerink, B. L., Tiwari, N. K., & Pilaz, L. J. (2020). Ariadne's Thread in the Developing Cerebral Cortex: Mechanisms Enabling the Guiding Role of the Radial Glia Basal Process during Neuron Migration. *Cells*, *10*(1). https://doi.org/10.3390/cells10010003

Michaelson, S. D., Ozkan, E. D., Aceti, M., Maity, S., Llamosas, N., Weldon, M., Mizrachi, E., Vaissiere, T., Gaffield, M. A., Christie, J. M., Holder, J. L., Jr., Miller, C. A., & Rumbaugh, G. (2018). SYNGAP1 heterozygosity disrupts sensory processing by reducing touch-related activity within somatosensory cortex circuits. *Nat Neurosci*, *21*(12), 1-13. https://doi.org/10.1038/s41593-018-0268-0

Mohrle, D., Ni, K., Varakina, K., Bing, D., Lee, S. C., Zimmermann, U., Knipper, M., & Ruttiger, L. (2016). Loss of auditory sensitivity from inner hair cell synaptopathy can be centrally compensated in the young but not old brain. *Neurobiol Aging*, *44*, 173-184. https://doi.org/10.1016/j.neurobiolaging.2016.05.001

Moita, M. A., Rosis, S., Zhou, Y., LeDoux, J. E., & Blair, H. T. (2003). Hippocampal place cells acquire location-specific responses to the conditioned stimulus during auditory fear conditioning. *Neuron*, *37*(3), 485-497. https://doi.org/10.1016/s0896-6273(03)00033-3

Moxon, K. A., Gerhardt, G. A., Bickford, P. C., Austin, K., Rose, G. M., Woodward, D. J., & Adler, L. E. (1999). Multiple single units and population responses during inhibitory gating of hippocampal auditory response in freely-moving rats. *Brain Res*, *825*(1-2), 75-85. https://doi.org/10.1016/s0006-8993(99)01187-7

Munoz-Lopez, M. M., Mohedano-Moriano, A., & Insausti, R. (2010). Anatomical pathways for auditory memory in primates. *Front Neuroanat*, *4*, 129. https://doi.org/10.3389/fnana.2010.00129

Nguyen, P. V., Abel, T., Kandel, E. R., & Bourtchouladze, R. (2000). Strain-dependent differences in LTP and hippocampus-dependent memory in inbred mice. *Learn Mem*, *7*(3), 170-179. https://doi.org/10.1101/lm.7.3.170

Nicoll, R. A. (2017). A Brief History of Long-Term Potentiation. *Neuron*, *93*(2), 281-290. https://doi.org/10.1016/j.neuron.2016.12.015

Nimchinsky, E. A., Sabatini, B. L., & Svoboda, K. (2002). Structure and function of dendritic spines. *Annu Rev Physiol*, *64*, 313-353. https://doi.org/10.1146/annurev.physiol.64.081501.160008

Nornes, H. O., Dressler, G. R., Knapik, E. W., Deutsch, U., & Gruss, P. (1990). Spatially and temporally restricted expression of Pax2 during murine neurogenesis. *Development*, *109*(4), 797-809. https://doi.org/10.1242/dev.109.4.797

O'Donnell, C., Goncalves, J. T., Portera-Cailliau, C., & Sejnowski, T. J. (2017). Beyond excitation/inhibition imbalance in multidimensional models of neural circuit changes in brain disorders. *Elife*, *6*. https://doi.org/10.7554/eLife.26724

O'Keefe, J., & Dostrovsky, J. (1971). The hippocampus as a spatial map. Preliminary evidence from unit activity in the freely-moving rat. *Brain Res*, *34*(1), 171-175. https://doi.org/10.1016/0006-8993(71)90358-1

Ocak, E., Eshraghi, R. S., Danesh, A., Mittal, R., & Eshraghi, A. A. (2018). Central Auditory Processing Disorders in Individuals with Autism Spectrum Disorders. *Balkan Med J*, *35*(5), 367-372. https://doi.org/10.4274/balkanmedj.2018.0853

Ochoa-Lubinoff, C., Makol, B. A., & Dillon, E. F. (2023). Autism in Women. *Neurol Clin*, *41*(2), 381-397. https://doi.org/10.1016/j.ncl.2022.10.006

Oddi, D., Subashi, E., Middei, S., Bellocchio, L., Lemaire-Mayo, V., Guzman, M., Crusio, W. E., D'Amato, F. R., & Pietropaolo, S. (2015). Early social enrichment rescues adult behavioral and brain abnormalities in a mouse model of fragile X syndrome. *Neuropsychopharmacology*, *40*(5), 1113-1122. https://doi.org/10.1038/npp.2014.291

Ohyama, T., & Groves, A. K. (2004). Generation of Pax2-Cre mice by modification of a Pax2 bacterial artificial chromosome. *Genesis*, *38*(4), 195-199. https://doi.org/10.1002/gene.20017

Oliver, D. L., Izquierdo, M. A., & Malmierca, M. S. (2011). Persistent effects of early augmented acoustic environment on the auditory brainstem. *Neuroscience*, *184*, 75-87. https://doi.org/10.1016/j.neuroscience.2011.04.001

Orru, M., Guitart, X., Karcz-Kubicha, M., Solinas, M., Justinova, Z., Barodia, S. K., Zanoveli, J., Cortes, A., Lluis, C., Casado, V., Moeller, F. G., & Ferre, S. (2013). Psychostimulant pharmacological profile of paraxanthine, the main metabolite of caffeine in humans. *Neuropharmacology*, *67*, 476-484. https://doi.org/10.1016/j.neuropharm.2012.11.029

Palmen, S. J., van Engeland, H., Hof, P. R., & Schmitz, C. (2004). Neuropathological findings in autism. *Brain*, *127*(Pt 12), 2572-2583. https://doi.org/10.1093/brain/awh287

Pietropaolo, S., Goubran, M. G., Joffre, C., Aubert, A., Lemaire-Mayo, V., Crusio, W. E., & Laye, S. (2014). Dietary supplementation of omega-3 fatty acids rescues fragile X phenotypes in Fmr1-Ko mice. *Psychoneuroendocrinology*, *49*, 119-129. https://doi.org/10.1016/j.psyneuen.2014.07.002

Pintori, N., Piva, A., Mottarlini, F., Diaz, F. C., Maggi, C., Caffino, L., Fumagalli, F., & Chiamulera, C. (2024). Brief exposure to enriched environment rapidly shapes the glutamate synapses in the rat brain: A metaplastic fingerprint. *Eur J Neurosci*, *59*(5), 982-995. https://doi.org/10.1111/ejn.16279

Pirbhoy, P. S., Rais, M., Lovelace, J. W., Woodard, W., Razak, K. A., Binder, D. K., & Ethell, I. M. (2020). Acute pharmacological inhibition of matrix metalloproteinase-9 activity during development restores perineuronal net formation and normalizes auditory processing in Fmr1 KO mice. *J Neurochem*, *155*(5), 538-558. https://doi.org/10.1111/jnc.15037

Pofi, R., Giannetta, E., Feola, T., Galea, N., Barbagallo, F., Campolo, F., Badagliacca, R., Barbano, B., Ciolina, F., Defeudis, G., Filardi, T., Sesti, F., Minnetti, M., Vizza, C. D., Pasqualetti, P., Caboni, P., Carbone, I., Francone, M., Catalano, C., . . . Isidori, A. M. (2022). Sex-specific effects of daily tadalafil on diabetic heart kinetics in RECOGITO, a randomized, double-

blind, placebo-controlled trial. *Sci Transl Med*, *14*(649), eabl8503. https://doi.org/10.1126/scitranslmed.abl8503

Pollak, D. D., Scharl, T., Leisch, F., Herkner, K., Villar, S. R., Hoeger, H., & Lubec, G. (2005). Strain-dependent regulation of plasticity-related proteins in the mouse hippocampus. *Behav Brain Res*, *165*(2), 240-246. https://doi.org/10.1016/j.bbr.2005.07.028

Potter, L. R. (2011). Guanylyl cyclase structure, function and regulation. *Cell Signal*, *23*(12), 1921-1926. https://doi.org/10.1016/j.cellsig.2011.09.001

Prieto, G. A., Trieu, B. H., Dang, C. T., Bilousova, T., Gylys, K. H., Berchtold, N. C., Lynch, G., & Cotman, C. W. (2017). Pharmacological Rescue of Long-Term Potentiation in Alzheimer Diseased Synapses. *J Neurosci*, *37*(5), 1197-1212. https://doi.org/10.1523/JNEUROSCI.2774-16.2016

Queen, N. J., Boardman, A. A., Patel, R. S., Siu, J. J., Mo, X., & Cao, L. (2020). Environmental enrichment improves metabolic and behavioral health in the BTBR mouse model of autism. *Psychoneuroendocrinology*, *111*, 104476. https://doi.org/10.1016/j.psyneuen.2019.104476

Radwan, B., Dvorak, D., & Fenton, A. A. (2016). Impaired cognitive discrimination and discoordination of coupled theta-gamma oscillations in Fmr1 knockout mice. *Neurobiol Dis*, *88*, 125-138. https://doi.org/10.1016/j.nbd.2016.01.003

Rios, M., Fan, G., Fekete, C., Kelly, J., Bates, B., Kuehn, R., Lechan, R. M., & Jaenisch, R. (2001). Conditional deletion of brain-derived neurotrophic factor in the postnatal brain leads to obesity and hyperactivity. *Mol Endocrinol*, *15*(10), 1748-1757. https://doi.org/10.1210/mend.15.10.0706

Risher, W. C., Ustunkaya, T., Singh Alvarado, J., & Eroglu, C. (2014). Rapid Golgi analysis method for efficient and unbiased classification of dendritic spines. *PLoS One*, *9*(9), e107591. https://doi.org/10.1371/journal.pone.0107591

Roberts, T. P., Khan, S. Y., Rey, M., Monroe, J. F., Cannon, K., Blaskey, L., Woldoff, S., Qasmieh, S., Gandal, M., Schmidt, G. L., Zarnow, D. M., Levy, S. E., & Edgar, J. C. (2010). MEG detection of delayed auditory evoked responses in autism spectrum disorders: towards an imaging biomarker for autism. *Autism Res*, *3*(1), 8-18. https://doi.org/10.1002/aur.111

Rosenbrock, H., Giovannini, R., Schanzle, G., Koros, E., Runge, F., Fuchs, H., Marti, A., Reymann, K. G., Schroder, U. H., Fedele, E., & Dorner-Ciossek, C. (2019). The Novel Phosphodiesterase 9A Inhibitor BI 409306 Increases Cyclic Guanosine Monophosphate Levels in the Brain, Promotes Synaptic Plasticity, and Enhances Memory Function in Rodents. *J Pharmacol Exp Ther*, *371*(3), 633-641. https://doi.org/10.1124/jpet.119.260059

Rotaru, D. C., van Woerden, G. M., Wallaard, I., & Elgersma, Y. (2018). Adult Ube3a Gene Reinstatement Restores the Electrophysiological Deficits of Prefrontal Cortex Layer 5 Neurons in a Mouse Model of Angelman Syndrome. *J Neurosci*, *38*(37), 8011-8030. https://doi.org/10.1523/JNEUROSCI.0083-18.2018

Rotschafer, S. E., Marshak, S., & Cramer, K. S. (2015). Deletion of Fmr1 alters function and synaptic inputs in the auditory brainstem. *PLoS One*, *10*(2), e0117266. https://doi.org/10.1371/journal.pone.0117266

Rowitch, D. H., Kispert, A., & McMahon, A. P. (1999). Pax-2 regulatory sequences that direct transgene expression in the developing neural plate and external granule cell layer of the cerebellum. *Brain Res Dev Brain Res*, *117*(1), 99-108. https://doi.org/10.1016/s0165-3806(99)00104-2

Ruttiger, L., Zimmermann, U., & Knipper, M. (2017). Biomarkers for Hearing Dysfunction: Facts and Outlook. *ORL J Otorhinolaryngol Relat Spec*, *79*(1-2), 93-111. https://doi.org/10.1159/000455705

Sato, M., & Stryker, M. P. (2010). Genomic imprinting of experience-dependent cortical plasticity by the ubiquitin ligase gene Ube3a. *Proc Natl Acad Sci U S A*, *107*(12), 5611-5616. https://doi.org/10.1073/pnas.1001281107

Savitska, D., Hess, M., Calis, D., Marchetta, P., Harasztosi, C., Fink, S., Eckert, P., Ruth, P., Ruttiger, L., Knipper, M., & Singer, W. (2022). Stress Affects Central Compensation of Neural Responses to Cochlear Synaptopathy in a cGMP-Dependent Way. *Front Neurosci*, *16*, 864706. https://doi.org/10.3389/fnins.2022.864706

Scarborough, J., Mattei, D., Dorner-Ciossek, C., Sand, M., Arban, R., Rosenbrock, H., Richetto, J., & Meyer, U. (2021). Symptomatic and preventive effects of the novel phosphodiesterase-9 inhibitor BI 409306 in an immune-mediated model of neurodevelopmental disorders. *Neuropsychopharmacology*, *46*(8), 1526-1534. https://doi.org/10.1038/s41386-021-01016-3

Schneider, T., Turczak, J., & Przewlocki, R. (2006). Environmental enrichment reverses behavioral alterations in rats prenatally exposed to valproic acid: issues for a therapeutic approach in autism. *Neuropsychopharmacology*, *31*(1), 36-46. https://doi.org/10.1038/sj.npp.1300767

Scott, K. E., Schormans, A. L., Pacoli, K. Y., De Oliveira, C., Allman, B. L., & Schmid, S. (2018). Altered Auditory Processing, Filtering, and Reactivity in the Cntnap2 Knock-Out Rat Model for Neurodevelopmental Disorders. *J Neurosci*, *38*(40), 8588-8604. https://doi.org/10.1523/JNEUROSCI.0759-18.2018

Scoville, W. B., & Milner, B. (1957). Loss of recent memory after bilateral hippocampal lesions. *J Neurol Neurosurg Psychiatry*, *20*(1), 11-21. https://doi.org/10.1136/jnnp.20.1.11

Selby, L., Zhang, C., & Sun, Q. Q. (2007). Major defects in neocortical GABAergic inhibitory circuits in mice lacking the fragile X mental retardation protein. *Neurosci Lett*, *412*(3), 227-232. https://doi.org/10.1016/j.neulet.2006.11.062

Selimbeyoglu, A., Kim, C. K., Inoue, M., Lee, S. Y., Hong, A. S. O., Kauvar, I., Ramakrishnan, C., Fenno, L. E., Davidson, T. J., Wright, M., & Deisseroth, K. (2017). Modulation of prefrontal cortex excitation/inhibition balance rescues social behavior in CNTNAP2-deficient mice. *Sci Transl Med*, *9*(401). https://doi.org/10.1126/scitranslmed.aah6733

SFARI Gene. (March 28, 2024). Retrieved June 13 from https://www.sfari.org/resource/sfari-gene/

Shrestha, B. R., Chia, C., Wu, L., Kujawa, S. G., Liberman, M. C., & Goodrich, L. V. (2018). Sensory Neuron Diversity in the Inner Ear Is Shaped by Activity. *Cell*, *174*(5), 1229-1246 e1217. https://doi.org/10.1016/j.cell.2018.07.007

Silverman, J. L., Yang, M., Lord, C., & Crawley, J. N. (2010). Behavioural phenotyping assays for mouse models of autism. *Nat Rev Neurosci*, *11*(7), 490-502. https://doi.org/10.1038/nrn2851

Simon, D. M., & Wallace, M. T. (2016). Dysfunction of sensory oscillations in Autism Spectrum Disorder. *Neurosci Biobehav Rev*, *68*, 848-861. https://doi.org/10.1016/j.neubiorev.2016.07.016

Singer, W., Panford-Walsh, R., & Knipper, M. (2014). The function of BDNF in the adult auditory system. *Neuropharmacology*, *76 Pt C*, 719-728. https://doi.org/10.1016/j.neuropharm.2013.05.008

Sohal, V. S., Zhang, F., Yizhar, O., & Deisseroth, K. (2009). Parvalbumin neurons and gamma rhythms enhance cortical circuit performance. *Nature*, *459*(7247), 698-702. https://doi.org/10.1038/nature07991

Stehle, D., Barresi, M., Schulz, J., & Feil, R. (2023). Heterogeneity of cGMP signalling in tumour cells and the tumour microenvironment: Challenges and chances for cancer pharmacology and therapeutics. *Pharmacol Ther*, *242*, 108337. https://doi.org/10.1016/j.pharmthera.2023.108337

Stevenson, R. A., Segers, M., Ncube, B. L., Black, K. R., Bebko, J. M., Ferber, S., & Barense, M. D. (2018). The cascading influence of multisensory processing on speech perception in autism. *Autism*, *22*(5), 609-624. https://doi.org/10.1177/1362361317704413

Stewart, M. E., Petrou, A. M., & Ota, M. (2018). Categorical Speech Perception in Adults with Autism Spectrum Conditions. *J Autism Dev Disord*, *48*(1), 72-82. https://doi.org/10.1007/s10803-017-3284-0

Stroganova, T. A., Komarov, K. S., Sysoeva, O. V., Goiaeva, D. E., Obukhova, T. S., Ovsiannikova, T. M., Prokofyev, A. O., & Orekhova, E. V. (2020). Left hemispheric deficit in the sustained neuromagnetic response to periodic click trains in children with ASD. *Mol Autism*, *11*(1), 100. https://doi.org/10.1186/s13229-020-00408-4

Sur, M., & Rubenstein, J. L. (2005). Patterning and plasticity of the cerebral cortex. *Science*, *310*(5749), 805-810. https://doi.org/10.1126/science.1112070

Tajima, T., Shinoda, T., Urakawa, N., Shimizu, K., & Kaneda, T. (2018). Phosphodiesterase 9 (PDE9) regulates bovine tracheal smooth muscle relaxation. *J Vet Med Sci*, *80*(3), 499-502. https://doi.org/10.1292/jvms.18-0011

Talbot, Z. N., Sparks, F. T., Dvorak, D., Curran, B. M., Alarcon, J. M., & Fenton, A. A. (2018). Normal CA1 Place Fields but Discoordinated Network Discharge in a Fmr1-Null Mouse Model of Fragile X Syndrome. *Neuron*, *97*(3), 684-697 e684. https://doi.org/10.1016/j.neuron.2017.12.043

Tamura, R., Ono, T., Fukuda, M., & Nakamura, K. (1992). Spatial responsiveness of monkey hippocampal neurons to various visual and auditory stimuli. *Hippocampus*, *2*(3), 307-322. https://doi.org/10.1002/hipo.450020309

Thunemann, M., Wen, L., Hillenbrand, M., Vachaviolos, A., Feil, S., Ott, T., Han, X., Fukumura, D., Jain, R. K., Russwurm, M., de Wit, C., & Feil, R. (2013). Transgenic mice for cGMP imaging. *Circ Res*, *113*(4), 365-371. https://doi.org/10.1161/CIRCRESAHA.113.301063

Torres, M., & Giraldez, F. (1998). The development of the vertebrate inner ear. *Mech Dev*, *71*(1-2), 5-21. https://doi.org/10.1016/s0925-4773(97)00155-x

Tritsch, N. X., & Bergles, D. E. (2010). Developmental regulation of spontaneous activity in the Mammalian cochlea. *J Neurosci*, *30*(4), 1539-1550. https://doi.org/10.1523/JNEUROSCI.3875-09.2010

Tritsch, N. X., Yi, E., Gale, J. E., Glowatzki, E., & Bergles, D. E. (2007). The origin of spontaneous activity in the developing auditory system. *Nature*, *450*(7166), 50-55. https://doi.org/10.1038/nature06233

Tropea, D., Giacometti, E., Wilson, N. R., Beard, C., McCurry, C., Fu, D. D., Flannery, R., Jaenisch, R., & Sur, M. (2009). Partial reversal of Rett Syndrome-like symptoms in MeCP2 mutant mice. *Proc Natl Acad Sci U S A*, *106*(6), 2029-2034. https://doi.org/10.1073/pnas.0812394106

Tsimpolis, A., Kalafatakis, K., & Charalampopoulos, I. (2024). Recent advances in the crosstalk between the brain-derived neurotrophic factor and glucocorticoids. *Front Endocrinol (Lausanne)*, *15*, 1362573. https://doi.org/10.3389/fendo.2024.1362573

Tyzio, R., Nardou, R., Ferrari, D. C., Tsintsadze, T., Shahrokhi, A., Eftekhari, S., Khalilov, I., Tsintsadze, V., Brouchoud, C., Chazal, G., Lemonnier, E., Lozovaya, N., Burnashev, N., & Ben-Ari, Y. (2014). Oxytocin-mediated GABA inhibition during delivery attenuates autism pathogenesis in rodent offspring. *Science*, *343*(6171), 675-679. https://doi.org/10.1126/science.1247190

Uhlhaas, P. J., & Singer, W. (2013). High-frequency oscillations and the neurobiology of schizophrenia. *Dialogues Clin Neurosci*, *15*(3), 301-313. https://doi.org/10.31887/DCNS.2013.15.3/puhlhaas

van der Staay, F. J., Rutten, K., Barfacker, L., Devry, J., Erb, C., Heckroth, H., Karthaus, D., Tersteegen, A., van Kampen, M., Blokland, A., Prickaerts, J., Reymann, K. G., Schroder, U. H., & Hendrix, M. (2008). The novel selective PDE9 inhibitor BAY 73-6691 improves learning and memory in rodents. *Neuropharmacology*, *55*(5), 908-918. https://doi.org/10.1016/j.neuropharm.2008.07.005

Van Staveren, W. C., Steinbusch, H. W., Markerink-Van Ittersum, M., Repaske, D. R., Goy, M. F., Kotera, J., Omori, K., Beavo, J. A., & De Vente, J. (2003). mRNA expression patterns of the cGMP-hydrolyzing phosphodiesterases types 2, 5, and 9 during development of the rat brain. *J Comp Neurol*, *467*(4), 566-580. https://doi.org/10.1002/cne.10955

Varghese, M., Keshav, N., Jacot-Descombes, S., Warda, T., Wicinski, B., Dickstein, D. L., Harony-Nicolas, H., De Rubeis, S., Drapeau, E., Buxbaum, J. D., & Hof, P. R. (2017). Autism spectrum disorder: neuropathology and animal models. *Acta Neuropathol*, *134*(4), 537-566. https://doi.org/10.1007/s00401-017-1736-4

Vazdarjanova, A., Ramirez-Amaya, V., Insel, N., Plummer, T. K., Rosi, S., Chowdhury, S., Mikhael, D., Worley, P. F., Guzowski, J. F., & Barnes, C. A. (2006). Spatial exploration induces ARC, a plasticity-related immediate-early gene, only in calcium/calmodulin-dependent protein kinase II-positive principal excitatory and inhibitory neurons of the rat forebrain. *J Comp Neurol*, *498*(3), 317-329. https://doi.org/10.1002/cne.21003

Vermeersch, P., Buys, E., Sips, P., Pokreisz, P., Marsboom, G., Gillijns, H., Pellens, M., Dewerchin, M., Bloch, K. D., Brouckaert, P., & Janssens, S. (2009). Gender-specific modulation of the response to arterial injury by soluble guanylate cyclase alpha1. *Open Cardiovasc Med J*, *3*, 98-104. https://doi.org/10.2174/1874192400903010098

Von Békésy, G. (1960). Experiments in hearing.

Wallace, M. L., Burette, A. C., Weinberg, R. J., & Philpot, B. D. (2012). Maternal loss of Ube3a produces an excitatory/inhibitory imbalance through neuron type-specific synaptic defects. *Neuron*, *74*(5), 793-800. https://doi.org/10.1016/j.neuron.2012.03.036

Wang, J., Ethridge, L. E., Mosconi, M. W., White, S. P., Binder, D. K., Pedapati, E. V., Erickson, C. A., Byerly, M. J., & Sweeney, J. A. (2017). A resting EEG study of neocortical hyperexcitability and altered functional connectivity in fragile X syndrome. *J Neurodev Disord*, *9*, 11. https://doi.org/10.1186/s11689-017-9191-z

Wardle, R. A., & Poo, M. M. (2003). Brain-derived neurotrophic factor modulation of GABAergic synapses by postsynaptic regulation of chloride transport. *J Neurosci*, *23*(25), 8722-8732. https://doi.org/10.1523/JNEUROSCI.23-25-08722.2003

Wen, T. H., Afroz, S., Reinhard, S. M., Palacios, A. R., Tapia, K., Binder, D. K., Razak, K. A., & Ethell, I. M. (2018). Genetic Reduction of Matrix Metalloproteinase-9 Promotes Formation of Perineuronal Nets Around Parvalbumin-Expressing Interneurons and Normalizes Auditory Cortex Responses in Developing Fmr1 Knock-Out Mice. *Cereb Cortex*, *28*(11), 3951-3964. https://doi.org/10.1093/cercor/bhx258

Werling, D. M., & Geschwind, D. H. (2013). Understanding sex bias in autism spectrum disorder. *Proc Natl Acad Sci U S A*, *110*(13), 4868-4869. https://doi.org/10.1073/pnas.1301602110

Whitehead, M. L., Stagner, B. B., Martin, G. K., & Lonsbury-Martin, B. L. (1996). Visualization of the onset of distortion-product otoacoustic emissions, and measurement of their latency. *J Acoust Soc Am*, *100*(3), 1663-1679. https://doi.org/10.1121/1.416065

Wilde, M., Constantin, L., Thorne, P. R., Montgomery, J. M., Scott, E. K., & Cheyne, J. E. (2022). Auditory processing in rodent models of autism: a systematic review. *J Neurodev Disord*, *14*(1), 48. https://doi.org/10.1186/s11689-022-09458-6

Wizemann, T. M., & Pardue, M. L. (2001). In *Exploring the Biological Contributions to Human Health: Does Sex Matter?* https://doi.org/10.17226/10028

Wolter, S., Mohrle, D., Schmidt, H., Pfeiffer, S., Zelle, D., Eckert, P., Kramer, M., Feil, R., Pilz, P. K. D., Knipper, M., & Ruttiger, L. (2018). GC-B Deficient Mice With Axon Bifurcation Loss Exhibit Compromised Auditory Processing. *Front Neural Circuits*, *12*, 65. https://doi.org/10.3389/fncir.2018.00065

Wong, F. K., Bercsenyi, K., Sreenivasan, V., Portales, A., Fernandez-Otero, M., & Marin, O. (2018). Pyramidal cell regulation of interneuron survival sculpts cortical networks. *Nature*, *557*(7707), 668-673. https://doi.org/10.1038/s41586-018-0139-6

Woo, C. C., Miranda, B., Sathishkumar, M., Dehkordi-Vakil, F., Yassa, M. A., & Leon, M. (2023). Overnight olfactory enrichment using an odorant diffuser improves memory and modifies the uncinate fasciculus in older adults. *Front Neurosci*, *17*, 1200448. https://doi.org/10.3389/fnins.2023.1200448

Xiao, Y. (2017). Environmental enrichment intervention in animal models of autism. *Journal of Psychiatry and Brain Science*, *2*(6).

Yamaguchi, H., Hara, Y., Ago, Y., Takano, E., Hasebe, S., Nakazawa, T., Hashimoto, H., Matsuda, T., & Takuma, K. (2017). Environmental enrichment attenuates behavioral abnormalities in valproic acid-exposed autism model mice. *Behav Brain Res*, *333*, 67-73. https://doi.org/10.1016/j.bbr.2017.06.035

Yang, M., Perry, K., Weber, M. D., Katz, A. M., & Crawley, J. N. (2011). Social peers rescue autism-relevant sociability deficits in adolescent mice. *Autism Res*, *4*(1), 17-27. https://doi.org/10.1002/aur.163

Yashiro, K., Riday, T. T., Condon, K. H., Roberts, A. C., Bernardo, D. R., Prakash, R., Weinberg, R. J., Ehlers, M. D., & Philpot, B. D. (2009). Ube3a is required for experience-dependent maturation of the neocortex. *Nat Neurosci*, *12*(6), 777-783. https://doi.org/10.1038/nn.2327

Yusuf, P. A., Hubka, P., Tillein, J., & Kral, A. (2017). Induced cortical responses require developmental sensory experience. *Brain*, *140*(12), 3153-3165. https://doi.org/10.1093/brain/awx286

Zhang, X., & Gan, R. Z. (2013). Dynamic properties of human round window membrane in auditory frequencies running head: dynamic properties of round window membrane. *Medical engineering & physics*, *35*(3), 310-318.

Zola-Morgan, S., Squire, L. R., Alvarez-Royo, P., & Clower, R. P. (1991). Independence of memory functions and emotional behavior: separate contributions of the hippocampal formation and the amygdala. *Hippocampus*, *1*(2), 207-220. https://doi.org/10.1002/hipo.450010208

Zuccotti, A., Kuhn, S., Johnson, S. L., Franz, C., Singer, W., Hecker, D., Geisler, H. S., Kopschall, I., Rohbock, K., Gutsche, K., Dlugaiczyk, J., Schick, B., Marcotti, W., Ruttiger, L., Schimmang, T., & Knipper, M. (2012). Lack of brain-derived neurotrophic factor hampers inner hair cell synapse physiology, but protects against noise-induced hearing loss. *J Neurosci*, *32*(25), 8545-8553. https://doi.org/10.1523/JNEUROSCI.1247-12.2012

Zucker, I., Prendergast, B. J., & Beery, A. K. (2022). Pervasive Neglect of Sex Differences in Biomedical Research. *Cold Spring Harb Perspect Biol*, *14*(4). https://doi.org/10.1101/cshperspect.a039156

STATEMENT OF CONTRIBUTION

For all experiments, genotyping of mice was performed by Wibke Singer, Elina Molden, and Alma Assenheimer.

Section 3.1, "Characterizing the Central Phenotype of *Bdnf*^{Pax2} KO Mice." Hearing measurements were performed and analyzed by the author (**Figure 3.1**). For quantification of excitatory and inhibitory molecular markers (**Figure 3.2**), staining was performed by Karin Rohbock; imaging and quantification were performed by the author. EEG measurements (**Figure 3.3–5**) were conducted by the author, along with Dila Calis, Stefan Fink, Rüdiger Land, and Philine Marchetta; analysis was performed by Konrad Dapper. For analysis of dendritic spines (**Figure 3.6**), staining was performed by the author and Philine Marchetta, imaging was performed by the author, and analysis was performed by the author and Dila Calis.

Section 3.2, "Investigating the Origin of the *Bdnf*^{Pax2} KO Phenotype." EEG measurements (**Figure 3.7**) were conducted by the author, along with Dila Calis, Stefan Fink, Rüdiger Land, and Philine Marchetta; analysis was performed by Konrad Dapper. Electrocochleography measurements and analysis (**Figure 3.8–9**) were performed by Philine Marchetta. For MOC efferent adaptation (**Figure 3.10**), measurements and analysis were conducted by the author.

Data from sections 3.1 and 3.2 are included in the publication Marchetta et al., 2024.

Section 3.3, "Treatment of *Bdnf*^{Pax2} KO Mice Using a Cognitive Stimulator." For corticosterone level analysis (**Figure 3.11**), ELISAs were performed by the author with assistance from Elina Molden; analysis was performed by the author. All hearing measurements (**Figure 3.12–14**) were performed and analyzed by the author. All fEPSP recordings (**Figure 3.15–17**) were performed and analyzed by the author. In situ hybridization for analysis of NO-GC mRNA (**Figure 3.18–21**) was performed by Wibke Singer; imaging and quantification were performed by the author.

Section 3.4, "Treatment of *Bdnf*^{Pax2} KO Mice Using Acoustic Enrichment." All hearing measurements (**Figure 3.22–25**) were performed and analyzed by the author. Immunohistochemical staining of cochleae (**Figure 3.23**) was performed by Karin Rohbok, Nadine Heckmann, Alma Assenheimer, and the author; imaging and quantification were performed by the author. All behavioral experiments (**Figure 3.26**, **Figure 3.30**) were conducted and analyzed by the author. All fEPSP recordings (**Figure 3.27–29**) were performed and analyzed by the author.

Section 3.5, "A Note on Sex Differences." All hearing measurements were performed and analyzed by the author.

The present work was written entirely by the author with the following exceptions, which were adapted from publications written and edited by the author of the present work:

Sections 2.7, 2.8, 2.10.2, 2.11, 2.13, 3.1, 3.2.1, 3.2.2, and 3.2.3 were adapted from Marchetta et al., 2024.

Sections 2.6 and 2.14 were adapted from Savitska et al., 2022.

Section 2.14 was additionally adapted from Calis et al., 2023.

Sections 2.4.3, 2.5.1, and 2.9 were adapted from the master thesis of the author of the present work.

ACKNOWLEDGEMENTS

First and foremost, my deepest gratitude goes to Professor Marlies Knipper. Pursuing a doctoral title in your lab with a project I became passionate about has been one of the most fulfilling (and challenging) experiences of my life. Your mentorship over the years has helped me grow both scientifically and personally. Thank you for pushing me out of my comfort zone, nurturing my strengths, and supporting me in areas where I had weaknesses.

I would also like to extend my thanks to Professor Steffen Hage and Professor Peter Ruth for being part of my advisory board over the past three years. Your feedback and guidance have provided crucial direction for my project, and I deeply appreciate our fruitful discussions. Additionally, I am grateful to Professor Steffen Hage for serving as the second evaluator of my thesis.

My gratitude also goes to Junior Professor Lena Veit for agreeing to be an examiner at my defense.

I would like to thank the GRK 2381 "cGMP, from Bedside to Bench" for the opportunity to be an associated member of this prestigious program and for expanding my interests with such diverse, interdisciplinary seminars.

I am especially grateful to Dr. Wibke Singer for quietly advocating for me when I couldn't do so for myself. Your unwavering support helped me through the hardest days of this doctoral journey, and your German lessons never failed to put a smile on my face—word of the day? Our scientific discussions always managed to clarify even the most confusing results, and I am deeply thankful for these conversations. I would also like to express my thanks to Professor Lukas Rüttiger for your mentorship, fresh perspectives, and patience in explaining complex technical aspects. Finally, I am grateful to all past and present members of the Knipper Lab who supported me during my time there.

I am also grateful to all of the people who supported me on a personal level during these past years.

To my mother, for encouraging me when I said I wanted to move halfway across the world (then following me), for always giving me advice when I needed it, for believing in me and carrying me through my hardest moments, for unfailingly making me laugh when I'm on the verge of tears, and for raising me up when I hit the dust. To my grandmother, for being my go-to call before a conference, for listening to me practice my presentations and telling me what I should (and shouldn't) wear to conferences. To my grandfather, for always picking up the phone and reminding me of the sweetness of home, for making me laugh with your sometimes-terrible jokes, and for always trying to get me to schedule my trips home during hunting season! And to all of my aunts, uncles, cousins, and the rest of the Hesses for supporting me on this journey and for always making my time back home special.

To my best friend Marta, who always answers the phone knowing that she can judge how bad my mental state is by how often I call her. To Hannes, Rüya, Valentina, Robin, Krithika, and Marleen for being there with me to celebrate my successes and grieve my failures. Finally, I am deeply grateful to my partner who has always been a peaceful reprieve from the everyday troubles of the PhD, who has helped me learn how to relax, and whose quiet strength I could always fall back on when mine failed.

"I wanna thank me for believing in me. I wanna thank me for doing all this hard work. I wanna thank me for having no days off. I wanna thank me for never quitting." — Snoop Dogg